UNIVERSITY OF KWAZULU-NATAL

DIFFUSE RADIO EMISSION IN ACTPOL CLUSTERS

by

Sinenhlanhla Precious Sikhosana

Submitted in fulfillment of the
academic requirements for the degree of
Doctor of Philosophy (Science)
in the
School of Mathematics, Statistics, and Computer Science,
University of KwaZulu-Natal

Durban
April, 2021

As the candidate's supervisor I have approved this thesis for submission.

Signed: ..... Name: ..... Date: .....

For my family, whose unwavering support
cushioned me in moments of defeat.

For every young girl who dares to dream.

ABSTRACT

Low-frequency radio observations of galaxy clusters reveal cluster-scale diffuse emission that is not associated with individual galaxies. Studying the properties of these diffuse radio sources gives insight into astrophysical processes such as cosmic ray transportation in the intracluster medium (ICM). Observations have linked the formation of radio halos and relics with turbulence caused by cluster mergers and the formation of mini-halos to gas sloshing in cool-core clusters. Statistical studies of large galaxy cluster samples have been used to determine how the radio properties of diffuse emission scale with the mass and X-ray luminosity of the host clusters. Such studies are crucial for refining the formation theories of diffuse emission. New generation telescopes with wide bandwidths and high sensitivity such as the upgraded Giant Metrewave Radio Telescope (uGMRT) and MeerKAT are advantageous for the study of faint extended emission in large cluster samples.

The main aim of this thesis was to do an in-depth study of the diffuse radio emission using a cluster sample that spans a wider mass and redshift range compared to the currently studied parameter space. We developed data reduction techniques for calibrating data from telescopes such as uGMRT and MeerKAT. The wide bandwidth of these telescopes introduces directional dependent effects (DDEs) that make the calibration process extremely complicated. However, such observations are excellent for studies of the faint diffuse emission and in-band spectral indices of this emission.

In the first part of this thesis, we focused on the study of diffuse radio emission in a Sunyaev-Zeldovich (SZ) selected sample of clusters. These clusters were observed by the Atacama Cosmology Telescope's Polarimetric extension (ACTPol). We used archival and new GMRT observations for the radio analysis of this sample. We reported newly detected diffuse emission in the following clusters: a radio halo and revived fossil plasma in ACT-CL J0137.4−0827, a radio relic in ACT-CL J2128.4+0135, and a candidate relic in ACT-CL J0022.2−0036. The radio analysis of the full sample revealed that the fraction of clusters in the sample hosting diffuse emission is 26.7% excluding candidate emission and 30% when it is included. The detection rate of the diffuse emission over all categories is lower than the detection rates reported in literature. We note that this may be because the sample comprised high redshift ($z > 0.5$) and low mass clusters ($M_{500c,SZ} < 5 \times 10^{14}$ $M_{\odot}$), though future more sensitive observations of these clusters could reveal fainter diffuse emission structures. We compared our results to the most recent radio halo and radio relic scaling relations. The radio halo $P_{1.4GHz} - M_{500}$ scaling relation plot indicates that a few flatter spectrum radio halos are located in the region previously known to be populated by ultra-steep spectrum radio halos (USSRHs). Finally, we presented preliminary results of the uGMRT wideband backend (GWB) data reduction for ACT-CL J0034.4+0225, ACT-CL J0137.4−0827, and ACT-CL J2128.4+0135. We prioritised these clusters because the narrowband data revealed that they host diffuse emission. However, once the data reduction algorithm is improved, we will reduce the remaining clusters with non-detections. Comparing the GWB results to the narrowband GMRT data, we note that the radio halo observed in ACT-CL J0137.4−0827 is more extended in the GWB data. The diffuse emission is detected at a higher signal-to-noise ratio in the GWB images for the three clusters. We note that an improvement in the GWB reduction algorithm might reveal diffuse emission that was not detected in the narrowband data.

In the second part of the thesis, we used MeerKAT observations to study diffuse emission in the Bullet Cluster (1E0657−56), RXC J1314.4−2515, Abell 3562, and Abell 3558. We detected new extended features in the radio halos hosted by the Bullet cluster and Abell 3562. We assume that the decrement feature in the Bullet cluster might be an indication of a second wave of merger activity. The ridge feature in the peripheral region of the radio halo in Abell 3562 overlaps with the edge of the X-ray emission. Hence, we assume that the feature might be related to a shock

region. We also reported the detection of a new mini-halo in Abell 3558. MeerKAT's sensitivity and wide bandwidth enabled us to perform in-band spectral index studies and produce spectral index maps for the Bullet cluster, RXC J1314.4−2515, and Abell 3562. The spectral index maps of the relics in the Bullet cluster and RXC J1314.4−2515 indicate a spectral steepening towards the cluster center, while the spectral index map of the radio halo in the Bullet cluster indicates radial spectral steepening. The spectral index map of Abell 3562 indicates that the radio halo and ridge have similar spectral index variations, which suggests that the ridge feature is related to the radio halo.

ACKNOWLEDGMENTS

My PhD journey was faced with many challenges, however, I was blessed to have a team of supervisors that supported me throughout the journey. I would like to thank Prof. Kavilan Moodley, my main supervisor and mentor since undergrad. His work ethic and mentorship has pushed me beyond my limits. The sincerity he shares for my personal life has also greatly contributed to my decision of pursuing a PhD. I would like to thank my co-supervisor Prof. Matt Hilton for always assisting me when I needed new software installed, when load shedding affected the supercomputers I was working on, and when I faced many other technical glitches. I thank Dr. Kenda Knowles for always being my sounding board and going an extra mile in ensuring that I completed my thesis on time. I would like to thank all the academic staff, administrators, and students that are part of the University of KwaZulu-Natal's Astrophysics Research Centre for always crating a conducive work environment.

The reduction of data from new generation telescopes required unprecedented calibration skills. I was able to acquire these skills through the help of many national and international collaborators. I would like to thank Prof. Ian Heywood for always making time to meet and for providing insight on how to solve the calibration challenges I was facing. I thank Prof. Ishwar Chandra and Dr. Ruta Kale for hosting me in India and for assisting with the challenges I was facing with the uGMRT data. I thank Dr. Sphesihle Makhathini for also contributing in my data analysis procedures. I would also like to thank Prof. Oleg Smirnov and the Rhodes

university's Centre for Radio Astronomy Techniques and Technologies team for permitting to use their computing facilities.

The financial support from the South African Radio Astronomy Observatory's Human Capital Development program was pivotal for my academic journey. I have received their scholarship from first year undergraduate up until my PhD. These scholarships ensured that I pursued my passion for academic with ease because I could also make financial contributions at home. The research grants from L'oreal-UNESCO For Women In Science young talents programme and the South African Women in Science Awards also assisted with my financial needs.

Finally, I would like to thank all my family and friends for their support throughout the journey. The prayers of my mother and grandmother carried me through the challenging times. Their pride in me always propelled me to keep going. My sister's assistance with any personal administrative work I needed kept me sane in moments of crazy work schedules. My friend Amanda Msomi has graciously cared for me from the beginning of the PhD journey. I am truly blessed to have her by my side, our conversations always left me hopeful.

PREFACE

The work described in this thesis was carried out in the School of Mathematics, Statistics, and Computer Science, University of KwaZulu-Natal from September 2017 to January 2021. This dissertation was completed under the supervision of Prof. K. Moodley, with co-supervision by Dr K. Knowles and Prof. M. Hilton.

This study represents original work by the author and has not been submitted in any form for any degree or diploma to any other tertiary institution. Where use was made of the work of others it has been duly acknowledged in the text.

DECLARATION OF NON-PLAGIARISM

I, **Sinenhlanhla Precious Sikhosana** declare that

1. The research reported in this thesis, except where otherwise indicated, is my original research.

2. This thesis has not been submitted for any degree or examination at any other university.

3. This thesis does not contain other persons' data, pictures, graphs or other information, unless specifically acknowledged as being sourced from other persons.

4. This thesis does not contain other persons' writing, unless specifically acknowledged as being sourced from other researchers. Where other written sources have been quoted, then:

   (a) Their words have been re-written but the general information attributed to them has been referenced.

   (b) Where their exact words have been used, then their writing has been placed in italics and inside quotation marks, and referenced.

5. This thesis does not contain text, graphics or tables copied and pasted from the Internet, unless specifically acknowledged, and the source being detailed in the thesis and in the References sections.

Signed in Springfield, KwaZulu-Natal: ..... Date: .....

DECLARATION OF PUBLICATIONS

Details of contribution to publications that form part of and/or include research presented in this thesis:

Section 3.3

MeerKAT's View of the Bullet Cluster 1E 0657−55.8

Sikhosana S.P, Hilton M., Knowles K., Moodley K., et al. (2021), in preparation.

Signed in Springfield, KwaZulu-Natal: ..... Date: .....

CONTENTS

LIST OF TABLES

LIST OF FIGURES

CHAPTER 1

INTRODUCTION

The hot Big Bang theory is currently the most widely accepted theory which describes the formation and evolution of the Universe. According to this theory, the Universe began as a small and infinitely dense region. After 10^{-35} seconds of its formation, the Universe expanded exponentially (Guth, 1981). As the expansion slowed down, it cooled to temperatures where nuclei and later atoms could form (Peebles and Yu, 1970). The growth in primordial perturbations resulted in larger gravitational potential wells accreting more matter leading to the formation of stars, galaxies, and clusters of galaxies (Peebles, 1980).

The evolutionary history of the Universe can be probed using various observables such as the cosmic microwave background (CMB; Penzias and Wilson, 1965), the baryon acoustic oscillation's (BAO's; Eisenstein and White, 2004; Bassett and Hlozek, 2010; Aubourg et al., 2015) signature, and Type Ia supernovae studies (Riess et al., 1998). Galaxy clusters are also good tracers of the history of our Universe. They can be used as probes for dark matter (Zwicky, 1933; Clowe et al., 2004; Monteiro-Oliveira et al., 2018), and the evolution and distribution of the large scale structure in the Universe (Böhringer, 2008; Allen et al., 2011; Weinberg et al., 2013). Measuring the evolutionary number density of galaxy clusters as a function of mass and redshift $N(M, z)$ is also used as a tool to constrain cosmological parameters such as the mean

matter density and the dark energy density and equation of state (Carlstrom et al., 2002; Planck Collaboration et al., 2016; Bocquet et al., 2019). Galaxy clusters are also excellent laboratories for studying turbulence, plasma physics, and cosmic ray transportation in gravitationally bound, dense large scale structures.

1.1 Galaxy Clusters

According to the concordance Λ-cold dark matter (ΛCDM) model, the Universe is made up of $\sim$70% dark energy, $\sim$25% dark matter, and $\sim$5% baryonic matter (Planck Collaboration et al., 2020). This model further postulates that matter in the Universe originates from initial density perturbations and forms hierarchically. Smaller objects form first, and as the gravitational potential well grows, larger structure forms (Peebles, 1980; Kravtsov and Borgani, 2012; Springel et al., 2018). Galaxy clusters are large scale structures that consist of $\sim$1000s of galaxies bound by gravity. Galaxy clusters, as the largest virialised systems in the universe, are at the top of the structure formation hierarchy. They form through mergers of sub-clusters and the accretion of matter from the cosmic web. Mergers of massive clusters are the most energetic events since the Big Bang (Sarazin, 2002; Molnar, 2015). The energy released during cluster mergers (up to 10^{64} ergs) is dissipated through turbulence. The turbulent motions result in the amplification of magnetic fields and cosmic ray electrons (CRe) being rejuvenated to relativistic speeds. The interactions of the CRe with the magnetic fields lead to cluster-scale synchrotron emission (Brunetti and Jones, 2014).

Dark Matter constitutes the largest portion (80%) of the mass in galaxy clusters: 15% is in the form of the hot dense plasma called the intracluster medium (ICM), and the rest (5%) is the baryonic matter in galaxies. As shown in Figure 1.1, the different constituents of galaxy clusters can be probed using observations at different wavelengths. Hence, multi-wavelength studies give a complete view of these systems (Andersson et al., 2011; Buddendiek et al., 2015; Takey et al., 2019; Zhu et al., 2019; Zenteno et al., 2020).

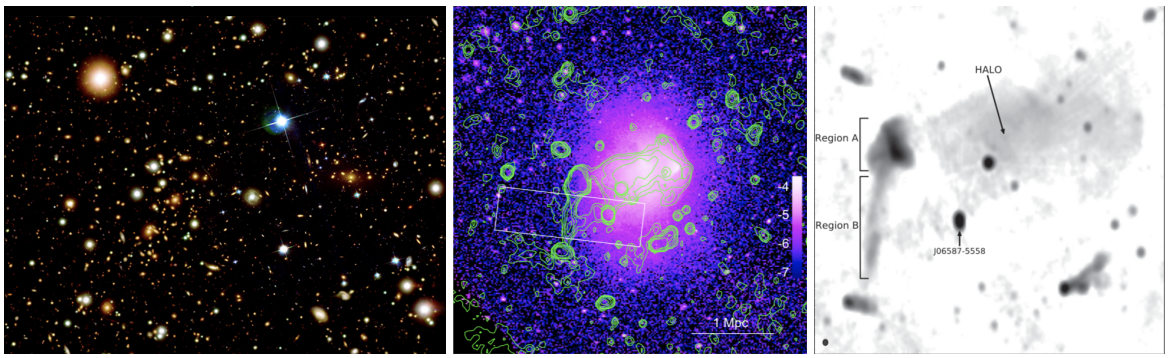

Figure 1.1: Multi-wavelength images of the Bullet cluster. *Left:* Hubble telescope's optical image. Source: hubblesite.org. *Middle: Chandra* telescope's X-ray image overlaid with radio contours from the Australia Telescope Compact Array (ATCA). The rectangular strip was the region used to calculate the X-ray surface brightness across the radio relic. Source: Shimwell et al. (2015). *Right:* ATCA's radio image of the Bullet cluster. Source: Adapted from Shimwell et al. (2015).

1.1.1 The Intracluster Medium

The bulk ($\sim$80%) of the baryonic content in galaxy clusters is found in the ICM; a low-density plasma ($n_e \sim 10^{-3}$ cm^{-3}) that emits radiation at X-ray wavelengths (Springel et al., 2018). The gas collisions in the ICM result in the electrons emitting bremsstrahlung radiation with X-ray luminosities $L_{\rm X}$ $\sim 10^{43-45}$ ergs/s. Dynamical disturbances in clusters appear as discontinuities in the X-ray brightness distribution. Hence, X-ray studies can be used to study the morphology and merger-state of galaxy clusters (Markevitch et al., 2000; Zwicky, 1933; Markevitch and Vikhlinin, 2007; Parekh et al., 2015).

Hard X-ray and radio observations of galaxy clusters have revealed that the ICM contains cosmic rays and magnetic fields (Kronberg, 1994; Rephaeli and Gruber, 2003). The cosmic rays are deposited in the ICM by energetic activities such as active galactic nuclei (AGN) jets, and supernovae (Fermi, 1949; Ryu et al., 2003; Dorman, 2019). The origin of the magnetic fields in the ICM is not well understood. Models predict that magnetic fields either originate from astrophysical processes such as AGN jets, or they are primordial (Carilli and Taylor, 2002; Hu et al., 2020). Observations have measured the cluster magnetic field strengths to be $\sim 0.1 - 1$

μG (Vogt et al., 2005; Bonafede et al., 2010; Johnson et al., 2020). Observations have shown that magnetic field strengths of galaxy clusters at high redshift ($z \gtrsim 0.6$) are similar to those in nearby clusters (Lindner et al., 2014; Di Gennaro et al., 2020). These results indicate that there was a fast amplification of magnetic field strengths during the initial formation stages of galaxy clusters. The evolution and amplification of magnetic fields are also still under investigation (Clarke et al., 2001; Donnert et al., 2018; Gaensler et al., 2004). However, it is well established that magnetic fields play a crucial role in the transportation of energy in the ICM, resulting in the increased life-times of cosmic rays (Sarazin, 1988; Ehlert et al., 2020).

1.1.2 Cluster Detection Methods

1.1.2.1 Optical Surveys

Galaxy clusters were first detected at optical wavelengths using catalogues from photographic plates (Zwicky, 1938; Abell, 1958; Zwicky and Kowal, 1968). Scientists visually inspected photographic plates and categorised clusters as regions with a dense population of galaxies. Earlier optical studies were restricted by instruments that could only probe low-redshift clusters due to the dimming effect on high redshift ($z \gtrsim 0.8$) clusters (Calvi et al., 2014). Technological advancements have led to the construction of powerful optical telescopes that probe deeper in the sky; this resulted in larger catalogues with higher redshift detections (Rykoff et al., 2016; Radovich et al., 2017; Gao et al., 2020). The photometric and spectroscopic data from optical catalogues can be used to determine the dynamical state of galaxy clusters (Aguerri and Sánchez-Janssen, 2010; Wen and Han, 2013; Boschin et al., 2020). However, optical detections are only sensitive to galaxies, which only make-up $\sim 5\%$ of the total mass of galaxy clusters. Determining the optical survey's selection function is a major constraint since optical clusters rely on empirical things like calibrating 'richness'[1] against other cluster mass proxies. Optical surveys also have other problems such as projection effects. The projection effects are caused by contamination due to objects along the line of sight. These effects become more severe at higher redshifts and can lead to false detections (Yee and Gladders, 2002; Ramos-Ceja et al., 2019). Other observational

[1]The number of galaxies associated with a galaxy cluster.

probes are required for more complete cluster detections.

1.1.2.2 X-ray Surveys

The first catalogue of X-ray clusters was observed by the *UHURU* satellite (Giacconi et al., 1972). X-ray surveys detect galaxy clusters via the X-ray luminosity of the ICM (Giacconi et al., 1972; Henriksen and Mushotzky, 1986; Vikhlinin et al., 1998; Boschin, 2002; Jimenez-Gallardo et al., 2020; Sahlén et al., 2009; Ebrahimpour et al., 2018; Käfer et al., 2020). High-resolution X-ray observations can also probe the dynamical disturbance and morphology of clusters (Buote and Tsai, 1995; Nurgaliev et al., 2017; Yuan and Han, 2020). However, X-ray observations are also flux-limited which gives rise to biases in the selection function (Eckert et al., 2011; Andrade-Santos et al., 2017). Low-angular-resolution X-ray satellites can also result in surveys with biased cluster catalogues due to cluster-projection effects (Ramos-Ceja et al., 2019). The projected 2D morphology of clusters impacts the derivation of cluster masses because such studies rely on the assumption that galaxy clusters are spherically symmetric. Hence, although X-ray surveys have more robust algorithms for detecting galaxy clusters compared to optical surveys, studies at other wavelengths were necessary to further improve the detection of galaxy clusters.

1.1.2.3 Clusters Detected using the SZ Effect

The thermal Sunyaev-Zel'dovich effect (Sunyaev and Zeldovich, 1970, 1972) is used to probe galaxy clusters at millimetre wavelengths. The SZ effect is observed as a distortion in the CMB's black body spectrum, where there appears to be a change in sign of the cluster intensity at $\sim$220 GHz against the CMB background. The shift in the CMB's blackbody spectrum appears as shown in Figure 1.2. The spectral distortion is caused by the inverse Compton scattering of CMB photons as they travel through the hot ($\sim 10^{7-8}$ K) ICM gas. The observed SZ signal is calculated as the integrated Comptonisation parameter across the cluster's solid angle

$$Y = \int_{\Omega} y \, d\Omega \, , \tag{1.1}$$

where

$$y = \frac{\sigma_T}{m_e c^2} k_B \int n_e T_e \, dl \tag{1.2}$$

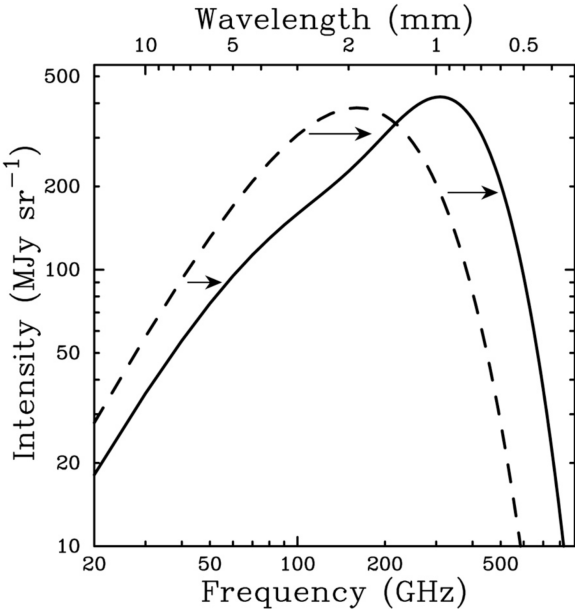

Figure 1.2: The dashed line shows the undistorted CMB spectrum, and the solid line shows the CMB spectrum after it is distorted by the SZ effect. Source:(Carlstrom et al., 2002).

and

$$d\Omega \propto \frac{1}{D_A^2} \ , \tag{1.3}$$

where σ_T is the Thomson cross-section, k_B is the Boltzmann constant, m_e is the electron mass, and n_e and T_e are the electron number density and temperature, respectively. $D_{\rm A}$ is the angular diameter distance. The SZ signal is redshift- independent, hence it is not strongly affected by redshift dimming. Since SZ surveys are not limited by cluster redshifts, they provide mass-limited cluster catalogues. The lowest detectable mass is determined by the noise level of the survey (Birkinshaw, 1999; Carlstrom et al., 2002; Mroczkowski et al., 2019). This property of the SZ signal allowed for the expansion of the targetable parameter space of galaxy clusters. Millimetre telescopes such as the *Planck* satellite (Planck Collaboration et al., 2014, 2016), the ground-based Atacama Cosmology Telescope (ACT; Hasselfield et al., 2013; Hilton et al., 2018, 2020), and the South Pole Telescope (SPT; Bleem et al., 2015, 2020) have been used to detect galaxy clusters. The SZ signal is expected to correlate with the cluster mass and is not significantly affected by the cluster dynamics (Sifón et al., 2013; Dietrich et al., 2019). Hence, SZ surveys

have allowed for the exploration of galaxy clusters using well defined selection functions.

1.2 Non-thermal Diffuse Emission in Galaxy Clusters

Non-thermal diffuse emission in galaxy clusters was first discovered in the Coma cluster (Large et al., 1959; Willson, 1970; Giovannini et al., 1993; Brown and Rudnick, 2011; Bonafede et al., 2020). This discovery was a confirmation of the existence of relativistic electrons and magnetic fields in the ICM (Sarazin, 1988; Kravtsov and Borgani, 2012; Shalchi, 2020). The interactions of the electrons with magnetic fields results in cluster-scale synchrotron emission (see Ferrari et al., 2008; Feretti et al., 2012; Brunetti and Jones, 2014; van Weeren et al., 2019, for review). The energy distribution of the CRe can be described using the power law (Blandford and Eichler, 1987):

$$n(E)\ dE \propto E^{-p}\ dE\ , \tag{1.4}$$

where

$$p = 1 - 2\alpha\ . \tag{1.5}$$

α is the radio spectral index which can be related to the integrated flux in the following manner:

$$S_\nu \propto \nu^{-\alpha}\ . \tag{1.6}$$

The synchrotron emitting electrons ($\gamma \sim 10^4$ GeV) lose energy very fast. Their radiative lifetime is given by

$$t_{age}[yr] \approx 3.2 \times 10^{10} \frac{B^2}{B^2 + B^2_{CMB}} [(1+z)\nu]^{-1/2}\ . \tag{1.7}$$

where $B_{\rm CMB}$ is the magnetic field strength of the CMB ($B_{\rm CMB}$ (μGauss) $\approx$3.25 (1 + z)^2), B is the measured cluster magnetic field intensity, ν is the observing frequency in MHz, and z is the redshift of the observed source. The typical radiative lifetimes of these electrons are t$_{age}$ $\lesssim 10^8$ yrs and their diffusion length-scales are a few kpc (Blasi, 2001). The presence of large scale ($\sim$100 kpc to few Mpc) synchrotron emission gives rise to what is known as the *diffusion problem*. The radiative lifetime of electrons (see Equation 1.7) is much shorter than the diffusion

time required for electrons to cover such large scales. There must exist acceleration mechanisms (Jaffe, 1977; Petrosian and Bykov, 2008) that produce the observed diffuse radio emission.

Diffuse radio emission can be categorised into various groups based on size, morphology, and cluster dynamics. The main groups are radio halos, which can be further sub-divided into giant radio halos (GRHs; Raja et al., 2021) and radio mini-halos (RMHs; Timmerman et al., 2020), radio relics (RRs; Rajpurohit et al., 2020c), and the recently detected revived fossil plasma (Giacintucci et al., 2020). Many theories have been derived to explain the formation mechanisms of these sources. Observational scaling relations (Cassano et al., 2013; Cuciti et al., 2015) have also been used to distinguish the theories that best explain the observables. However, until recently, observations have been primarily limited by telescope sensitivity due to the difficulty in extracting emission in the presence of bright sources. The restricted samples limited the investigation of how the diffuse emission's radio power scales with various cluster properties. The current scaling relations have been derived from cluster samples restricted to high mass and low redshift clusters. Expanding the parameter space is crucial for understanding the cosmological evolution of these sources and their connection to cluster mergers. The new generation telescopes such as the LOw-Frequency ARray (LOFAR; van Haarlem et al., 2013), MeerKAT (Jonas and MeerKAT Team, 2016), and the upgraded Giant Metrewave Radio Telescope (uGMRT; Gupta et al., 2017), have opened up a new window which will lead to the refinement of the formation theories (Knowles et al., 2019; Raja et al., 2021; van Weeren et al., 2020). We now examine each of these classes of diffuse emission in turn.

1.2.1 Giant Radio Halos

GRHs are extended diffuse radio sources, located in central regions of clusters. They usually have smooth spherical morphology that overlaps with the X-ray brightness and their size is $\sim 1-2$ Mpc. The polarisation percentages of these sources are typically $< 10\%$, with a few exceptions (Govoni et al., 2005; Bonafede et al., 2009). The GRH in the Coma cluster (see Figure 1.3) is the prototype of these sources. Multi-frequency radio observations of GRHs enable us to study their spectral index properties. Most studies report that GRHs have steep spectra ($\alpha \leqslant -1$). Two

main theories have been derived to explain their formation mechanisms; the hadronic model and the re-acceleration model (Jaffe, 1977; Dennison, 1980). There also exists hybrid models, which suggest that the observed diffuse radio halo emission can result from the re-acceleration of electrons produced by hadronic proton-proton collisions (Miniati et al., 2001; Brunetti and Blasi, 2005; Brunetti et al., 2017).

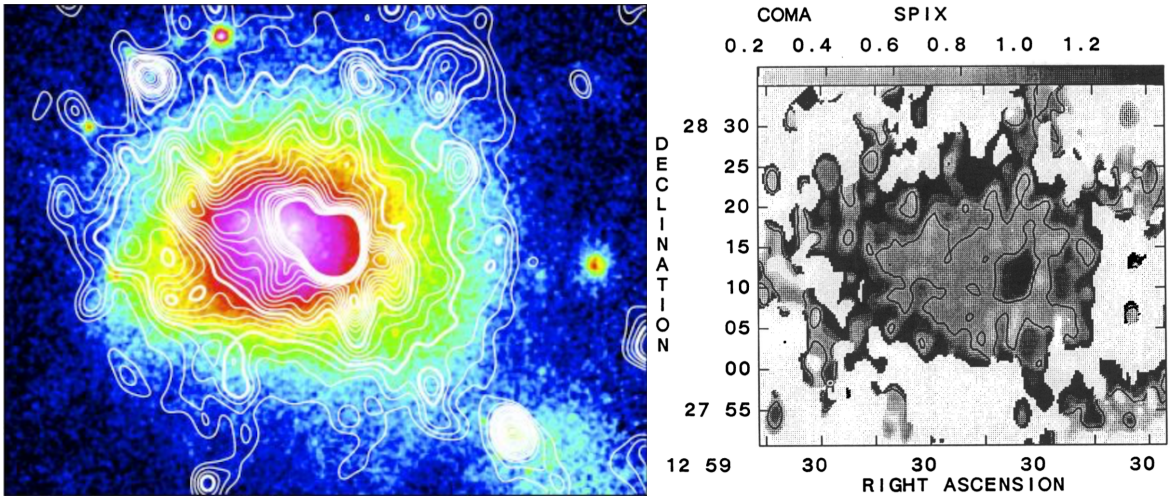

Figure 1.3: *Left: ROSAT* X-ray image of the Coma cluster with radio halo contours from the Westerbork Synthesis Radio Telescopes observations. The GRH in the Coma cluster is a prototype of these sources and has been extensively studied (Willson, 1970; Jaffe et al., 1976; Venturi et al., 1990; Thierbach et al., 2003; Bonafede et al., 2020). Source: Adapted from Brown and Rudnick (2011). *Right:* A spectral index map of the Coma cluster. Source: Giovannini et al. (1993).

1.2.1.1 Formation Mechanisms

Re-acceleration Model

Currently, the most widely accepted model is the re-acceleration model (Jaffe, 1977; Brunetti et al., 2001; Donnert and Brunetti, 2014). According to this model, a pool of pre-existing electrons (Pinzke et al., 2017) is re-accelerated through second-order Fermi mechanism by ICM turbulence developed during cluster mergers. The turbulent energy dissipated from cluster mergers

is not sufficient to accelerate the thermal electrons in the ICM. However, pre-existing relativistic electrons can be re-accelerated to the ∼Mpc scales as observed in radio halos. Observations have found that these sources are significantly affected by the dynamics of the host cluster (Markevitch et al., 2005; Cassano et al., 2011; Lindner et al., 2014; Knowles et al., 2016b; Cassano et al., 2019). The power of the radio emission has been found to correlate with thermal host cluster properties. Non-detections are located an order of magnitude below the correlation (Brunetti et al., 2007; Cassano et al., 2013; Cuciti et al., 2015), as predicted by the re-acceleration model. The observed spectral properties of these sources, including ultra steep spectrum radio halos (USSRHs; Wilber et al., 2018), are fully accounted for by the re-acceleration model (Brunetti and Jones, 2014).

Although the re-acceleration theory is accepted as the primary mechanism, there are still a few aspects that need further investigation. The main open question is the source of the pre-existing population of electrons. The suggested sources include electrons deposited in the ICM by AGN activity, thermal protons pre-accelerated by cluster merger shocks, and the hadronic secondary electrons (Brunetti and Blasi, 2005; Shimwell et al., 2016; de Gasperin et al., 2017b). Another mystery is the presence of radio halos in clusters that show no trace of merger activity (Venturi et al., 2017b; Kale et al., 2019). Other models, such as magnetic re-connection, attempt to resolve such constraints (Brunetti and Lazarian, 2016).

Hadronic Model

According to the hadronic model, secondary CRe are produced by the interactions between CR protons and thermal protons in the ICM (Dennison, 1980; Blasi and Colafrancesco, 1999; Keshet, 2010; Enßlin et al., 2011). These interactions yield CRe throughout the ICM. The radio power and X-ray scaling relations of radio halos favour this model since the radio emission traces the thermal emission. However, there are various constraints of this model, including the unobserved gamma-ray emission. The proton-proton interactions emit gamma rays as a by-product. Many studies have targeted clusters in search of these gamma rays. There have been no detections thus far; only upper limits have been derived (Reimer et al., 2003; Ackermann et al., 2010;

Colavincenzo et al., 2020). $Fermi$-Large Area Telescope (LAT; Atwood et al., 2009) observations of the Coma cluster conclusively excluded the hadronic model as a primary formation mechanism for the radio halo (Brunetti et al., 2017). Other observational constraints include the break-frequency spectrum (Brunetti et al., 2013), the spatial distribution of radio halo emission (Brunetti and Jones, 2014, for review), and USSRHs. The hadronic model does not account for these observables. Even though observations rule out hadronic models as the primary source of radio halo emission, hybrid models suggest that these hadronic interactions may produce a seed population of electrons that is then re-accelerated to form GRHs (Brunetti and Blasi, 2005; Brunetti et al., 2017).

1.2.1.2 Spectral Index Properties

The spectral index properties of radio halos are essential for constraining the origin of these sources. However, there are difficulties in studying the radio spectrum since it is directly related to the measured flux of radio halos at broad frequency ranges. Flux measurements have many uncertainties; these include flux-scale errors, point source subtraction uncertainties, and calibration errors. These uncertainties make it difficult to extract the faint radio halo emission fluxes. However, some studies have probed spectral properties of radio halos. The radio halo spectral properties can be investigated using the integrated spectra and the spatially resolved spectra.

The integrated spectral indices of most radio halos are typically found to be $-1.5 \lesssim \alpha \lesssim -1$, except for USSRHs which have been found to have spectral indices $\alpha < -1.5$. Thierbach et al. (2003) studied the integrated spectra of the GRH in the Coma cluster using radio observations covering a frequency range of $2.7-4.9$ GHz. They found that there was a steepening at higher frequencies. They concluded that the spectral steepening was not related to the SZ signal decrement but might be an indication of the break frequency of the CRe (Schlickeiser et al., 1987; Donnert et al., 2010). Most study findings indicate that the integrated spectra follow the power-law distribution (Shimwell et al., 2014; Rajpurohit et al., 2020d). Studies of samples of radio halos have investigated the relation of the integrated spectra with X-ray properties and found a mild correlation between the spectra and X-ray temperature (Feretti et al., 2004b; Giovannini

et al., 2009). Kale and Dwarakanath (2010) indicated that the results obtained from correlation studies of thermal temperatures and spectral indices might give inconclusive results.

Spatially resolved spectral studies use a pixel by pixel spectral index fit to produce maps. The maps trace the spatial spectral index distribution in the region of the radio halo. The spectral index map of the radio halo in the Coma cluster showed that there was a steepening in the spectra at the outskirt regions (Giovannini et al., 1993). More recent studies have shown that the spectral index maps have variations in the distributions of the substructures, while others indicate a uniform pattern (Giacintucci et al., 2005; Xie et al., 2020). Orrú et al. (2007) reported a correlation between the X-ray temperature and the spectral index distribution. Recent studies have not been able to reproduce this correlation (Vacca et al., 2014; van Weeren et al., 2016).

1.2.1.3 Scaling Relations

Statistical studies of uniformly selected, large samples of galaxy clusters that host radio halos, are important for the confinement of statistical and theoretical models. Studies of large populations of radio halos show that these sources are not ubiquitous (Hanisch, 1982; Kempner and Sarazin, 2001). Their radio power is correlated with their X-ray properties (Liang, 2000; Yuan et al., 2015), the largest linear size (LLS; Giovannini et al., 2009), and the integrated inverse Compton parameter (Basu, 2012). SZ studies have also shown that there is a higher occurrence rate of radio halos compared to the rate predicted by previous studies of X-ray selected samples (Basu, 2012; Sommer and Basu, 2014; Cuciti et al., 2015, 2021a).

The correlation of the radio halo power and the X-ray luminosity has been observed in many clusters (Venturi et al., 2008; Kale et al., 2015). Cassano et al. (2006) performed a detailed study of the scaling relation of radio halo power and X-ray properties such as mass (M_X), temperature (T_X) and luminosity (L_X) using radio observations at 1.4 GHz. This study and more recent studies (Cuciti et al., 2015; Yuan et al., 2015; Duchesne et al., 2017) have confirmed the $P_{1.4GHz} - M_X$ and $P_{1.4GHz} - T_X$ correlation. Initial statistical analyses carried out using X-ray selected samples revealed that there was a dichotomy in the correlations of the population that host radio halos and those no evidence of diffuse emission (Brunetti et al., 2007). Radio followups of SZ-

selected samples detected USSRHs, which filled the region between correlations and upper limits (Cassano et al., 2013; Sommer and Basu, 2014). Scaling relations derived from larger samples, spanning wider mass and redshift ranges, are still required to probe if the dichotomy is due to underlying astrophysical processes or cluster selection functions.

1.2.2 Radio Mini-Halos

RMHs have similar morphology and polarisation percentages as GRHs. However, their physical scale is $\sim$100$-$500 kpc, and they are generally found in cool-core clusters around the brightest cluster galaxies (BCGs; see Gitti et al., 2015, for review). The prototype of these sources is the RMH hosted by the Perseus cluster (see Figure 1.4). For diffuse emission to be classified as a RMH, the centre of the radio source needs to coincide with the X-ray emission, and the radio emission should envelop a BCG (Murgia et al., 2009; Giacintucci et al., 2017). The presence of the bright radio emission from the BCG makes it challenging to extract the faint radio halo emission, mainly because the emission is relatively small in angular size. However, telescopes with high angular resolution and dense short baselines, which trace the extended emission, have been used to disentangle RMHs from BCGs (Kale et al., 2015; Giacintucci et al., 2019). RMHs are formed either by re-acceleration of pre-existing electrons or proton-proton interactions (Gitti et al., 2002; Pfrommer and Enßlin, 2004).

1.2.2.1 Formation Mechanisms

In the hadronic model scenario, relativistic electrons form as a by-product of the collision of thermal proton and CRp ejected by AGN activity (Pfrommer and Enßlin, 2004; Zandanel et al., 2014; Ignesti et al., 2020). The streaming of the CRp results in instabilities that heat the ICM, thus reducing the gas cooling. This model is used to account for the *cooling flow* problem (Gaspari et al., 2013; McDonald et al., 2019). The angular size of RMHs does not need gamma-ray detections as a restriction of the hadronic model. The re-acceleration model assumes that there is a pool of seed electrons deposited into the ICM by AGNs or type Ia supernovae (Fujita et al., 2007; Omar, 2019; Richard-Laferrière et al., 2020). These electrons are re-accelerated by turbulent ac-

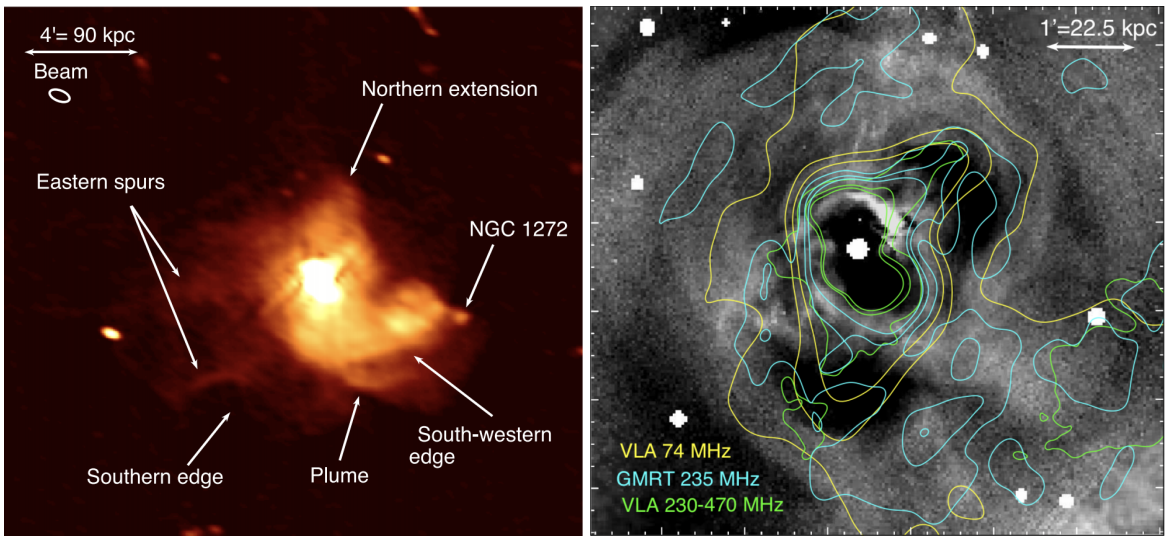

Figure 1.4: The prototype RMH was observed in the Perseus cluster (Miley and Perola, 1975; Gendron-Marsolais et al., 2020). *Left:* VLA observations of the RMH. Source: Adapted from Gendron-Marsolais et al. (2020). *Right: Chandra* X-ray image of the Perseus cluster, overlaid with multiple radio observations contours. Source: Gendron-Marsolais et al. (2020).

tivity and result in the formation of RMHs. The re-acceleration mechanisms are still unclear because RMHs are usually found in cool-core clusters that exhibit minor or no merger activity. Observations and simulations (ZuHone et al., 2015; Giacintucci et al., 2014a; Timmerman et al., 2020) have linked the turbulence to cold gas sloshing in the cluster core. The Hitomi Collaboration et al. (2016) used the *Hitomi* X-ray telescope to directly measure the turbulent motion of the core of the Perseus cluster, known to host a RMH (see Figure 1.4). Their findings indicated that the cool-core had turbulence that could efficiently re-accelerate electrons. These findings and the observed confinement of the radio emission between cold fronts make the re-acceleration model a leading contender for the RMH formation mechanism. However, observations of large samples of RMH and studying their spectral index properties is essential to constrain these models as some observations deviate from the norm. Savini et al. (2018) discovered a cluster hosting both a GRH and a RMH; these kinds of cases prove the need to probe a broader mass and redshift parameter spaces to model RMH correctly.

1.2.2.2 Scaling Relations

Giacintucci et al. (2019) used a sample of 23 RMHs, currently the largest sample, to study statistical properties of RMH. They confirmed that there is no strong correlation between radio power and the mass of the host cluster. They discovered a strong correlation between RMH power and cluster core bolometric X-ray luminosity. Kale et al. (2013) and Giacintucci et al. (2017) reported that there is a high occurrence ($\geqslant 50\%$) of RMH in massive cool-core clusters. Ignesti et al. (2020) used a combination of observations and simulations to explore the connection between the host cluster's X-ray properties and RMH power. They found a linear correlation between radio power and X-ray brightness. More studies are required to properly investigate the connection between RMH power and X-ray properties of the host cluster.

1.2.3 Radio Relics

Galaxy cluster radio relics (or radio shocks) are typically elongated, $\sim$Mpc scale diffuse radio sources located at the cluster outskirts (Feretti et al., 2012; Brüggen and Vazza, 2020). They tend to have higher polarisation percentages ($\gtrsim 20\%$) in comparison to radio halos. RRs can further be subdivided into double relics, and relics and halos (see Figure 1.5). Double relics occur when two relics are found in one cluster mostly situated opposite each other (Duchesne et al., 2020). In some instances, a cluster hosts both a GRH and a RR (Bîrzan et al., 2019) or a GRH and two or more relics (Govoni et al., 2001; Lindner et al., 2014; Bonafede et al., 2018). van Weeren et al. (2019) classified revived fossil plasma as a subgroup of radio relics, we discuss these sources in detail in Section 1.2.4. It is now well established that radio relics are predominantly found at cluster shocks (Botteon et al., 2016; Eckert et al., 2016). However, the origin of CRe is still an open question. Studies of spectral index properties can help constrain the models for the CRe origin.

1.2.3.1 Formation Mechanisms

In the diffusive shock acceleration (DSA) mechanism, CR protons and electrons are accelerated from the thermal pool up to relativistic energies at the cluster merger shocks (Krymskii, 1977;

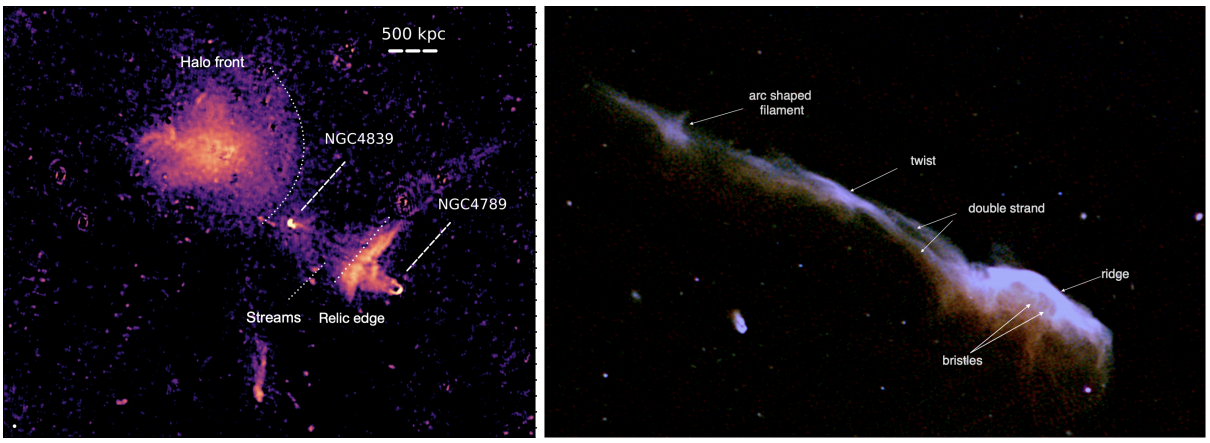

Figure 1.5: Left: LOFAR observations of the radio relic and halo in the Coma cluster. This RR was among the first to be observed and has been extensively studied. Source: Bonafede et al. (2020). *Right:* A combination of GMRT and VLA observations of the complex 'Toothbrush' relic. Source: Rajpurohit et al. (2020c).

Drury, 1983; Yokoyama and Ohira, 2020). The energy of the thermal electrons is boosted when they cross the cluster shock region while flowing up or downstream. The main constraint for this mechanism is that the Mach numbers for the shock regions of the observed RR are very low. According to the DSA model, weak shocks would result in RR with ultra-steep spectra (Botteon et al., 2020). The observed spectra of radio relics are much flatter than predicted by the DSA of thermal electrons. Locatelli et al. (2020) reported the discovery of a RR in Abell 2249. The host clusters X-ray properties and magnetic field strength suggest that the RR might have formed through DSA. This LOFAR observation indicates that lower frequency observations might reveal a population of RR that fit the DSA requirements. However, Vazza and Brüggen (2014) also reported tension between the gamma-ray upper limits and the expected gamma-ray emission produced by DSA. Gamma-ray emission in clusters is yet to be detected (Colavincenzo et al., 2020).

The second mechanism proposes the re-acceleration of fossil CR electrons via DSA at the cluster shocks (Enßlin and Gopal-Krishna, 2001b; Miniati et al., 2001; Stuardi et al., 2019). The proposed origin of the fossil electrons is again AGN activity. The connection between AGNs and radio relics has been established in a few observed cases (Bonafede et al., 2014; van Weeren et al.,

2017). This mechanism reproduces the observed spectrum (de Gasperin et al., 2014; Shimwell et al., 2015; Ge et al., 2019). It also does not require shocks to have large Mach numbers as the pre-existing electrons have enough energy to be re-accelerated to relativistic speeds (Brunetti and Jones, 2014). However, this mechanism also presents challenges as there are RRs detected in clusters where shock regions cannot be traced. A model by Zimbardo and Perri (2017, 2018) focuses on the role magnetic fields play in the formation of relics. They derive that under specific configurations, magnetic fields could allow electrons to reach relativistic speeds via the shock drift acceleration mechanism (DSA; Guo et al., 2014; Caprioli and Spitkovsky, 2014). However, the role of cluster magnetic fields and their amplification by low Mach number shocks is still poorly constrained (Stuardi et al., 2019). Studies of statistical properties of these sources will help discriminate between the two mechanisms.

1.2.3.2 Spectral Index Properties

Studies of spectral properties of RRs have shown that these sources have steep integrated spectra ($-1.5 < \alpha < -1$) that follow a power-law (Feretti et al., 2012; Rajpurohit et al., 2020d). A few clusters host radio relics with a much flatter spectral index ($\alpha \sim -0.8$) (Brentjens, 2008; HyeongHan et al., 2020). The flat spectrum observations challenge particle acceleration models as shown by van Weeren et al. (2012). Spectral index maps of RRs tend to exhibit spectral steepening feature in regions close to the cluster centre. This feature is attributed to the inverse Compton losses and indicates shock regions with downstream electron motions (Clarke and Ensslin, 2006b; Shimwell et al., 2015; Rajpurohit et al., 2020b).

1.2.3.3 Connection to Cluster Shocks

Shock waves propagating in galaxy clusters are defined as regions where there is a steep transition in fluid flow. The upstream flow is supersonic, and the downstream flow is subsonic. The propagating collisionless shock waves heat thermal electrons and accelerate them. This process transforms thermal electrons to relativistic non-thermal cosmic rays. Three main astrophysical processes produce shock waves: the accretion of matter onto clusters by the intergalactic

medium, AGN jets creating bubbles in the ICM, and the mergers of sub-clusters (see Brüggen et al., 2012, for a review). Radio relics are associated with the shocks generated by cluster mergers. The thermal or non-thermal pool of electrons in the cluster outskirts is (re-)accelerated to relativistic speeds via DSA. This results in the formation of the arc-like, steep spectrum, synchrotron sources (van Weeren et al., 2011; Domínguez-Fernández et al., 2020). Cluster shock properties can be probed using X-ray and SZ studies (Markevitch and Vikhlinin, 2007; Di Mascolo et al., 2019a).

Multiple observational properties link RRs to cluster shocks. The most prominent evidence, provided by X-ray observations, is that the structure of the relics coincides with that of the X-ray shock region. A study by Golovich et al. (2017) found that the merger axis of the host clusters is usually in the plane of the sky and that double relics form along the merger axis. Polarisation studies reveal that strongly polarised relics are confined in shock regions where the magnetic field is compressed (Clarke and Ensslin, 2006a; Urdampilleta et al., 2018; Stuardi et al., 2019). The final evidence is the observed spectral steepening of relics in the downstream shock regions (Rajpurohit et al., 2020b).

1.2.4 Revived Fossil Plasma

Low-frequency radio observations of galaxy clusters have revealed the presence of faint, steep spectra ($\alpha < -1.5$) radio sources that fall outside the traditional categories of GRHs, RMHs and RRs. These sources exhibit various morphology and can currently be grouped into radio phoenices (Slee and Reynolds, 1984; Giacintucci et al., 2020) and gently re-energized tails (GReEts; de Gasperin et al., 2017b; Bîrzan et al., 2020). Radio phoenices are linked to the re-energised fossil plasma from AGN lobes. According to the favoured formation mechanism, the AGN fossil plasma is gently re-accelerated by shock compression resulting in synchrotron emitting CRe (Enßlin and Gopal-Krishna, 2001a; Kang and Ryu, 2015). There are two proposed formation mechanisms for GReETs; compression of the radio tails by weak shocks or re-energisation of the tail by turbulence caused by the Rayleigh-Taylor and Kelvin-Helmholtz instabilities (de Gasperin et al., 2017b; van Weeren et al., 2019). Figure 1.6 shows the GReET

discovered by de Gasperin et al. (2017b) and a typical radio phoenix. Only a small number of these revived fossil plasma have been observed. More detections are required to further distinguish their origin.

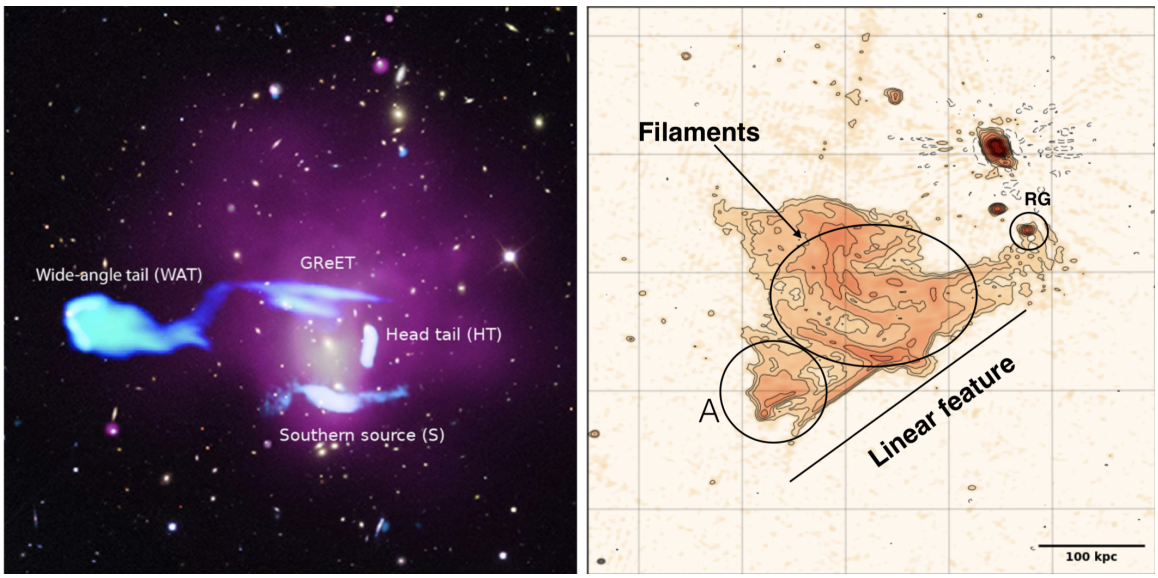

Figure 1.6: *Left:* Image of a GReET observed by LOFAR. The background optical image is from SDSS, purple indicates *Chandra* X-ray Observations, and blue traces the radio emission observed by LOFAR. Source: de Gasperin et al. (2017b). *Right:* LOFAR observation of a radio phoenix. Source: Mandal et al. (2020).

1.3 Thesis Outline

Understanding the non-thermal components of the ICM is essential for having a complete view of galaxy clusters and their cosmological evolution. Cluster-scale synchrotron emission is a powerful tracer of the non-thermal ICM. However, the origin and evolution of these tracers is still much debated. Statistical studies of large, uniformly selected samples of galaxy clusters spanning a wide mass and redshift parameter space are required to constrain existing formation theories. The current robust statistical studies are based on cluster samples limited to high mass and low redshifts (Venturi et al., 2008; Kale et al., 2013; Cuciti et al., 2015, 2021a). The availability of

newly built state-of-the-art radio telescope has allowed for the observations of higher redshift and lower mass clusters (Bernardi et al., 2016; van Weeren et al., 2020; Raja et al., 2021). However, larger samples are still required to further probe the cosmological evolution of diffuse radio emission. The study of larger samples will also reveal how the dynamics of the host clusters affected the type of diffuse emission observed. Our thesis aims to further expand the sample of observed diffuse emission and to study the statistical properties of these objects at higher masses and lower redshifts.

The layout of this thesis is as follows. In Chapter 2, we discuss our cluster selection process, we present the Giant Metrewave Radio Telescope (GMRT) observations, and we discuss our data reduction. We then present the results from our GMRT sample, including the statistical properties. In Chapter 3, we present our analysis and results of the MeerKAT observations of the Bullet cluster, Abell 3558, Abell 3562 and RXC J1314.4−2515. In the final chapter, we summarise our results and conclusions and describe avenues for future work.

In this thesis we adopt a ΛCDM flat cosmology with H_0 = 70 km s^{-1} Mpc^{-1}, $\Omega_{\rm m}$ = 0.3, and Ω_Λ = 0.7. For our radio analysis, we assume $S_\nu \propto \nu^{-\alpha}$.

CHAPTER 2

DIFFUSE EMISSION IN ACTPOL CLUSTERS FROM GMRT OBSERVATIONS

The main aim of this thesis is to study the properties of diffuse radio emission hosted by clusters spanning a broad mass and redshift range. To achieve this, we observed a cluster sample with lower-mass and higher-redshift clusters compared to previously studied samples (de Gasperin et al., 2014; Kale et al., 2015; Giacintucci et al., 2017; Giovannini et al., 2020; Cuciti et al., 2021a). We then followed up these clusters, for which there wasn't archival data of sufficient quality for our purposes, using a sensitive radio interferometer, from which we could extract faint extended diffuse emission. In this chapter, we begin by outlining radio interferometry basics which form the basis of our data reduction. We then describe our targeted sample and detail the Giant Metrewave Radio Telescope software backend (GSB) observations and data processing for the archival and new datasets. We highlight the methodology used to extract faint diffuse emission in cluster regions and present the GSB results. Finally, we discuss the GMRT wideband backend (GWB) data reduction procedures explored. We present preliminary results for the

clusters which had GWB data and diffuse emission detections in the GSB images.

2.1 Radio Interferometry Basics

Observing the radio sky began with an experiment that was led by the engineer named Karl Jansky who was based at the Bell Labs. For the experiment, Karl Jansky used a single radio antenna to investigate sources of interference at radio wavelength transmissions. Jansky (1933) reported the serendipitous discovery of radio waves from extrasolar sources, later confirmed as radio waves from the center of the Milky Way. Since then, the radio astronomy field has evolved and advanced tremendously. Presently, radio observations are able to probe the distant Universe using highly sensitive radio interferometers. The large wavelengths of the radio waves require extremely large ($\sim$100 m) single dishes, such as the Green Bank Telescope. The construction of these single dishes is challenging and they still do not achieve the required angular resolution to resolve faint point sources. Radio interferometers were introduced to achieve angular resolution similar to optical telescopes (Ryle and Vonberg, 1946).

Radio interferometers are a group of two or more antennae that are correlated to form one single telescope. A schematic of a two-element interferometer is shown in Figure 2.1. The separation between two antennae is called a baseline. The longest baseline determines the resolution of the full array. The electromagnetic signals arrive at the two antennae at different time intervals. The geometric delay is characterised by:

$$\tau_g = \vec{b} \cdot \vec{s}/c \ , \tag{2.1}$$

where $\vec{b}$ is the baseline between two antennae, $\vec{s}$ is the direction of the observed source and c is the speed of light. The two signals are then multiplied by the correlator and stored as complex visibilities ,$V(u, v)$, as shown in Figure 2.1. Based on the van Cittert–Zernike theorem (Thompson et al., 2017), for co-planar interferometers with small fields of view, the complex visibilities can be related to the sky brightness using a Fourier transform in the following manner

$$V(u, v) = \int_{\infty}^{\infty} \int_{\infty}^{\infty} I_{lm} e^{-2\pi i(ul+vm)} dl dm \ , \tag{2.2}$$

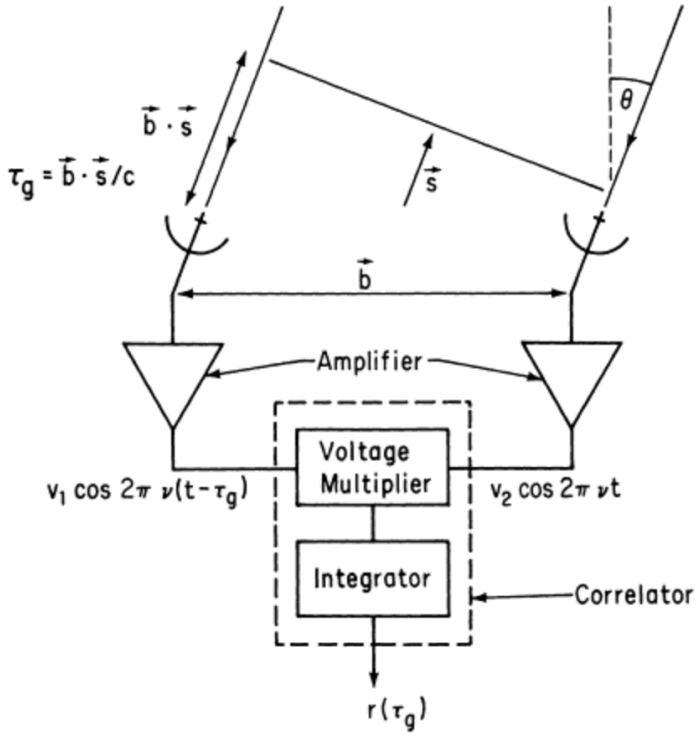

Figure 2.1: Diagram indicating how the two signals arriving at each antenna are correlated. Source: (Thompson, 1999)

where (u, v) are the visibility plane coordinates and (l, m) are the direction cosines.

With new generation telescopes such as the upgraded GMRT the 2D approximation does not hold because the antennas do not lie on the same plane and the telescopes have wider field of views. For such instruments, the w-projection needs to be taken into account, hence, the visibility equation becomes

$$V(u,v) = \int_{\infty}^{\infty}\int_{\infty}^{\infty} \frac{I_{lm}}{\sqrt{1-l^2-m^2}} e^{-2\pi i(ul+vm+wn)} dldm\,, \tag{2.3}$$

where w is the axis normal to the uv-plane and n is the direction cosine in the direction of w. Equation 2.3, can be reduced to a 2D Fourier transform under the following constrains. We can rotate the coordinate system so that the w-axis points to the center of the region of interest and make use of the small angle approximation

$$n = cos\gamma = \sqrt{1-sin^2\gamma} = \sqrt{1-\theta^2} = 1-\theta^2/2, \tag{2.4}$$

where θ is the polar angle from the centre of the image (see Figure 2.2). The visibility equation then becomes

$$V(u,v) = e^{-2\pi iw} \int_{\infty}^{\infty} \int_{\infty}^{\infty} \frac{I_{lm}}{\sqrt{1-l^2-m^2}} e^{-2\pi i(ul+vm-w\theta^2/2)} dldm\,. \tag{2.5}$$

Since we assume the small angle approximation, $w\theta^2 << 1$. Hence the visibility equation can be written as a 2D Fourier transform

$$V'(u,v) = \int_{\infty}^{\infty} \int_{\infty}^{\infty} \frac{I_{lm}}{\sqrt{1-l^2-m^2}} e^{-2\pi i(ul+vm)} dldm\,, \tag{2.6}$$

where $V'(u,v)$ = $V(u,v)e^{2\pi iw}$.

The power collected by a single antenna for a source with brightness I is given by

$$P = A_e(\nu,\theta,\phi)\ I(\nu,\theta,\phi)\Delta\Omega\ \Delta\nu\,, \tag{2.7}$$

where A_e is the effective collecting area, θ and ϕ are the direction coordinates on the sky, $\Delta\Omega$ is the solid angle, and $\Delta\nu$ is the frequency bandwidth. The power pattern associated with A_e of a single antenna is shown in Figure 2.2. This pattern is known as the *primary beam*, which is the Fourier transform of the aperture of the antenna. For circular dishes this pattern is given by a sinc function[1].

Hamaker et al. (1996) introduced the radio interferometer measurement equation (RIME), which is a mathematical representation of how the observed visibilities relate to the true sky brightness. Based on the formalism by Smirnov (2011) the RIME is given by:

$$\mathbf{V}_{pq} = \mathbf{G}_p \left(\iint_{lm} \mathbf{B}(l,m) e^{-2\pi i(u_{pq}l+v_{pg}m)/\lambda} dldm \right) \mathbf{G}_q^H \tag{2.8}$$

$$B_{pq} = \mathbf{E}_p\ B\ \mathbf{E}_q\ , \tag{2.9}$$

where $\mathbf{G}_p$ are the Jones matrices representing antenna related direction independent effects, $\mathbf{B}(l,m)$ is the sky brightness matrix, and $\mathbf{E}_p$ are the Jones matrices incorporating direction dependent effects (e.g ionospheric effects, primary beam attenuation, etc.). As in equation 2.2, (u,v) are the visibility plane coordinates, and (l,m) are the intensity plane coordinates. The process

[1] `https://www.sciencedirect.com/topics/engineering/sinc-function`

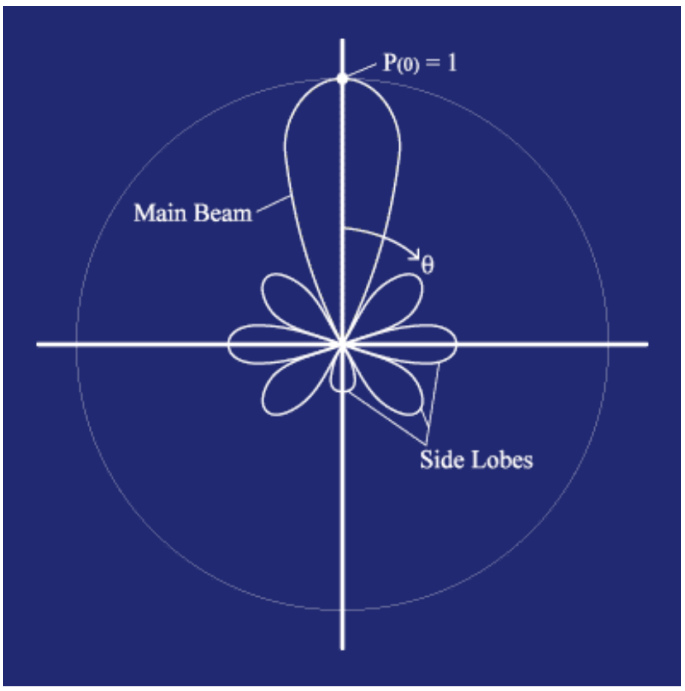

Figure 2.2: The primary beam pattern of an antenna with a circular aperture. The primary beam is made up of a main beam with the peak antenna response at the pointing centre, as well as side lobes with non-negligible antenna response further away from the pointing centre. P(0) indicates the pointing center of the observation.

of correcting the antenna gains and recovering the true observed sky is known as calibration. **The older generation telescopes, which had smaller field of views and narrow bandwidth ($\sim$ 30 MHz), generally require only standard calibration processes (see Sections 2.1.1) to produce high quality images**. However, the new generation low frequency telescopes, such as LoFAR and uGMRT, have wider bandwidths ($\sim$100s of MHz) compared to the traditional interferometers. The wide bandwidths introduce ionospheric and beam variation effects that make calibration and imaging much more complex. **Hence, a further step of direction dependent calibration is necessary (see Section 2.1.2).**

Data reduction is a process that encompasses radio frequency interference (RFI) excision, correction of antenna pointing errors and gain amplitudes, deconvlotion, and imaging the observed visibilities. The aim of data reduction to obtain images that are a close approximation of the observed sky. The data reduction steps are explained in detail in the sections below.

2.1.1 Standard Calibration

The standard data reduction technique involves RFI removal (flagging), first generation calibration (1GC or cross-calibration), and second generation calibration (2GC or self-calibration) (Noordam and Smirnov, 2010; Offringa et al., 2012). There are various sources of RFI, including signals from cellphones and satellites. These objects emit high-amplitude radio signals that degrade the quality of radio observations. The new generation telescopes have broader bandwidths making them more susceptible to RFI induced errors. Therefore, for these telescopes, it is important to identify RFI signals in time, frequency and antenna space, and flag them prior to calibrating the data. Many software algorithms have been developed for RFI flagging, which include in-built automated flagging tasks in the Common Astronomy Software Applications (CASA; McMullin et al., 2007), and more recently AOFLAGGER and GRIDFLAG (Offringa et al., 2012; Sekhar and Athreya, 2018). Once the RFI is flagged, the next step is to calibrate the visibilities.

In the 1GC step, a well known, bright, point-like source is observed and used to correct for the baseline-based errors, the antenna-based gains, and to set the flux scale for the fainter target field. Typically, another point-like source, fainter but nearer on the sky to the target field, is observed and used to correct for phase variations. In some instances, one calibrator is used for both phase and gain calibration if the flux calibration source is close enough to the target. The solutions obtained from these sources are then applied to the target field. The cross-calibrated target data are then separated into a standalone dataset before further calibration is carried out.

2GC, also known as self-calibration, is the calibration step where the target data is used to improve its own calibration. This step encompasses the creation of a good target sky model while simultaneously correcting for antenna gains. The sky model is obtained by deconvolving the PSF, storing the clean components and imaging (see Section 2.1.3). The sky model is then used to produce phase and amplitude gain solutions. The gain solutions can be improved by first applying phase-only calibration to improve antenna gain phases. After this one can proceed to amplitude-only and phase-and-amplitude calibrations. 2GC is computed iteratively until the desired image quality is achieved. There are various software tools that can be used for 2GC calibration and imaging; the main tools include CASA, CUBICAL (Kenyon et al., 2018), and

WSCLEAN (Offringa et al., 2014).

2.1.2 Direction Dependent Calibration

Traditional radio interferometers allowed for the simplification of the RIME by assuming that each baseline observed the same sky. This resulted in the assumption that the E-Jones matrices were the same for all baselines, making $\mathbf{E}_p \equiv \mathbf{E}$. However, for the new generation interferometers such as uGMRT and MeerKAT, this simplification does not hold. These interferometers have non-coplanar long baselines, wide bandwidths, and high sensitivities. These properties result in multiple direction-dependent effects (DDEs), including primary beam attenuation, varying in-band source spectra, and ionospheric effects. The conventional 2GC software tools can not successfully calibrate all these errors. Fortunately, the Hamaker et al. (1996) RIME formalism allows for the calibration of the E-Jones matrices which accounts for the DDEs. This calibration step was first introduced by Noordam and Smirnov (2010) and they labelled it third generation calibration (3GC). The two main methods for 3GC are *peeling* (Noordam, 2004) and *facet-based* calibration (Cotton et al., 2004).

Peeling is the process of finding DDEs solutions for the brightest source in the field, calibrating the visibilities with the solutions, then subtracting the source from the visibilities and solving for the next brightest source. Peeling is done iteratively until all the bright sources in the target field are corrected for DDEs. Facet-based calibration divides the observed field into regular or irregular (Voronoi tesselation) facets, and tagging the brightest source as the center of each facet (Tasse et al., 2018; Vavilova et al., 2020). Self-calibration is then performed on each facet independently. KILLMS[2] uses facet based calibration to solve for the E-Jones matrices. The source peeling and atmospheric modelling software (SPAM; Intema, 2014) uses a combination of peeling and facetting to solve for the DDEs. Beyond calibration, wide-field imaging tools are also required to further correct for DDEs. Software tools such as CASA-MTMFS, WSCLEAN, and DDFACET (Tasse et al., 2018), take into account the source flux frequency dependence and primary beam corrections. A combination of the calibration and imaging tools results in high-

[2] https://github.com/saopicc/killMS

dynamic range images. 3GC is being computationally expensive compared to 1GC and 2GC, hence, super-computing power is required for this step. We use these tools to reduce the radio observations of clusters selected from the ACTPol sample, which is described in the next section.

2.1.3 Imaging

As shown in Equation 2.2, the visibilities are related to the true sky brightness by a Fourier transform. Hence, once the visibilities are corrected for, one can Fourier transform them into the image plane to recover the observed target's intensity. The angular resolution of the resulting image is derived from the longest baseline visibilities. However, the 'true' intensity map of the sky cannot be fully recovered because the uv-plane is sparsely sampled. Directly imaging the corrected visibilities produces a 'dirty' image, which is a convolution of the point spread function (PSF) and the true intensity.

$$I_{dirty}(l,m) = \beta(l,m) \circledast I_{true}(l,m) \ , \tag{2.10}$$

where $\beta(l,m)$ is the PSF or the dirty beam, which is a Fourier transform of the sampling of the visibilities in the uv-plane. The CLEAN algorithm introduced by Högbom (1974), involves the deconvolution of the the PSF, filling the unsampled $uv - plane$ with non-zero extrapolated values, and baseline based weighting of the visibilities. This algorithm produces a 'CLEANed' image which best represents the true sky intensity.

The quality of the images can be improved by setting various parameters while applying the CLEAN algorithm. To improve the the signal-to-noise ratio and the dynamic range of the recovered image, weighting parameters can be applied. This enables different weights to be applied on the visibilities. The two extreme cases of weighting visibilities are natural weighting and uniform. Natural weighting applies equal weights to all visibilities. This results in a higher sampling of the dense short-baseline visibilities, high signal-to-noise, but also results in larger angular resolution. Uniform weighting applies the same weighting for visibilities of equal scale. This produces an image with the smallest possible angular resolution but poor noise quality. Ideally, the best image is produced by a compromise between

the natural and uniform weighting. The algorithm introduced by Briggs (1995) allows for a compromise between natural and uniform weighting. The 'robust' parameter allows one to select the best value ('-2' uniform and '2' natural) suited for particular scientific needs. One can also restrict the range of visibilites used by applying the 'uv-taper' parameter. The taper can be used to produce high-resolution or low-resolution images based on the specified 'uv-range'. The tapering of visibilities enables one to enhance the image features of interest (e.g. large scale diffuse emission).

2.2 ACTPol Sample Selection

Previous statistical studies of diffuse radio emission in galaxy clusters were constrained to observations of high mass and low redshift systems selected using X-ray telescopes (Venturi et al., 2008; Kale et al., 2015). The X-ray selected samples had relatively low diffuse emission detection rates ($\sim$20$\%$). Andrade-Santos et al. (2017) studied the fraction of cool-core clusters in a X-ray selected sample from *Chandra* versus a SZ selected sample from *Planck*. The study revealed that the X-ray sample had a higher fraction ($\sim$44$\%$) of cool-core clusters in comparison to the SZ sample ($\sim$28$\%$). These findings in conjunction with the poor resolution ($\sim$1.8$'$) of *ROSAT*, which was mainly used for the X-ray samples, may account for the low detection rates of diffuse emission in X-ray selected samples.

As described in Chapter 1, the thermal SZ effect is a powerful probe for high-redshift clusters due to the fact that it is not affect by dimming. Hence, the SZ survey catalogues offer an almost redshift independent selection function. Essentially, cluster samples from SZ surveys are restricted by cluster masses based on the sensitivity of the observing instrument. The three main microwave telescopes that have been used to detect galaxy clusters are the Atacama Cosmology Telescope (ACT; Swetz et al., 2011), the *Planck* satellite (Planck Collaboration et al., 2011), and the South Pole Telescope (SPT; Carlstrom et al., 2011).

For our project we use the galaxy cluster catalogue from the ACT's Polarimetric extension (ACTPol; Hilton et al., 2018) to select our sample. The ACTPol catalogue was constructed using the D56 region, shown in Figure 2.3, which covers an area of 548 deg^2 with a sky coverage

of $-7.2^o < \delta < 4^o$ and $352^o < \alpha < 41^o$ (Louis et al., 2017). The final catalogue consists of 182 optically confirmed clusters. For a signal-to-noise (SNR) > 4 the sample spans a mass and redshift range of $1.6 < 10^{14}$ $M_\odot < 9.1$, and $0.1 < z < 1.4$, respectively. The 90% sample completeness cut-off is $M_{500c} > 4.5 \times 10^{14}\,M_\odot$ for SNR > 5 and a redshift range of $0.2 < z < 1.0$. M_{500c} is the mass measured within a radius that encloses a region with an average density that is 500 times the critical density at the cluster redshift and assuming the SZ-signal scales with mass as described in Arnaud et al. (2010).

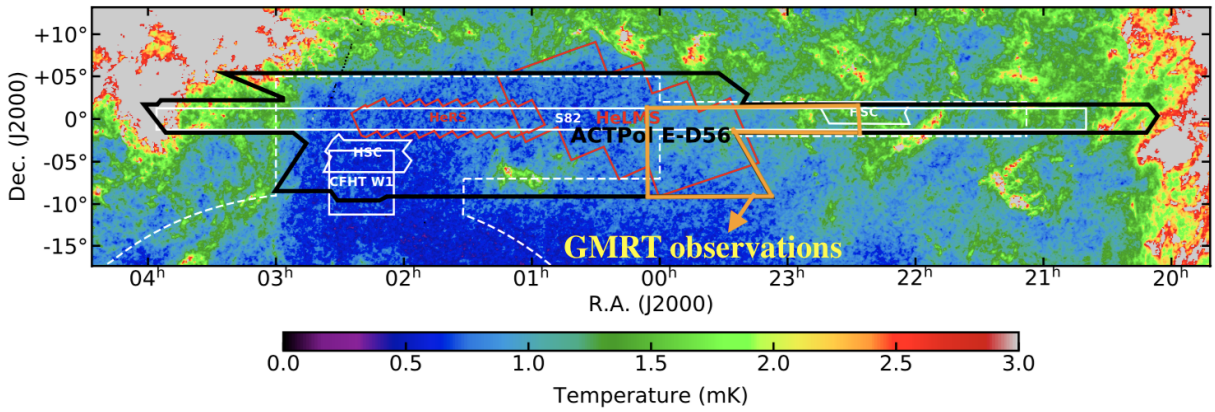

Figure 2.3: The *Planck* 353 GHz temperature map overlaid with the ACTPol E-D56 region (shown in black) and the overlapping multi-wavelength surveys. The region enclosed by the magenta polygon indicates the region of the selected final sample which we followup using u/GMRT observations. Source: Adapted from Hilton et al. (2018).

For our sample, we considered all the clusters with a SNR > 5. We then applied a mass and redshift cut of $M_{500,SZ} > 4\times10^{14}\,M_\odot$ and $0.1 < z < 0.8$. This results in a sample of 40 clusters which formed the basis of our sample. We aimed to follow up at low-frequency using the wide-band upgraded Giant Metrewave Radio Telescope (uGMRT; Gupta et al., 2017) and to also utilise existing archival narrowband GMRT data. As of November 2020, there were 17 clusters with pre-existing GMRT legacy software backend (GSB) observations. We also successfully proposed to observe 13 clusters using the upraged GMRT wideband backend (GWB) observations which had simultaneous GSB data. These clusters were observed over three semesters. The archival data and new observations resulted in a total of 30 clusters which is our main cluster sample

for this thesis. In future work and future proposals on GMRT we aim to complete the radio observations of the remaining 10 clusters in the sample. The properties of the cluster sample are listed in Table 2.1. In Figure 2.4, we compare our sample of 40 clusters to *Planck* and SPT samples which were used for similar studies. Our sample covers a wider redshift range compared to both samples. We also cover lower mass clusters compared to the *Planck* sample. The SPT sample overlaps with ours at higher redshifts however, it does not cover lower redshifts ($z < 0.33$).

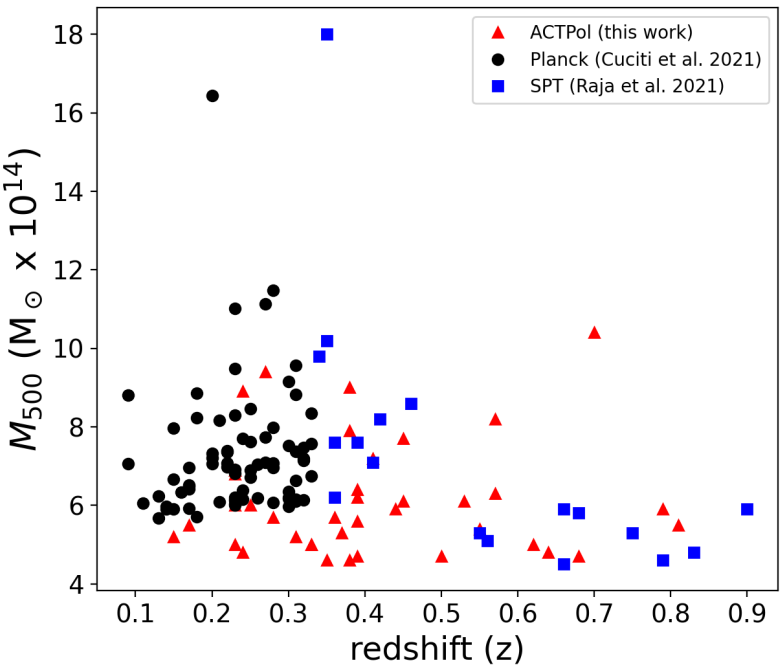

Figure 2.4: Our ACTPol sample in comparison to the Planck sample (Cuciti et al., 2021b) and SPT (Raja et al., 2021) sample used for statistical studies of diffuse emission.

2.3 GMRT Observations

The array configuration of the Giant Metrewave Radio Telescope (GMRT; Swarup et al., 1991) makes it an excellent instrument for studying faint extended diffuse emission in galaxy cluster

Table 2.1: The full sample of ACTPol clusters ordered in descending mass. Columns: (1) ACT cluster catalogue name. (2) J2000 Right Ascension of the ACT SZ peak. (3) J2000 Declination of the ACT SZ peak. (4) Cluster redshift. (5) The central Comptonization parameter measured using a filter with $2.4'$ angular scale. (6) ACT SZ-derived mass within R_{500c}. (7) Alternate cluster designation.

ACT-CL	RA_{J2000} deg	DEC_{J2000} deg	z	$\bar{y}_o$ 10^{-4}	$M_{500,SZ}$ $10^{14}\,M_\odot$	Alternate Name
J2327.4−0204*	351.862	−2.0763	0.699	4.49 ± 0.19	$10.4^{+1.8}_{-1.5}$	RCS J2327−0204
J0019.6+0336*	4.9058	3.6074	0.269	2.99 ± 0.24	$9.4^{+2.0}_{-1.7}$	NSCS J001937+033655
J0034.4+0225	8.6067	2.422	0.382	3.10 ± 0.25	$9.0^{+1.8}_{-1.5}$	
J0248.1−0216*	42.0468	−2.2750	0.238	2.70 ± 0.21	$8.9^{+2.0}_{-1.6}$	ACO 384
J0137.4−0827	24.3521	−8.4598	0.568	3.08 ± 0.27	$8.2^{+1.5}_{-1.3}$	PSZ1 G155.25-68.42
J0239.8−0134*	39.9669	−1.5782	0.375	2.65 ± 0.16	$7.9^{+1.5}_{1.3}$	ACO 0370
J0140.0−0554*	25.0004	−5.9144	0.454	2.67 ± 0.24	$7.7^{+1.5}_{-1.2}$	1RXS J014001.8−055513
J0159.8−0849*	29.9541	−8.8289	0.408	2.39 ± 0.28	$7.2^{+1.5}_{1.2}$	PSZ2 G167.66−65.59
J2135.2+0125*	323.8123	1.4212	0.23	2.04 ± 0.17	$6.9^{+1.7}_{-1.4}$	ACO 2355
J0152.6+0100*	28.1732	1.0068	0.229	2.04 ± 0.28	$6.9^{+1.5}_{-1.2}$	ACO 267
J0003.1−0605*	0.7993	−6.0877	0.233	2.03 ± 0.25	$6.8^{+1.6}_{-1.3}$	ACO 2697
J2351.7−0859	357.9469	−8.9870	0.392	2.08 ± 0.31	$6.4^{+1.4}_{-1.2}$	WHL J357.962−08.99151
J0248.1+0238	42.0487	2.6339	0.556	2.16 ± 0.25	$6.3^{+1.2}_{-1.0}$	RM J024813.0+023827.9
J2015.3−0126‡	303.8366	−1.4464	0.39	1.99 ± 0.31	$6.2^{+1.5}_{-1.2}$	
J0326.8−0043	51.7129	-0.7331	0.447	2.01 ± 0.23	$6.1^{+1.2}_{-1.0}$	MCS J0326.8−0043
J0014.8−0057*	3.7249	−0.9506	0.533	2.06 ± 0.18	$6.1^{+1.1}_{-0.9}$	GMBCG J003.72543−00.95236
J2341.2−0901*	355.3153	−9.0226	0.251	1.79 ± 0.42	$6.0^{+1.8}_{-1.4}$	ACO 2645
J2129.6+0005*	322.4115	0.092	0.234	1.74 ± 0.24	$6.0^{+1.4}_{-1.2}$	RXC J2129.6+0005
J0154.4−0321	28.6122	−3.3531	0.444	1.90 ± 0.22	$5.9^{+1.2}_{-1.0}$	RM J015426.9−032119.9
J0129.0−0845	22.2503	−8.7539	0.358	1.79 ± 0.34	$5.7^{+1.4}_{-1.1}$	RM J012900.7−084520.2
J0059.1−0049*	14.7808	−0.8296	0.787	2.21 ± 0.18	$5.9^{+1.0}_{-0.9}$	
J2337.6+0016*	354.4092	0.2711	0.277	1.71 ± 0.14	$5.7^{+1.2}_{-1.0}$	ACO 2631
J2128.4+0135	322.1041	1.5995	0.386	1.76 ± 0.36	$5.6^{+1.4}_{-1.1}$	PSZ2 G054.95−33.39
J0301.6+0155‡	45.4131	1.9212	0.167	1.45 ± 0.31	$5.5^{+1.7}_{-1.3}$	ZwCl 0258+0142
J0022.2−0036*	5.5506	−0.6005	0.805	2.02 ± 0.19	$5.5^{+0.9}_{-0.8}$	
J0045.2−0152*	11.3025	−1.8808	0.548	1.79 ± 0.19	$5.4^{+1.0}_{-0.9}$	PSZ2 G119.30−64.68
J0008.1+0201	2.044	2.0238	0.366	1.63 ± 0.15	$5.3^{+1.0}_{-0.9}$	WHL J000810.4+020112
J0303.3+0155‡	45.8315	1.9268	0.153	1.34 ± 0.32	$5.2^{+1.7}_{-1.3}$	ACO 409
J0033.8−0751*	8.4664	−7.8657	0.305	1.57 ± 0.25	$5.2^{+1.2}_{-1.0}$	ACO 56
J2156.1+0123‡	329.0398	1.3839	0.227	1.43 ± 0.27	$5.0^{+1.4}_{-1.1}$	RCS J215609+0123.3
J2058.8+0122‡	314.7216	1.3794	0.329	1.49 ± 0.29	$5.0^{+1.2}_{-1.0}$	PSZ1 G050.07−27.29
J2050.7+0122‡	312.6851	1.3758	0.334	1.50 ± 0.28	$5.0^{+1.2}_{-1.0}$	1RXS J205043.1+012346
J2050.5−0055	312.6279	−0.9315	0.623	1.64 ± 0.24	$5.0^{+1.0}_{-0.8}$	
J2029.2+0029‡	307.3217	0.4998	0.240	1.37 ± 0.27	$4.8^{+1.3}_{-1.0}$	
J0026.2+0120	6.5597	1.3392	0.64	1.58 ± 0.19	$4.8^{+0.9}_{-0.8}$	
J2307.6+0130	346.9133	1.5127	0.389	1.42 ± 0.34	$4.7^{+1.3}_{-1.0}$	ZwCl 2305+0114
J0106.1−0619	16.5435	−6.3204	0.50	1.46 ± 0.26	$4.7^{+1.0}_{-0.8}$	RM J010608.9−061844.6
J0206.2−0114‡	31.5552	−1.2415	0.676	1.55 ± 0.15	$4.7^{+0.8}_{-0.7}$	
J0027.1−0843‡	6.7759	−8.7169	0.350	1.35 ± 0.032	$4.6^{+1.2}_{-1.0}$	
J0127.2+0020‡	21.8187	0.349	0.380	1.36 ± 0.17	$4.6^{+0.9}_{-0.8}$	

Notes: † R_{500} is the cluster radius that encloses a mean mass over-density that is 500 times that of the cosmic critical density at the cluster redshift. *Clusters with archival GMRT data at 325 or 610 MHz. ‡ clusters that have not been observed with GMRT. The clusters without alternate names were newly detected by ACTPol.

environments. The short baselines in the dense core (see Figure 2.5) trace the extended structure, while the antennas in the long arms result in simultaneous high resolution. High resolution is required to disentangle the compact sources embedded in the diffuse emission. The GMRT was recently upgraded to include wideband receiver systems and is now referred to as the uGMRT. The uGMRT has four bands, with bandwidths spanning a range of 100 MHz to 450 MHz. The increased bandwidth is an added advantage for diffuse emission studies because one can also perform in-band spectral index studies.

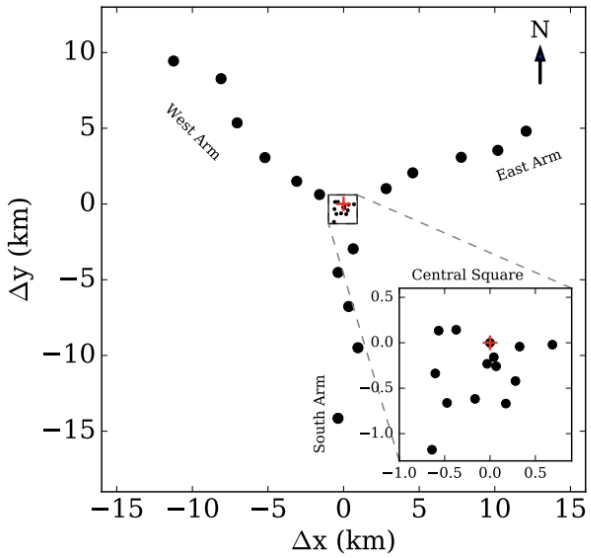

Figure 2.5: GMRT array configuration. Source: Patra et al. (2019)

Seventeen clusters in our target sample had useful low-frequency archival GMRT data. For the other thirteen clusters, we obtained simultaneous GSB and GWB data using the uGMRT's Band-3, which operates between 300 MHz and 500 MHz (proposal IDs: 32_012, 33_010, 36_050). To determine the amount of hours we needed for the GWB observations, we first assume that each cluster in our sample hosts a radio halo with a size R_H, where R_H is calculated from the $R_H - R_{vir}$ relation (Cassano et al., 2007). Given that our observations are at lower frequencies, where the emission in known to be brighter and more extended, we multiplied R_H by a factor of 2. We estimated the rest-frame 1.4 GHz halo radio power, $P_{1.4GHz}$, using the $P_{1.4GHz} - M_{500}$ scaling relation from Cassano et al. (2013). We use these values to extrapolate the flux density of

the radio halo at 375 MHz, which is the central frequency of uGMRT's Band-3, using a fiducial spectral index value of α = 1.2. We used the halo model discussed above to calculate the required integration times per cluster using a MATLAB-based simulation code. We use the on-source integration times which ensured that we would detect the estimated peak halo flux density up to a signal-to-noise of 10, with 90% flux recovery for the extended halo structure. The criteria we use is conservative given that the simulations do not account for point source contamination in the cluster region. Since uGMRT was operating in 'shared risk' mode, we increase the integration times by 30% to account for RFI flagging or other issues that might have occurred during observations. For the cycle 36 proposal, we used the uGMRT Exposure Time Calculator (ETC)[3] to calculate the integration times. The ETC is used for all GWB proposals since cycle 36.

In the proposal cycles 32, 33, and 36, we proposed to observe 18, 16, and 12 clusters, respectively. However, we were not awarded the full requested time for our proposals, hence, we had to adjust the number of clusters to be observed. In cycle 32 (GMRT proposal ID: 32_016, PI: Knowles) we were awarded 45.0 hours and observed eleven clusters. For our cycle 32 proposal, we used an early version of the ACTPol catalogue, with preliminary mass estimates. The final catalogue used better calibrated maps for deriving the masses. The change in mass estimates for the ACTPol catalogue resulted in a sample different to the one we had submitted in the cycle 32 proposal. Only three of the eleven clusters that were observed in cycle 32 are part of our final sample. In cycle 33 (GMRT proposal ID: 33_010, PI: Knowles) we were allocated 20.0 hours which was sufficient to observe three more clusters. In cycle 36 (GMRT proposal ID: 36_050, PI: Knowles) we were allotted 72 hours. We observed seven new clusters and also re-observed two clusters from cycle 33 which had poor data quality. In total, we observed a subset of thirteen clusters in our sample. All our observations were at band three (250−500 MHz) using the GMRT wideband backend (GWB). For our observations, we requested for full Stokes (RR,LL,RL,LR) and dump times of ∼16 seconds (cycle 32), ∼8 seconds (cycle 33), and ∼4 seconds (cycle 36). The cross-polarisation visibilities assist with improving RFI detection. We also learned from the previous observations, that a higher dump rate is needed to improve RFI excision. Hence, we

[3] http://www.ncra.tifr.res.in:8081/~secr-ops/etc/rms/rms.html

decreased the dump time on later proposals. Although our proposals were for the GWB observations, the observational setups also provided data from the legacy GMRT software backend (GSB) at 325 MHz. The majority of the clusters with archival data had GSB observations at 610 MHz. We summarise the u/GMRT observation details in Table 2.2. For a homogeneous approach in our data reduction strategy, we began by reducing and analysing the GSB datasets for the full sample.

2.4 GMRT GSB Data Reduction

We use the source peeling and atmospheric modeling (SPAM; Intema, 2014; Intema et al., 2017) calibration **pipeline's version 19.11.07′** to reduce the GSB data for all 30 clusters. SPAM is a fully automated Python pipeline that uses the PARSELTONGUE (Kettenis et al., 2006) interface to access and execute the Astronomical Image Processing System (AIPS; van Moorsel et al., 1996) tasks. The pipeline is divided into two steps; the 'pre-calibrate targets' step and the 'process target' step. The data reduction steps are as follows:

1. In the 'pre-calibrate target' step performs cross-calibration step of the standard calibration procedure. The pipeline uses the primary calibrator(s) to determine the channels affected by RFI, determine the flux scale, and to produce cross calibration tables. The flags and calibration tables are then applied to the target source. Finally, the calibrator and target visibilities are split into separate UVFITS files.

2. The 'process target' step begins by taking the cross-calibrated (1GC) target data and applying 2GC (or self calibration) . For 2GC, the target visibilities are imaged using the facet-based method established by Cornwell and Perley (1992). The point sources covering the primary beam are obtained from a sky model extracted from the VLA low-frequency sky survey (VLSS; Cohen et al., 2007) and the NRAO VLA sky survey (NVSS; Condon et al., 1998). The observed field is then faceted based on the sky model. The deconvolution is done using the Cotton-Schwab CLEAN algorithm (Condon et al., 1998). The CLEANED visibilities are calibrated using the sky model. Then the calibrated visibilities are imaged

Table 2.2: Summary of the GMRT observations for the sample. Columns: (1) ACT cluster catalogue name. *Clusters with archival observations. (2) GMRT observation proposal ID. (3) Narrow band GMRT observation frequencies. (4) Clusters with GWB band 3 observations from our proposals. (5) On source observation time. (6) Synthesised beam of the full resolution image. (7) rms noise of the full resolution image. (8) Total flagged percentage of the MS after data reduction.

Cluster Name ACT-CL	Obs. ID	GSB MHz	GWB?	t_{src} hrs	Synthesised Beam ($'' \times ''$, deg)	RMS (μJy/beam)	Flagged %
J0003.1−0605*	07CRA01	610		2.2	4.8×4.2, -65.1	193.2	27.5
J0008.1+0201	36_050	325	✓	6.4	9.7×7.6, -81.5	46.4	15.8
J0014.8−0057*	22_044	610		6.3	5.7×3.9, 64.9	25.2	11.7
J0019.6+0336*	25_018	325		6.5	18.7×8.2, -84.4	144	14.5
J0022.2−0036*	26_031	610		7.4	5.2×4.0, 85.0	33.4	13.6
J0026.2+0120	36_050	325	✓	5.9	16.6×6.9, 67.1	60.8	17.2
J0033.8−0751*	26_021	610		3.7	5.4×4.4, 78.6	63.5	11.8
J0034.4+0225	32_016	325	✓	4	14.2×18.1, 48.2	75.8	17.1
J0045.2−0152*	26_031	610		7.3	6.3×4.5, -76.3	27	11
J0059.1−0049*	26_031	610		6.7	5.3×4.3, 70.9	46.1	11
J0106.1−0619	36_050	325	✓	6	16.4×7.5, 65.9	142.3	15
J0129.0−0845	36_050	325	✓	5.6	10.2×7.5, 31.7	47.9	19
J0137.4−0827	32_016	325	✓	6.6	12.8×7.6, 18.1	74.5	14.7
J0140.0−0554*	30_012	610		4.9	5.9×4.5, 20.9	22.3	12
J0152.6+0100*	16_117	610		4.4	6.1×3.7, 71.2	89.9	37.5
J0154.4−0321	32_016	325	✓	4.8	10.1×9.3, -8.6	84.6	15.9
J0159.8−0849*	27_052	610		3.7	8.1×4.6, 78.4	48.7	12.2
J0239.8−0134*	31_037	325		3	11.7×7.9, 24.7	123.2	15.8
J0248.1+0238	33_010	325	✓	5.1	10.7×7.8, 32.9	57.1	16
J0248.1−0216*	26_021	610		3.6	5.6×3.9, 65.0	32.4	10.7
J0326.8−0043	36_050	325	✓	6	9.4×7.3, 46.1	69.6	18.5
J2050.5−0055	36_050	325	✓	6.6	9.7×8.1, 89.2	64.6	18
J2128.4+0135	36_050	325	✓	6.5	16.0×6.9, 65.9	134	22.1
J2129.6+0005*	22_029	610		6	5.8×3.7, 66.1	51.3	11.7
J2135.2+0125*	34_030	325		3.4	14.8×8.9, 48.0	190.3	18.5
J2307.6+0130	36_050	325	✓	5.8	16.6×6.7, 67.4	78.7	18.1
J2327.4−0204*	26_031	610		7.6	5.1×4.6, 89.2	64.6	10.5
J2337.6+0016*	07CRA01	610		6.3	5.3×4.2, 68.9	45.8	26
J2341.2−0901*	10CRA01	610		3.3	4.8×4.4, -68.9	60.8	27.2
J2351.7−0859	36_050	325	✓	5.5	17.0×6.4, 57.7	105.1	19.3

to produce a better sky model and improved calibration solutions. This self calibration cycle is applied three times. **For the wide-field imaging, the pipeline performs a single-scale CLEAN deconvolution down to 3 times the central background noise (σ), using automated CLEAN boxes placed at positive peaks of at least 5σ.**

3. The second part of the 'process target' step is to correct for DDEs (3GC), which include ionospheric effects (Lonsdale, 2005). For each 3GC cycle, the brightest source in the field is peeled. The ionospheric effects of the brightest source are modelled and phase corrected solutions for the peeled model are obtained. SPAM uses a phase screen model to extend the ionospheric phase solutions of the single source to the full field. Then the solutions are applied to each facet during imaging. This cycle is repeated six times and each time the brightest source is selected and corrected for DDEs. This repeats until all the bright sources are corrected for DDEs. Finally, the astrometic corrections are applied on the DDEs corrected image and the image is primary beam corrected thereafter.

We used default data reduction parameters for all the clusters. The default setting of the number of pixels is $\sim$3780, with a pixel size of $\sim$1.9$''$. The statistics of the primary beam corrected images for the full sample are summarised in Table 2.2. The average flagged percentage of the reduced visibilities is $\sim$19.8%. **For some fields (e.g J0003.1$-$0605, J2135.2+0125, J0019.6+0336, and J0106.1$-$0619), noise levels are much higher than the theoretical square root scaling laws. A major factor that contributed to the high RMS values is ionospheric effects that were affecting the bright sources in the field. Other contributing factors are RFI and poor uv coverage (see Section 2.7).** The full field of view, primary beam corrected images are shown in Appendix A.

2.5 GMRT GSB Radio Analysis and Results

After our primary data reduction, we proceeded to search for extended diffuse radio emission in the region of our clusters. To carry out this search, we produced low resolution images for all the GSB observations. Our low resolution imaging process was done using the SPAM pipeline. We first imaged the compact sources by applying a uv-range cut at baselines $\geqslant$ 3 kλ. At this uv-range all the point source emission is captured, while higher uv cuts resulted in residual point source emission and lower uv cuts also captured the extended diffuse structure. We then used the high resolution imaging step to create model visibilities that only contained the point sources. **For the high resolution images, we used a Briggs robust parameter of -0.8.** We subtracted the point sources in the visibility plane. We then produced a full resolution point-source-subtracted image to ensure that the subtraction was successful. Finally, we imaged the visibilities in the uv-range $\leqslant$ 8 kλ whilst applying a uv-taper at 5 kλ **and using a Briggs robust parameter of 0.8.** These tapering and uv-cut values were ideal for capturing the full extension of the emission while producing images with decent resolution and rms noise levels (see Table 2.3). Figure 2.6 highlights the low resolution imaging process for ACT-CL J0248.1+0238. Based on the 3σ low-resolution contours (green contours), we conclude that this cluster has no extended emission in the cluster region. The cyan contours plotted in the point source subtracted full resolution images and low resolution images indicate that there was no residual point source emission in the low resolution images. However, the artefacts around the bright sources are also picked up in the high-resolution image. We use the same approach for the full sample. If a radio source in the cluster region that is detected at or above 3σ and is not related to an individual radio galaxy, it is classified as diffuse emission.

From our analysis of the low resolution images, we detect diffuse emission in seven clusters, namely,
ACT-CL J0019.6+0336, ACT-CL J0034.4+0225, ACT-CL J0137.4$-$0827, ACT-CL J0248.1$-$0216, ACT-CL J0159.8$-$0849, ACT-CL J2129.6+0005, ACT-CL J2128.4+0135, and candidate emission in ACT-CL J0022.2$-$0036. We did not recover the candidate emission in ACT-CL J0014.8$-$0057 and ACT-CL J0045.2$-$0152, which was reported by Knowles et al. (2019). This non-detection

is likely due to the high noise levels in our images. The noise variations may be due to different approaches in the data reduction strategies. We then proceed to the analysis and classification of the diffuse emission in each cluster.

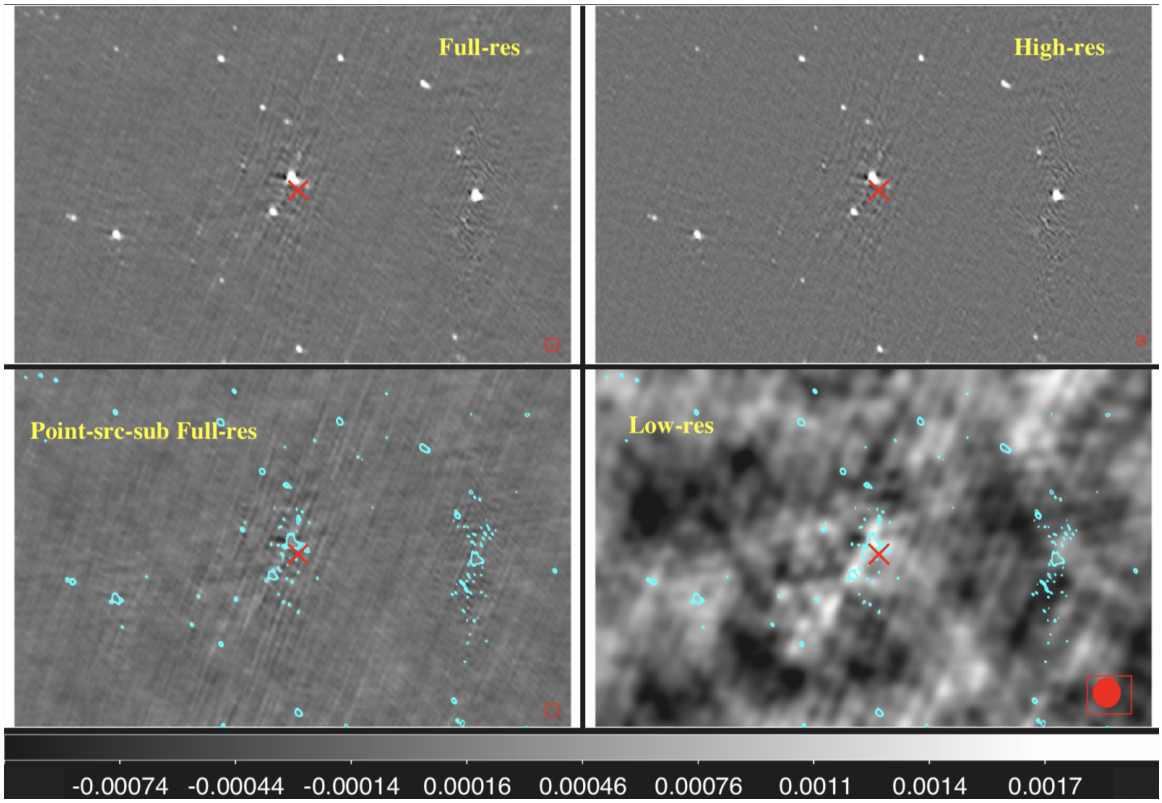

Figure 2.6: The low resolution imaging procedure for ACT-CL J0248.1+0238. For each panel, the red crosses indicate the ACT SZ peak and the red ellipses enclosed in boxes indicate the beams. All the panels are on the same color scale. *Top left:* The full resolution image has an rms of 57.3 μJy/beam and a beam size of ($10.7'' \times 7.8''$, p.a. 32.9^o). *Top right:* The high resolution image has an rms of 58.7 μJy/beam and a beam size of ($9.6'' \times 6.7''$, p.a. 32.2^o). *Bottom left:* The full resolution point-source-subtracted image has an rms of 74.42 μJy/beam and a beam size of ($12.7'' \times 9.6''$, p.a. 27.8^o). The cyan contours are from the high resolution images and the contour levels are $\sigma \times$[4,6,12]. *Bottom right:* The low resolution image has an rms of 0.49 mJy/beam and a beam size of ($37.9'' \times 35.3''$, p.a. 88.3^o). The cyan contours also from the high resolution image with the same contour levels as in the point-source-subtracted image.

Table 2.3: Summary of low resolution image statistics for all the clusters with archival or new GMRT observations. Columns: (1) Cluster name. (2) Synthesised beam of the low resolution image. (2) Diffuse emission detected in the low resolution images.

Cluster Name ACT-CL	Synthesised Beam ($'' \times ''$, deg)	RMS mJy/beam	Diffuse Emission?
J0003.1−0605	39.3×36.5, 78.2	1.41	No
J0008.1+0201	36.5×32.1, 83.1	0.28	No
J0014.8−0057	49.7×45.0, 43.59	0.35	No
J0019.6+0336	53.0×47.9, 59.94	0.91	Yes
J0022.2−0036	39.4×34.8, 74.1	0.37	Yes
J0026.2+0120	42.1×38.1, 84.7	0.37	No
J0033.8−0751	50.0×36.3, -86.4	0.6	No
J0034.4+0225	44.6×37.1, 28.6	0.58	Yes
J0045.2−0152	47.7×35.5, 52.2	0.22	No
J0059.1−0049	39.2×35.4, 49.9	0.85	No
J0106.1−0619	46.3×41.3, 18.1	0.52	No
J0129.0−0845	39.3×36.3, 48.0	0.30	No
J0137.4−0827	45.0×37.7, 63.3	0.51	Yes
J0140.0−0554	39.7×35.9, 43.5	22.3	No
J0152.6+0100	35.8×31.2, -89.7	1.10	No
J0154.4−0321	41.3×35.5, -62.4	0.61	No
J0159.8−0849	40.2×37.8, 73.4	0.39	Yes
J0239.8−0134	41.3×38.2, 68.3	0.81	No
J0248.1+0238	37.9×35.3, 88.3	0.49	No
J0248.1−0216	29.3×26.3, -73.5	0.15	Yes
J0326.8−0043	40.4×35.0, -67.2	0.52	No
J2050.5−0055	38.8×34.7, -85.0	0.65	No
J2128.4+0135	37.8×33.1, 73.1	0.75	Yes
J2129.6+0005	40.1×35.5, 41.61	0.40	Yes
J2135.2+0125	46.8×39.7, 52.3	0.92	No
J2307.6+0130	40.4×34.0, 72.1	0.44	No
J2327.4−0204	40.4×36.7, 36.1	2.4	No
J2337.6+0016	42.1×38.9, 80.8	0.41	No
J2341.2−0901	38.2×32.3, 69.1	0.70	No
J2351.7−0859	40.6×38.7, 39.1	0.46	No

2.5.1 Flux density, spectral index, and $P_{1.4GHz}$ calculations

We use polygon regions guided by 3σ contours to measure the flux densities of the detected diffuse emission in the low resolution images. The error associated with the flux measurements is given by

$$\Delta S = \sqrt{(\delta S \times S)^2 + N\sigma^2}\,, \tag{2.11}$$

where S is the measured flux density, δS is the calibration uncertainty which is $\sim$10% for GMRT (Chandra et al., 2004), and N is the number of beams within the region that the flux density was measured. σ is the rms noise of the low resolution images which is measured using a background region tagged in DS9.

For clusters with archival multi-frequency radio observations, we calculate the corresponding spectral index value of the extended emission. The multi-frequency observations were either from GMRT or MeerKAT. We computed the integrated spectral index values using $S_\nu \propto \nu^{-\alpha}$, where ν is the central frequency of the observation and S_ν is the measured flux at that frequency. The error associated with the spectral indices was calculated arithmetically, with the assumption that the assumption that the flux-density measurement errors at the two frequencies are independent. For the MeerKAT observations, the flux calibration uncertainty is $\sim$5%. This uncertainty is accounted for during the flux density calculations in Knowles et al. (2020). We note that the derived integrated spectral index values might have discrepancies given that the flux densities are measured using different apertures, and in some cases, using different instruments.

We use the spectral index values to extrapolate the radio power at 1.4 GHz. For clusters with single frequency observations, we use a fiducial spectral index value of $\alpha \sim 1.3$ (see Venturi et al., 2013) to calculate the radio power. We use the following equation to calculate the k-corrected radio power at 1.4 GHz

$$\frac{P_{1.4\mathrm{GHz}}}{\mathrm{WHz}^{-1}} = 4\pi \left(\frac{D_L}{\mathrm{m}}\right)^2 \left(\frac{S_\nu}{\mathrm{m}^{-2}\mathrm{WHz}^{-1}}\right) \left(\frac{1.4\mathrm{GHz}}{\nu}\right)^{-\alpha} (1+z)^{-(-\alpha+1)}\,, \tag{2.12}$$

where D_L is the luminosity distance of a cluster at redshift z, S_ν is the flux density at frequency ν, and α is the power law spectral index. We also measure the largest angular size (LAS) and

the largest linear size (LLS) of the diffuse emission. The LLS is calculated by dividing the LAS by the angular size distance (D_A). We use the measured properties of the diffuse emission to classify if it falls in the category of radio halos, mini-halos, radio relics, revived fossil plasma, or candidate emission (see Chapter 1). We now examine each cluster in turn in detail.

2.5.2 Known diffuse emission

We begin by analysing the diffuse emission that has been reported in literature. For ACT-CL J0019.6+0336 and ACT-CL J0034.4+0225 the emission is detected for the first time at 325 MHz and for ACT-CL J0248.1−0216 and ACT-CL J0159.8−0849 the emission is detected for the first time at 610 MHz. All the detection reported in literature for these clusters were at higher frequencies ($\sim$1 GHz). We also re-detected the diffuse emission in ACT-CL J2129.6+0005.

2.5.2.1 ACT-CL J0019.6+0336

ACT-CL J0019.6+0336 (alternative name: NSCS J001937+033655) is a massive cluster, (M_{500c} = 9.4$\times 10^{14}$ M$_\odot$) at redshift 0.269 (Hilton et al., 2018). At this cluster redshift, 1 arcsecond corresponds to 4.124 kpc and the luminosity distance is 1369.9 Mpc. This cluster, and all the clusters in our sample, have optical observations from the Dark Energy Survey (DES) Abbott et al. (2018). Currently, there are no multi-wavelength studies of the dynamical state of ACT-CL J0019.6+0336. Knowles et al. (2020) observed the cluster using MeerKAT at L-band (1.28 GHz). They reported a detection of a radio halo with a flux density of 9.16 $\pm$ 0.57 mJy and a LLS of 810 kpc.

From our re-analysis of archival data (PI: Annalisa Bonafede, ID: 25_018), we observe the diffuse emission for the first time at 325 MHz, and confirm the presence as detected at 1.28 GHz by Knowles et al. (2020) (see Figure 2.7). We measure an integrated flux density of $S_{323\mathrm{MHz}}$ = 35.64 $\pm$ 4.37 mJy and a LAS of 2.98$'$ $\times$ 2.01$'$, which corresponds to a LLS of 985 kpc $\times$ 497 kpc. Using our results and the 1.28 GHz flux density measurement from Knowles et al. (2020) we measure a spectral index of 1.07 $\pm$ 0.09. We use the spectral index value to derive a halo radio power at 1.4 GHz and we obtain P$_{1.4\mathrm{GHz}}$ = (1.73 $\pm$ 0.08) $\times 10^{24}$ WHz^{-1}.

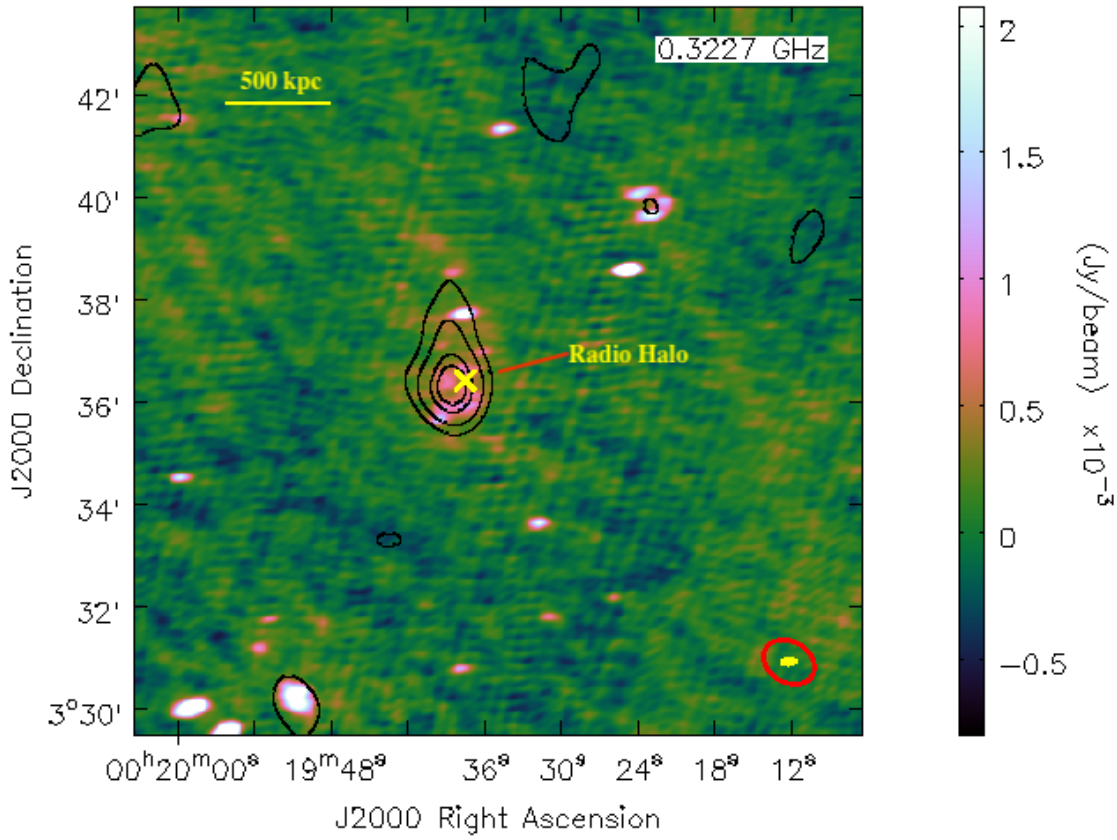

Figure 2.7: Full resolution image of ACT−CL J0019.6+0336 which has an rms of 144.0 μJy/beam. The contours are from the low resolution point-source-subtracted image. The rms (σ) of the low resolution image is 0.91 mJy/beam and the contour levels are $\sigma\times$[-3,3,5,8,10]. The beams of the full resolution and the low resolution images are shown by the yellow ellipse and the red ellipse, respectively. The beam sizes of the full resolution and low resolution images are (18.7″ × 8.2″, p.a. -84.4) and (53.0″ × 47.9″, p.a. 59.94), respectively. The yellow cross indicates the ACT SZ peak.

The recovered emission has the same morphological structure as the radio halo in Knowles et al. (2020). From the optical image in Figure 2.8 we note that the brightest cluster galaxy (BCG) does not coincide with the ACT SZ peak, however it is embedded in the diffuse emission region. Although studies have shown that mini-halo emission usually surrounds a BCG this, the diffuse emission detected in this cluster is larger than the typical size of mini-halos (Giacintucci et al., 2019). Comparing the diffuse emission in Figure 2.7 with the *XMM-Newton* contours in Figure 2.8, the diffuse emission roughly follows the morphology of the X-ray emitting gas. This is often observed for radio-halo emission (Cuciti et al., 2021b). Hence, we deduce that the detected diffuse emission falls in the category of radio halos. We note that this radio halo has a flatter spectrum compared to reported radio halo spectral indices which are typically $\sim$1.3.

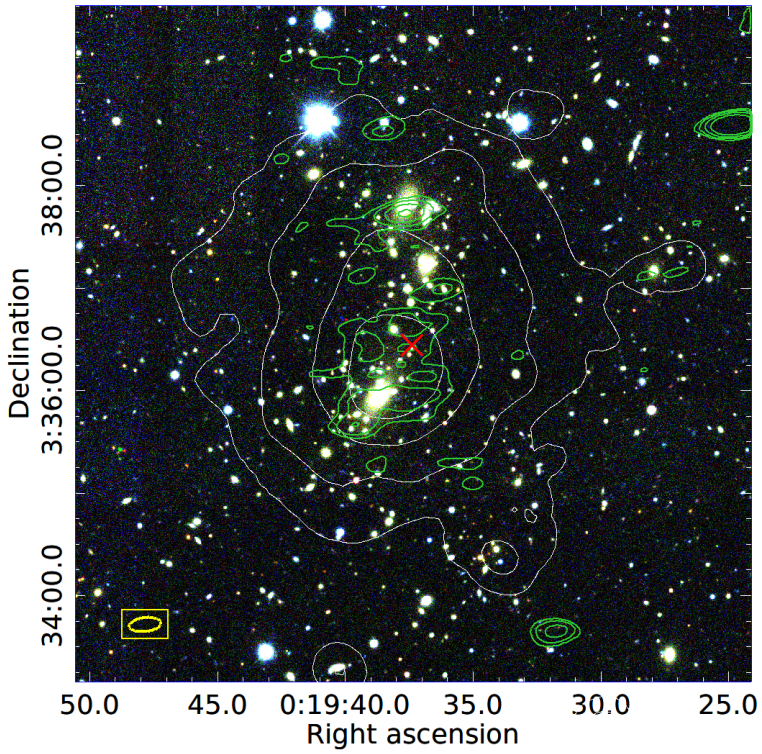

Figure 2.8: Optical image of ACT−CL J0019.6+0336 from the dark energy survey's first data release (DES DR1). The white contours are from the *XMM-Newton*. The corresponding contour levels are [3,6,12,24]×counts. The green contours are from the full resolution image. The contour levels are $\sigma\times$[3,5,10,20], where σ = 144.0 μJy/beam. The beam size is indicated by the yellow ellipse. The red cross indicates the ACT SZ peak.

2.5.2.2 ACT-CL J0034.4+0225

ACT-CL J0034.4+0225 is at redshift 0.382 and has a mass of M_{500c} = 9.0$\times 10^{14}$ M$_{\odot}$ (Hilton et al., 2018). At this cluster redshift, 1 arcsecond corresponds to 5.223 kpc and the luminosity distance is 2057.4 Mpc. Carrasco et al. (2017) used data from the FOcal Reducer and low dispersion Spectrograph 2 (FORS2; Appenzeller et al., 1998) which is mounted at Very Large Telescope (VLT) to study the galaxy cluster. From their observations they derived that the cluster has a rest-frame velocity dispersion of 713 $\pm$ 179 kms^{-1} and a dynamical mass of (3.37 $\pm$ 2.19) $\times 10^{14}$ M$_{\odot}$. MeerKAT L-band observations by Knowles et al. (2020) indicated that the cluster hosts a candidate radio halo. From their observations, they measured the flux density of the radio halo to be $S_{1.16\mathrm{GHz}} = 1.26 \pm 0.2$ mJy and it has LLS of 348 kpc.

From our 325 MHz GSB data (PI: Kenda Knowles, ID: 32_016), we observe the diffuse emission for the first time at this frequency, and confirm the presence as detected at 1.16 GHz by Knowles et al. (2020) (See Figure 2.9). The emission we detect has a larger extent than that detected in Knowles et al. (2020) due to the observations being at a lower frequency. The flux density of the detected diffuse emission is $S_{323\mathrm{MHz}} = 18.77 \pm 2.31$ mJy, and the LAS is 2.32$'$ $\times$ 1.46$'$, corresponding to a LLS of 726 kpc $\times$ 459 kpc. **We note that the flux density measurements might contain residual emission from the BCG that is embedded in the radio halo** .Using our results and the 1.16 GHz flux density measurement from Knowles et al. (2020) we calculated the spectral index of the radio halo and found it to be 2.11 $\pm$ 0.77. This indicates that the radio halo is an ultra steep steep spectrum. We used the spectral index to extrapolate the halo radio power at 1.4 GHz and found it to be (0.62 $\pm$ 0.12) $\times 10^{24}$ WHz^{-1}. The optical image shows that the BCG does not overlap ACT SZ peak while the peak X-ray brightness contours overlap with the ACT SZ peak which is the region where the emission is detected (see Figure 2.10). Given the extent of the diffuse emission, the central location, and its regular morphology, we conclude that it falls in the category of radio halos. We also note that the irregular morphology of the X-ray emission might be an indication of merger activity given that this cluster is paired with ACT-CL J0034.9+0233 (Hilton et al., 2018).

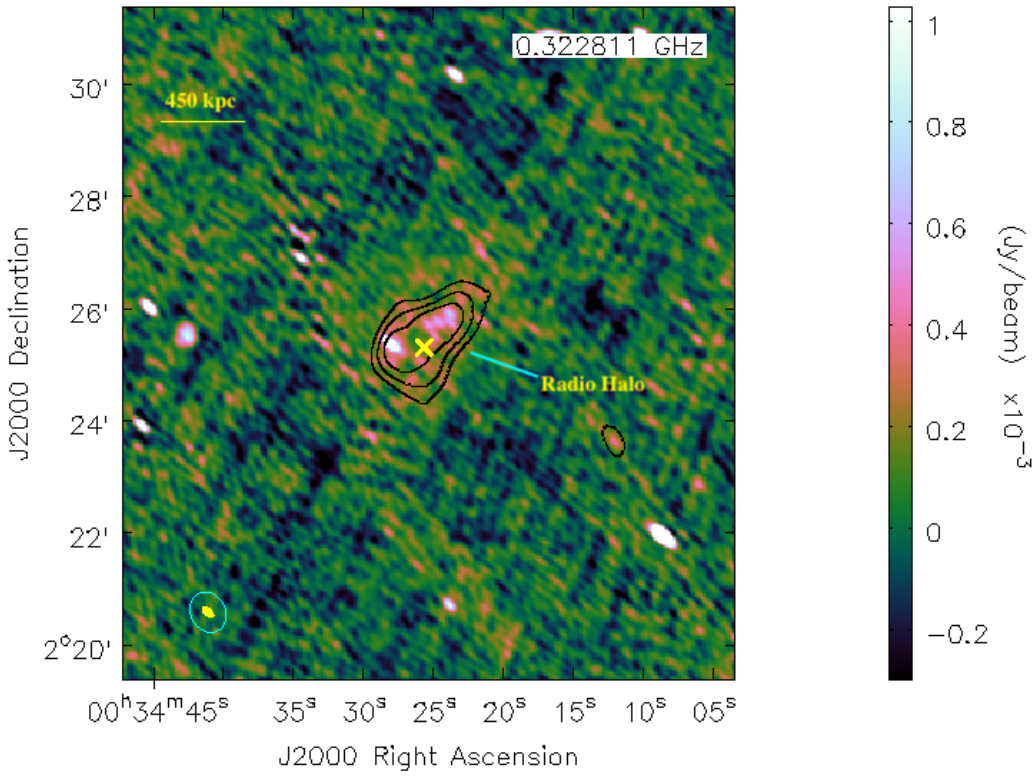

Figure 2.9: Full resolution image of ACT−CL J0034.4+0225 which has an rms of 75.8 μJy/beam. The contours are from the low resolution point-source-subtracted image. The rms (σ) of the low resolution image is 0.58 mJy/beam and the contour levels are $\sigma\times$[-3,3,4,6]. The yellow cross indicates the ACT SZ peak. The beam sizes of the full resolution and the low resolution images are shown by the yellow ellipse and the cyan ellipse, respectively. The beam sizes of the full resolution and low resolution images are ($14.2'' \times 18.1''$, p.a. 48.2) and ($44.6'' \times 37.1''$, p.a. 28.6), respectively.

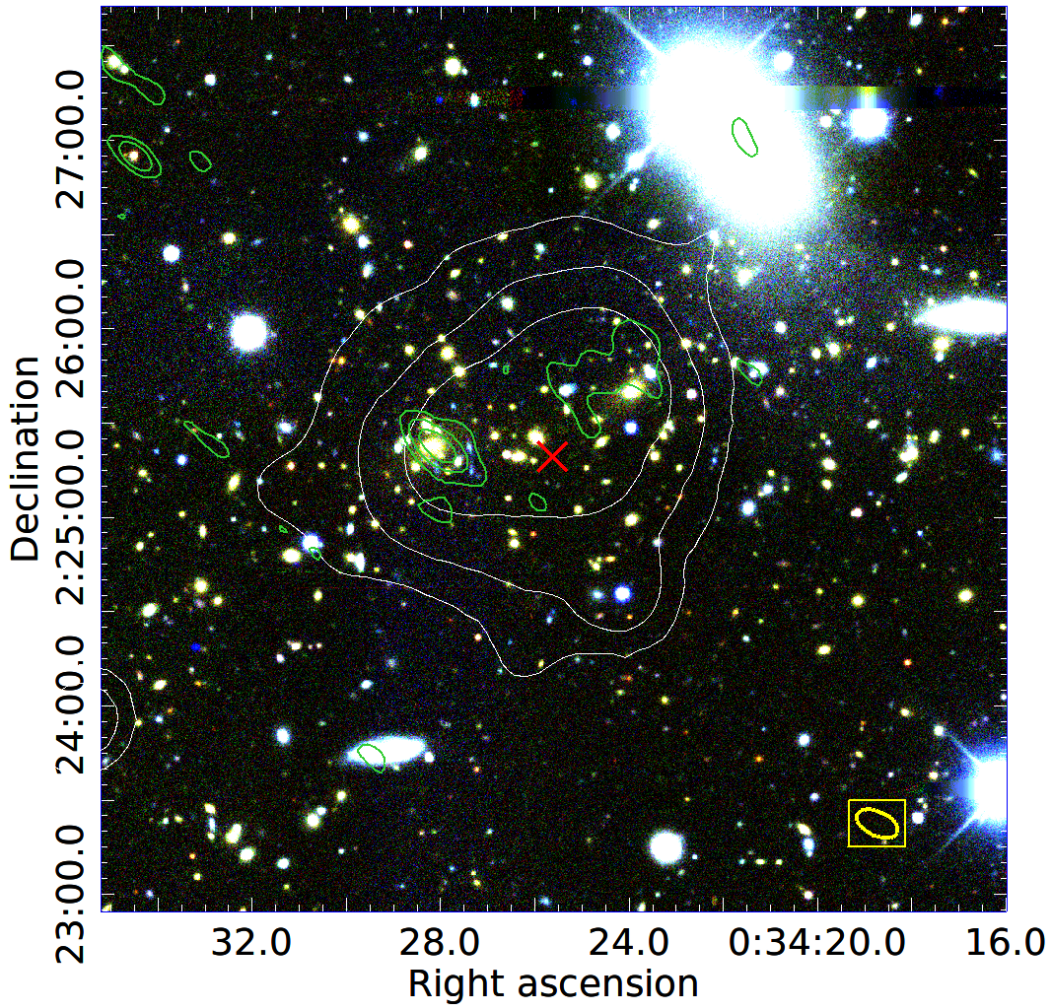

Figure 2.10: DES DR1 image of ACT−CL J0034.4+0225. The white contours are from *Chandra*. The corresponding contour levels are [3,6,12,24]×counts. The green contours are from the full resolution image. The contour levels are $\sigma \times$[5,10,20], where σ = 75.8 μJy/beam. The beam size is indicated by the yellow ellipse. The red cross indicates the ACT SZ peak. The BCG is offset from the SZ peak and X-ray centre, indicating merger activity

2.5.2.3 ACT-CL J0248.1-0216

ACT-CL J0248.1−0216 (alternative name: Abell 384) is at redshift 0.238 and has a mass of M_{500c} = 8.9×10^{14} M$_{\odot}$ (Hilton et al., 2018). At this cluster redshift, 1 arcsecond corresponds to 3.770 kpc and the luminosity distance is 1191.8 Mpc. Currently, there are no published multi-wavelength dynamical studies for this cluster. Knowles et al. (2020) reported a detection of a radio halo in the cluster from MeerKAT L-band observations. The extent of the detected diffuse emission was measured to be 656 kpc and the integrated flux density was $S_{1.28\mathrm{GHz}} = 6.46 \pm 0.41$ mJy.

From our analysis of archival data (PI: Rossella Cassano, ID: 26_021), we observe the diffuse emission for the first time at 610 MHz, and confirm the presence as detected at 1.28 GHz by Knowles et al. (2020). We measure a flux density of $S_{608\mathrm{MHz}} = 13.92 \pm 1.38$ mJy, a LAS of 2.44′ × 2.06′, which corresponds to a LLS of 552 kpc × 466 kpc. The morphology of the emission is similar to the radio halo in Knowles et al. (2020). We recover a larger extent of the emission, and this is because our observations are at a lower frequency. The 1.28 GHz flux density measurement from Knowles et al. (2020) in combination with our results indicate that the halo has a spectral index value of 1.03 ± 0.05. We use the spectral index to derive the halo radio power at 1.4 GHz, we find that P$_{1.4\mathrm{GHz}}$ = (1.01 ± 0.22) ×10^{24} WHz^{-1}. The diffuse emission we detect has regular morphology and it is located at the ACT SZ peak. From Figure 2.11 there is an indication of two BCGs and there is an offset between the SZ peak and the BCGs, giving credence to this being a merger system. We also note that diffuse emission falls within the peak X-ray brightness contours. The morphology, location, hints of merger activity, and extent of the emission indicates that it falls in the category of radio halos.

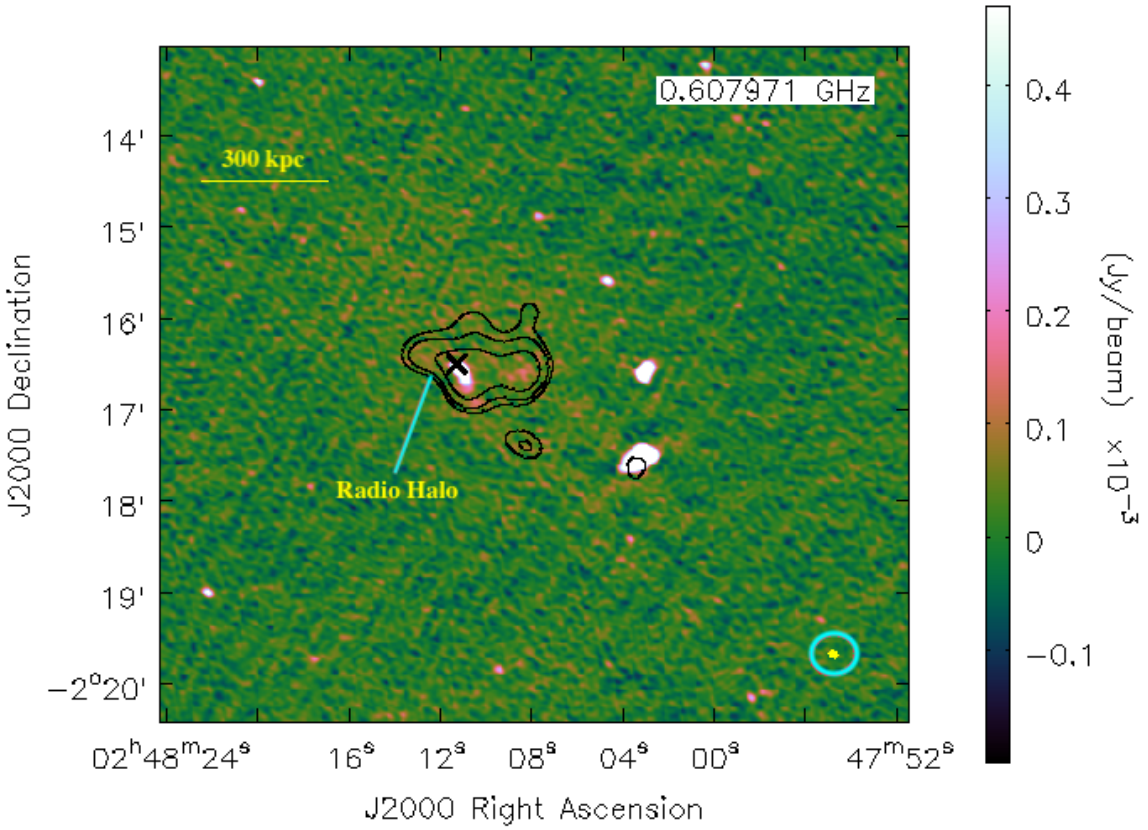

Figure 2.11: Full resolution image of ACT−CL J0248.1−0216 which has an rms of 32.4 μJy/beam. The contours are from the low resolution point-source-subtracted image. The rms (σ) of the low resolution image is 0.15 mJy/beam and the contour levels are $\sigma\times$[-3,3,4,6]. The beams of the full resolution and the low resolution images are shown by the yellow ellipse and the cyan ellipse, respectively. The beam sizes of the full resolution and low resolution images are ($5.6'' \times 3.9''$, p.a. 65.0) and ($29.3'' \times 26.3''$, p.a. -73.5), respectively. The black cross indicates the ACT SZ peak.

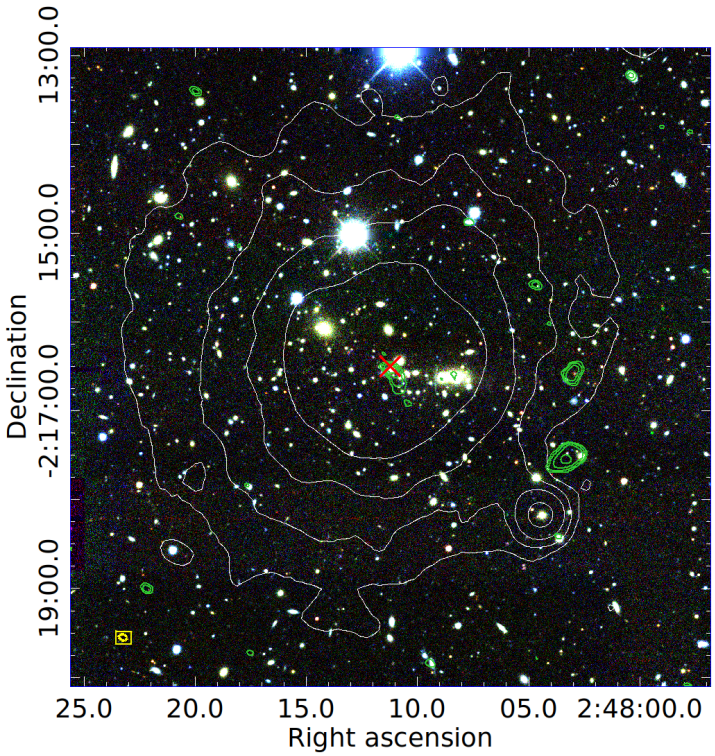

Figure 2.12: DES DR1 image of ACT−CL J0248.1−0216. The white contours are from the *XMM-Newton*. The corresponding contour levels are [3,6,12,24]×counts. The green contours are from the full resolution image. The contour levels are $\sigma\times$[4,10,30,90], where σ = 32.4 μJy/beam. The beam size is indicated by the yellow ellipse. The red cross indicates the ACT SZ peak.

2.5.2.4 ACT-CL J0159.8-0849

ACT-CL J0159.8−0849 (alternative name: PSZ2 G167.66−65.59) is a cool-core cluster with a regular X-ray morphology (Maughan et al., 2008; Cavagnolo et al., 2009). This cluster has a mass of M_{500c} = 7.2×10^{14} M$_{\odot}$ and is at redshift z = 0.408 (Hilton et al., 2018). At this cluster redshift, 1 arcsecond corresponds to 5.438 kpc and the luminosity distance is 2223.5 Mpc. Giacintucci et al. (2014b) were the first to report that ACT-CL J0159.8−0849 hosted a candidate mini-halo. 1.3 GHz GMRT observations by Giacintucci et al. (2019) confirmed the detection of a min-halo. The most recent radio observations of ACT-CL J0159.8−0849 are from Giovannini et al. (2020). They used JVLA observations at 1.5 GHz to study the properties of the mini-halo. From their observations, they measure the integrated flux density of the mini-halo to be $S_{1.5\mathrm{GHz}} = 2.2 \pm 0.2$ mJy and a LLS of 90 kpc.

From our analysis of archival data (PI: Lijo Thomas George, ID: 27_052), we observe the diffuse emission for the first time at 610 MHz, and confirm the presence as detected at 1.5 GHz by Giovannini et al. (2020) (see Figure 2.13). We measure a flux density of $S_{608\mathrm{MHz}} = 6.17 \pm 1.08$ mJy, a LAS of $1.32' \times 0.67'$, which corresponds to a LLS of 430 kpc × 219 kpc. The size of the diffuse emission is much larger than what is reported in literature. This might affect the spectral index measurements. Using our results and the most recent 1.5 GHz flux density measurement from Giovannini et al. (2020), we derive the spectral index of the diffuse emission to be 1.14 ± 0.07. We calculated the halo radio power at 1.4 GHz and found P$_{1.4\mathrm{GHz}}$ = (1.48 ± 0.60) ×10^{24} WHz^{-1}. The diffuse emission we recover (see Figure 2.13) has similar morphology to the mini-halo in Giacintucci et al. (2014b) but much more extended. The optical image (Figure 2.14) also indicates the presence of a BCG at close to the ACT SZ peak. From our radio analysis we note that the size of the emission is larger that the usual size of mini-halos. However, the emission is embedded in a radio loud BCG and dynamical studies reported this cluster as a relaxed system (Maughan et al., 2008; Cavagnolo et al., 2009). We conclude that the diffuse emission falls in the category of mini-halos.

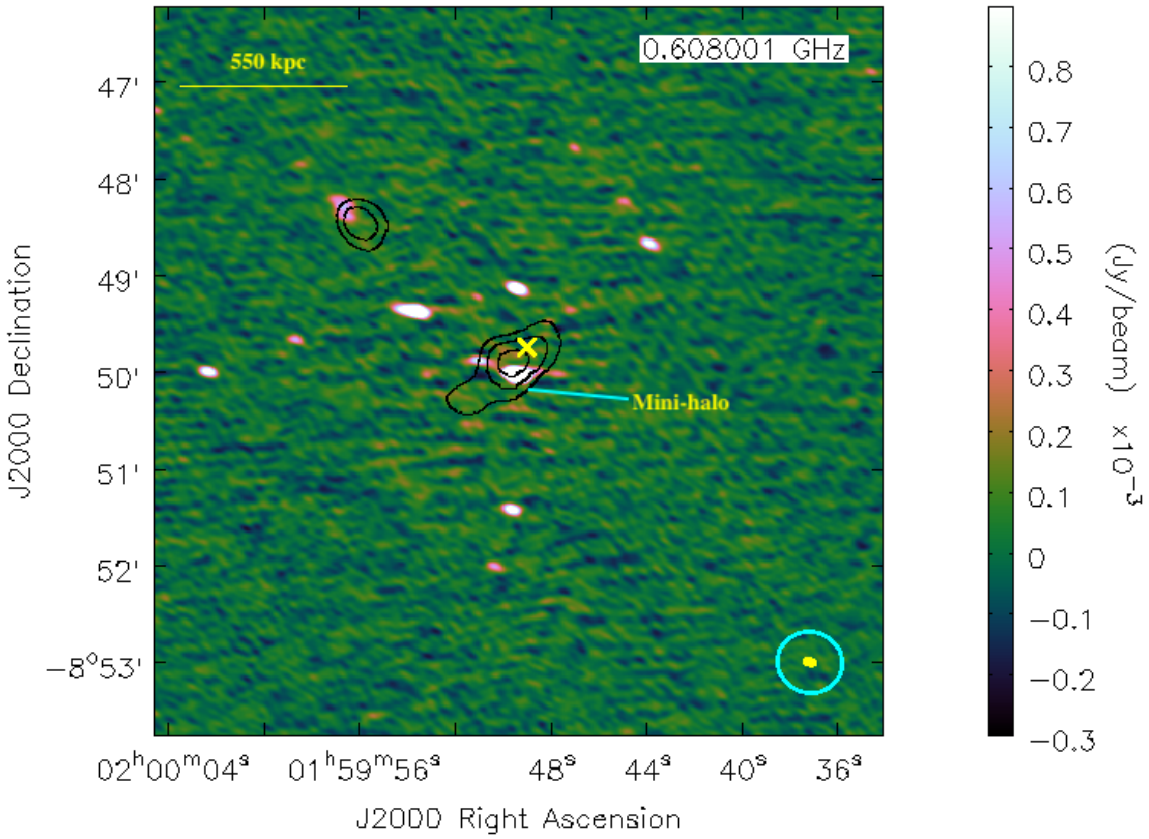

Figure 2.13: Full resolution image of ACT−CL J0159.8−0849 which has an rms of 48.7 μJy/beam. The contours are from the low resolution point-source-subtracted image. The rms (σ) of the low resolution image is 0.39 mJy/beam and the contour levels are $\sigma\times$[-3,3,6,8]. The beams of the full resolution and the low resolution images are shown by the yellow ellipse and the cyan ellipse, respectively. The beam sizes of the full resolution and low resolution images are ($8.1'' \times 4.6''$, p.a. 78.4) and ($40.2'' \times 37.8''$, p.a. 73.4), respectively. The yellow cross indicates the ACT SZ peak.

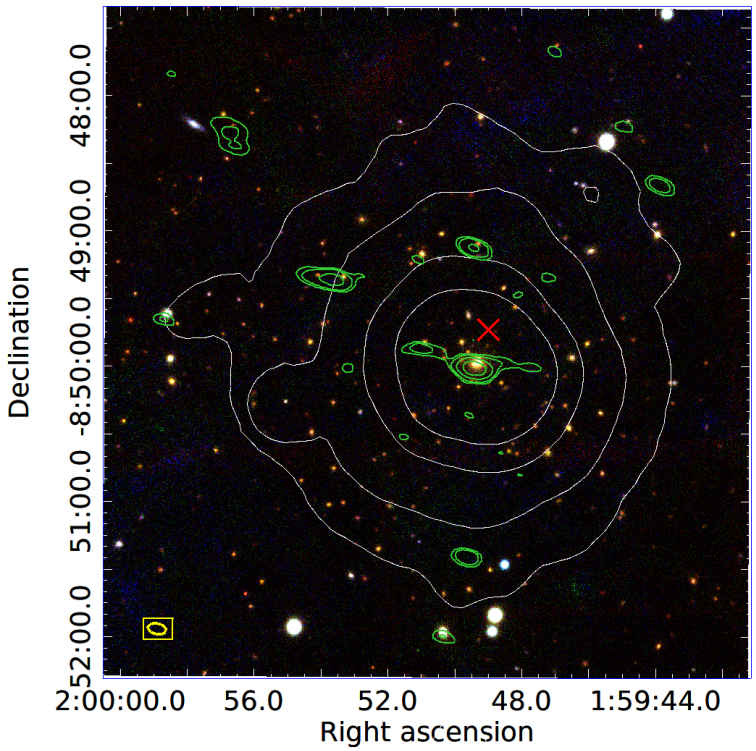

Figure 2.14: PanSTARRS image of ACT−CL J0159.8−0849. The white contours are from *Chandra*. The corresponding contour levels are [3,6,14,60]×counts. The green contours are from the full resolution GMRT image at 610 MHz. The contour levels are $\sigma\times$[5,10,40,160], where σ = 48.7 μJy/beam. The beam size is indicated by the yellow ellipse. The red cross indicates the ACT SZ peak.

2.5.2.5 ACT-CL J2129.6+0005

ACT-CL J2129.6+0005 (alternative name: RX J2129.6+0005) has a mass of M_{500c} = 6.0$\times 10^{14}$ M$_{\odot}$ and is at redshift z= 0.234 (Hilton et al., 2018). At this cluster redshift, 1 arcsecond corresponds to 3.722 kpc and the luminosity distance is 1169.1 Mpc. Multi-wavelength dynamical studies have classified this cluster as a relaxed cool-core cluster (Cavagnolo, 2008; Landry et al., 2013; Shitanishi et al., 2018). Kale et al. (2015) observed the cluster using GMRT at 610 MHz. They reported the detection of a mini-halo. They also confirmed the detection using archival data from the NRAO VLA Sky Survey (NVSS; Condon et al., 1998). The cluster was also part of the radio halo sample studies by Yuan et al. (2015); Knowles et al. (2019) and Giacintucci et al. (2019). Knowles et al. (2019) was not able to confirm the existence of the mini-halo, and hence derived its upper limits. The upper limit value they report for the mini-halo is $S_{610\mathrm{Hz}} < 10$ mJy/b 1.4 GHz GMRT observations by Giacintucci et al. (2019) confirmed the presence of the mini-halo. They measured the flux density of the halo to be $S_{1.4\mathrm{GHz}} = 2.4 \pm 0.2$ mJy and the corresponding LLS to be 80 kpc.

From our analysis of archival data (PI: Ruta Kale, ID: 22_029), we confirm the existence of diffuse emission in the cluster region (see Figure 2.15). We measure a flux density of $S_{613\mathrm{MHz}} = 5.45 \pm 1.76$ mJy, a LAS of $1.18' \times 0.77'$, which corresponds to a LLS of 264 kpc $\times$ 1742 kpc. The larger extent of the emission might result in inaccurate calculations of the spectral index. However, we still estimate the spectral index value using our results and the 1.4 GHz flux density measurement from Giacintucci et al. (2019). We calculated the spectral index value of the diffuse emission to be 1.00 $\pm$ 0.10. We then extrapolated the halo radio power at 1.4 GHz, which we estimated to be (0.39 $\pm$ 0.05) $\times 10^{24}$ WHz^{-1}. As seen in Figure 2.15, the diffuse emission is centred around a radio source which corresponds to the BCG (see Figure 2.16). From our radio analysis we deduce that the emission falls in the category of mini-halos.

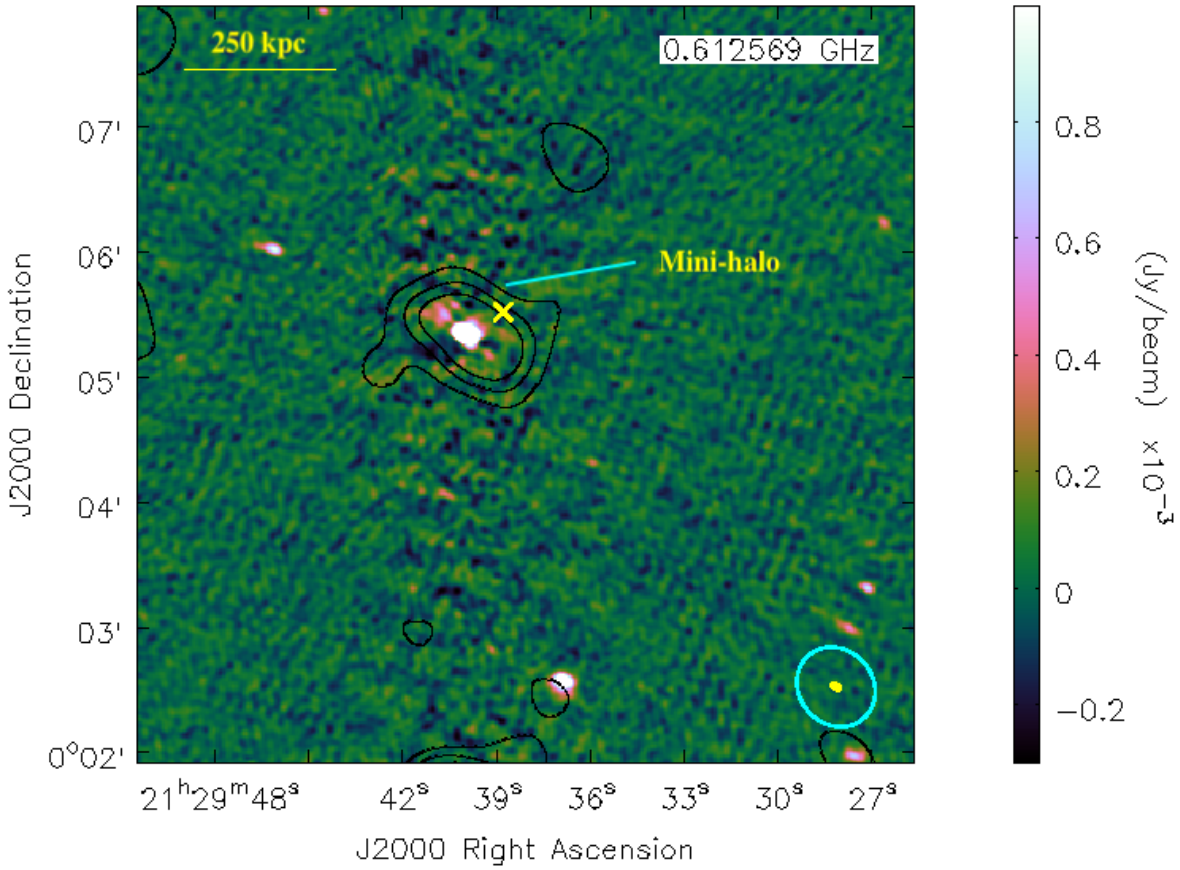

Figure 2.15: Full resolution image of ACT−CL J2129.6+0005 which has an rms of 51.3 μJy/beam. The contours are from the low resolution point-source-subtracted image. The rms (σ) of the low resolution image is 0.40 mJy/beam and the contour levels are $\sigma\times$[-3,3,6,8]. The yellow cross indicates the ACT SZ peak. The beams of the full resolution and the low resolution images are shown by the yellow ellipse and the cyan ellipse, respectively. The beam sizes of the full resolution and low resolution images are ($5.8'' \times 3.7''$, p.a. 66.1) and ($40.1'' \times 35.5''$, p.a. 41.61), respectively.

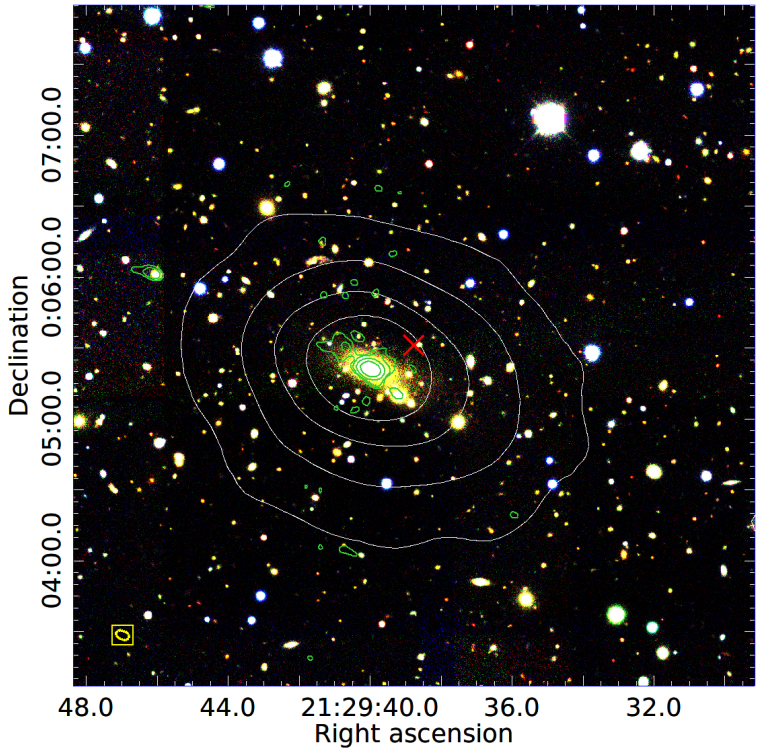

Figure 2.16: PanSTARRS. image of ACT−CL J2129.6+0005. The white contours are from the *XMM-Newton*. The corresponding contour levels are [3,6,12,24]×counts. The green contours are from the full resolution GMRT image at 610 MHz. The contour levels are $\sigma \times$[5,10,40,160], where σ = 51.3 μJy/beam. The beam size is indicated by the yellow ellipse. The red cross indicates the ACT SZ peak.

2.5.3 New detections

We report newly detected diffuse emission in ACT-CL J0137.4−0827, ACT-CL J2128.4+0135, and ACT-CL J0022.2−0036. All these clusters are at a high redshift ($z > 0.38$) in comparison to the cluster samples that have been used to derive scaling relations (Cassano et al., 2013; Kale et al., 2015; de Gasperin et al., 2014; Giacintucci et al., 2017; Cuciti et al., 2021a).

2.5.3.1 ACT-CL J0137.4-0827

ACT-CL J0137.4−0827 (alternative name: PSZ2 G155.27−68.42) is at redshift z = 0.568 and has a mass of M_{500c} = 8.2×10^{14} $M_{\odot}$ (Hilton et al., 2018). At this cluster redshift, 1 arcsecond corresponds to 6.514 kpc and the luminosity distance is 3303.2 Mpc. Bartalucci et al. (2019) used X-ray data from the European Photon Imaging Camera (EPIC; Strüder et al., 2001) to study the dynamical state of ACT-CL J0137.4−0827. Their results show that the cluster is dynamically disturbed. For the first time, we report the detection of extended diffuse radio emission in the cluster region (see Figure 2.17). The 325 MHz GSB data reveals that the cluster hosts extended diffuse emission with a flux density of $S_{323\mathrm{MHz}}$ = 19.72 ± 2.33 mJy, a LAS of 1.49′ × 1.10′, which corresponds to a LLS of 580 kpc × 429 kpc. There are no other radio observations for this cluster, hence, we used a fiducial spectral index value of 1.3 and extrapolated $P_{1.4\mathrm{GHz}}$ = (4.36 ± 0.27) ×10^{24} WHz^{-1}. The diffuse emission has an elongated morphology which is not that of typical radio halos (van Weeren et al., 2019) (see Figure 2.17). However, the diffuse emission coincides with the ACT SZ peak and X-ray surface brightness (see Figure 2.19), hence, we deduce that it is a radio halo and not a radio relic. Figure 2.17 also indicates that the BCG is offset from the SZ peak which might be an indication of merger activity. The low resolution image also showed extended emission (labelled FRII in Figure 2.17) in the peripheral region of the cluster. However, as seen in Figure 2.17,this emission is from a radio source with a Fanaroff-Riley Class II (FRII; Fanaroff and Riley, 1974) morphology. We also detect a roundish source that is ∼1.23 Mpc away from the cluster center. The angular size of the source is 0.99′ × 0.95′, which corresponds to a LLS of 387 kpc × 371 kpc. We measure the flux density of this source to be $S_{323\mathrm{MHz}}$ = 3.9 ± 0.8 mJy. Given the location and shape of this source, we predict that it is

a revived fossil plasma source (see van Weeren et al., 2019, for review). Using a fiducial spectral index value of 1.3 we measure the power of the revived fossil plasma to be $(2.19 \pm 0.57) \times 10^{23}$ WHz^{-1}.

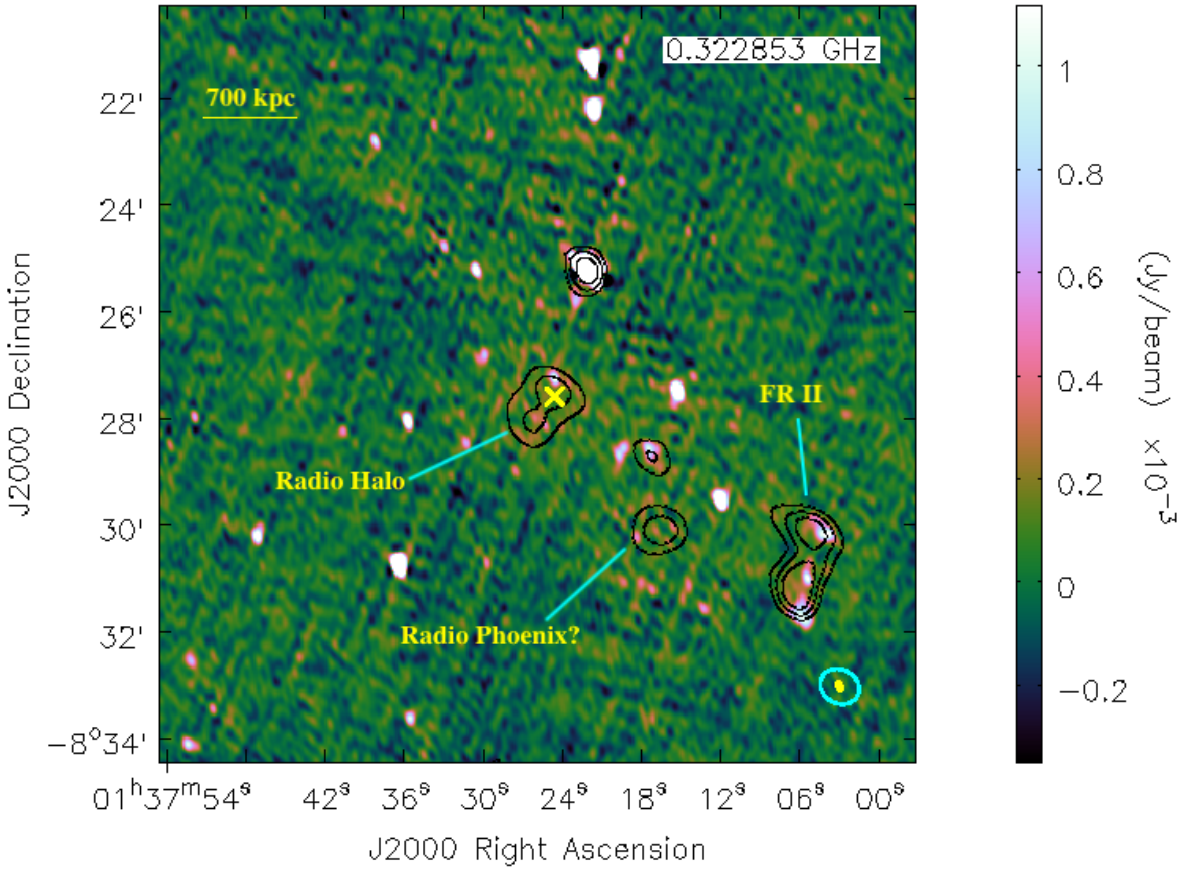

Figure 2.17: Full resolution image of ACT−CL J0137.4−0827 which has an rms of 74.5 μJy/beam. The contours are from the low resolution point-source-subtracted image. The rms (σ) of the low resolution image is 0.51 mJy/beam and the contour levels are $\sigma\times$[-3,3,6,8]. The yellow cross indicates the ACT SZ peak. The beams of the full resolution and the low resolution images are shown by the yellow ellipse and the cyan ellipse, respectively. The beam sizes of the full resolution and low resolution images are (12.8″ × 7.6″, p.a. 18.1) and (45.0″ × 37.7″, p.a. 63.3), respectively.

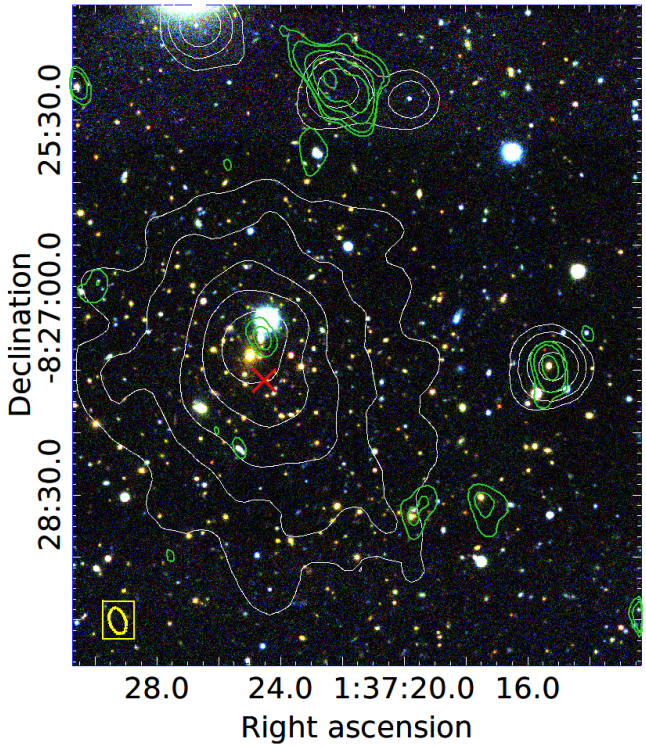

Figure 2.18: DES DR1 image of ACT−CL J0137.4−0827. The green contours are from the full resolution GMRT image at 325 MHz. The contour levels are $\sigma\times$[5,10,40,160,640], where σ = 74.5 μJy/beam. The white contours are from the *XMM-Newton*. The corresponding contour levels are [2,3,5,8,12]$\times$counts. The beam size is indicated by the yellow ellipse. The red cross indicates the ACT SZ peak.

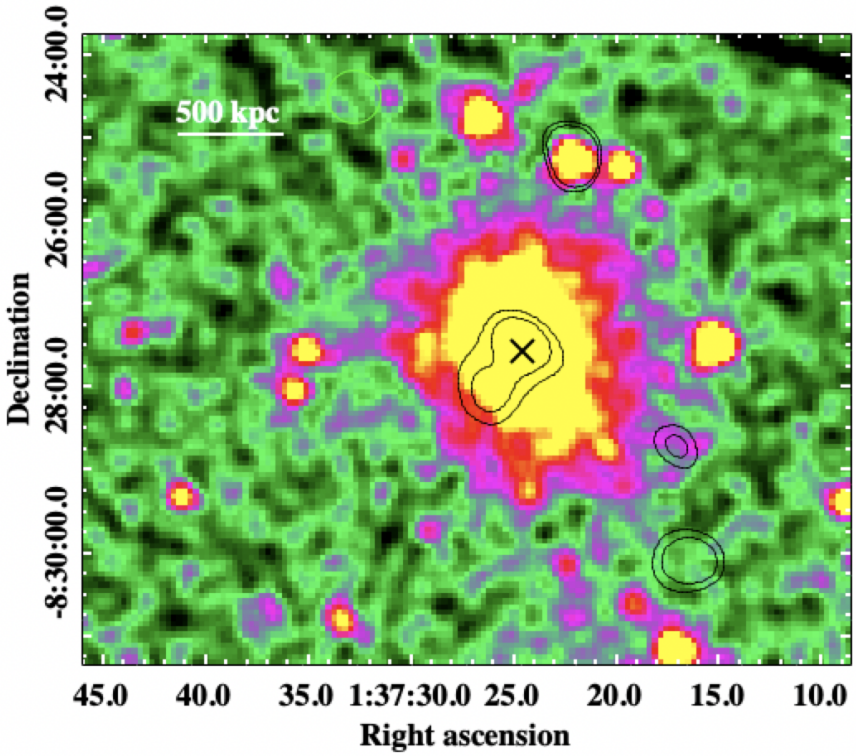

Figure 2.19: *XMM-Newton* image of ACT−CL J0137.4−0827. The black contour levels are from the low resolution image and increase as $\sigma\times$[-3,3,6,], where σ is 0.51 mJy/beam. The black cross corresponds to the SZ peak.

2.5.3.2 ACT-CL J2128.4+0135

ACT-CL J2128.4+0135 (alternative name: PSZ2 G054.95−33.39) is at redshift z = 0.386 and has a mass of M_{500c} = 5.6×10^{14} $M_{\odot}$ (Hilton et al., 2018). At this cluster redshift, 1 arcsecond corresponds to 5.256 kpc and the luminosity distance is 2082.8 Mpc. Menanteau et al. (2013) reported that the cluster has an X-ray luminosity of 4.63 ± 1.36×10^{44} ergss^{-1}. Dynamical studies using optical data indicated that the cluster is dynamically disturbed (Sifón et al., 2016).

ACT-CL J2128.4+0135 hosts intriguing diffuse emission within the cluster region. There is a bent-tail radio galaxy (Dehghan et al., 2014) that coincides with the ACT SZ peak and an FR II in the peripheral region. The low resolution contours in Figure 2.20 indicate extended emission in the both the bent-tail and FRII regions. Further processing would be required to indicate if there is a radio halo embedded in the bent-tail galaxy. The extended nature of this source makes it difficult to model and subtract it, hence the low resolution emission is most likely residual emission. We also recover a diffuse radio source that does not coincide with extended radio galaxies on the outskirt of the cluster. This emission doesn't correspond to any individual optical counterpart (see Figure 2.21). We measured the integrated flux density of the extended diffuse emission to be $S_{323\mathrm{MHz}}$ = 9.77 ± 1.13 mJy. The emission has a LAS of 1.55′ × 0.93′, which corresponds to a LLS of 489 kpc × 293 kpc. The distance from the ACT SZ peak to the emission in 2.09′, which corresponds to a linear scale of 916 kpc. There are no other radio observations for this cluster, hence, we use a fiducial spectral index value of 1.3 to derive the corresponding radio power at 1.4 GHz. We calculated $P_{1.4\mathrm{GHz}}$ to be (8.29 ± 0.91) ×10^{24} WHz^{-1}. The extended structure is at the periphery of the cluster, hence we categorise it as a radio relic.

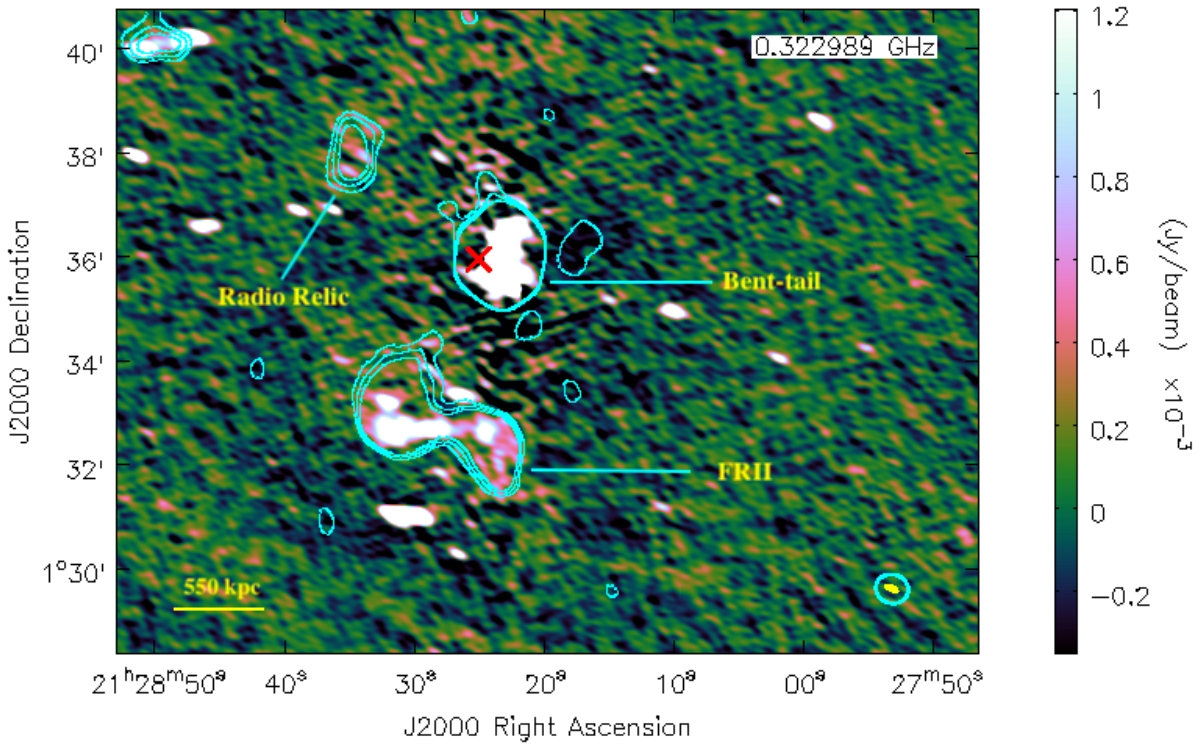

Figure 2.20: Full resolution image of ACT−CL J2128.4+0135 which has an rms of 134.0 μJy/beam. The contours are from the low resolution point-source-subtracted image. The rms (σ) of the low resolution image is 0.75 mJy/beam and the contour levels are $\sigma\times$[-3,3,4,5]. The beams of the full resolution and the low resolution images are shown by the yellow ellipse and the cyan ellipse, respectively. The beam sizes of the full resolution and low resolution images are ($16.0'' \times 6.9''$, p.a. 65.9) and ($37.8'' \times 33.1''$, p.a. 73.1), respectively. The black cross indicates the ACT SZ peak.

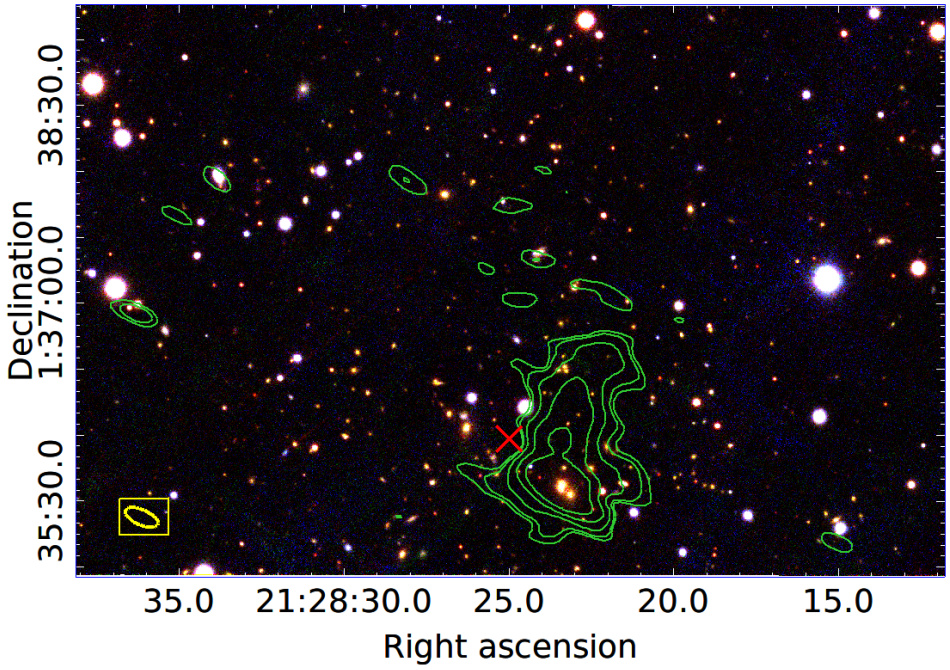

Figure 2.21: PanSTARRS image of ACT−CL J2128.4+0135. The green contours are from the full resolution GMRT image at 325 MHz. The contour levels are $\sigma \times$[4,8,12,30], where σ = 134.0 μJy/beam. The beam size is indicated by the yellow ellipse. The red cross indicates the ACT SZ peak.

2.5.3.3 ACT-CL J0022.2-0036

ACT-CL J0022.2−0036 (alternative name: WHL J002213.0-003634) has a mass of M_{500c} = 5.5×10^{14} $M_{\odot}$ and z = 0.805 (Hilton et al., 2018), which makes it the highest redshift cluster in our sample. At this cluster redshift, 1 arcsecond corresponds to 7.524 kpc and the luminosity distance is 5056.1 Mpc. X-ray images from *Chandra* observations indicated that the cluster has a cool-core and also showed hints of gas sloshing at the cluster core (Knowles et al., 2019). Spectroscopic studies by Sifón et al. (2016) indicated that the cluster is dynamically disturbed. Further dynamical studies are required to conclusively classify this cluster as relaxed or unrelaxed. Knowles et al. (2019) reported that the cluster hosts a mini-halo, which made it the highest known cluster to host a mini-halo. From their GMRT observations (610 MHz), they measure the mini-halo flux density to be $S_{610\mathrm{MHz}} = 6.4 \pm 1.8$ mJy.

From our re-analysis of archival data (PI: Kenda Knowles, ID: 26_031), we recover extended emission, shown by black contours in Figure 2.22. However unlike the diffuse emission reported in Knowles et al. (2019), the detected emission is located in the peripheral region of the cluster. The optical image does not indicate individual optical counterparts that might give rise to this emission (see Figure 2.23). Hence, we attribute it to the intracluster medium. We measure the integrated flux density of the diffuse emission to be $S_{608\mathrm{Hz}} = 5.9 \pm 1.35$ mJy. The emission has a LAS of $1.04' \times 0.55'$, which corresponds to a LLS of 428 kpc × 249 kpc. The distance from the ACT SZ peak to the extended radio source is $1.09'$ which corresponds to a physical linear scale of 492 kpc. There are no other radio observations for this cluster, hence, we use a fiducial spectral index value of 1.3 to derive the corresponding radio power at 1.4 GHz which we calculated to be $P_{1.4\mathrm{GHz}} = (7.30 \pm 0.65) \times 10^{24}$ WHz^{-1}. The detection of the diffuse emission is marginal, hence, we categorise it as a candidate radio relic. If the relic emission is a true detection, it would be amongst the highest-redshfit relics known with the relics hosted by El Gordo (Lindner et al., 2014) being at the highest redshift (z = 0.87).

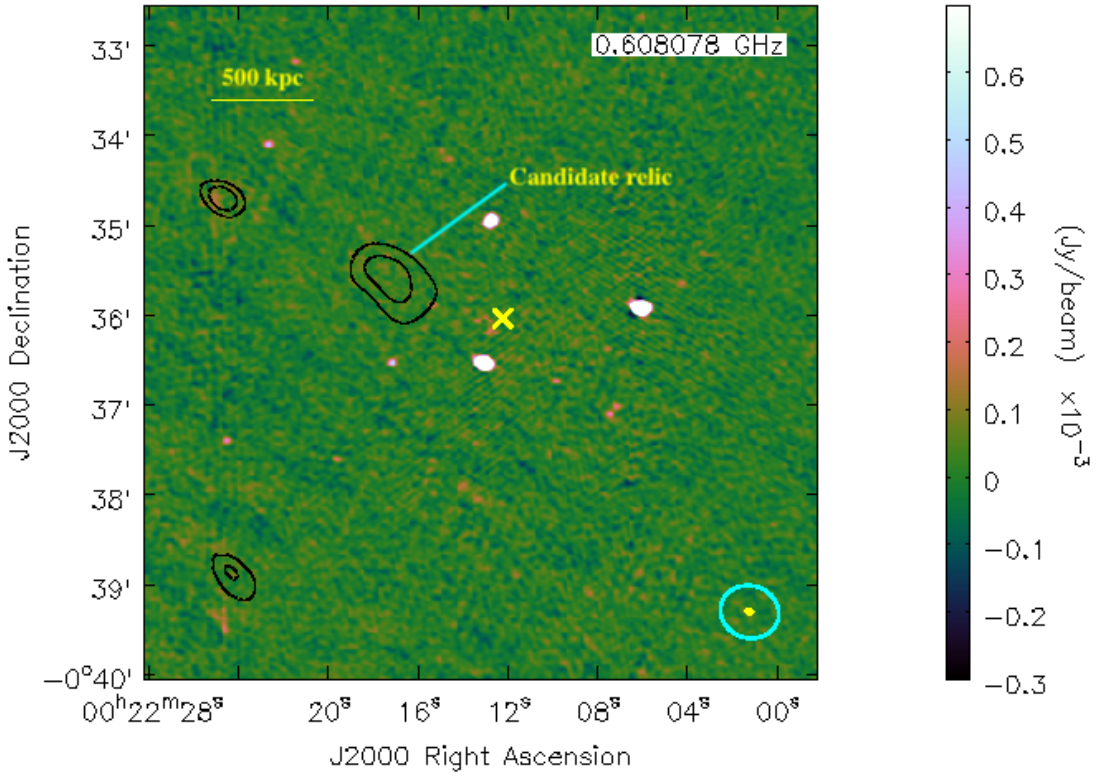

Figure 2.22: Full resolution image of ACT−CL J0022.2−0036 which has an rms of 27.0 μJy/beam. The contours are from the low resolution point-source-subtracted image. The rms (σ) of the low resolution image is 0.37 mJy/beam and the contour levels are $\sigma\times$[-3,3,5]. The beams of the full resolution and the low resolution images are shown by the yellow ellipse and the cyan ellipse, respectively. The beam sizes of the full resolution and low resolution images are ($5.2'' \times 4.0''$, p.a. 85.0) and ($39.4'' \times 34.8''$, p.a. 74.1), respectively. The yellow cross indicates the ACT SZ peak.

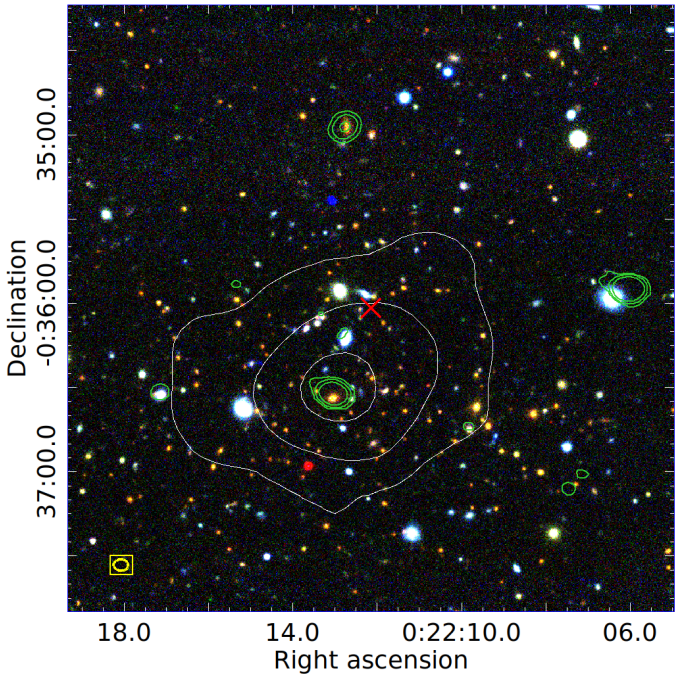

Figure 2.23: DES DR1 image of ACT−CL J0022.2−0036. The white contours are from *Chandra*. The corresponding contour levels are [3,6,12,24]×counts. The green contours are from the full resolution GMRT image at 610 MHz. The contour levels are $\sigma\times$[5,20,80], where σ = 27.0 μJy/beam. The beam size is indicated by the yellow ellipse. The red cross indicates the ACT SZ peak.

Table 2.4: The occurrence fractions of halos, min-halos, relics, and revived fossil plasma detected in the sample of 30 clusters. Columns: (1) Type of emission detected (total number). (2) Occurrence fraction when excluding candidate emission. (3) Occurrence fraction when including candidate emission.

Diffuse Emission	Percentages (excl candidate)	Percentages (incl candidate)
Overall (9)	26.7%	30.0%
Radio halos (4)	13.3 %	13.3 %
Mini-halos (2)	6.7%	6.7%
Radio relics (2)	3.3%	6.7%
Revived fossil plasma (1)	3.3%	3.3%

2.6 Cluster diffuse emission sample statistics

From our sample, the overall occurrence fraction of diffuse emission is 26.7%, excluding candidate emission, and 30% if the candidate emission is included. The occurrence fraction of radio halos is 13.3%, that of mini-halos is 6.7%. For radio relics, the overall occurrence fraction is 3.3% (6.67 %) excluding (including) the candidate relic, and for the revived fossil plasma it is 3.3%. The occurrence percentages are summarised in Table 2.4. The occurrence fractions the mini-halos, radio relics, and radio halos in our sample is lower than what has been reported in literature (Kale et al., 2015; Giacintucci et al., 2017; Giovannini et al., 2020; Cuciti et al., 2021a). The typical occurrence fraction for radio halos is $\sim$25% and for mini-halos it is $\sim$15%, these percentages are even higher ($\sim$30%) for more recent studies (Giovannini et al., 2020; Raja et al., 2021; Cuciti et al., 2021a).

Our sample covered a wide mass and redshift range. Theoretical studies predicted that for clusters at redshift > 0.6, the occurrence rate of halos decreases by 10% (Cassano et al., 2006). Hence, the low occurrence rates might be an indication of this drop predicted by theory. The detections may also be affected by the poor quality of the final low resolution images. Extracting faint extended radio sources requires high fidelity images. For radio halos, the low occurrence fraction might also be due to the fact that our sample selection was blind to the dynamical state

Table 2.5: Summary of the radio analysis results. Columns: (1) ACTPol cluster name. (2) Central effective frequency of the observation. (3) Integrated flux density. (4) Radio power at 1.4 GHz. (5) Largest angular size. (6) Largest linear size. (7) Classifications: radio halo (RH), mini-halo (mH), radio relic (RR), and candidate (c).

Cluster Name ACT-CL	ν_0 MHz	S_{ν_0} mJy	$P_{1.4GHz}$ 10^{24} WHz^{-1}	LAS $'$	LLS kpc	Classifications
J0019.6+0336	322	35.64 ± 4.37	1.73 ± 0.08	3.98×2.01	985×497	RH
J0034.4+0225	323	18.77 ± 2.31	0.62 ± 0.12	2.32×1.46	726×459	RH
J0248.1−0216	608	13.92 ± 1.38	1.01 ± 0.22	2.44×2.06	552×466	RH
J0137.4−0827	323	19.72 ± 2.33	4.36 ± 0.27	1.49×1.10	580×429	RH
J0137.4−0827	323	3.90 ± 0.8	0.22 ± 0.06	0.99×0.95	387×371	Fossil plasma
J0159.8−0849	608	6.17 ± 1.08	1.48 ± 0.60	1.32×0.67	430×219	mH
J2129.6+0005	612	5.45 ± 1.76	0.39 ± 0.05	1.18×0.77	264×1742	mH
J2128.4+0135	323	9.77 ± 1.15	8.29 ± 0.91	1.55×0.93	489×293	RR
J0022.2−0036	608	5.9 ± 1.35	7.30 ± 0.65	1.04×0.55	428×249	cRR

of the cluster. The selection function was solely based of the SZ parameters of the clusters. The occurrence fraction of mini-halos may have also been affected by the poor quality of our observations which resulted in images with high noise levels. All the clusters hosting diffuse emission have $M_{500c} > 5.5 \times 10^{14}\, M_{\odot}$. Based on the radio halo and relic mass-power relations, we can conclude that the non-detections may be due to faint emission with low radio power.

Due to the low detection rates, we are unable to perform statistical studies with our sample. Therefore, we compare the radio power − mass relation of the radio halos in our sample to the sample with the most recently derived scaling relations, which is found in Cuciti et al. (2021a) (see Figure 2.24). Cuciti et al. (2021a) used the $P_{1.4GHZ} - M_{500}$ correlation formula taken from Cassano et al. (2013). This formula allows us to relate the radio power of the halo with the mass of the host cluster in the following manner

$$\log\left(\frac{P_{1.4GHz}}{10^{24.5}WHz^{-1}}\right) = B\ log\left(\frac{M_{500}}{10^{14.9}M_{\odot}}\right) + A\ , \tag{2.13}$$

where B is the slope of the correlation line and A is the intercept. Cuciti et al. (2021a) used the BCES-bisector fitting method (Akritas and Bershady, 1996) to obtain the best-fit values for B and A. For the slope, the best-fit value was B=3.92 $\pm$ 0.79, and for the intercept, the best-fit

value was $A = -0.15 \pm 0.10$.

The sample in Cuciti et al. (2021a) was restricted to clusters at redshift $z < 0.33$. The radio halos are detected in our sample are hosted by clusters with a redshift range of $0.238 - 0.568$. ACT-CL J0034.4+0225 and ACT-CL J0137.4−0827 are at redshift 0.382 and 0.568, respectively. These system are at a higher redshift in comparison to the sample in Cuciti et al. (2021a). From Figure 2.24, we see that the three flatter spectrum ($\sim$1) radio halos, in ACT-CL J0019.6+0336, ACT-CL J0248.1−0216, and ACT-CL J0034.4+0225, fall in the region below the $P_{1.4GHz} - M_{500}$ correlation line **even though the bias of flatter spectrum should result in higher $P_{1.4GHz}$ values.** This trend has also been observed in Cuciti et al. (2021a). This region was previously known to be populated by ultra steep spectrum radio halos (USSRH). These radio halos are hosted by galaxy clusters at redshifts $z \geqslant 0.238$. The radio halos in the SPT high-redshift sample also fall bellow the correlation line (Raja et al., 2021). Hence, this might be an indication that at higher redshifts, there needs to be an adjustment to the currently existing scaling relations. However, larger samples of high-redshift clusters hosting radio halos are needed for a statistically significant conclusion (Knowles et al., 2016a).

We also compare the radio relics in our sample to the relics used to derive the $P_{1.4\mathrm{GHz}} - M_{500}$ scaling relation in Kale et al. (2017). This relation was first reported by de Gasperin et al. (2014). The best fit line for the sample in Kale et al. (2017) was found to have a slope of 2.76 $\pm$ 0.37. From Figure 2.25, we see that the relics in our sample are also in agreement with the $P_{1.4\mathrm{GHz}}$-M_{500} scaling relation. This indicates that this relation holds even for the high-redshift (z = 0.805) relics.

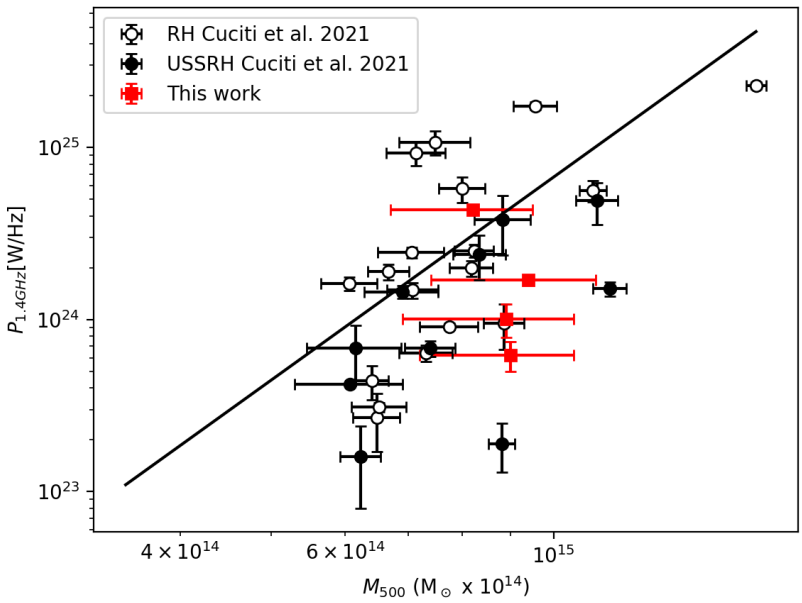

Figure 2.24: The power-mass relation for radio halos, with the four detections in our sample shown by red squares. The black circles are from the literature with filled (open) ones indicating ultra steep spectrum radio halos (radio halos). We fit the regression line from the latest scaling relation results in Cuciti et al. (2021a).

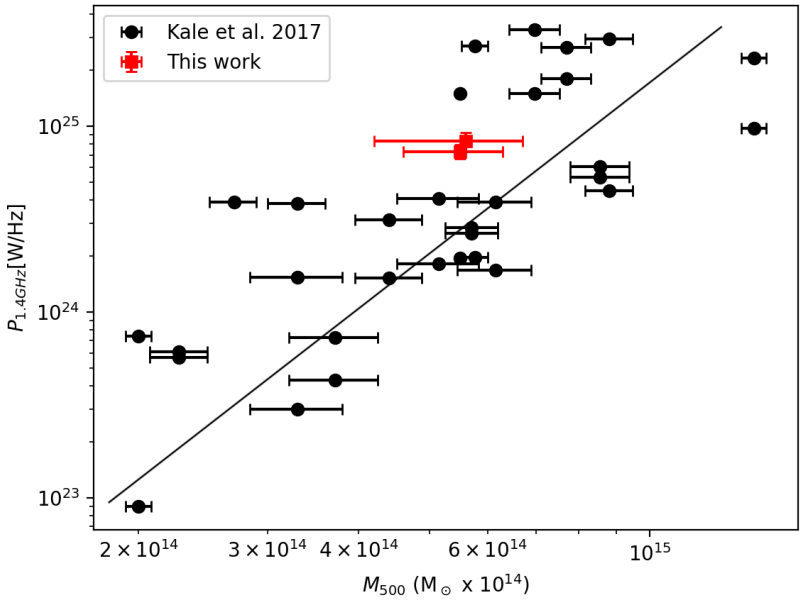

Figure 2.25: The power-mass relation for radio relics, with the two detection in our sample shown by red squares. The black circles being from the literature. The plot was produced using the slope in Kale et al. (2017). The sample of relics are taken from clusters in de Gasperin et al. (2014, 2015, 2017a) and Kale et al. (2017), we only include clusters with available SZ masses.

2.7 uGMRT GWB data reduction for new detections

From the eight clusters which showed evidence of diffuse emission in the GSB data, we have GWB data for three of them, namely ACT-CL J0034.4+0225, ACT-CL J0137.4−0827, and ACT-CL J2128.4+0135. Since we had GWB data in-hand for these clusters, we explored data reduction methods to investigate if this data showed any features that are not detected in the GSB data. We prioritise these clusters for follow-up GWB analysis because these were new detections. The wide bandwidth of the upgraded GMRT simultaneously provides increased sensitivity and opportunity for in-band spectral index studies. However, the calibration and imaging of GWB data is a complex procedure.

The main challenges with reducing the wide-band, wide-field data are as follows. The primary beam pattern is dependent on the observing frequency, as shown in Equation 2.7. Hence, for wide bandwidth observations, this pattern varies across the band. The flux density of radio sources correlates with the frequency ($S_\nu \propto \nu^{-\alpha}$). Hence, the point source models in the imaging steps also need to take into account this variation. The uGMRT observations were carried out at low-frequencies (band 3 = 300 − 500 MHz) which resulted in various directional dependent effects (e.g. ionospheric effects). Our GWB data were particularly affected by RFI, which corrupts data if not properly modelled and removed. The level of RFI in our data makes the reduction process more difficult and leads to images with significantly lower-than-expected quality. The resulting images had significantly higher-than-predicted noise floors. Another challenge for our sample was that it is in the equatorial region ($-7.2^o < \delta < 4^o$) so, despite the wide bandwidth and hours of integration time, uv coverage is more sparse because aperture synthesis not as effective for equatorial sources (see Figure 2.26). The poor sampling of the visibility space results in north-south artefacts from bright sources, which are a reflection of the poor sampling function.

To overcome these challenges, we explored various pipelines to deal with the intensive RFI flagging and direction-dependent effects. Once the data reduction pipelines are refined, We plan to reduce the remaining wideband data to determine if we can detect lower surface brightness diffuse emission in clusters with non-detections in the GSB data, and enhanced features of the existing diffuse emission detections in other clusters. The pipelines we explored are summarised

below.

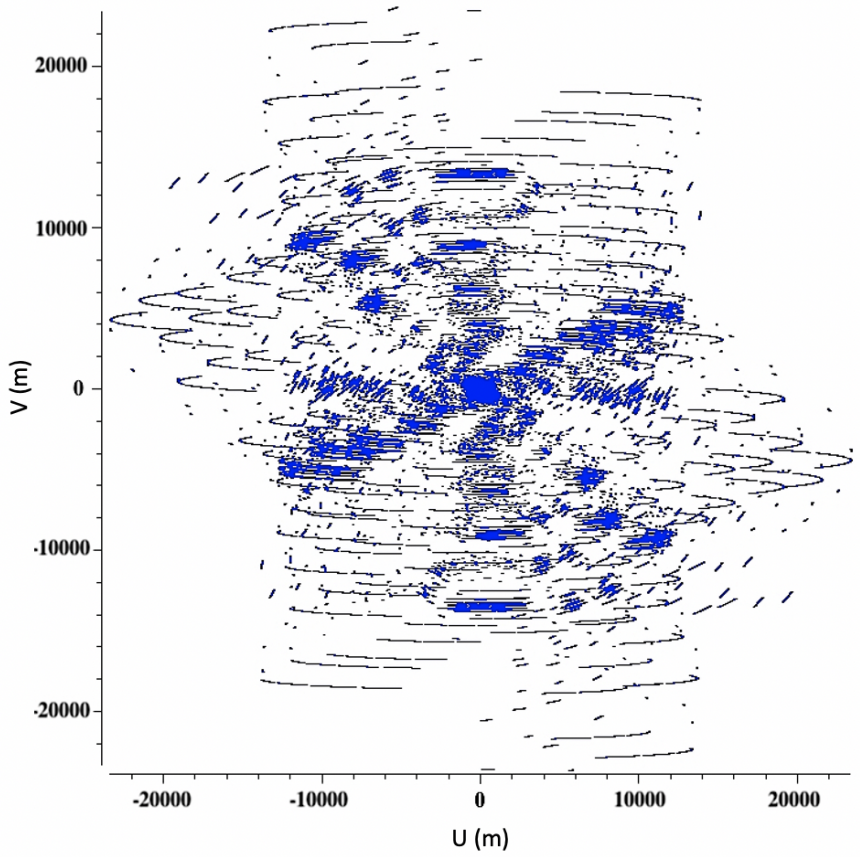

Figure 2.26: GMRT uv coverage for ACT-CL J0034.4+0225. Despite the 4 hours on-source and the 200 MHz of bandwidth, the equatorial declination **results in sparse uv-coverage which reduces the effectiveness of aperture synthesis.**

2.7.1 CASA pipeline

The CASA pipeline we use is an adaptation of the CAPTURE pipeline (Kale and Ishwara-Chandra, 2020). For this pipeline, flagging, calibration and imaging is done using in-built CASA tasks. Firstly, we remove RFI using the manual and automated `flagdata` tasks. We apply the auto-flag separately for the different fields. For auto-flagging we use the `tfcrop` mode which identifies and removes outliers on the time-frequency plane. We set the flagging threshold parameters higher for the calibrator fields in comparison to the target field because these fields are usually much brighter and are detected at a higher SNR. The `timecutoff` and `freqcutoff` devi-

ation parameters for the calibrators were set to 5.0, while for the target they were set to 6.0. These values place constraints on the deviation of data points from the fitted time and frequency polynomial. Data points with higher deviation values are regarded as RFI.

We then apply a cycle of cross-calibration. We begin by setting the flux scale using the standard models from Perley and Butler (2013). Thereafter we produce calibration tables. The delay calibration solution interval is 10 minutes and we only have one solution interval for bandpass and gain calibration. We transfer the flux and phase calibration solutions to the target. After the first cycle of cross-calibration, we apply flagging once more. We do this because after calibration, low-level RFI not picked up before could be more apparent. This time we use `tfcrop` and `rflag` mode. The `rflag` mode calculates statistics per time chunk and and set thresholds which indicate the outliers that need to be flagged. We apply `rflag` post calibration because it tends to result in higher flag percentages if applied on uncalibrated data. **Finally, we produce calibration solutions from the second cycle of cross-calibration and apply this solutions to the target.**

After this, we separate the target visibilities and begin with 2GC. We apply multiple cycles of phase-only calibration on the data we stop once the quality of the image is no longer improving, for most data sets the four cycles were sufficient. We then apply multiple cycles of phase and amplitude calibration until the noise quality of the images reaches a plateau, three cycles were sufficient for most datasets. **For both pahes-only and phase and amplitude calibration, we begin with a solution interval of 16 minutes and decrease the interval per cycle by dividing the initial solution interval by a factor of two times the number of the cycle.** Our imaging during self-cal is done using `tclean`'s `mtmfs` deconvolver, with nterms = 2 and robust parameter = 0. **The number of iterations is set 2500 and increases per cycle by a factor of 2^n, where n is the cycle number. The mask is set to auto-multithreshold. The CLEANing threshold is 0.01 mJy while the sidelobe threshold is set to 3σ. The resulting images have 5880 pixels with a cell size of $2''$.**

The resulting images are shown in the top left panels of Figures 2.27 and 2.28, for ACT-CL J0034 and ACT-CL J0137, respectively. The GSB image is included in the panels for comparison purposes. Even after the 2GC cycles, there were still artefacts around the bright sources. We tried

to improve these by flagging using AOFLAGGER instead of CASA in-built function because it is known to better model the RFI. However this resulted in > 70 % of the data being flagged, these percentages were worse than those of CASA which were typically $\sim$50%. The results of this pipeline were unsatisfactory for our science goals, specifically for the datasets where GSB data showed detections. Hence, we explored other pipelines which apply DDEs calibration (3GC). Due to time constraints, we began with the datasets that showed detection in the GSB data.

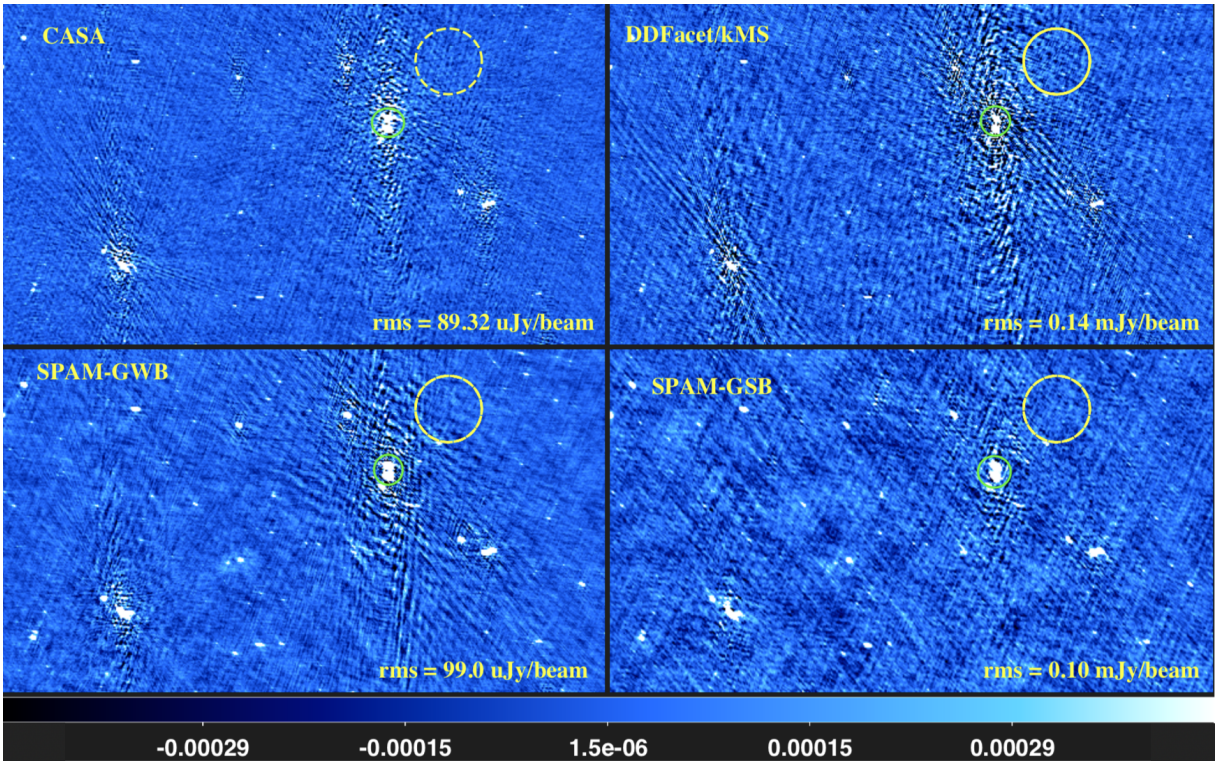

Figure 2.27: Gallery of GWB pipeline images of the ACT-CL J0034.4+0225 field which indicates the severity of the DDEs in our observations. The lower left panel shows the GSB image for comparison. In each panel, the green circle indicates the source used to measure peak brightness , and the yellow circle indicates the region, with the rms value indicated at the lower left. The colour scale is the same for all panels. *Top left:* CASA (see Section 2.7.1) *Top right:* DDFacet-killMS (see Section 2.7.2). *Bottom left:* Experimental wide-band spam (see Section 2.7.3).

2.7.2 DDFacet/killMS pipeline

The KILLMS and DDFACET based pipeline attempts to correct for DDEs by solving the full Jones matrix (see Section 2.1). This pipeline starts with a measurement set (MS) that has been

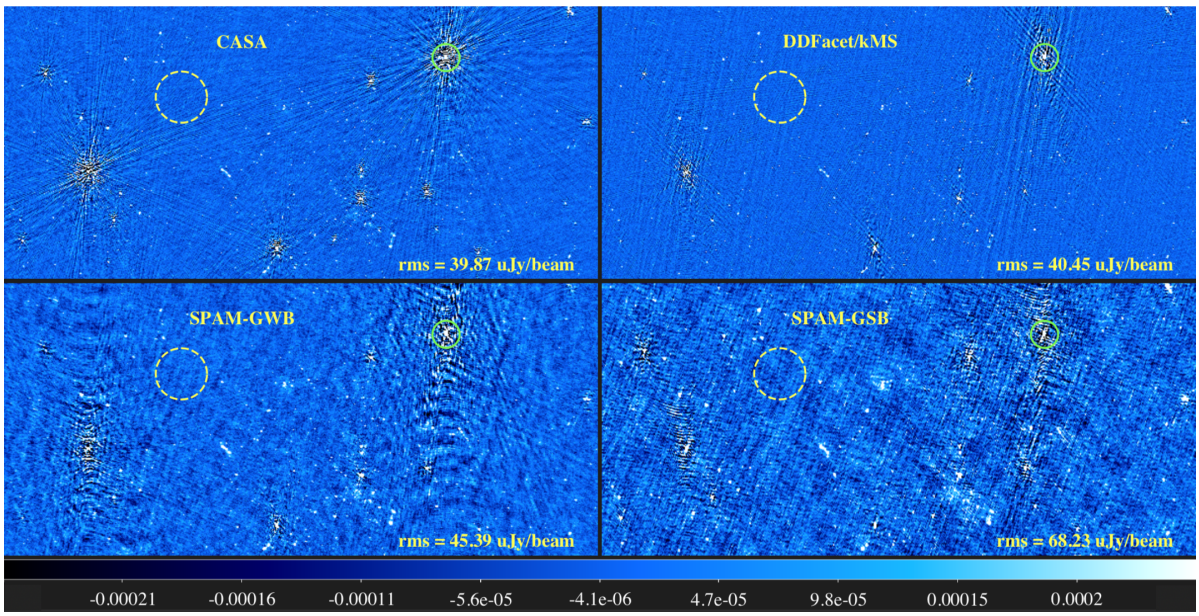

Figure 2.28: Gallery of GWB pipeline images of the ACT-CL J0137.4−0827 field which indicates the severity of the DDEs in our observations. The lower left panel shows the GSB image for comparison. In each panel, the green circle indicates the source used to measure peak brightness , and the yellow circle indicates the region, with the rms value indicated at the lower left. The colour scale is the same for all panels. *Top left:* CASA (see Section 2.7.1) *Top right:* DDFacet-killMS (see Section 2.7.2). *Bottom left:* Experimental wide-band spam (see Section 2.7.3).

calibrated using the CASA pipeline. From our investigation of the CASA pipeline, we found that more cycles of 2GC calibration resulted in images with low peak fluxes. Hence, for this pipeline the 2GC is only applied once for phase-only calibration. We use the image produced after 2GC to create a mask **using a theshold of 10σ to ensure we create a sky model that does not contain residual artefacts**. Thereafter, we image the visibilities using DDFACET. **The imaging parameters used were as follows. We applied 3 major iterations and 90000 minor iterations with a deconvolution peak factor of 0.001. The resulting images have 7425 pixels with a cell size of 1″. These parameters were fixed even for the post-KILLMS imaging cycle.**

We then examine the 2GC image and locate the brightest sources (>0.1 Jy) in DS9 (Joye and Mandel, 2003) and create a bright-source region file. **A minimum of three sources is tagged for each field and a maximum of 6 sources are tagged for fields with numerous bright sources.** We use the region file to divide the target field into facets equal to the number of bright sources in the region file, with the tagged sources being at the phase centre of each facet. We use KILLMS

to obtain direct-independent set of solutions for each facet separately, which is combined into a set of direct-dependent solutions for the field. **We apply the COHJONES solver with a time solution interval of 5 minutes and freequency interval of 8 channels per solution. The number of directions we solve for is equivalent to the number of the bright sources that are tagged per field.** Finally, we use DDFACET to apply the KILLMS solutions and produce the DDEs corrected image. DDFACET also applies direction-dependent PSF deconvolution which explicitly accounts for the time variation and bandwidth fluctuation effects. We perform the KILLMS and DDFACET loops iteratively, improving the mask and increasing the time solution intervals with each loop until we get an image with significantly reduced artefacts.

The resulting images are shown in the top right panels of Figures 2.27 and 2.28 for ACT-CL J0034 and ACT-CL J0137, respectively. We note that in both cases the noise floor has gone up compared to CASA. The percentage increase in ACT-CL J0034 is $\sim 4\%$ and in ACT-CL J0137 it is $\sim 36.2\%$. However, the sources in this pipeline have a more point-like structure compares to CASA. This indicated that the pipeline improved the phase corrections for the fields. Although the phase corrections had improved in comparison to the CASA pipeline, the north-south artefacts were still not significantly reduced. Such artefacts would have been problematic for the point source subtraction, which is often required when extracting measurements for faint extended emission. We tried various calibration solution intervals (30s $-$ 2min) and facet numbers (3 $-$ 7), however, these did not improve our results. The range of calibration solution intervals produced the same results while increasing the facet numbers resulted in some facets having higher noise levels due to fewer sources in each facet.

2.7.3 Experimental SPAM wideband pipeline

The final pipeline we explored was the experimental wideband SPAM pipeline [4]. This pipeline begins by splitting the GWB data into $\sim$7 sub-bands of $\sim$30 MHz each. Thereafter, it follows the conventional GSB narrow-band data reduction for the individual sub-bands (see Section 2.4). The calibrated sub-band visibilities are then converted into MS files and concurrently imaged

[4] http://www.intema.nl/doku.php?id=huibintemaspampipeline

Table 2.6: ACT-CL J0034.4+0225 GWB data reduction pipelines' image comparison. Columns: (1) Name of pipeline. (2) Effective observing frequency. (3) Synthesised beam of the image. (4) Flagged data. (5) RMS near the region with artefacts. The regions are shown as yellow circles in Figures 2.27 and 2.28. (6) Peak brightness of the double lobed source.

Pipeline	ν_o	Flags	Synthesised beam	RMS	Peak brightness
	MHz	%	($'' \times ''$, deg)	(μJy/beam)	Jy/beam
CASA	46.8	397	8.0×4.9, 60.5	38.9	0.13
DDFACET/KILLMS	397	35.6	7.9×4.5, 52.4	40.5	0.19
SPAM GWB	398	24.4	14.0×7.6, 65.3	45.4	0.27
SPAM GSB	323	14.7	14.2×18.1, 48.2	68.2.0	0.34

using WSCLEAN. **For the WSCLEAN wide bandwidth imaging step, we used a Briggs robust = 0, number of iterations = 150000, threshold = 1 μJy, auto-mask = 9σ, multiscale scales of (10,20,30), and the number of pixels was 10395 with a cell size of 1$''$.**

As seen in the bottom left panels of Figures 2.27 and 2.28, and Tables 2.7 and 2.6 for ACT-CL J0034 and ACT-CL J0137, respectively, this pipeline produced the best phase calibration which resulted in an improvement in the structure of the brightest sources. Although the noise levels are higher compared the CASA pipeline for both images, the improvement of the phase calibrations meant we would be able to extract the bright point sources, which is a necessary step when extracting faint diffuse emission. The peak fluxes of the sources in the SPAM-reduced images were much higher in than those in the CASA-reduced and DDFACET/KILLMS-reduced images. This indicates that the phase and amplitude calibration is improved, despite the higher noise floor, so that less of the real signal is being fractured into artefacts or sidelobes. However, further steps are needed to improve the algorithm so that the 3GC strategy is more robust. These steps include more comprehensive ionospheric corrections in the sub-band data reduction and primary beam correction for the full bandwidth image. Due to necessary computing facilities being unexpectedly unavailable due to rolling black outs and generator problems, we were unable to use the SPAM pipeline to reduce all the GWB datasets in hand. Hence, we used this pipeline to reduce the datasets that showed a detection of diffuse emission in the GSB data.

Table 2.7: ACT-CL ACT-CL J0137.4−0827 SPAM GWB data reduction pipelines' image comparison. Columns: (1) Name of pipeline. (2) effective observing frequency. (3) Synthesised beam of the image. (4) Flagged data. (5) RMS near the region with artefacts. The regions are shown as yellow circles in Figures 2.27 and 2.28. (6) Peak brightness of the double lobed source.

Pipeline	ν_o	Flags	Synthesised beam	RMS	Peak brightness
	MHz	%	($'' \times ''$, deg)	(μJy/beam)	Jy/beam
CASA	398	61.1	6.6×5.7, 47.8	89.3	0.13
DDFACET/KILLMS	398	47.7	5.4×5.3, 70.2	140.0	0.12
SPAM GWB	389	23.8	9.6×8.7, 58.7	99.0	0.25
SPAM GSB	323	17.1	12.8×7.6, 18.1	100.0	0.25

2.7.4 GWB results

The resulting full resolution image statistics for the three clusters reduced are summarised in Table 2.8 and the full field of view images are in Appendix A. The rms measurements for these images were taken near the cluster centre, hence, the noise differences in comparison to the noise quoted in Tables 2.7 and 2.6. We used the sub-band reduced uGMRT GWB data to produce point source subtracted visibilities. We then used WSCLEAN to produce low resolution images using the full bandwidth GWB data. The low resolution image properties for these clusters are in Table 2.9. Although the primary beam correction hasn't been applied yet, we proceed to extract flux densities of the emission because we only care about inner regions ($<10'$), so the primary beam correction is not pivotal for our results. We discuss the detected emission in the sections below.

2.7.4.1 Radio halo in ACT-CL J0034.4+0225

From the GWB data (PI: Kenda Knowles, ID: 32_016), we detect extended diffuse emission in the central region of the cluster. We measure the LAS of the diffuse emission to be $2.31' \times 1.48'$, corresponding to a LLS of 723 kpc × 463 kpc. This is similar is size to the GSB detection (LLS $\sim$ 726 x 459 kpc). The sizes and morphology of the diffuse emission are similar for both the GWB and the GSB images (See Figures 2.9 and 2.29). Hence, we retain the radio halo classification in Section 2.5.2.2.

Table 2.8: The SPAM-reduced full resolution GWB image properties for clusters with GSB detections and GWB data in-hand. Columns: (1) ACT cluster catalogue name. (2) Synthesised beam of the full resolution GWB image. (3) rms noise of the full resolution GWB image. (4) Total flagged percentage of the MS after data reduction. (5) Synthesised beam of the full resolution GSB image. (6) rms noise of the full resolution GSB image.

Cluster Name ACT-CL	$\theta^{\rm GWB}_{\rm synth}$ ($'' \times ''$, deg)	$\sigma_{\rm GWB}$ (μJy/beam)	Flags %	$\theta^{\rm GSB}_{\rm synth}$ ($'' \times ''$, deg)	$\sigma_{\rm GSB}$ (μJy/beam)
J0034.4+0225	14.0×7.6, 65.3	45.9	23.8	14.2×18.1, 48.2	75.8
J0137.4−0827	9.6×8.7, 58.7	47.1	24.4	12.8×7.6, 18.1	74.5
J2128.4+0135	12.9×4.8, 73.2	41.6	23.6	16.0×6.9, 65.9	134.0

Table 2.9: The SPAM-reduced low resolution GWB image properties for clusters with GSB detections and GWB data in-hand. Columns: (1) ACT cluster catalogue name. (2) Synthesised beam of the full resolution GWB image. (3) rms noise of the low resolution GWB image. (4) Synthesised beam of the full resolution GSB image. (5) rms noise of the full resolution GSB image.

Cluster Name ACT-CL	$\theta^{\rm GWB}_{\rm synth}$ ($'' \times ''$, deg)	$\sigma_{\rm GWB}$ (mJy/beam)	$\theta^{\rm GSB}_{\rm synth}$ ($'' \times ''$, deg)	$\sigma_{\rm GSB}$ (μJy/beam)
J0034.4+0225	43.5×31.1, 150.7	0.29	44.6×37.1, 28.6	0.58
J0137.4−0827	41.5×34.9, 157.1	0.28	45.0×37.7, 63.3	0.51
J2128.4+0135	43.7×38.3, 160.6	0.25	37.8×33.1, 73.1	0.75

The flux density of the radio halo for the GWB observations is $S_{398\mathrm{MHz}} = 8.14 \pm 1.55$ mJy. We use this value and the 1.16 GHz flux density measurement from Knowles et al. (2020) to calculate the spectral index of the radio halo. We determine a spectral index of $\alpha_{398}^{1160} = 1.74 \pm 0.12$, consistent within the uncertainties of that determined using the GSB measurement. Using our GWB flux density and measured spectral index, we determine a 1.4 GHz radio power of $(0.61 \pm 0.10) \times 10^{24}$ WHz^{-1}, in agreement with the GSB extrapolated value. We recover the radio halo at a higher SNR in the GWB data. The halo radio power is in agreement for both the GWB and GSB derived values. For this cluster, the GWB data did not significantly add any new scientific information for the radio halo. However, we note that this dataset was amongst those severely affected by RFI. The bright sources make this field an extreme data reduction challenge and is therefore a good candidate to test future SKA pipelines.

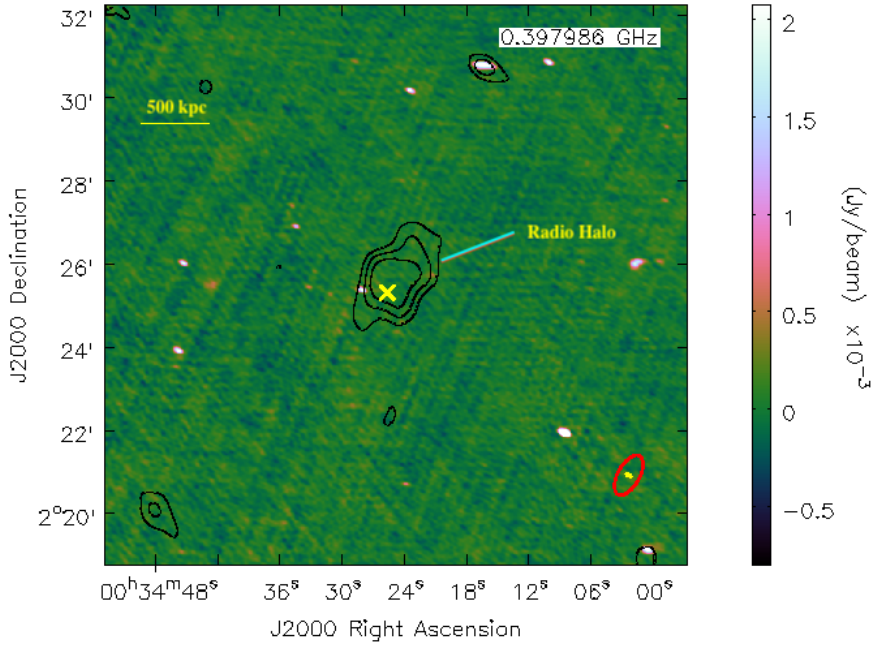

Figure 2.29: Full resolution image of ACT−CL J0034.4+0225 from the experimental spam pipeline. The rms in the cluster region is 45.9 μJy/beam. The contours are from the low resolution point-source-subtracted image. The rms (σ) of the low resolution image is 0.29 mJy/beam and the contour levels are $\sigma\times$[-3,3,5,8]. The yellow cross indicates the ACT SZ peak. The synthesised beam for the full resolution and the low resolution images are shown by the yellow ellipse and the red ellipse, respectively. The synthesised beam for the full resolution and low resolution images are ($14.0'' \times 7.6''$, p.a. 65.3) and ($43.5'' \times 31.1''$, p.a. 150.7), respectively.

2.7.4.2 Radio halo in ACT-CL J0137.4-0827

The GWB data confirms that the cluster hosts extended diffuse emission. We measure the angular size of the diffuse emission to be $3.28' \times 1.89'$, which corresponds to a LLS of 1282 kpc $\times$ 739 kpc. The size of the diffuse emission is larger and more elongated in the GWB image compared to the GSB image (LLS $\sim$580 kpc $\times$ 429 kpc). The morphology of the emission is more elongated than the usual regular morphology of radio halos (see Figures 2.30 and 2.17). However, the size and positioning of the emission leads us to conclude that, as classified in Section 2.5.3.1, the detected emission is a radio halo.

From the GWB data we measured a flux density of $S_{389\mathrm{MHz}} = 15.28 \pm 2.13$ mJy. There are no other radio observations and a different frequency for this cluster, hence, we used a fiducial spectral index value of 1.3 and extrapolated $\mathrm{P_{1.4GHz}}$ = (4.3 $\pm$ 0.32) $\times 10^{24}$ $\mathrm{WHz^{-1}}$. The flux density and $\mathrm{P_{1.4GHz}}$ in the GSB image was measured to be $S_{323\mathrm{MHz}} = 19.72 \pm 2.33$ mJy and $\mathrm{P_{1.4GHz}}$ = (4.36 $\pm$ 0.27) $\times 10^{24}$ $\mathrm{WHz^{-1}}$, respectively. As expected, we measure a lower flux density because the central frequency (389 MHz) of the data is higher compared to the GSB data (323 MHz).

We do not recover the revived fossil plasma source that is detected in the GSB data. We assume that this might be due to the ultra-steep spectral nature (see Chapter 1) of this source and that the frequency at $\sim$323MHz (GSB) might be the cut-off frequency for the revived fossil plasma. The FR II is much more resolved in the GWB data. This dataset indicates that GWB observations can be more sensitive to extended structure in comparison to GSB observations.

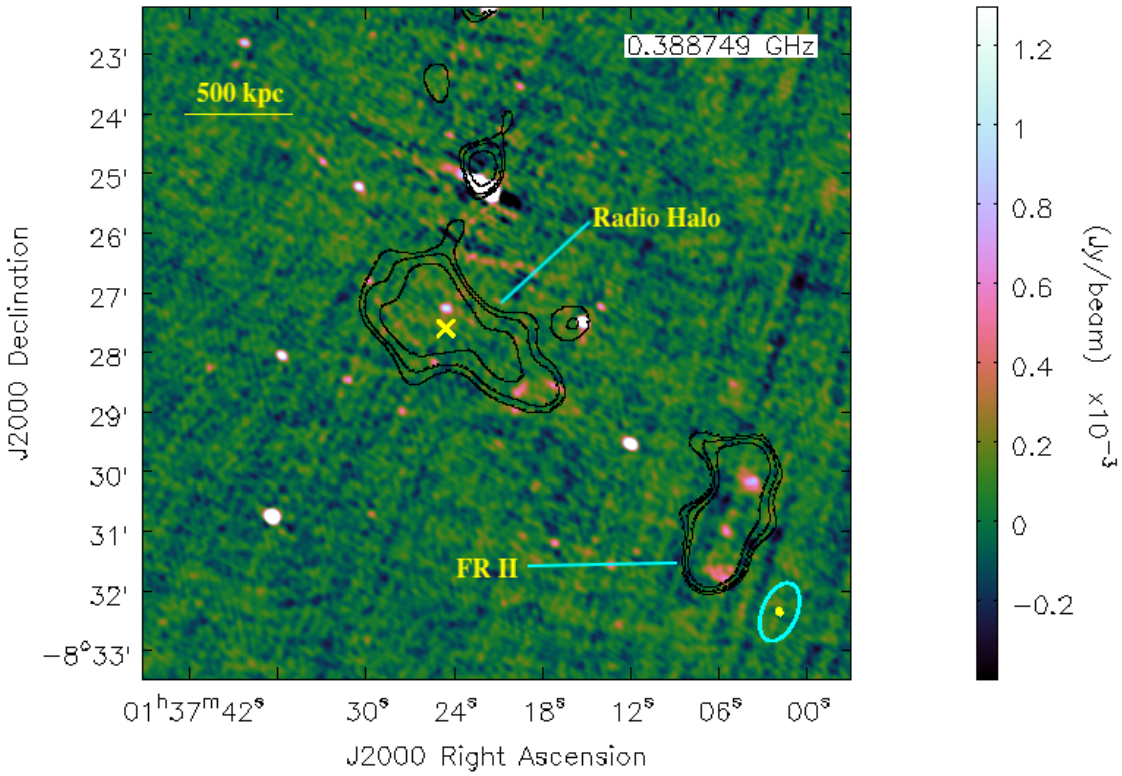

Figure 2.30: Full resolution image of ACT−CL J0137.4−0827 from the experimental spam pipeline. The rms in the cluster region is 47.1 μJy/beam. The contours are from the low resolution point-source-subtracted image. The rms (σ) of the low resolution image is 0.28 mJy/beam and the contour levels are $\sigma\times$[-3,3,5,8]. The yellow cross indicates the ACT SZ peak. The synthesised beam for the full resolution and the low resolution images are shown by the yellow ellipse and the cyan ellipse, respectively. The synthesised beam for the full resolution and low resolution images are ($9.6'' \times 8.7''$, p.a. 58.7) and ($41.5'' \times 34.9''$, p.a. 157.1), respectively.

2.7.4.3 Radio relic in ACT-CL J2128.4+0135

The GWB data confirms the existence of a radio relic in this cluster. In the GWB image, the radio relic has a LAS of $1.18' \times 1.03'$, which corresponds to a LLS of 372 kpc $\times$ 324 kpc. The distance from the ACT SZ peak to the emission in $2.09'$, which corresponds to a linear scale of 916 kpc. The relic is significantly more extended in the GSB image compared to the GWB (LLS 489 kpc $\times$ 293 kpc). However, the resolution of the GWB data enables us to easily disentangle extended emission from radio galaxies.

From the GWB image, we measure the integrated flux density of the radio relic to be $S_{389\mathrm{MHz}} = 6.96 \pm 1.1$ mJy. There are no other radio observations for this cluster, hence, we use a fiducial spectral index value of 1.3 to derive the corresponding radio power at 1.4 GHz. We calculated $\mathrm{P}_{1.4\mathrm{GHz}}$ to be $(0.75 \pm 0.09) \times 10^{24}$ WHz^{-1}. The flux density and radio power of the GSB image were measured to be $S_{323\mathrm{MHz}} = 9.77 \pm 1.13$ mJy and $(8.29 \pm 0.91) \times 10^{24}$ WHz^{-1}, respectively. This indicates that the relic radio power is higher at lower frequencies. We also recover the morphology of the bent-tail and FRII radio galaxies at higher resolution. This indicates that the GWB data might produce better results for the point-source subtraction. If this is the case, it would be ideal to use the GWB data for clusters with mini-halos, which are known to be embedded in BCGs.

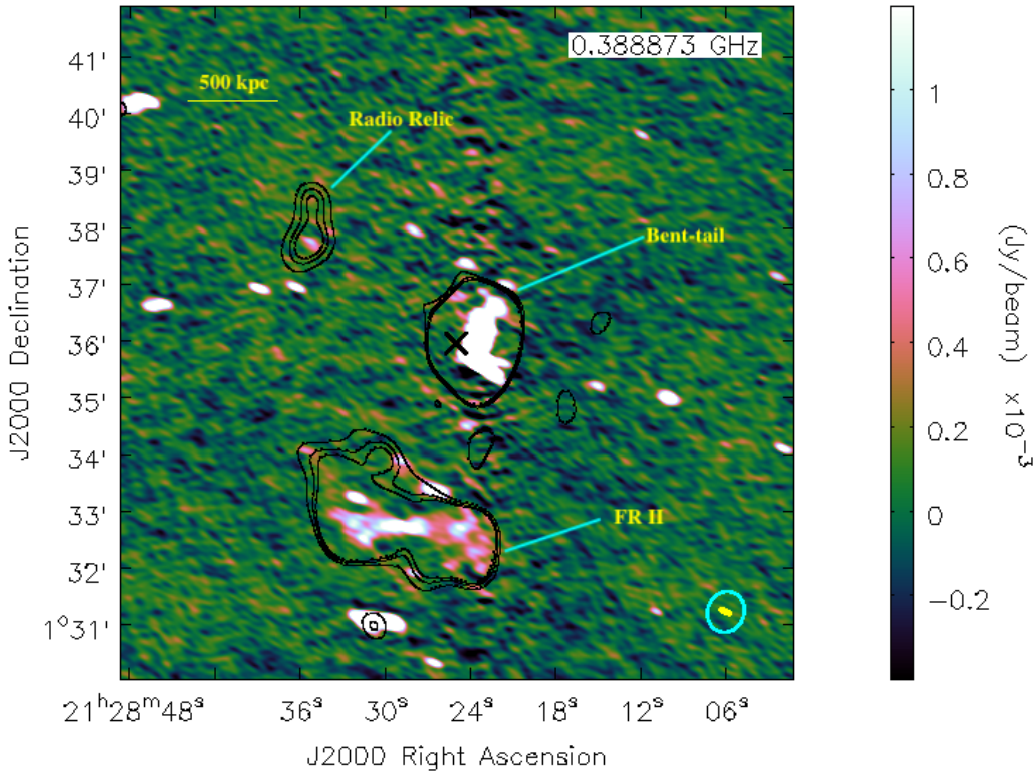

Figure 2.31: Full resolution image of ACT−CL J2128.4+0135 from the experimental spam pipeline. The rms in the cluster region is 41.6 μJy/beam. The contours are from the low resolution point-source-subtracted image. The rms (σ) of the low resolution image is 0.25 mJy/beam and the contour levels are $\sigma\times$[-3,3,6,8]. The synthesised beam for the full resolution and the low resolution images are shown by the yellow ellipse and the cyan ellipse, respectively. The black cross indicates the ACT SZ peak. The synthesised beam for the full resolution and low resolution images are (12.9″ × 4.8″, p.a. 73.2) and (43.7″ × 38.3″, p.a. 160.6), respectively.

2.8 Summary of Results

The analysis of the GMRT GSB data resulted in the detection of four radio halos, two mini-halos, two radio relics and a revived fossil plasma candidate. The overall occurrence fraction in our sample is 30%. Although our sample had a low detection rate, 66.7% of the detected emission is hosted by clusters at redshift $z > 0.38$. This indicates that it is necessary to have cluster samples that target high-redshift galaxy clusters. The MeerKAT Extended Relics, Giant Halos, and Extragalactic Radio Sources (MERGHERS; Knowles et al., 2016a) survey, aims at targeting such cluster samples. The survey aims to obtain a sample of $\sim$200 clusters uniformly selected from the Advanced Atacama Cosmology Telescope (AdvACT; Hilton et al., 2020) cluster sample spanning a wide mass and redshift range. Thereafter they will use this sample to study scaling relations for samples including low mass and high redshift clusters. Statistically significant samples of such nature will be crucial for establishing if the currently existing scaling relations hold even at high-redshifts. Such studies will help in refining the formation theories of the extended diffuse emission.

The results from the GWB data reduction indicate that the sensitivity of uGMRT can be ideal for extracting faint extended diffuse structure. The radio halo emission in ACT-CL J0137.4−0827 was captured in a larger extent in the GWB image compared to the GSB image. However, the central frequency of the GSB data was also ideal for capturing steep spectrum sources such as the revived fossil plasma candidate observed in in ACT-CL J0137.4−0827. A combination of the GSB and GWB data might be the ideal strategy for studying spectral indices of the diffuse emission. Once our GWB data reduction algorithm is optimised, we will proceed to reduce those clusters that had non-detections in the GSB data.

CHAPTER 3

DIFFUSE EMISSION IN CLUSTERS AS SEEN BY MEERKAT

As part of early science operations with the full MeerKAT array, and with a view to providing science datasets for South African astronomy research capacity development, the South African Radio Astronomical Observatory observed several well-studied galaxy clusters. We were provided proprietary access to datasets of four of these clusters, namely the Bullet Cluster (1E0657-56), RXC J1314.4−2515, Abell 3562, and Abell 3558. All these clusters are known to be undergoing major merger activity. Three of the four clusters (excluding Abell 3558) have known diffuse radio emission. Our aim was to study the diffuse emission in these clusters, focusing on the new information and insights provided by the MeerKAT observations. In this chapter, we discuss the MeerKAT observations, data reduction techniques, and the results obtained from our image analysis.

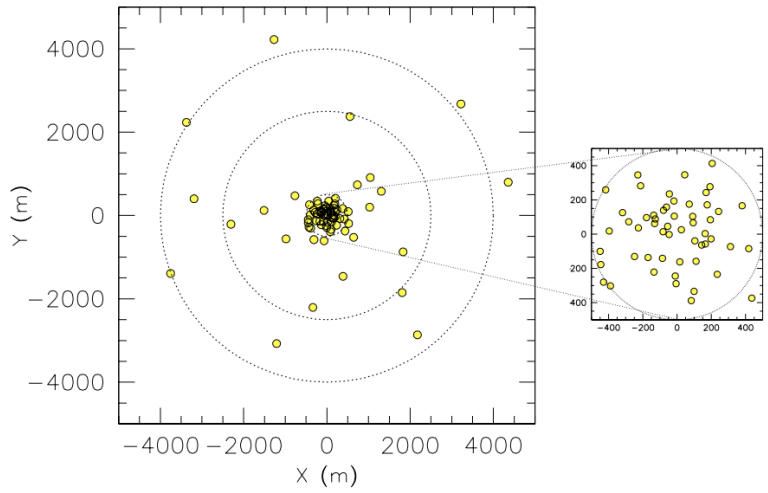

Figure 3.1: MeerKAT array positions. Source: (Booth et al., 2009)

3.1 MeerKAT observations

The MeerKAT telescope is a precursor for the Square Kilometre Array (SKA). It is one of the most sensitive radio arrays in the pre-SKA era. The full MeerKAT array has 64 antennas, with 70% of the dishes located at the core (<400 m) of the array (see Figure 3.1). The minimum baseline for the array is 29 m and the maximum baseline is 7.7 km. The array configuration makes MeerKAT an excellent instrument for studying faint extended diffuse emission in galaxy clusters. Extracting the extended emission requires short baselines, while long baselines are needed to disentangle compact source emission. Both the requirements are simultaneously available for MeerKAT's full array observations.

Additionally, MeerKAT's high sensitivity significantly reduces the integration time required to detect faint diffuse emission. As seen in Figure 3.2, the uv coverage of a snapshot is reasonably populated and the 12 hr synthesis is densely populated. According to MeerKAT's online sensitivity calculator[1], a dataset observed in 1 hr produces an image with a theoretical rms of 7.7 μJy/beam (for a robust weighting = 0). As a result of superior sensitivity, particularly in the core, shorter observations from MeerKAT detect faint features in the diffuse emission that similar in-

[1] `https://archive-gw-1.kat.ac.za/public/tools/continuum_sensitivity_calculator.html`

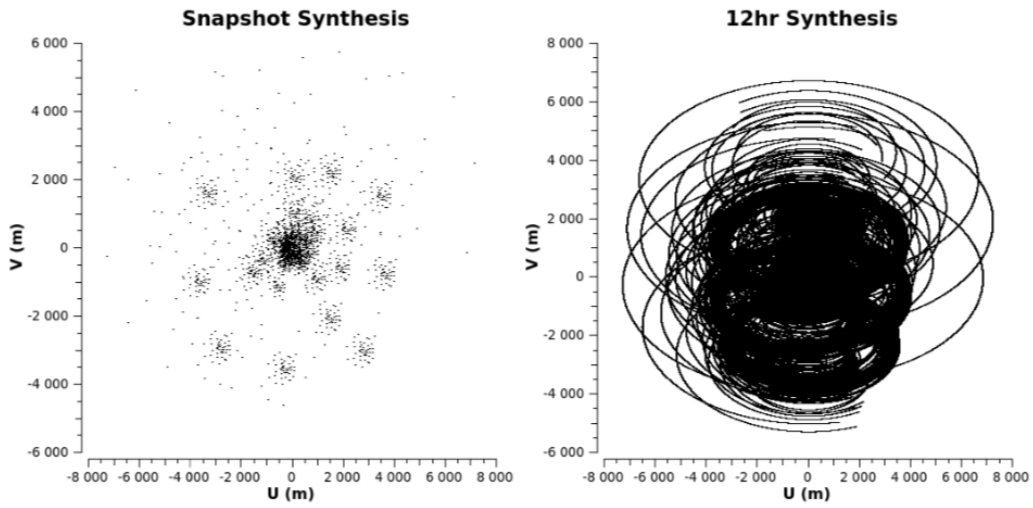

Figure 3.2: MeerKAT Snapshot vs 12 hr synthesis uv-coverage. Source: (Knowles et al., 2016a).

struments require significantly longer integration times (sometimes at different configurations) to reproduce.

All the observations were taken in the period of June/July 2018 with at least 60 antennas using MeerKAT's L-band receiver (900 MHz−1.67 GHz). The observational setup used the 4K mode (4096 channels), eight seconds integration times, and full Stokes polarization. The full observation times for the datasets were approximately 4 to 11 hours. For the shorter observations, only one phase and amplitude calibrator was observed. For longer observations multiple phase and amplitude calibrators were observed. Table 3.1 provides a summary of the observations for the four clusters.

3.2 Data Reduction and Analysis

For all four clusters we perform similar data reduction and image analysis tasks. After calibrating the data and producing a full resolution image we then proceed to extract diffuse emission in the field. We first remove point sources in the region of the diffuse emission. We then produce low resolution images and measure fluxes of the diffuse emission. We were able to produce in-band spectral index maps for 1E 0657−55.8, RXC J1314.4−2515 and Abell 3562. **The diffuse**

Table 3.1: Summary of the MeerKAT L-band observations. Columns: (1) Name of the Cluster. (2) Date of the observation. (3) Observed amplitude calibrator. (4) Observed phase calibrator. (5) The total on-source integration time

Cluster Name	Date YYYY-MM-DD	Amplitude Calibrator	Phase Calibrator	t_{src} hrs
1E 0657−55.8	2018-06-24	J0408−6545 & J1331+303	J0825−5010 & PKS 0647−475	7.7
RXC J1314.4−2515	2018-07-08	3C286 & PKS 1934−638	PKS 1308−220	4.5
Abell 3562	2018-07-06	3C286 & PKS 1934−638	J1313+333	7.5
Abell 3558	2018-07-03	J1331+303	J1311−2216	1.9

emission in Abell 3558 is too faint to extract in the sub-band images, hence, we could not produce an in-band spectral index map.

3.2.1 Data reduction pipeline

The data were reduced using the OXKAT[2] pipeline (Heywood, 2020). OXKAT is a set of Python-based scripts that perform the traditional first-generation calibration (1GC), flagging, second-generation calibration (2GC), and third-generation calibration (3GC) steps. For the various calibration and imaging stages, the pipeline uses astronomy tools such as CASA (McMullin et al., 2007), WSCLEAN[3] (Offringa et al., 2014), DDFACET (Tasse et al., 2018), and KILLMS[4] (Tasse, 2014; Smirnov and Tasse, 2015). The data reduction steps are summarised below.

For our study, we only required the Stokes I polarisation. Hence, we split the data and use the measurement set (MS) containing only the Stokes I observations. To compress the data and increase the processing speed, the data were averaged from 4096 channels to 1024 channels. After this, manual and automated flagging was performed using CASA. A significant portion ($\sim$40%) of the data observed at L-band is flagged due to known RFI. The known RFI bands (900 MHz− 960 MHz, 1.17 GHz − 1.30 GHz, 1.38 GHz − 1.39 GHz, and 1.53 GHz − 1.63 GHz) were flagged manually, and the calibrator visibilities were flagged using in-built CASA

[2] https://github.com/IanHeywood/oxkat

[3] https://https://gitlab.com/aroffringa/wsclean

[4] https://github.com/saopicc/killMS

automated flagging tasks. The primary and secondary calibrator models were used to calibrate the target field. **One solution interval was used for the delay, bandpass, and gain calibration solutions.** After applying the calibration solutions, the calibrator and target visibilities were then split into separate Measurements Sets (MS). All these 1GC steps were performed using CASA.

Prior to imaging, the target data were automatically flagged using TRICOLOUR[5]. The targets were then imaged using WSCLEAN with an auto-mask (Offringa and Smirnov, 2017) threshold $\mathbf{5}\sigma$ and eight sub-band channels. Masks were then produced using this image and WSCLEAN was used to re-image the targets using the masks. The resulting images were used to predict the model for the target fields. The predicted models are then used for the self-calibration cycle. One cycle of phase and amplitude self-calibration was done in CASA. Final 2GC-calibrated images were produced using WSCLEAN, with updated masks from the previous runs. **For all the WSCLEAN cycles, the robust parameter was 0 and the number of CLEANing iterations was 120000 with a threshold of 5μJy. The resulting images have 10240 pixels with a cell size of 1.1$''$.**

2GC was only sufficient for the Bullet cluster because there were no bright sources near the region with diffuse emission. For RXC J1314.4−2515, Abell 3562, and Abell 3558, an extra step was needed to reduce artefacts around the bright ($\sim$1 Jy) sources in the observed field. To produce images with minimal artefacts around the diffuse emission, we applied a peeling script, to remove bright interfering sources from the data. For the peeling step, the brightest source is tagged in DS9 (Joye and Mandel, 2003), and modelled in WSCLEAN. For the three clusters, there was only one source in the field with bright artefacts, hence, we only apply the peeling step once and not iteratively. The application of calibration solutions in the direction of the sources and the subtraction of the bright sources were done in CUBICAL (Kenyon et al., 2018). **In CUBICAL, the calibration solutions' frequency interval was set to 256 channels and the time interval 4.5 minutes.** The visibilities with the subtracted sources were then re-imaged in WSCLEAN. Peeling resulted in images with reduced artefacts. The local rms ($\sim$12 μJy/beam) in the region with diffuse emission was also reduced. Hence, we proceeded to apply primary beam corrections. The post-peeling images were primary beam corrected using KATBEAM[6]. The resulting image

[5] https://github.com/ska-sa/tricolour

[6] https://github.com/ska-sa/katbeam

Table 3.2: Summary of the full resolution image statistics of the image produced by the OXKAT pipeline. (1) Cluster name. (2) Central frequency after the data reduction. (3) Synthesised beam of the full resolution image. (4) rms noise of the image. (5) Flagged percentage's post data reduction. (6) Diffuse emission in the cluster.

Cluster	ν_0 GHz	Synthesised Beam, p.a $\prime\prime \times \prime\prime$, deg	RMS μJy/beam	Flagged %	Diffuse Emission
1E 0657−55.8	1.284	6.4×5.9, 61.7	8.5	50.2	RH and relic
RXC J1314.4−2515	1.284	6.2×5.6, 146.2	9.3	46.0	RH and double relic
Abell 3562	1.284	6.2×5.9, 102.7	8.2	43.8	RH
Abell 3558	1.284	6.3×5.1, 145.8	12.8	45.2	mH*

Note: *New min-halo detection.

properties for the four clusters are summarised in Table 3.2 and the full field of view images are in Appendix B.

3.2.2 Point source subtraction

Prior to measuring the flux densities of the diffuse emission, we subtracted the bright point sources in a fixed region that covered the extent of the diffuse emission. The point source subtraction was done to ensure that the flux density measurements for the diffuse emission had no contamination from compact emission embedded. We also remove point sources to ensure that the compact sources do not blend with the extended emission when we produce low resolution maps. The point source subtraction was implemented using CRYSTALBALL[7] and MSUTILS[8]. CRYSTALBALL uses a source list from WSCLEAN to create a column, in the MS file, that only contains the tagged point sources. MSUTILS then subtracts the newly created column from the column that contains the calibrated data and creates a new column containing the point-source-subtracted visibilities. We then use the resulting visibilities to produce low resolution maps.

[7] https://github.com/paoloserra/crystalball

[8] https://github.com/SpheMakh/msutils

Table 3.3: Summary of the low resolution image properties. (1) Cluster name. (2) Synthesised beam of the low resolution image. (4) rms noise of the image.

Cluster	Synthesised Beam, p.a ($'' \times ''$, deg)	RMS μJy/beam
1E 0657−55.8	13.1×11.7, 120.6	10.07
RXC J1314.4−2515	11.2×10.6, 146.5	10.34
Abell 3562	31.2×26.9, 118.6	21.50
Abell 3558	25.5.1×20.9, 131.5	22.14

3.2.3 Low resolution maps

The short baselines of a radio interferometer are sensitive to extended radio sources. Hence, we produce low resolution maps to increase the sensitivity of the large-scale emission in the four fields. For the Bullet cluster and RXC J1314.4−2515, we imaged using a uvrange $\leqslant 13$ kλ ($\sim$1.6 Mpc), and a Briggs robust = 0.0. The diffuse emission in these clusters is extremely bright and the flux density of the brightest regions is also captured in longer baselines. Hence, we used a higher uv-cut to ensure that we capture all the flux. For the Abell clusters (A3558 and A3562), we imaged using a uv range of $\leqslant 6$ kλ ($\sim$750 kpc), and a Briggs robust = 0.8. The emission in A3558 and A3562 is fainter, hence, we were able to apply a lower uv-cut and still recover the emission. We also use a robust weighting that leans towards 'natural' weighting because it places larger weightings on the shorter baselines, further tracing out the extended structures. The low resolution image properties are summarised in Table 3.3. We use the resulting images to measure flux densities and to produce spectral index maps.

3.2.4 Integrated flux density measurements

We use polygon regions guided by the 3σ contours to create regions in which we measure the flux densities. We then use DS9's radioflux[9] plug-in to measure the flux densities. The measured flux densities are quoted in Sections 3.3.1, 3.4.1, 3.6, and 3.7. The error on the measured flux

[9] https://github.com/mhardcastle/radioflux

densities is given by $\Delta S = \sqrt{(\delta S \times S)^2 + N\sigma^2}$, where S is the measured flux density, δS is the 5% MeerKAT flux calibration uncertainty, N is the number of beams within the region that the flux density was measured, and σ is the local rms noise of the image.

3.2.5 In-band spectral index maps

MeerKAT's wide bandwidth and sensitivity enables us to produce in-band spectral index maps from single observations. To perform spectral index studies of the radio halo and relics in the Bullet cluster, RXC J1314.4−2515 and Abell 3562, we divided the point source subtracted MS into eight sub-bands (∼96 MHz bandwidth) and imaged each band using the multi-frequency mode in WSCLEAN (Offringa and Smirnov, 2017). The synthesised beam of all the sub-band images were set to be the same as the synthesised beam of the lowest frequency sub-band image. Each image was primary beam corrected using KATBEAM. The spectral index maps were produced using Broadband Radio Astronomy Tools (BRATS, Harwood et al., 2013, 2015). To calculate the spectral index maps, BRATS[10] uses the power law in the form of $S_\nu \propto \nu^{-\alpha}$ to fit the spectral index map values. This fit is performed using a pixel by pixel weighted least squares method where the weights are the inverse variance. BRATS has an inbuilt flux density measurement function which requires the user to input the percentage calibration error for the flux density error approximations.

To produce the spectral index maps along with the error maps, we load the low resolution maps into BRATS. We then load a DS9 region file encompassing the extended diffuse emission along with a off-source background region. BRATS uses the background region to calculate the rms noise of the low resolution maps. We set the source detection limit to be five times the rms noise. To produce spectral index maps BRATS uses adaptive regions. These regions are set by a function written to group pixels into regions based on a specified set of parameters. We set the signal-to-noise parameter to be 6 and use the default settings for the rest of the parameters. For the final spectral index maps we only use the sub-band images centred at 963.9 MHz and 1.65 GHz. We select these images because they are the least affected by RFI flagging and have lower

[10] http://www.askanastronomer.co.uk/brats/

local rms noise. Using these images results in spectral index maps with the least spectral index errors in comparison to using all the eight sub-band images.

3.3 The Bullet Cluster (1E0657-56)

Tucker et al. (1995, 1998) were the first to detect the Bullet cluster using the *ROSAT* satellite (Voges, 1992), the Advanced Satellite for Cosmology and Astrophysics (ASCA; Tanaka et al., 1994), and the Einstein IPC instrument (Giacconi et al., 1979). There have since been many multi-wavelength follow-ups of this cluster, some even leading to the evidence of dark matter (Clowe et al., 2004). Barrena et al. (2002) used spectroscopic data from the ESO New Technology Telescope (NTT; Tarenghi and Wilson, 1989) to study the dynamical state of the cluster. Their results showed that there is a subcluster which is offset from the main cluster position by 0.7 Mpc in the western direction. They found that the subcluster had a virial mass of $1.3\times10^{13}\mathrm{M}_{\odot}$ and the main virial mass of the main cluster $1.3\times10^{15}\mathrm{M}_{\odot}$. They conclude the mass of the subcluster was significantly larger at the pre-merger stage. Hence, they concluded that the Bullet cluster has recently (within the past 0.15 Gyr) experienced a major merger. Clowe et al. (2004) used Very Large Telescope 1 (VLT1; Enard, 1991) data to reconstruct weak lensing maps of the Bullet cluster. Their weak lensing and X-ray comparison studies revealed that the X-ray centroid peak and reconstructed cluster mass were misaligned, hence showing that the total mass of the system does not trace the baryonic mass. This was the first observational evidence of the existence of dark matter. Other weak lensing studies have further solidified these findings (Clowe et al., 2006; Bradač et al., 2006; Paraficz et al., 2016). Clowe et al. (2004) also measured that the bullet cluster has a spectroscopic redshift of z=0.296.

Chandra X-ray studies by Markevitch et al. (2002) and Markevitch (2006) showed that the merger was a 'textbook' example of a bow shock merger. They measured the Mach number of the bow shock to be $\mathcal{M}$ = 3.0 $\pm$ 0.4. The velocity of the cluster was found to be $3000-4000$ km/s. Their observations also indicated that the subcluster traversed the main cluster $0.1-0.2$ Gyrs ago and is in its final stage of being destroyed by dynamic gas instabilities. They studied the temperature profile across the shock and found that the electrons are fast heated at the bow shock

Table 3.4: Multi-wavelength properties of 1E 0657−55.8. The redshift is extracted from Clowe et al. (2004). SZ values are from the ACT catalog (Hasselfield et al., 2013). The X-ray properties are from Menanteau et al. (2010).

R.A.$_{\rm J2000}$	$06^h58^m32^s.7$
Dec.$_{\rm J2000}$	$-55^o57'19''.0$
redshift	0.296
$Y_{500,\rm SZ}$ $(10^{-4}\rm arcmin^2)$	26.6 ± 3.2
$M_{500,\rm SZ}$ $(10^{14}\ M_\odot)$	10.3 ± 1.9
$L_{500,\rm X}$ $(10^{44}$ erg s$^{-1})$	20.69 ± 0.05
$T_{\rm X}(keV)$	13.56 ± 0.14
$Z_{\rm X}$ $(Z_\odot)$	0.36 ± 0.02

front. Di Mascolo et al. (2019b) used Atacama Large Millimeter/submillimeter Array (ALMA) and Atacama Compact Array (ACA) SZ observations to study the bow shock in the cluster. They found an SZ-derived Mach number of $\mathcal{M}$ = $2.53^{+0.33}_{-0.25}$, in agreement with their X-ray-derived value of $\mathcal{M}_X$ = 2.57 ± 0.23, obtained after reprocessing archival *Chandra* data. The multi-wavelength properties of the Bullet cluster are summarised in Table 3.4. There is a known halo and relic in this cluster (Liang et al., 2000; Shimwell et al., 2014, 2015; Malu et al., 2016), making the Bullet an excellent science confirmation target for MeerKAT.

3.3.1 Radio halo and relic

Liang et al. (2000) were the first to report the detection of a radio halo hosted by the Bullet cluster. They observed the cluster using the Australia Telescope Compact Array (ATCA) at 1.3, 2.4, 4.9, 5.9, and 8.8 GHz. There have since been various other studies of the radio emission using deeper, and higher frequency, ATCA observations (Shimwell et al., 2014, 2015; Malu et al., 2016). The first detection of an intriguing 'toothbrush' relic was reported by Shimwell et al. (2015). They measured an integrated flux density of 77.8 ± 3.1 and 4.8 ± 0.6 mJy, α was $\sim -1.07 \pm 0.03$ and -1.66 ± 0.14 for regions A, and B (see Figure 3.4), and $\rm P_{1.4GHz}$ = 2.3 ± 0.1 $\times 10^{25}$ W Hz^{-1}. Their X-ray analysis revealed that the relic coincides with a shock opposite the western bow shock. The Mach number of the shock was measured to be $\mathcal{M}$ = 2.5. We also detect both

Table 3.5: Summary of radio analysis for the Bullet cluster

Source	Integrated Flux Density (mJy)	$\alpha_{1.6GHz}^{0.9GHz}$	$P_{1.4GHz}$ (10^{24} WHz^{-1})	LAS (arcmin)	LLS (kpc)
Halo	101±6.0	1.55±0.31	29.9±1.5	6.15×4.73	1632×1250
Relic region A	98.85±1.7	1.22±0.27	26.8±0.3	1.63	432
Relic region B	8.23±1.4	1.78±0.32	2.5±0.4	2.10	556
Relic	107.04 ±2.1	1.39±0.29	30.4±0.5	3.73	988

the known radio halo and radio relic in the MeerKAT L-band imaging of the Bullet cluster.

The full-resolution MeerKAT L-band image of the Bullet cluster cluster is shown in Figure 3.3, with the low-res, compact-source-subtracted image presented in Figure 3.4. The detected radio halo has a largest angular size (LAS) of $6.15' \times 4.73'$, and the corresponding largest linear size (LLS) is 1632 kpc × 1250 kpc. The radio relic has a LAS of $3.73'$, and corresponding to a LLS of 988 kpc. MeerKAT's dense short baselines and sensitivity enables us to detect diffuse emission beyond the regions detected from ATCA observations in Shimwell et al. (2014). However, the morphology of the radio halo and relic is consistent with the diffuse emission in Shimwell et al. (2014) and Shimwell et al. (2015). We measure integrated flux densities for all diffuse structure using the low-res map, within the regions indicated in Figure 3.4. The observational properties of the structures are summarised in Table 3.5.

We detect a fainter region of the radio halo (see Figure 3.3 and 3.4). The extended faint emission appears to have a decrement below the bow shock region, as labelled in Figure 3.3 and 3.4. This faint emission, including the decrement, traces the X-ray surface brightness (see Figure 3.5). The edge of the radio halo overlaps with the 'bow' shock region. Comprehensive dynamical studies are required to determine if the fainter emission and decrement relate to any merger activity in the peripheral region of the cluster. We also observe that region A of the radio relic is much brighter than region B. Shimwell et al. (2015) proposed that region A might be connected to the remnants of a radio galaxy. This scenario supports the theory that postulates that the cosmic ray electrons in radio relics come from a pre-existing pool of relativistic electrons.

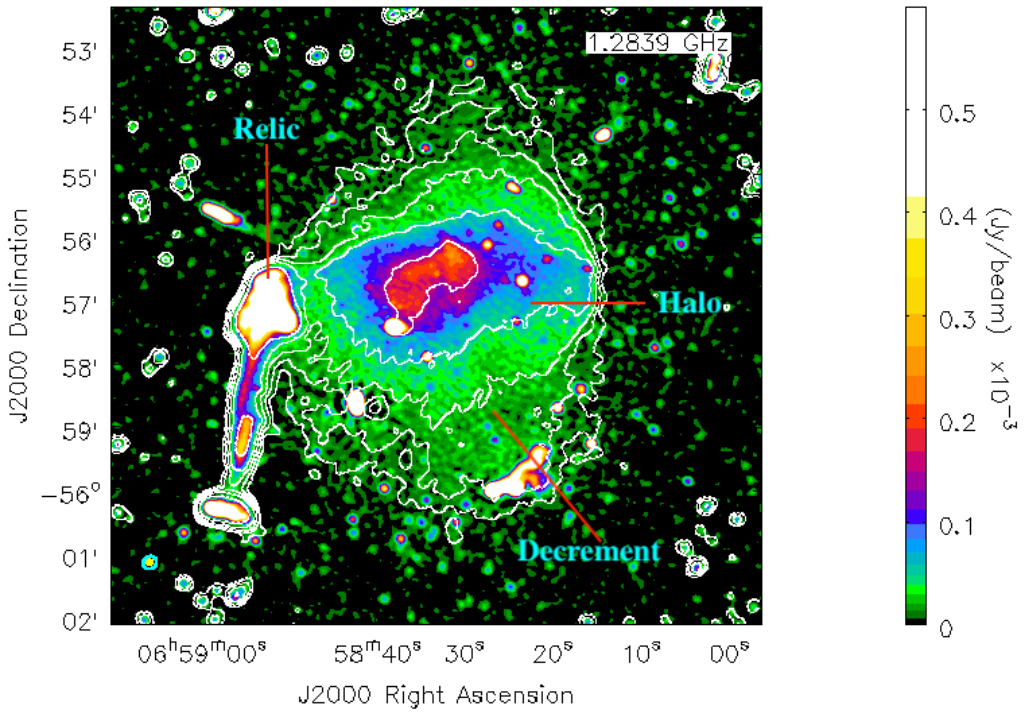

Figure 3.3: Full resolution MeerKAT 1.28 GHz image of the Bullet cluster. The diffuse halo and relic features are labelled, along with an apparent decrement in the south-western region of the halo. Contours are from the low resolution image, with levels of [-3,3,6,12,24,72]$\times\sigma$ where σ = 10.07 μJy/beam. In the lower left corner are the synthesised beams of the full resolution and low resolution images; they are indicated by the filled yellow ellipse and cyan ellipse, respectively.

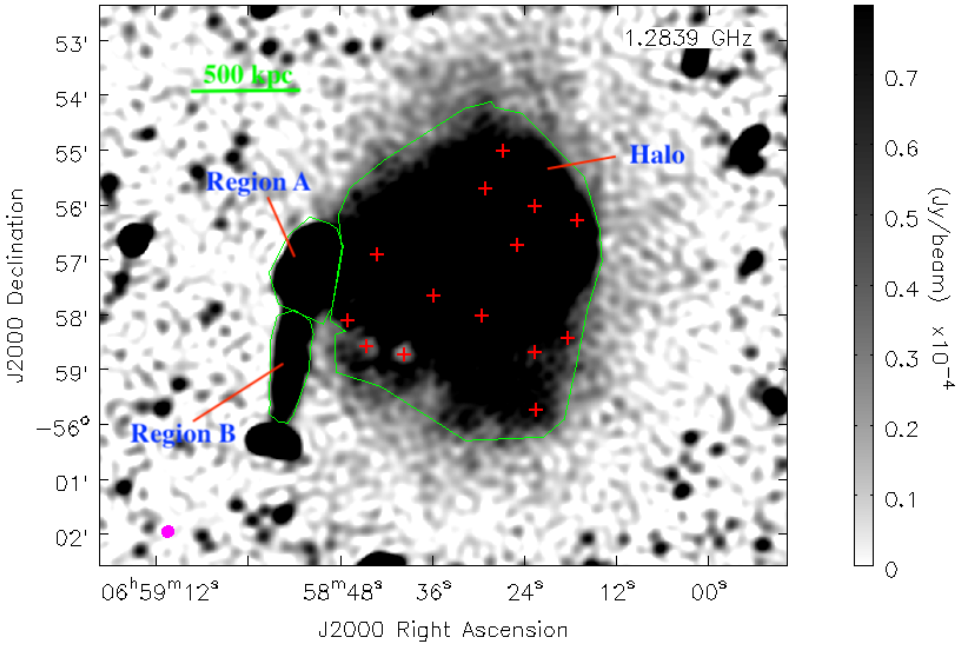

Figure 3.4: Low resolution MeerKAT 1.28 GHz image of the Bullet cluster. The regions used to measure the flux of the halo and the relic are labelled. Region A and B of the relic indicates the brightest region and fainter extension of the relic, respectively. The physical linear scale at the cluster redshift is indicated in the upper left. The rms of the image is 10.07 μJy/beam. The synthesised beams of the image is indicated by the magenta ellipses in the lower left corner. The red crosses indicated all the point sources that were subtracted.

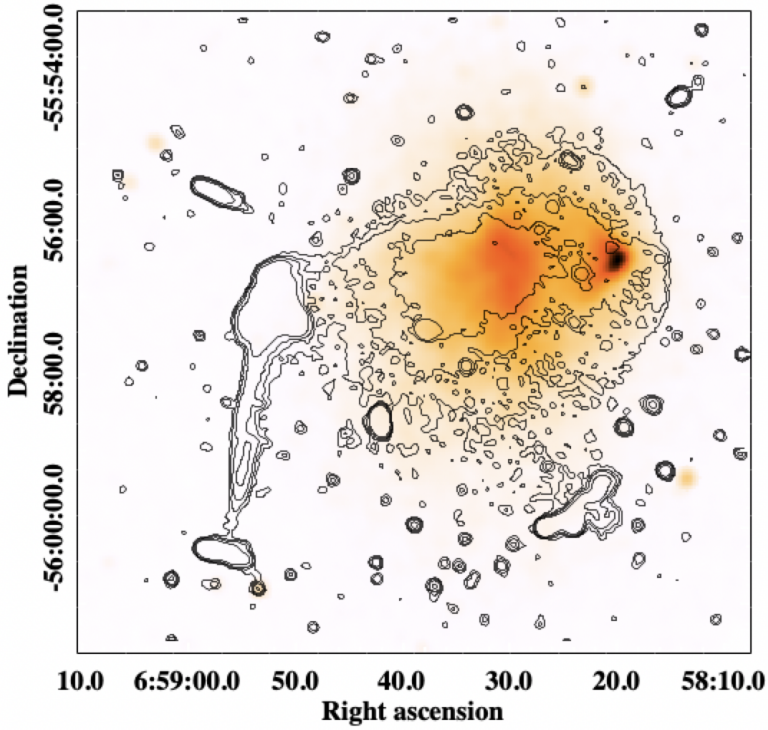

Figure 3.5: Archival *Chandra* X-ray image of the Bullet cluster showing the two sub clusters. The faintest radio halo regions match the morphology of the X-ray-emitting gas . The contours are from the MeerKAT 1.28 GHz full resolution image. The contour levels are $\sigma \times$[3,6,12,30], where σ is 8.5 μJy/beam.

3.3.2 Spectral index properties of the radio halo and relic

MeerKAT's wide bandwidth also enabled us to perform in-band spectral index studies of the radio halo and the relic. Using sub-band images centred at 963.9 MHz and 1.65 GHz, we calculate the integrated spectral index of the radio halo and the full relic structure to be 1.55 ± 0.31 and 1.39 ± 0.29, respectively. For region A and B of the relic we measure the integrated spectral index values to be 1.22 ± 0.27 and 1.78 ± 0.32, respectively. Our spectral index values are similar to those in quoted in Shimwell et al. (2014) and Shimwell et al. (2015).

The spectral index maps obtained from the 963.9 MHz and 1.65 GHz sub-band images are shown in Figure 3.6. The crosses in these maps indicate the regions in which the point sources were removed. The spectral index maps we obtain (see Figure 3.6) have a higher spatial resolution compared to those derived by Shimwell et al. (2014, 2015). We also capture a larger region of the radio halo spectral index map. The spectral index map in the radio halo region varies across the central region of halo and steepens towards the edge. The variation in the central region is $\alpha \sim 0.9 - 1.8$ and the steepened edges the spectral index values are $\sim$1.9. The inner region of the halo has a flatter ($\sim$0.9) spectral index values. This region indicates presence of more energetic radiating particles, and/or of a larger value of the local magnetic field strength (Feretti et al., 2004a; Rajpurohit et al., 2020a). The radial steepening pattern has been previously reported for radio halos hosted by the Coma cluster, Abell 665, and Abell 2163 (Giovannini et al., 1993; Feretti et al., 2004a). Currently it is not clear whether this feature is of astrophysical origin or if it reflects discrepancies in the data.

The spectral index map of the relic resembles that of a 'toothbrush' relic (Rajpurohit et al., 2020c). The relic's spectral index map indicates a spectral steepening in the E$-$W direction, towards the cluster centre. The spectral steepening feature is observed in most relics (Clarke and Ensslin, 2006b; Shimwell et al., 2015; Rajpurohit et al., 2020b). This trend is attributed to the downstream regions of shock waves where relativistic particles slow down.

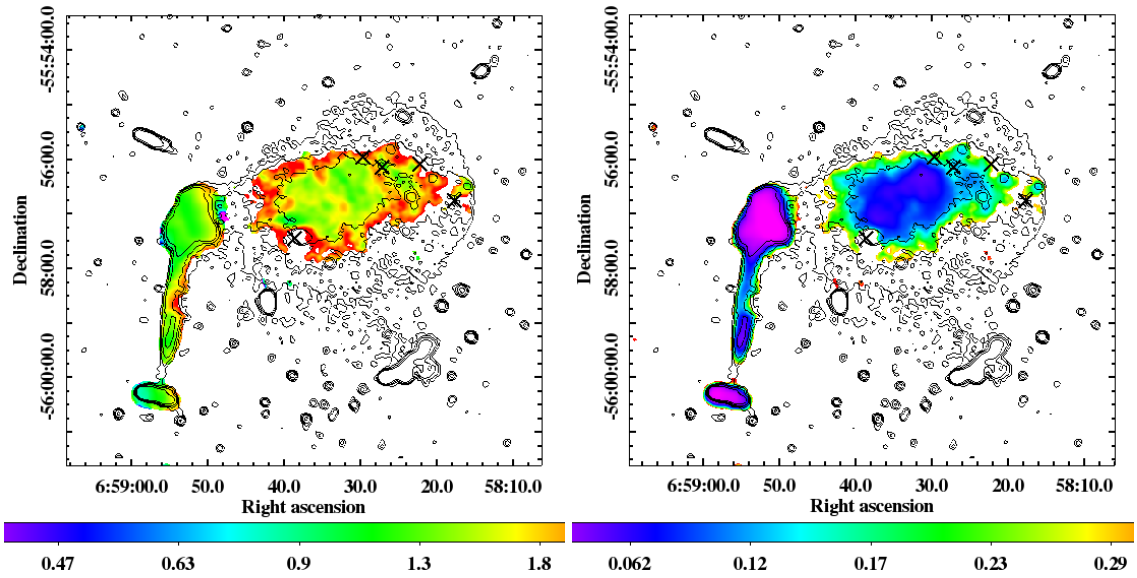

Figure 3.6: The spectral index map and the corresponding error map of the diffuse emission region in the Bullet cluster. The contours are from the full resolution radio image. The black crosses indicate regions where the brightest sources embedded in the halo were subtracted. Contours are from the low resolution image, with levels of [3,6,12,]$\times\sigma$ where σ = 8.5 μJy/beam.

Table 3.6: Multi-wavelength properties of RXC J1314. The redshift value is extracted from Valtchanov et al. (2002). SZ values are from Planck Collaboration et al. (2016). The X-ray properties are from Piffaretti et al. (2011).

R.A.$_{\rm J2000}$	$13^h14^m28^s$
Dec.$_{\rm J2000}$	$-25^o15'41''$
redshift	0.247
$Y_{500,\rm SZ}$ $(10^{-4}\rm arcmin^2)$	19.3
$M_{500,\rm SZ}$ $(10^{14}\ M_\odot)$	6.7
$L_{\rm X[0.1-2.4keV]}$ $(10^{44}$ erg s$^{-1})$	9.89

3.4 RXC J1314.4-2515

RXC J1314.4−2515 (henceforth RXC J1314) was first detected by the *ROSAT* All Sky Survey (RASS; Voges et al., 1999) and has since been observed and studied at various wavelengths. X-ray observations by Valtchanov et al. (2002) showed that the cluster had irregular morphology indicating merger activity. Their study also showed that the X-ray emission had two central peaks and was elongated in the SE−NW direction. They also derived that RXC J1314 has a spectroscopic redshift of z = 0.247. Mazzotta et al. (2011) used *XMM-Newton* observations to study the merger shock properties. Their study revealed that the cluster went through a major merger event and had an M-shaped shock. The merger's shock Mach number was measured to be $\sim$2.5. Optical studies showed that there was a bimodal clustering of galaxies within the clusters (Valtchanov et al., 2002). Golovich et al. (2019) confirmed the bimodality and also concluded that since the sub-clusters have similar velocity dispersions, the mass ratio of the merger is 1:1 which indicates a major merger. The multi-wavelength properties of RXC J1314 are summarised in Table 3.6. RXC J1314 is known to host a radio halo and double relics (Valtchanov et al., 2002; Feretti et al., 2005; Venturi et al., 2013; Stuardi et al., 2019) which makes it an excellent science confirmation target for MeerKAT.

3.4.1 Radio halo and relics

Observations from ATCA, at 1.384 GHz and 2.496 GHz (∼9" resolution), showed a tentative detection of extended diffuse emission which was categorised as candidate double relics (Valtchanov et al., 2002) . Feretti et al. (2005) confirmed the existence of the double relics using Very Large Array (VLA) observations at 1.4 GHz. They also reported radio halo emission that extends to the western radio relic. The diffuse emission has been also studied at lower frequencies (88−610 MHz) using the GMRT and the Murchison Widefield Array (MWA) (Venturi et al., 2007, 2013; George et al., 2017). X-ray studies by Mazzotta et al. (2011) revealed that the M-like shock front coincides with the western relic. The most recent study of the diffuse emission in RXCJ1314 was by Stuardi et al. (2019), using JVLA observations. They used observations over the range 1−4 GHz to study the flux, polarisation, and spectral index properties of the diffuse emission. They measured 1.5 GHz flux densities for the eastern relic, western relic, and radio halo to be 11.3 ±0.6 mJy, 33±2 mJy, and 5.3±0.3 mJy, respectively. The largest linear size (LLS) of the eastern relic, western relic, and radio halo was measured to be ∼500 kpc, ∼550 kpc, and ∼250 kpc, respectively. The measured polarisation fraction for both relics was ∼31% at 3 GHz. Finally, the integrated spectral indices of the eastern relic, western relic, and radio halo were measured to be 1.0±0.1, 1.6±0.1, and 1.3±0.2 respectively. We also detect the known radio halo and radio relics in the MeerKAT L-band imaging of the RXC J1314.

The full-resolution MeerKAT L-band image of RXC J1314 is shown in Figure 3.7, with the low-res, compact-source-subtracted image presented in Figure 3.8. We detect a radio halo with a LAS of 3.17′ × 2.05′, corresponding to a LLS of 742 kpc × 480 kpc. We also detect diffuse emission of both the eastern and the western relic. The LAS of the eastern relic is 2.88′, which corresponds to a LLS of 674 kpc. The LAS of the western relic is 4.16′, which corresponds to a LLS of 973 kpc. We used the 6σ contours surrounding the eastern relic emission to define the boundary of the radio halo. We recover larger LLS form the halo and both the relics in comparison to the emission detected in Stuardi et al. (2019).

We measure integrated flux densities for all diffuse structure using the low-res map, within the regions indicated in Figure 3.8. For the radio halo we measure an integrated flux density of

Table 3.7: Summary of radio analysis for RXC J1314.

Source	Integrated Flux Density (mJy)	$\alpha_{1.6GHz}^{0.9GHz}$	$P_{1.4GHz}$ (10^{24} WHz^{-1})	LAS (arcmin)	LLS (kpc)
Halo	11.26 $\pm$1.2	1.5$\pm$0.1	2.1$\pm$0.3	3.17$\times$2.05	742$\times$480
E Relic	13.71$\pm$0.7	1.2$\pm$0.3	2.5$\pm$0.2	2.88	674
W Relic	31.37$\pm$1.2	1.4$\pm$0.1	5.5$\pm$0.3	4.16	973

11.26 $\pm$1.2 mJy. Stuardi et al. (2019) indicated that there is a narrow-angle tailed (NAT) radio galaxy embedded in the eastern relic. They further mention that the NAT's lobes have a LLS of $\sim$90 kpc and fade into the radio relic. The NAT has extended emission hence it was visible even when we applied the 13 kλ uv-cut, hence we are unable to disentangle the NAT from the relic. The flux densities of the eastern and western relic were measured to be 13.71$\pm$0.7 mJy and 31.37$\pm$1.2 mJy, respectively. The embedded radio galaxy further supports the re-acceleration model, which predicts that relics are produced by the shock-induced re-acceleration of fossil plasma.

The morphology of the relics and the halo are similar to that in Stuardi et al. (2019). Feretti et al. (2005) were the first to report that the radio halo extended to the western relic. Our images also indicate that there is continuous emission between the radio halo and the western relic (see Figure 3.7). Markevitch (2010) established that this 'bridge' feature can be explained by the turbulence and merger shocks resulting from the cluster merger. As shown in Figure 3.9, the radio halo emission traces the brightest region of the cluster's X-ray surface brightness. The archival optical image from DSS in Figure 3.9 indicates bright sources embedded in the eastern relic. These sources are possible optical counterparts of AGN. If true, these AGNs would be the source of fossil plasma that is re-accelerated to form the relic.

3.5 Spectral index properties of the radio halo and relics

MeerKAT's wide bandwidth also enabled us to perform in-band spectral index studies of the radio halo and the relic. Using sub-band images centred at 963.9 MHz and 1.65 GHz, we calcu-

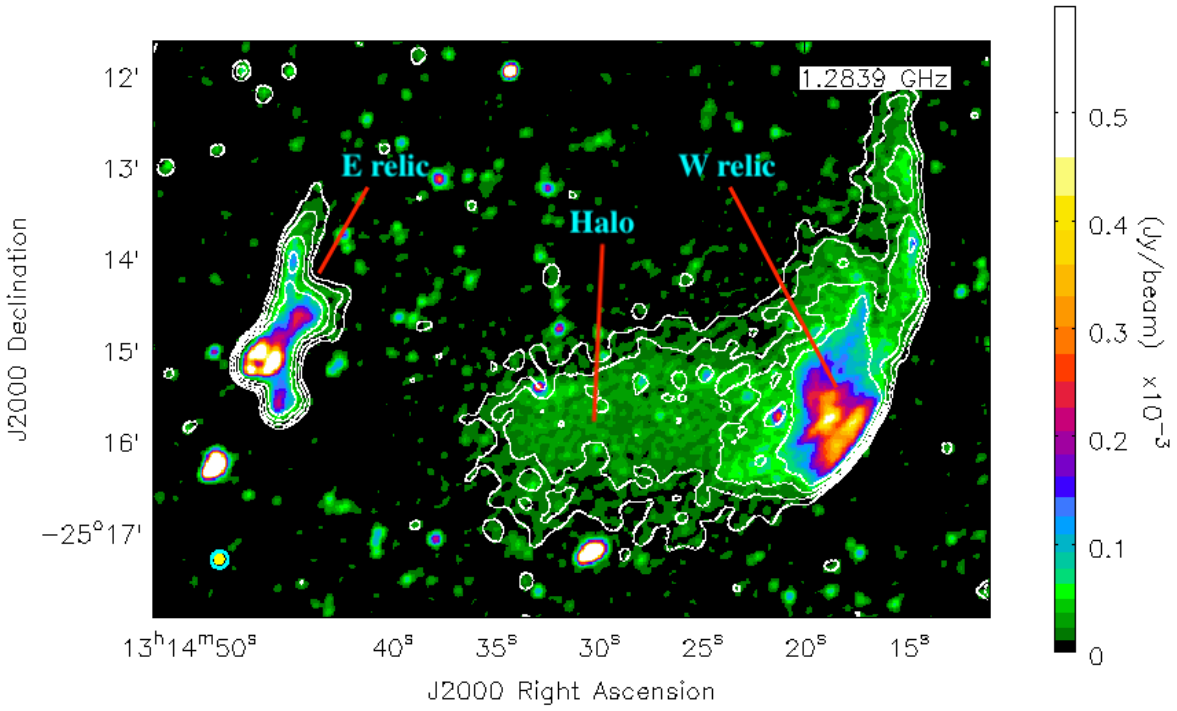

Figure 3.7: Full resolution MeerKAT 1.28 GHz image of RXC J1314. The diffuse halo and the eastern and western relic features are labelled. Contours are from the low resolution image, with levels of [-3,3,6,12,24]$\times\sigma$ where σ = 10.34 μJy/beam. In the lower left corner are the synthesised beams of the full resolution and low resolution images; they are indicated by the filled yellow ellipse and cyan ellipse, respectively.

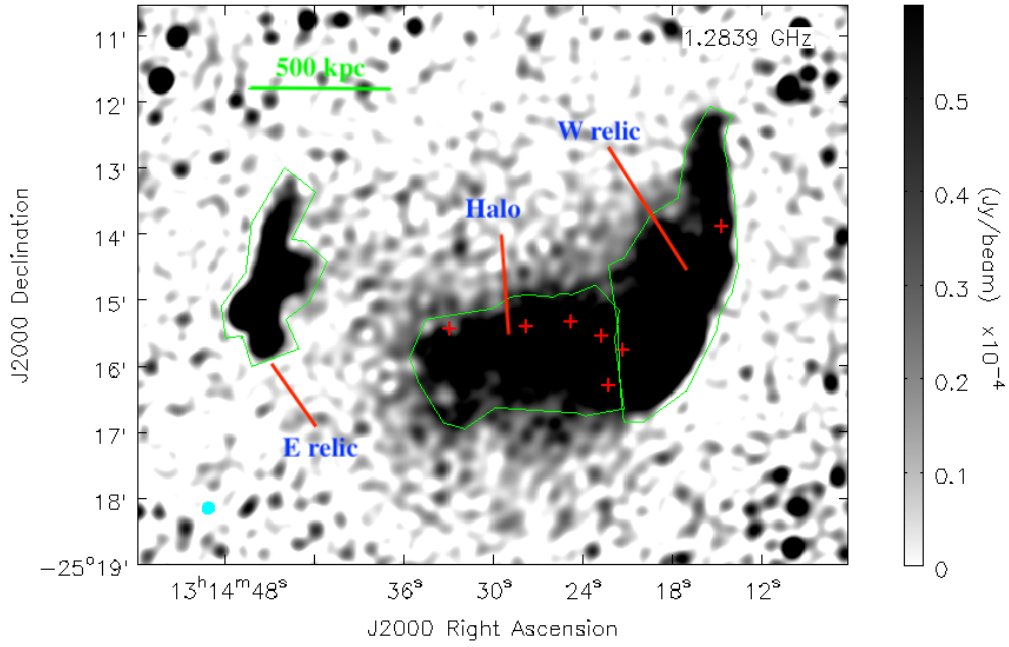

Figure 3.8: Low resolution MeerKAT 1.28 GHz image of RXC J1314. The polygon regions indicate the regions used to measure the flux densities of the halo and relics. The halo and western relic were separated using the 12σ contours, which outline the relic region. The physical linear scale at the cluster redshift is indicated in the upper left. The rms noise of the image 10.34 μJy/beam. The synthesised beam of the low resolution image is indicated by the cyan ellipse on the lower left.

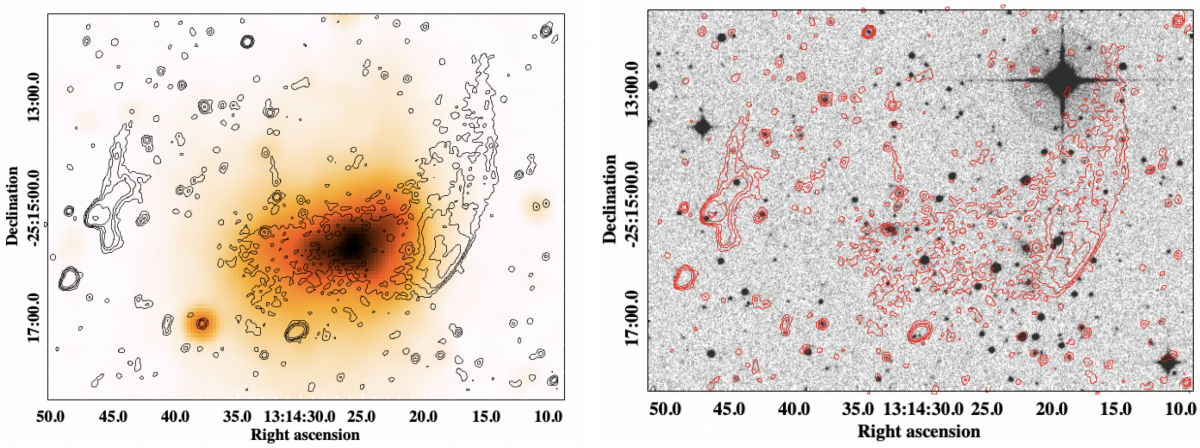

Figure 3.9: Multi-wavelength images of RXC J1314 with contours from MeerKAT 1.28 GHz full resolution image. The contour levels are $\sigma \times$[3,6,12,30], where σ is 9.3 μJy/beam. *Left:* Archival *XMM-Newton* X-ray image of RXC J1314. The western relic overlaps with the shock region while the halo emission traces the brightness peak. *Right:* Archival Optical r-band image from DSS. We could not locate recent observations covering the full field. The eastern relic overlaps with two bright galaxies which are possible AGN counterparts embedded in the halo.

late the integrated spectral index of the radio halo, the eastern relic, and the western relic to be 1.5 ± 0.1, 1.4 ± 0.1, and 1.2 ± 0.3, respectively. The integrated spectral index measurements of the radio relics and halo are in agreement with the values quoted in Stuardi et al. (2019). We also used the sub-band images centred at 963.9 MHz and 1.65 GHz to produce spectral index maps of the diffuse emission. The in-band spectral index map of the regions covering the eastern and the western relic are shown in Figure 3.10. Unlike Stuardi et al. (2019), we were unable to map the spectra of the faint radio halo. Our low-resolution sub-band images had a higher resolution compared to the images Stuardi et al. (2019). The halo's emission was also much fainter in our higher frequency image (1.65 GHz). This resulted in the poor mapping of the spectral index map of the radio halo.

Our maps show a spectral steepening trend similar to the relic in the Bullet cluster. The regions toward the cluster centre are steeper in both the eastern and the western relic. This is a typical trend for radio relics as steepening indicates downstream regions with lower energy electrons in comparison to the shock region. The western relic is known to coincide with a shock region. Although X-ray studies have not reported the detection of a shock in the eastern relic region, the location, extension and spectral index features do indicate that it is a relic. The spectral index map also reveals that there is likely an AGN embedded in the western relic. This will further motivate the notion of radio relics being linked to fossil plasma.

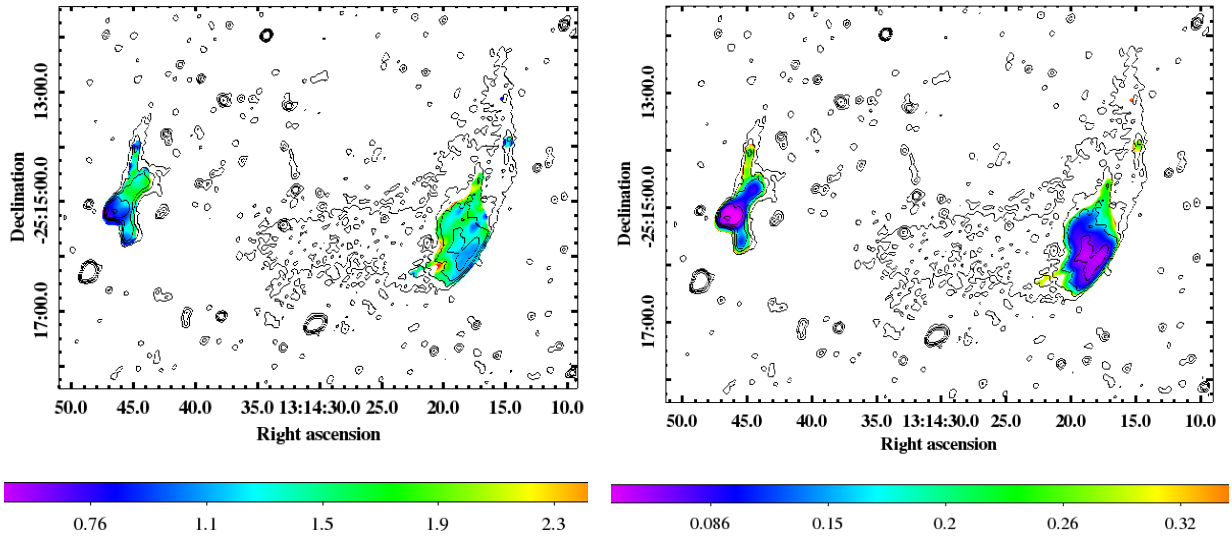

Figure 3.10: Spectral index map and the corresponding error map of RXC J1314. Contours are from the low resolution image, with levels of [3,6,12,30]$\times\sigma$ where σ = 9.3 μJy/beam.

3.6 Abell 3562

Abell 3562 (hereafter A3562) is part of the Shapley supercluster, the most massive supercluster in the local universe ($z < 0.05$), which was first discovered by Shapley (1930). The central region of the supercluster consists of five Abell clusters (A3558 (see Section 3.7), A3556, A3559, A3560, A3562) and two rich groups of galaxies (SC1327−312 and SC1329−313). Figure 3.11 shows the clusters which are members of the Shapley supercluster enclosed in the green polygon. The clusters we study are indicated by the magenta circles. X-ray observations by Kull and Böhringer (1999) showed that the core of the supercluster has complex morphology with filamentary structures connecting A3562, A3558, and A3556. Multi-wavelength studies of the Shapley supercluster have revealed that the region between A3558 and A3562 is dynamically unrelaxed (Ghizzardi et al., 2010; Merluzzi et al., 2015; Venturi et al., 2017a; Di Gennaro et al., 2018; Higuchi et al., 2020).

A3562 is an intriguing cluster that has been studied at multiple wavelengths. X-ray studies confirmed that the cluster is dynamically disturbed and shows traces of interactions with the galaxy group SC 1329–313 (Ettori et al., 2000; Finoguenov et al., 2004). The multi-wavelength properties of A3562 are summarised in Table 3.8. A study by Venturi et al. (2000) reported a tentative detection of a radio halo in the cluster region. VLA observations by Venturi et al. (2003) confirmed the existence of a faint, steep spectrum ($\alpha \sim 2$) radio halo in A3562. The most recent detailed study of the radio halo was done by Giacintucci et al. (2005). The VLA and GMRT observations, covering a frequency range of 240−1400 MHz, enabled them to extract the flux density of the halo and study its spectral index properties. At 1.4 GHz, they measured an integrated flux density of 20±2 mJy and a LLS of ∼475 kpc. The 332−1400 MHz spectral index was found to be ∼1.5. The faint radio halo observed in A3562 makes it an excellent target for MeerKAT's L-band sensitivity.

The full-resolution MeerKAT L-band image of the cluster is shown in Figure 3.12, with the low-res, compact-source-subtracted image presented in Figure 3.13. **Observations of Abell 3562 were not centred at the target. However, all the diffuse emission properties were extracted from primary beam corrected images. This accounts for primary beam variations**

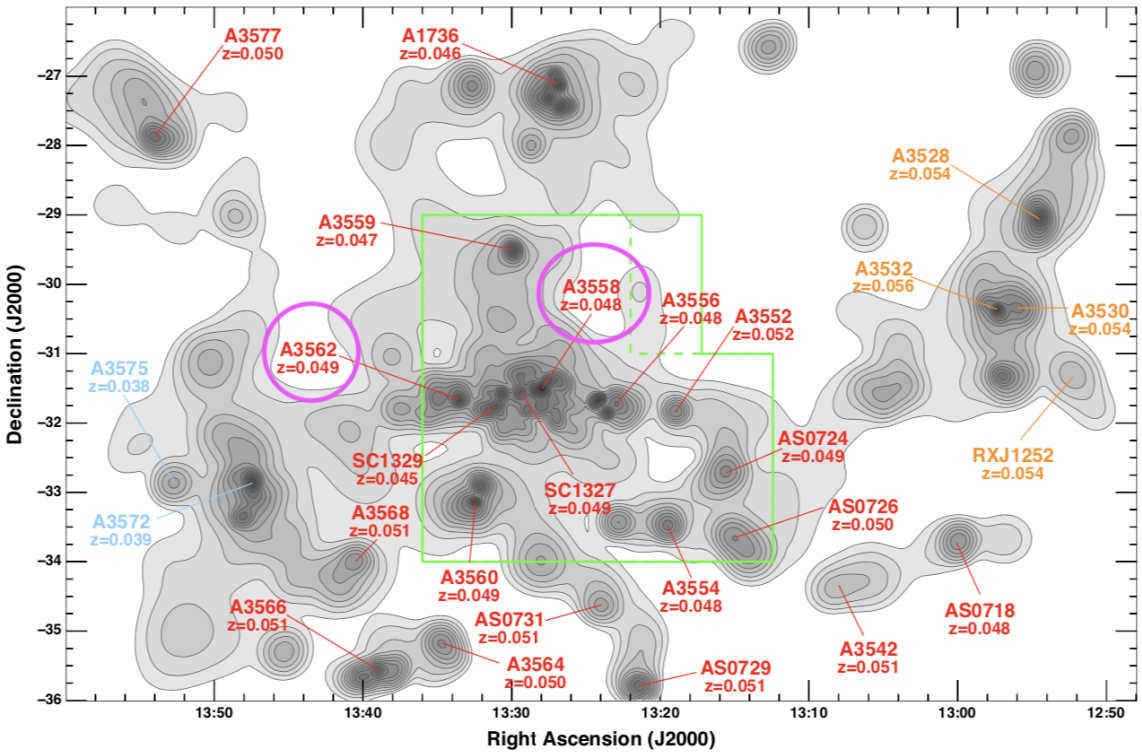

Figure 3.11: The Shapley supercluster. Abell clusters within the same redshift range are labelled with the same colour text, in red are the clusters whose recession velocities is within 1500 km s^{-1} of the central cluster Abell 3558; in cyan are clusters with range the redshift range of $0.035 \leqslant z < 0.040$; and in orange a redshift range of, $0.053 \leqslant z < 0.060$. The solid green box outlines the 23 deg^2 region covered by the Shapley supercluster. Source: (Higuchi et al., 2020).

at the position of the target. We detect a radio halo having a LAS of $8.85' \times 4.33'$, corresponding to a LLS of 493 kpc $\times$ 241 kpc. The LLS is slightly more extended than the LLS Giacintucci et al. (2005) measures at 1.4 GHZ. Using the polygon region indicated in Figure 3.13, we measure an integrated 1.28 GHz halo flux density of 35 ± 0.54 mJy.

The morphology of the radio halo (see Figure 3.12 and 3.13) significantly differs to that in Giacintucci et al. (2005). We detect a new 'ridge' feature in the peripheral SE region of the halo which connects to the brightest region of the halo. The X-ray image in Figure 3.14 shows that the ridge coincides with the edge of the X-ray surface brightness. Further X-ray studies are needed to determine whether the radio ridge coincides with a merger shock region. Shweta et al. (2020) also report a sharply defined ridge in the central region of a radio halo hosted by Abell 2163. They propose that the ridge might be a radio relic projected in the region of the halo. However, after

Table 3.8: Multi-wavelength properties of A3562. The cluster mass and redshift are taken from Higuchi et al. (2020). The X-ray properties are from Ettori et al. (2000).

R.A.$_{\rm J2000}$	$13^h33^m31^s.8$
Dec.$_{\rm J2000}$	$-31^o40'23''.0$
redshift	0.049
$Y_{500,\rm SZ}$ $(10^{-4}\rm arcmin^2)$	26.6 ± 3.2
M_{200} $(10^{14}\ h^{-1}\ M_\odot)$	$2.04^{+2.74}_{-1.78}$
$L_{\rm X,bol}$ $(10^{44}$ erg s$^{-1})$	2.2
$T_{\rm X}(keV)$	5.1 ± 0.02

further investigation, they conclude that this feature may be a result of re-energisation of fossil plasma due to merger-induced turbulence. Further multi-wavelength observations are required to establish if the 'ridge' feature is part of the radio halo or if it is a candidate Gently Re-Energised Tail (GReET; de Gasperin et al., 2017b).

The bright central region of the radio halo is also observed in Giacintucci et al. (2005). However, the 'ridge' feature results in a distinct 'wedge' structure in the radio halo. This feature is not common in radio halos as they are known to have regular morphology. Further lower frequency observations, possibly with MeerKAT's UHF band ($0.58-1.015$ GHz), are required to investigate if this is indeed a feature in the radio halo or contamination from the head-tail galaxy embedded in the halo.

The sensitivity of the MeerKAT L-band observation also enable us to produce a spectral index map of the radio halo. The spectral index varies across the region of the halo. The pattern in the halo region is similar to that in the extended ridge. This might be an indication that the ridge feature is related to the radio halo. The extent of the map region is much larger than the spectral index maps shown in Giacintucci et al. (2005). However, we note that the mapped region also includes the 'tail' region of the bent-tail galaxy. This indicates that there is residual emission from this source. We measure the integrated spectrum of the halo to be 1.06 ± 0.35, which is flatter compared to $\alpha = 1.5 \pm 0.1$ reported by Giacintucci et al. (2005).

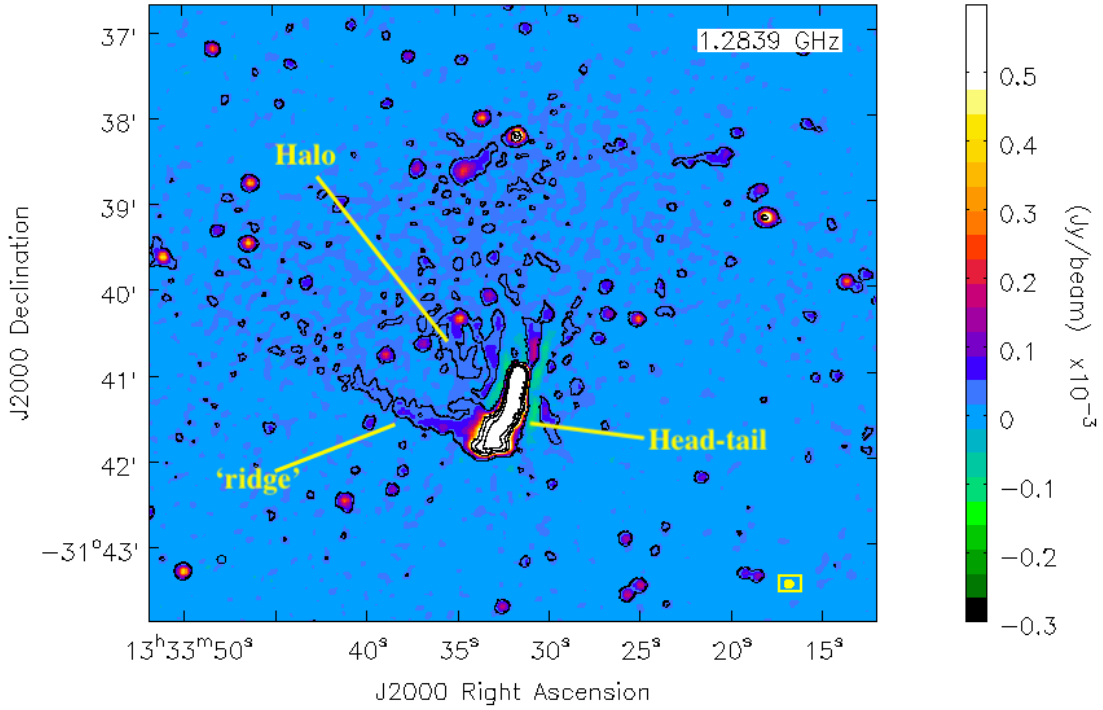

Figure 3.12: Full resolution MeerKAT 1.28 GHz image of A3562. The diffuse halo and ridge features are labelled. Contours are from the full resolution image, with levels of [-3,3,6,12,24]$\times\sigma$ where σ = 8.2 μJy/beam. The synthesised beam is indicated by the filled yellow ellipse in the lower right.

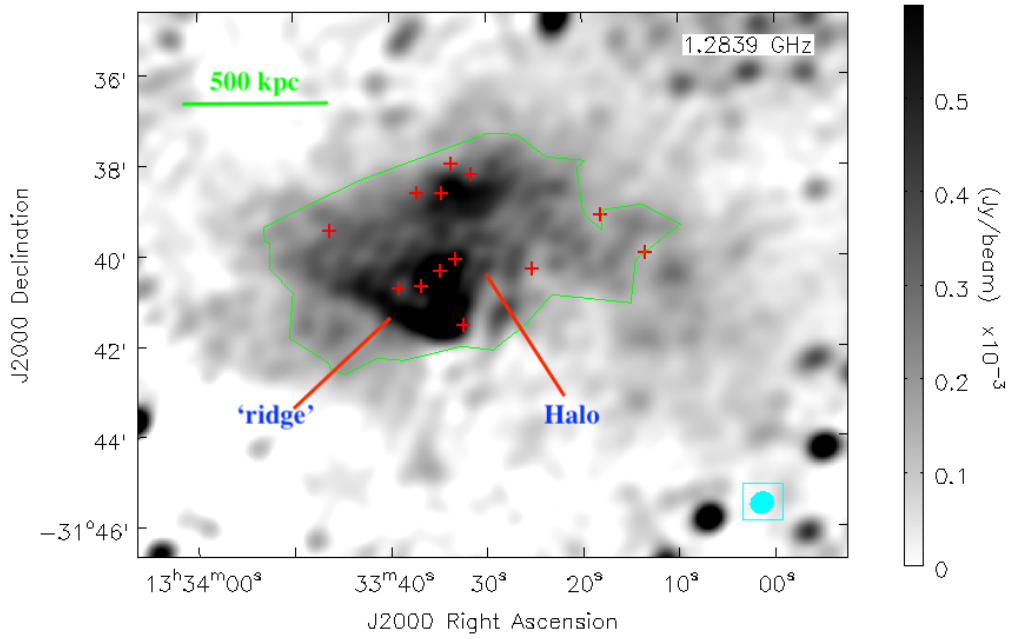

Figure 3.13: Low resolution MeerKAT 1.28 GHz image of A3562. The region used to measure the flux density of the halo is indicated by the polygon. The physical linear scale at the cluster redshift is indicated in the upper left. The rms noise of the low resolution image is 21.50 μJy/beam. The synthesised beam is indicated by the filled cyan ellipse in the lower right.

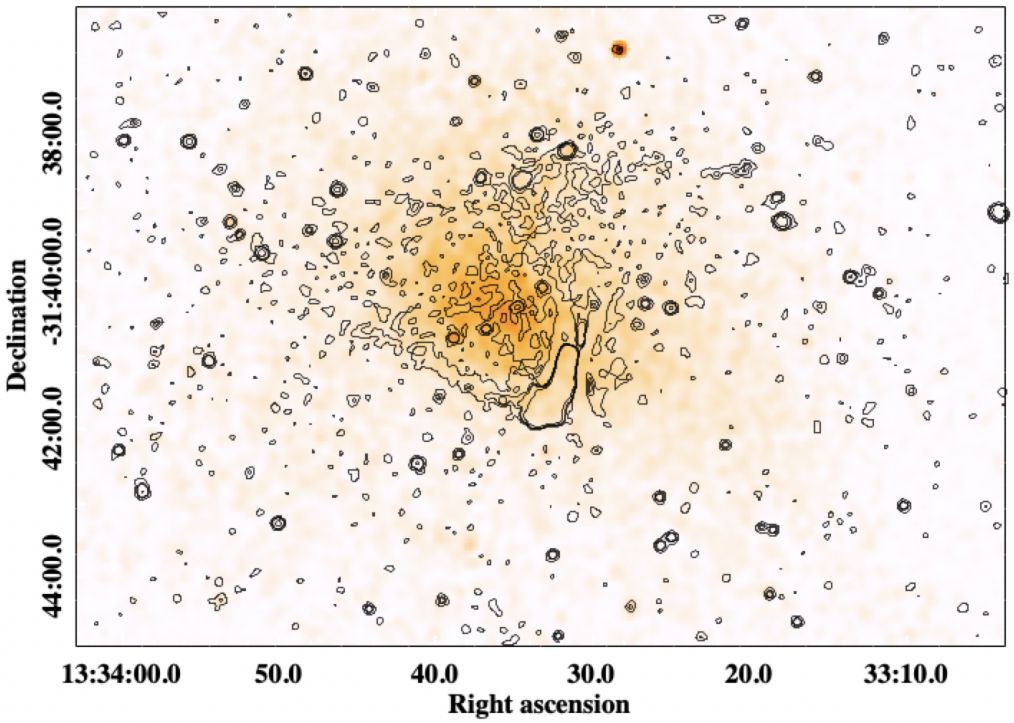

Figure 3.14: Archival *Chandra* X-ray image of A3562 with contours from MeerKAT 1.28 GHz full resolution image. The contour levels are $\sigma \times$[3,6,12,24], where σ is 8.2 μJy/beam. The radio ridge overlaps with the edge of the X-ray brightness distribution indicating that it might overlap with a shock region. The radio halo overlaps with the peak brightness

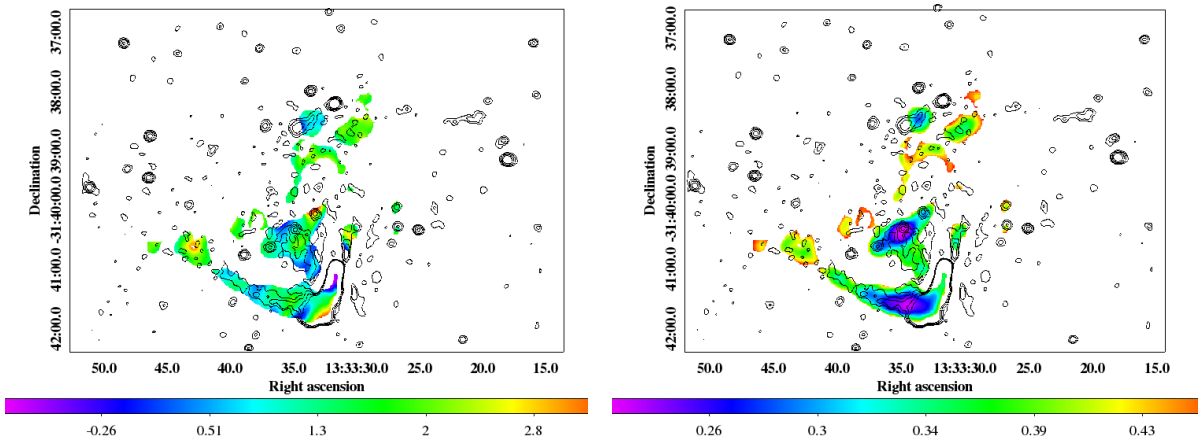

Figure 3.15: Spectral index map and the corresponding error map of A3562. The contours are from the full resolution radio image. Contours are from the full resolution image, with levels of [3,6,12,24]$\times\sigma$ where σ = 8.2 μJy/beam.

3.7 Abell 3558

Abell 3558 (hereafter A3558) is amongst the clusters at the core of the Shapley supercluster and is often referenced as the centre of the supercluster. Multi-wavelength studies have shown that the cluster has complex morphology and cannot be distinctively categorised as a relaxed or merging system. X-ray observations by Bardelli et al. (1996) showed that the cluster is elongated in the NW−SE directions. The study also highlighted that although there are traces of interactions between A3558 and other cluster and group members of the supercluster, the cluster exhibits a cool-core. The complex structure of A3558 was further probed by Bardelli et al. (1998); they concluded that the cluster has recently undergone a core-core collision or it has undergone multiple minor mergers. They indicated that further velocity dispersion studies are required to distinguish between the two scenarios.

Other X-ray studies, using instruments such as *ROSAT*, *XMM-Newton*, and *Chandra*, have confirmed that the cluster is asymmetric and that the X-ray brightness peaks at the core and radially declines (Markevitch and Vikhlinin, 1997; Akimoto et al., 2003; Rossetti et al., 2007). These studies also highlighted that although the cluster has an inner 'cool-core' it cannot be classified as a dynamically relaxed cluster since there are traces of infalling sub-groups. Optical observations have shown that A3558 has multiple sub-clumps and has a region with a highly concentrated number of galaxies (Quintana et al., 1995; Bardelli et al., 1998; Quintana et al., 2020). Merluzzi et al. (2015) and Higuchi et al. (2020) used optical data to reconstruct the mass of the cluster using gravitational weak lensing. These optical studies also confirm that there are substructures in Abell 3558, as reported by X-ray observations.

VLA and GMRT observations have been used to study the radio properties of A3558 (Venturi et al., 2000; Giacintucci et al., 2004; Mauduit and Mamon, 2007; Venturi et al., 2017a; Di Gennaro et al., 2018). Thus far, no extended diffuse emission has been detected. The radio studies showed that the radio galaxies in A3558 are less radio-luminous when compared to surrounding clusters. Di Gennaro et al. (2018) concluded that the difference in radio luminosity is due to the merger activity in the region of the cluster. The multi-wavelength properties of A3558 are summarised in Table 3.9. A3358 is an interesting target for MeerKAT because the complex

Table 3.9: Multi-wavelength properties of A3558. The cluster mass and redshift are taken from Higuchi et al. (2020). The X-ray properties are from Parekh et al. (2015).

R.A.$_{\rm J2000}$	$13^h28^m02^s.6$
Dec.$_{\rm J2000}$ (dd:mm:ss.s)	$-31^h29'35''.0$
redshift	0.048
M_{200} (10^{14} h^{-1} $M_\odot$)	$4.47^{+2.78}_{-2.38}$
$L_{\rm X,bol}$ (10^{44} erg s^{-1})	1.9
$T_{\rm X}(keV)$	4.88 ± 0.1

morphology and dynamical state of the cluster may be an indication that there is faint extended emission that hasn't been detected before due to sensitivity limitations.

For the first time, we report the detection of faint diffuse emission in the central region of A3558. We measure diffuse emission with a LAS of $7.0' \times 3.6'$, corresponding to a LLS of 390 kpc $\times$ 199 kpc. The diffuse emission traces the X-ray surface brightness (see Figure 3.18). Given the size of the emission and the fact that it is embedded in a radio-loud BCG (see Figures 3.16 and 3.18), we conclude that it falls in the category of mini-halos. The integrated flux density of the diffuse emission is 9.36 ± 0.3 mJy. However, the point source subtracted low resolution image still contains residual flux from the BCG embedded in the mini-halo region (source A in Figure 3.16). The archival DSS and *Chandra* images in Figure 3.18 show optical and X-ray counterparts of the BCG.The estimated residual flux density of the BCG is $\sim$1.47 mJy. Hence, the estimated flux density of the emission is $\sim$7.89 mJy. Source 'A' in Figure 3.16 had bright artefacts and resulted in some of the halo flux density being subtracted. Hence, the flux density of the emission might be underestimated.

X-ray studies of A3558 indicate that this cluster has a cool-core, hence, the cosmic ray electrons might be accelerated by the gas sloshing in the cool-core (see Section 1.2.2.1). However, these studies have also indicated that the X-ray emission has asymmetric morphology, which is typical in dynamically disturbed clusters. Optical studies found that the cluster had substructure which indicates merger activity. Hence, we propose that the mini-halo in this cluster might be in a transitional phase, as predicted by hybrid radio halo formation models (see Brunetti and Jones, 2014, for review). This transitional phase was also observed by Kale et al. (2019). They reported

that the radio halo in RXC J0232.2−4420 had a BCG embedded in the emission. They propose that the emission might be an indication of a mini-halo transitioning into a radio halo.

The on-source observation time for A3558 was only $\sim$2 hours. Observing the cluster for a longer time, and at lower frquencies (MeerKAT's UHF band), might result in improved radio images. This would enable us to disentangle the point source emission from the mini-halo emission. However, the emission we recover extends beyond the BCG, hence, there is a definite indication of extended emission. The faint mini-halo emission was undetectable in sub-band images, hence, we were unable to carry out spectral index studies.

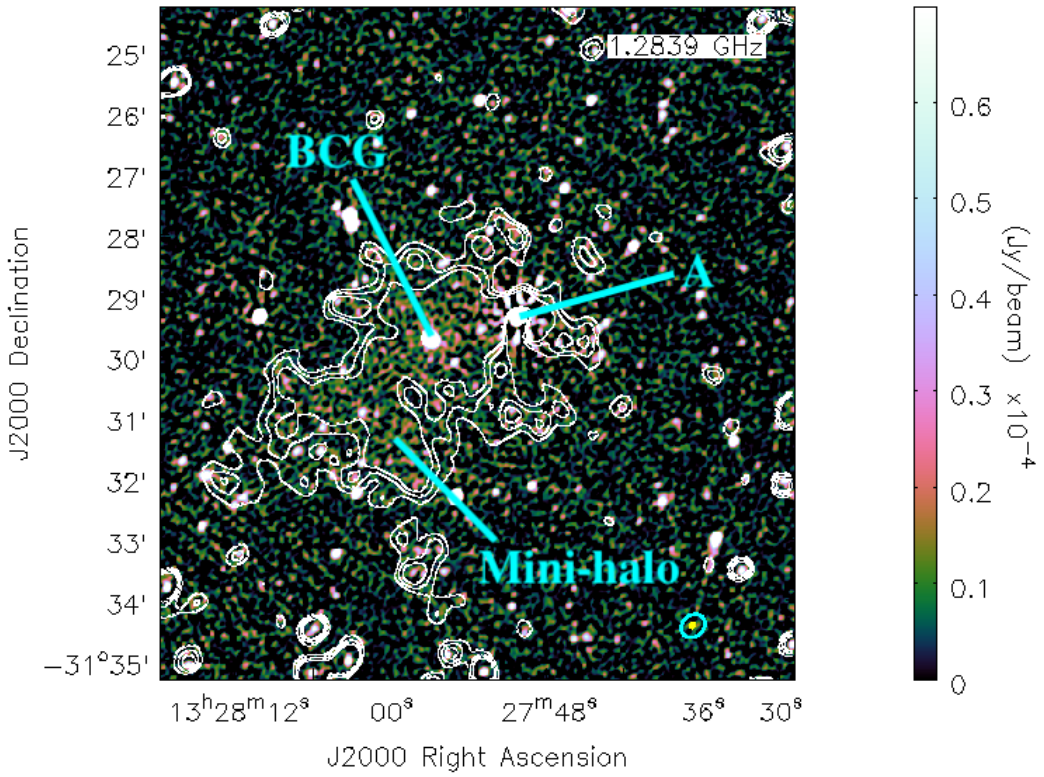

/

Figure 3.16: Full resolution MeerKAT 1.28 GHz image of A3558. The diffuse mini-halo feature is labelled, along with the BCG. Contours are from the low resolution image, with levels of [-3,3,5,7]$\times\sigma$ where σ = 22.14 μJy/beam. In the lower right corner are the synthesised beams of the full resolution and low resolution images; they are indicated by the filled yellow ellipse and cyan ellipse, respectively.

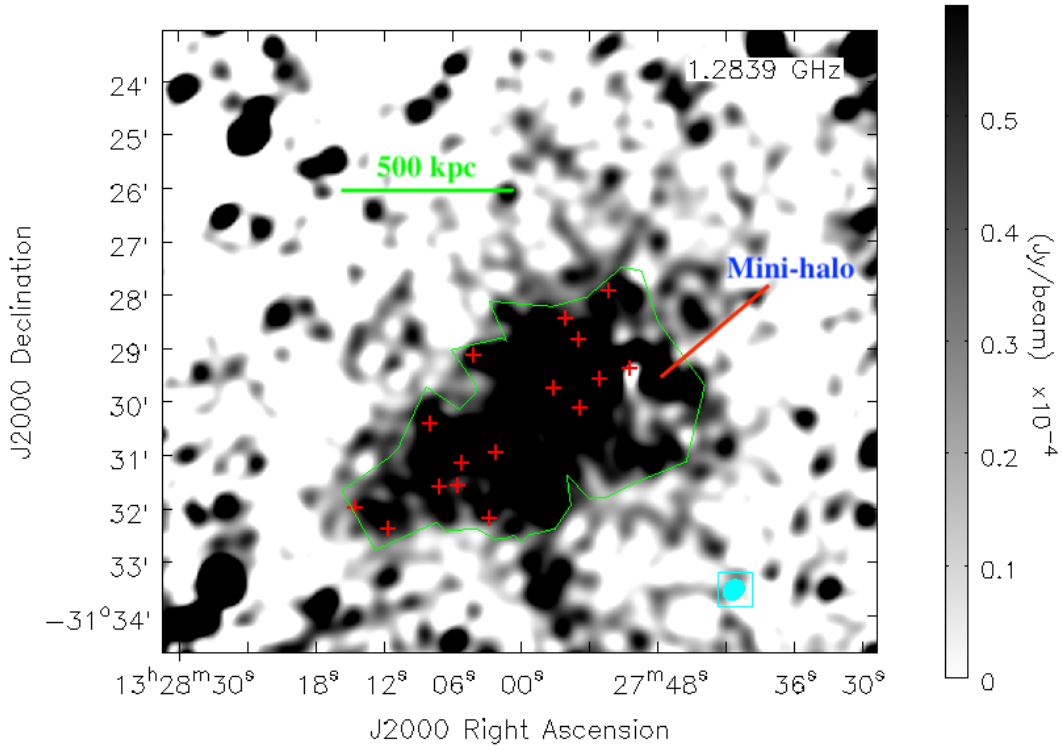

Figure 3.17: Low resolution MeerKAT 1.28 GHz image of A3558. The region used to measure the flux density of the mini-halo is indicated by the polygon. The physical linear scale at the cluster redshift is indicated in the upper left. The rms noise of the low resolution image is 22.14 μJy/beam. The synthesised beam is indicated by the filled cyan ellipse in the lower right.

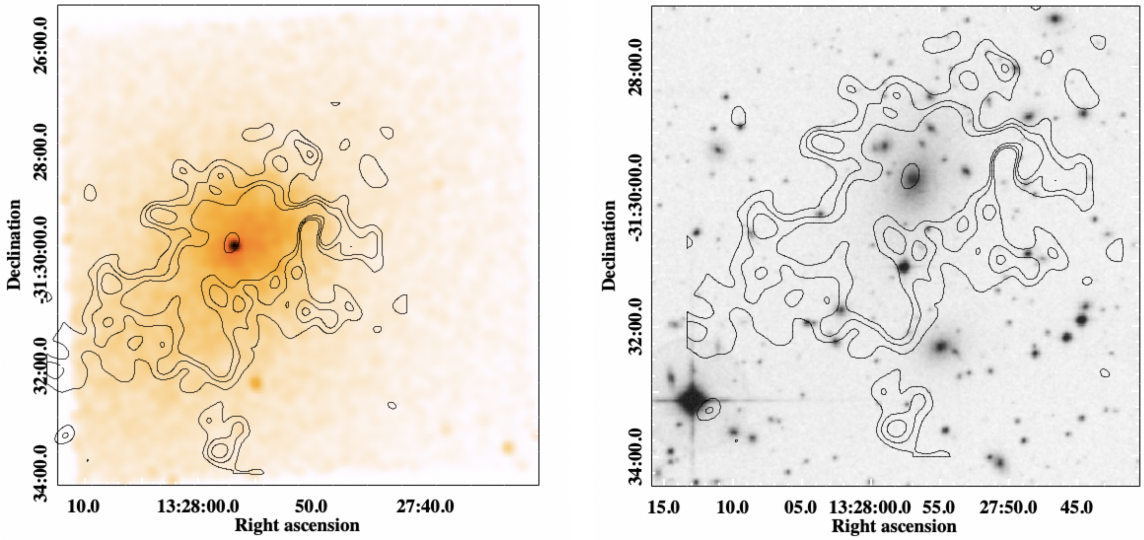

Figure 3.18: Multi-wavelength images of A3558 with contours from MeerKAT 1.28 GHz low resolution image. The contour levels are $\sigma \times [3,5,7]$, where σ is 22.14 μJy/beam. *Left:* Archival *Chandra* X-ray image of A3558. The minni-halo contours overlap with the X-ray brightness distribution and the BCG is also visible. *Right:* Archival optical r-band image from DSS, more recent observations covering the full field were not available. The BCG also has an optical counterpart.

3.8 Summary

The analysis of MeerKAT observations showed how powerful this instrument is for recovering faint diffuse emission in short observation times. It also displayed MeerKAT's ability to produce in-band spectral index maps for clusters with bright diffuse emission. We detected a larger extent of the radio halo and relic in the Bullet cluster. We also detected a decrement feature the peripheral south-eastern region of the radio halo. We also detected larger scales of the radio halos and relics in RXC J1314 in comparison to the most recent JVLA observations. In A3562, we reported a new 'ridge' feature embedded in the radio halo. We also produced spectral index maps for the radio halo. We detected a new min-halo in A3558. We also indicated that longer observations of this cluster will enable to to study the mini-halo more comprehensively. These results are a motivation for using MeerKAT to do larger sample surveys, such as MERGHERS (Knowles et al., 2016a).

CHAPTER 4

CONCLUSION AND OUTLOOK

In this thesis we uniformly selected a sample of 40 clusters from the Atacama Cosmology Telescope's Polarimetric extension (ACTPol). We used data from the Giant Metrewave Radio Telescope (GMRT) to study the faint diffuse emission in galaxy clusters that spanned a lower mass and higher redshift range in comparison to similar studies in literature. We compared our results to the most recently derived mass − radio power scaling relations of radio halos and relics. We also studied faint diffuse emission detected using data from the new generation telescopes with wide bandwidths and high sensitivity, namely, the upgraded GMRT and MeerKAT.

In Chapter 1 we performed a literature review of galaxy clusters highlighting the importance of studying these objects for the understanding of the evolution of large-scale structure. We introduced the different categories of diffuse emission, namely, radio halos, mini-halos, radio relics, and revived fossil plasma. We summarised the different formation theories for each category along with a discussion of which theory is currently supported by observations. We highlighted the current results on scaling relations and spectral index studies of the diffuse emission. Finally, we concluded that there is a need to expand the currently studied parameter space for these objects in order to capture their cosmological evolution.

In Chapter 2 we presented the first part of the thesis, focusing on radio observations of a

homogeneously selected cluster sample with a broad redshift range. We began by introducing radio interferometry basics that are required for reducing low-frequency radio observations. We described the cluster sample we selected using a catalogue from ACTPol. Our mass and redshift cuts of $M_{500c} > 4\times10^{14}$ $M_{\odot}$ resulted in a sample of 40 uniformly selected galaxy clusters. A subset of thirty clusters had archival or newly of observed GMRT software backend (GSB) data and thirteen had new uGMRT wideband backend (GWB) observations. We began by reducing the GSB data for all thirty clusters. The radio analysis we carried out revealed that eight of the thirty clusters hosted diffuse emissions. The diffuse emission in five clusters had been previously reported in the literature. We reported a newly detected radio halo and revived fossil plasma in ACT-CL J0137.4−0827, a radio relic in ACT-CL J2128.4+0135, and a candidate relic in ACT-CL J0022.2−0036.

The occurrence fraction in our sample is 13.3% for radio halos, 6.7% for mini-halos, 3.3% for revived fossil plasma, and 3.3% (6.7%) for radio relics excluding (including) candidate emission. The overall occurrence fraction was found to be 26.7% (30.0 %) including (excluding) candidate emission. For radio halos, we found that three of the four radio halos in our sample were below the $P_{1.4\mathrm{GHz}} - M_{500}$ correlation line. They were found to be in a region populated by ultra-steep spectrum radio halos even though they had flatter spectral indices. We concluded that this result provides a motivation to study larger samples spanning a wider mass and redshift range in order to derive scaling relations that capture the behaviour of these sources even at higher redshifts.

For the systems with GWB data we investigated several reduction software, with the data presenting a challenge due to direction dependent effects and RFI. The best results came from the experimental wideband SPAM. We prioritised the GWB data reduction for ACT-CL J0034.4+0225, ACT-CL J0137.4−0827, and ACT-CL J2128.4+0135 which had detections in the GSB data. In all cases, the GSB detection was observed with greater SNR in the GWB data. Future work on the analysis procedure for the wide-band, wide-field GWB data will yield further insights into the clusters observed with uGMRT. After the analysis of all the GWB data we will derive upper limits for the clusters with non-detections and plot the scaling relation for the full cluster sample that includes detections and non-detections. The clusters with newly detected emission will be studied at multiple wavelengths, including X-ray and optical, in order to undertake dynamical

studies and understand the merger geometry and history.

In Chapter 3 we presented the second thesis project, namely the processing and analysis of new MeerKAT data on four clusters with known or suspected diffuse cluster emission, namely, the Bullet cluster, RXC J1314.4−2515, Abell 3562, and Abell 3558. We used the OXKAT pipeline to reduce the data and the BRATS software to produce spectral index maps. In the Bullet cluster we observed a new decrement feature in the radio halo. The radio halo and relics we recovered in RXC J1314.4−2515 are similar in morphology to those reported in the literature. However MeerKAT's sensitivity enabled us to capture a larger extent of the diffuse emission. We confirmed the detection of a radio halo in Abell 3562. We also reported the detection of a radio 'ridge' feature embedded in the radio halo. We concluded that X-ray studies are needed to confirm if the ridge coincided with a shock region. Finally, we detected a new mini-halo in Abell 3558. The mini-halo has an extent of 390 kpc $\times$ 199 kpc and is centred on the radio-loud cluster BCG.

The sensitivity of MeerKAT at L-band enabled us to produce in-band spectral index maps for the diffuse emission in Bullet cluster, RXC J1314.4−2515, and Abell 3562. The spectral index map of the radio halo in the Bullet cluster indicates radial spectral steepening towards the cluster outskirts. The spectral index map of Abell 3562 indicates that the radio halo and ridge have similar spectral index distribution. This indicates that the ridge feature is related to the radio halo. The spectral index maps of the relics in the Bullet cluster and RXC J1314.4−2515 indicate a spectral steepening towards the cluster center. The MeerKAT data analysis demonstrated the power of this instrument for studying faint diffuse emission. Hence, MeerKAT observations will be ideal for studying diffuse emission larger samples with low mass and high redshift clusters. I will extend my work here through my involvement in the MeerKAT Extended Relics, Giant Halos, and Extragalactic Radio Sources (MERGHERS) survey, which aims to observe $\sim$200 uniformly selected SZ clusters. This study will be able to produce statistically significant results on the scaling relations for higher redshift and lower mass clusters. The results of these studies will be essential for distinguishing and refining existing formation theories of diffuse radio emission.

APPENDIX A

FULL FIELD OF VIEW IMAGES FROM THE ACTPOL SAMPLE

We present the full resolution images of a subset of the clusters which had archival or new observations. In Section A.1 we present all the images that were reduced using the SPAM narrowband pipeline and in Section A.2 we present the images of the three clusters that were reduced using the experimental SPAM wideband pipeline (See Chapter 1). **Some of the fields were severely affected by ionospheric effects, poor image synthesis due to sparse uv coverage and residual RFI. This resulted in images with noise levels significantly higher than the theoretical scaling laws.**

A.1 GSB primary beam-corrected full resolution radio images

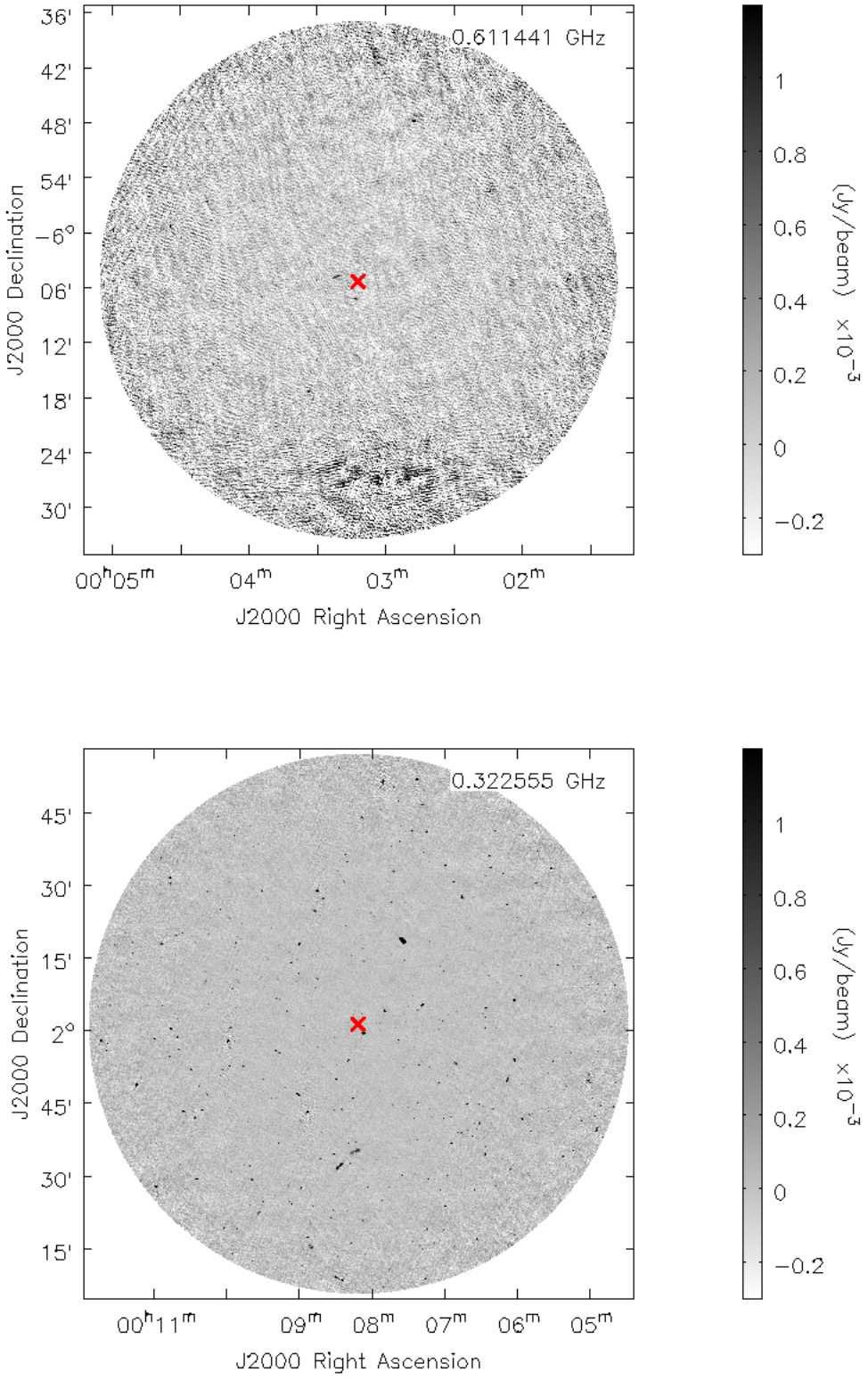

Figure A.1: full field of view GSB primary beam corrected images. The red crosses indicates the ACT SZ peak. *Top:* ACT-CL J0003.1−0605 is at redshift z = 0.233. The rms noise of the image is 193.2 μJy/beam, the poor uv coverage and bright off-axis source resulted in a significant increase of the noise levels. *Bottom:* ACT-CL J0008.1+0201 is at redshift z = 0.366. The rms noise of the image is 46.4 μJy/beam.

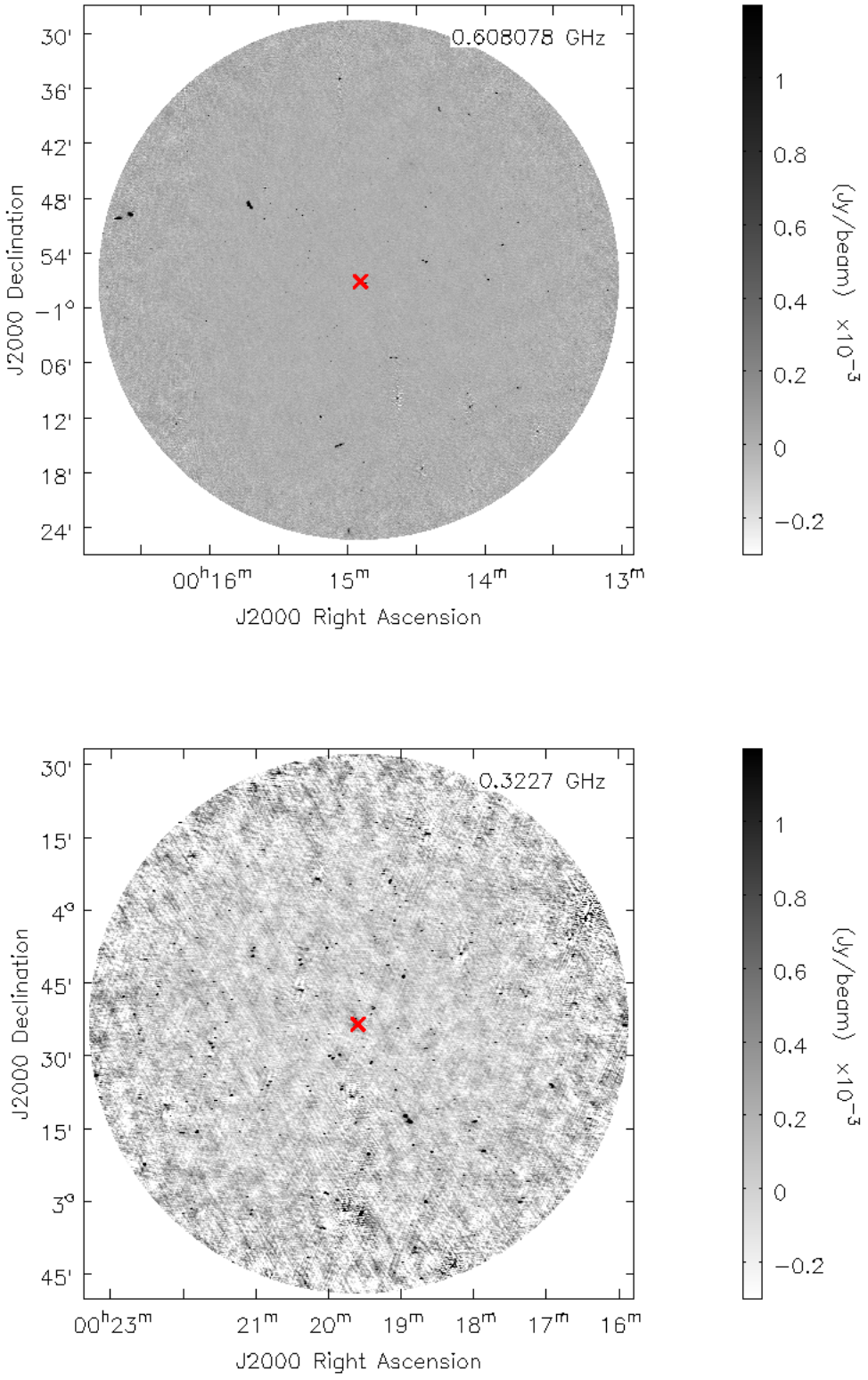

Figure A.2: full field of view GSB primary beam corrected images. The red crosses indicates the ACT SZ peak. *Top:* ACT-CL J0014.8−0057 is at redshift $z = 0.533$. The rms noise of the image is 25.2 μJy/beam. *Bottom:* ACT-CL J0019.6+0336 is at redshift $z = 0.269$. The rms noise of the image is 144.0 μJy/beam. This field was heavily affected by ionospheric effecrs around the bright sources, as a result the noise levels are higher that the theoretical scaling laws.

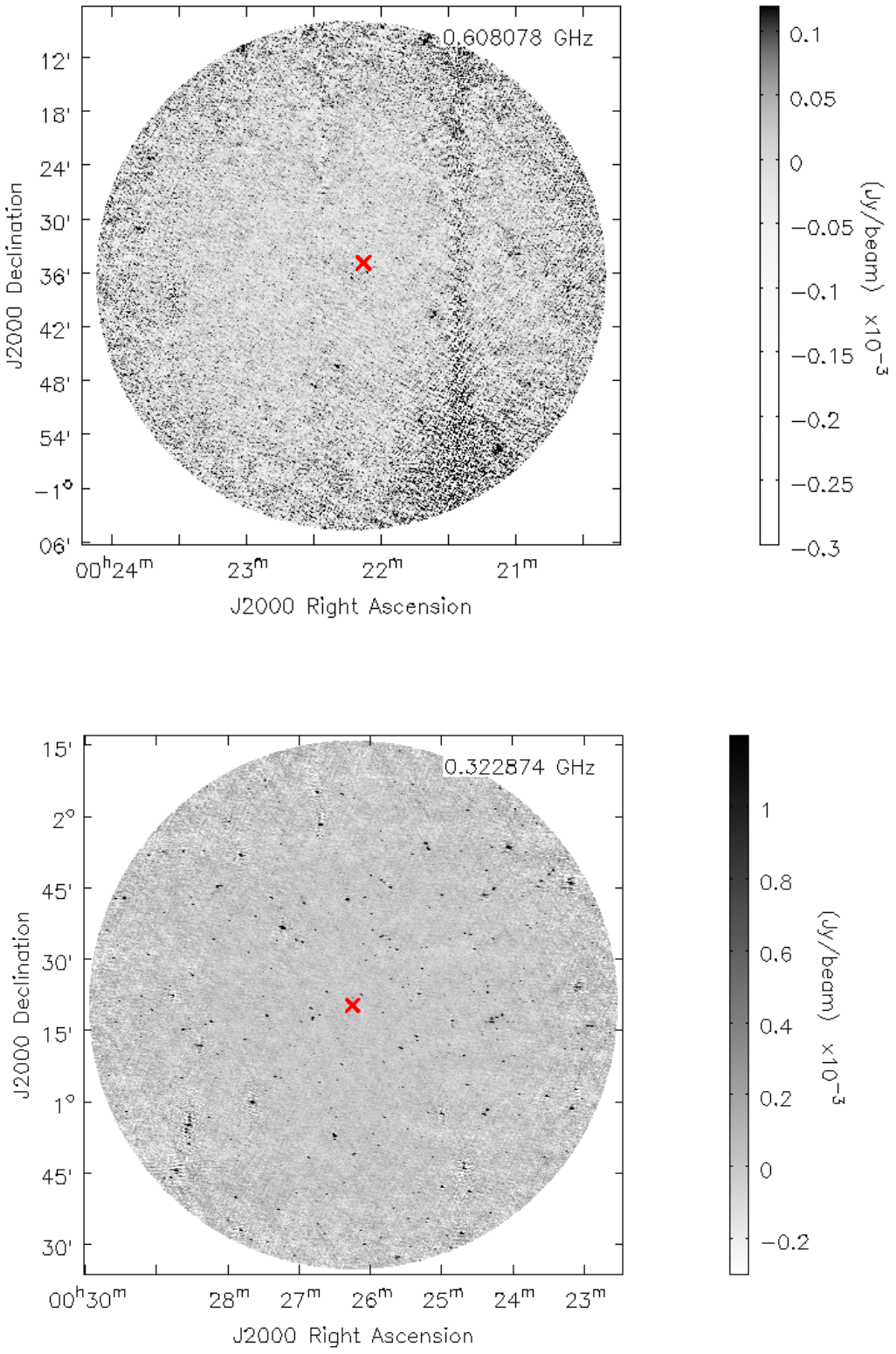

Figure A.3: full field of view GSB primary beam corrected images. The red crosses indicates the ACT SZ peak. *Top:* ACT-CL J0022.2−0036 is at redshift z = 0.805. The rms noise of the image is 33.4 μJy/beam. *Bottom:* ACT-CL J0026.2+0120 is at redshift z = 0.64. The rms noise of the image is 60.8 μJy/beam.

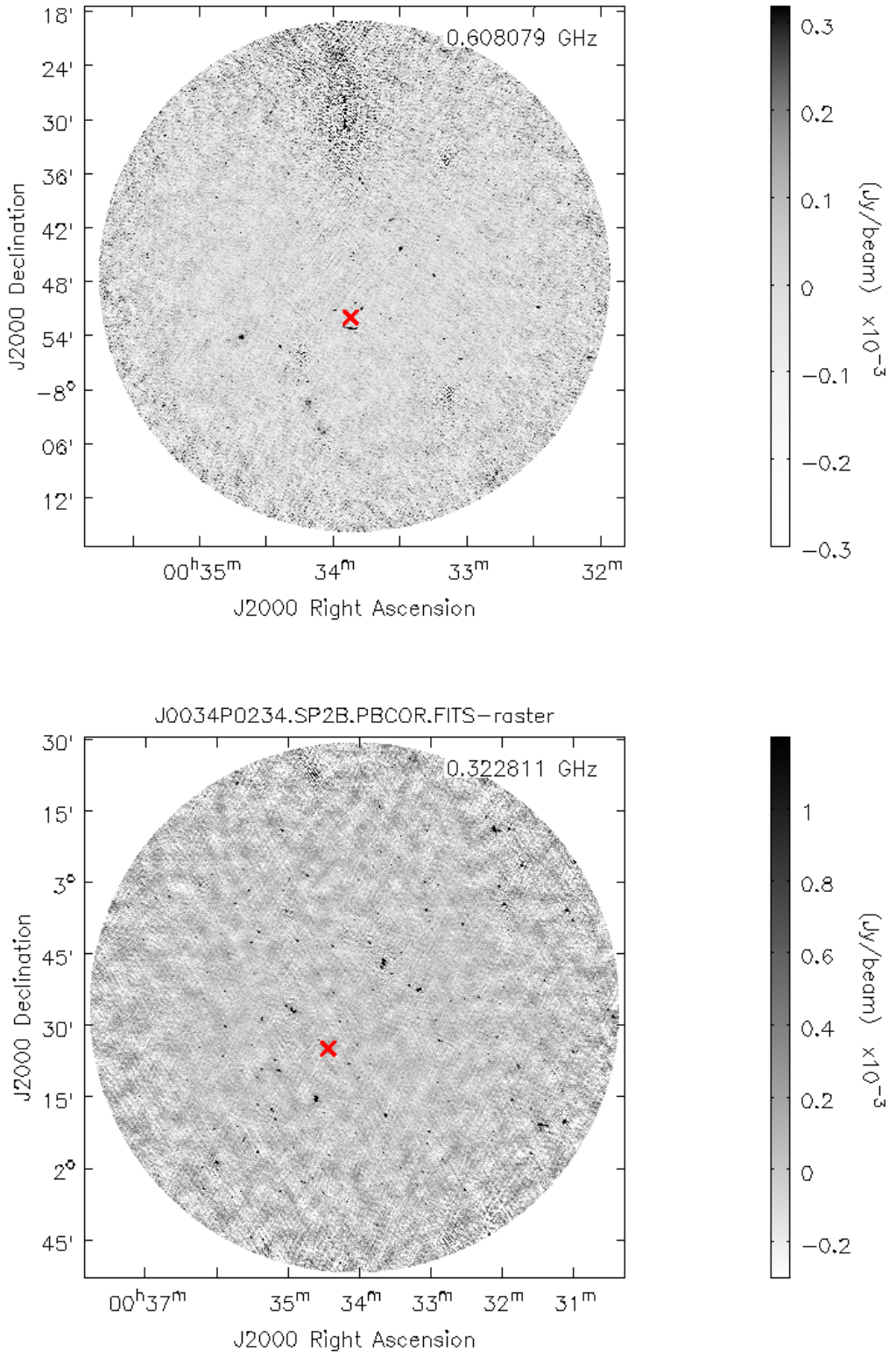

Figure A.4: full field of view GSB primary beam corrected images. The red crosses indicates the ACT SZ peak. *Top:* ACT-CL J0033.8−0751 is at redshift $z = 0.305$. The rms noise of the image is 63.5 μJy/beam. *Bottom:* ACT-CL J0034.4+0225 is at redshift $z = 0.382$. The rms noise of the image is 75.8 μJy/beam.

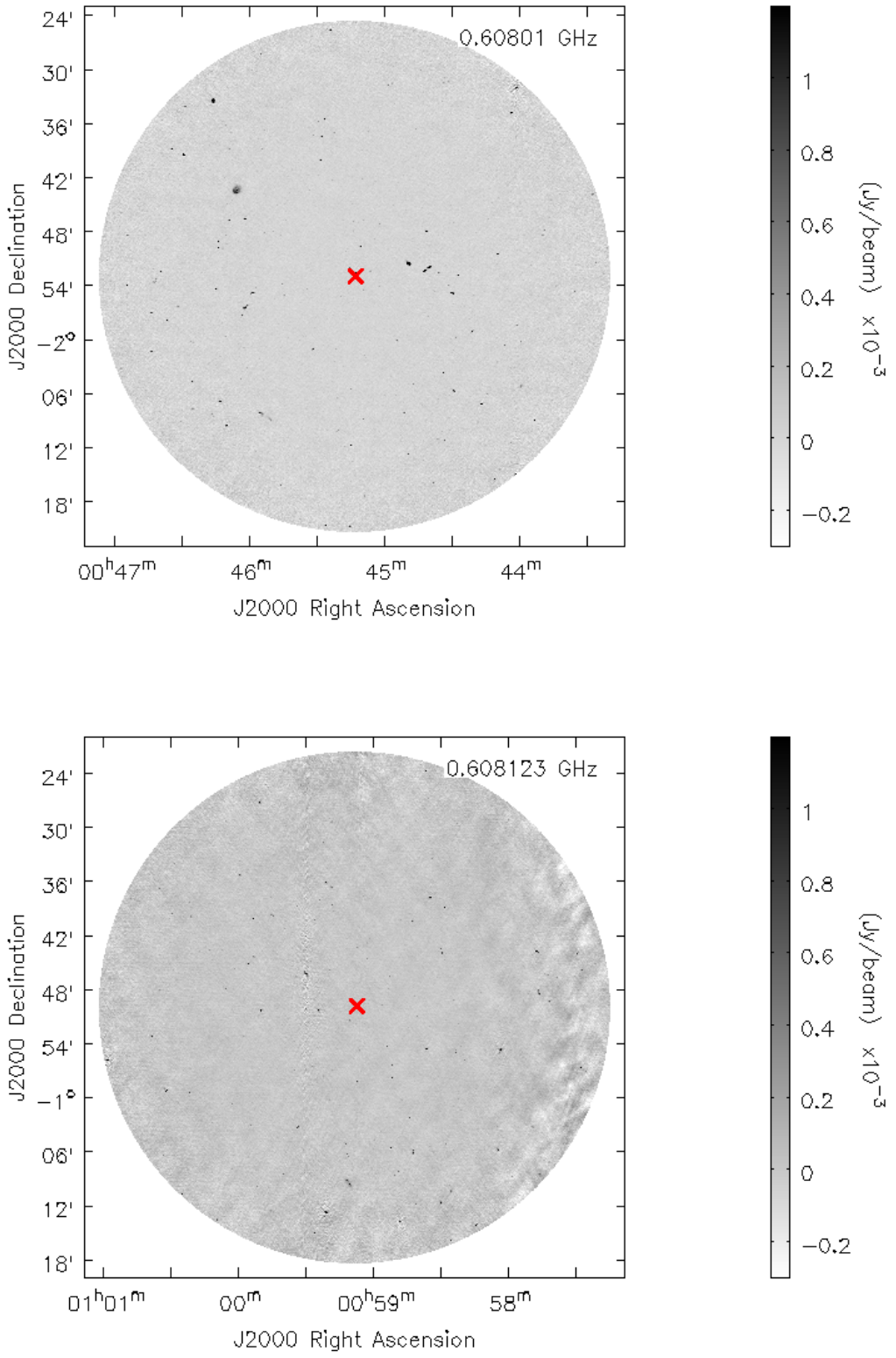

Figure A.5: full field of view GSB primary beam corrected images. The red crosses indicates the ACT SZ peak. *Top:* ACT-CL J0045.2−0152 is at redshift $z = 0.548$. The rms noise of the image is 27.0 μJy/beam. *Bottom:* ACT-CL J0059−0049 is at redshift $z = 0.787$. The rms noise of the image is 46.1 μJy/beam.

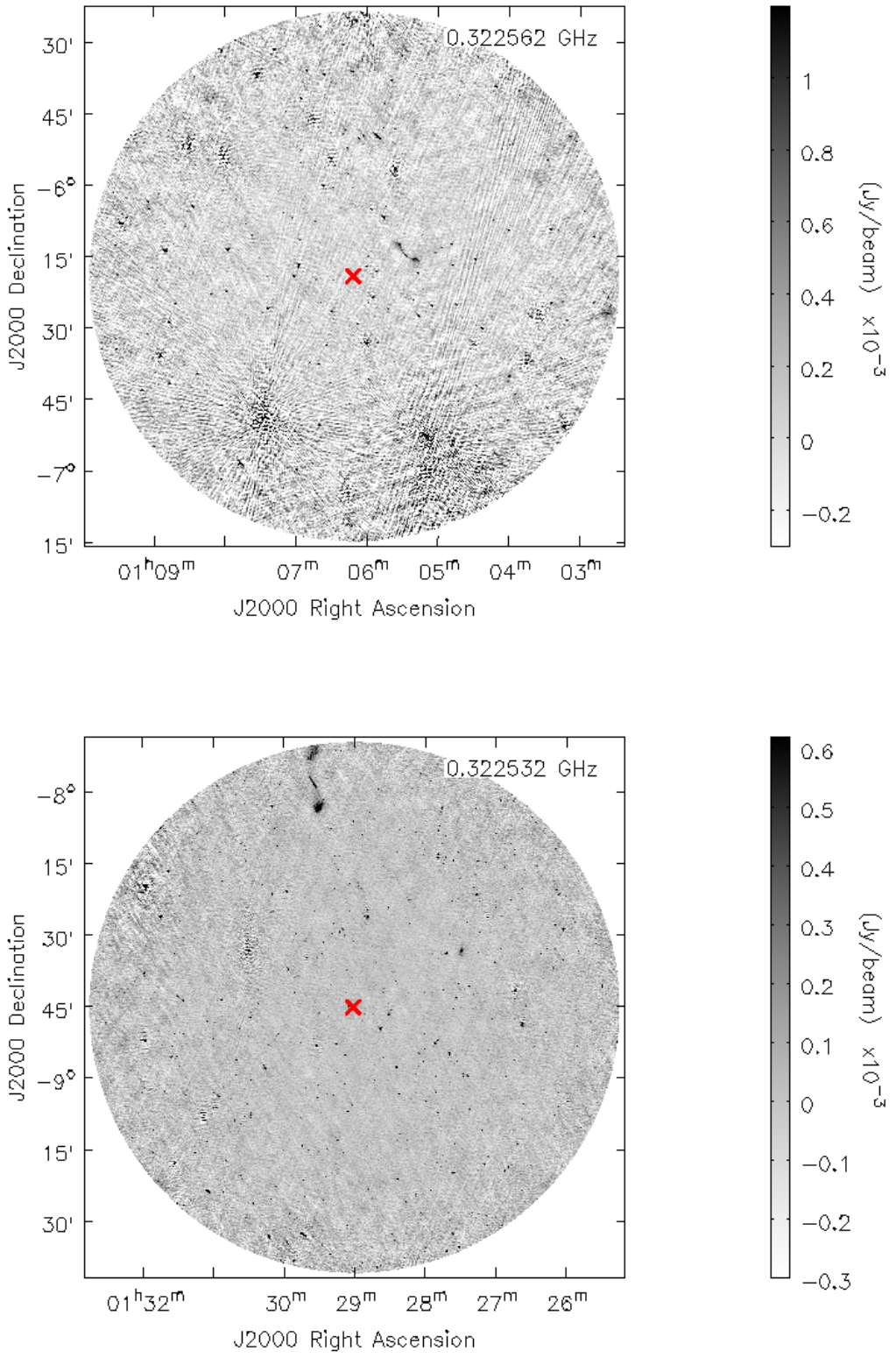

Figure A.6: full field of view GSB primary beam corrected images. The red crosses indicates the ACT SZ peak. *Top:* ACT-CL J0106.1−0619 is at redshift $z = 0.50$. The rms noise of the image is 142.3 μJy/beam. The off-axis bright sources are heavily affected by ionospheric effects causing higher noise levels. *Bottom:* ACT-CL J0129.0−0845 is at redshift $z = 0.358$. The rms noise of the image is 47.9 μJy/beam.

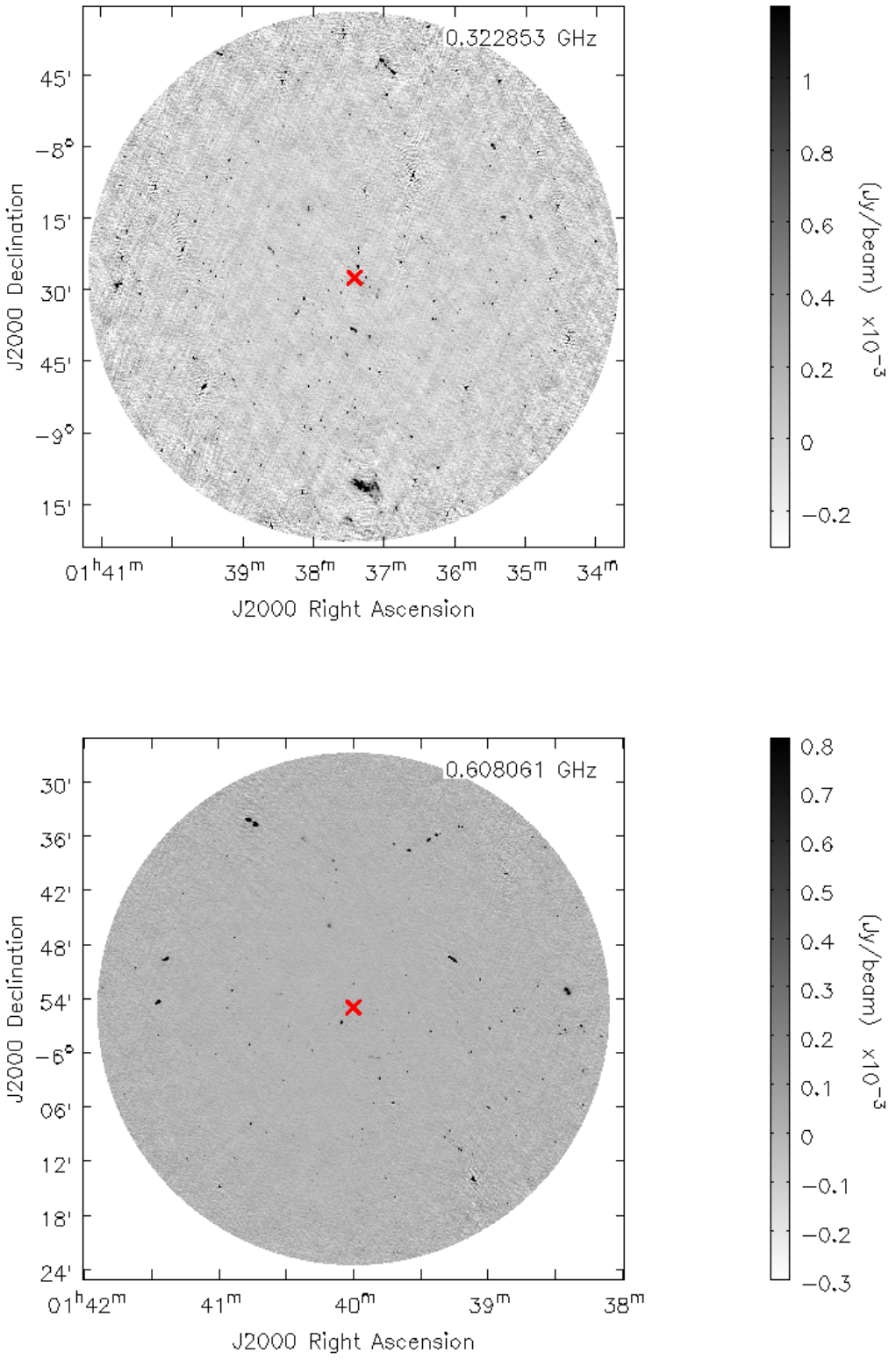

Figure A.7: full field of view GSB primary beam corrected images. The red crosses indicates the ACT SZ peak. *Top:* ACT-CL J0137.4−0827 is at redshift $z = 0.568$. The rms noise of the image is 74.5 μJy/beam. *Bottom:* ACT-CL J0140.0−0554 is at redshift $z = 0.454$. The rms noise of the image is 22.3 μJy/beam.

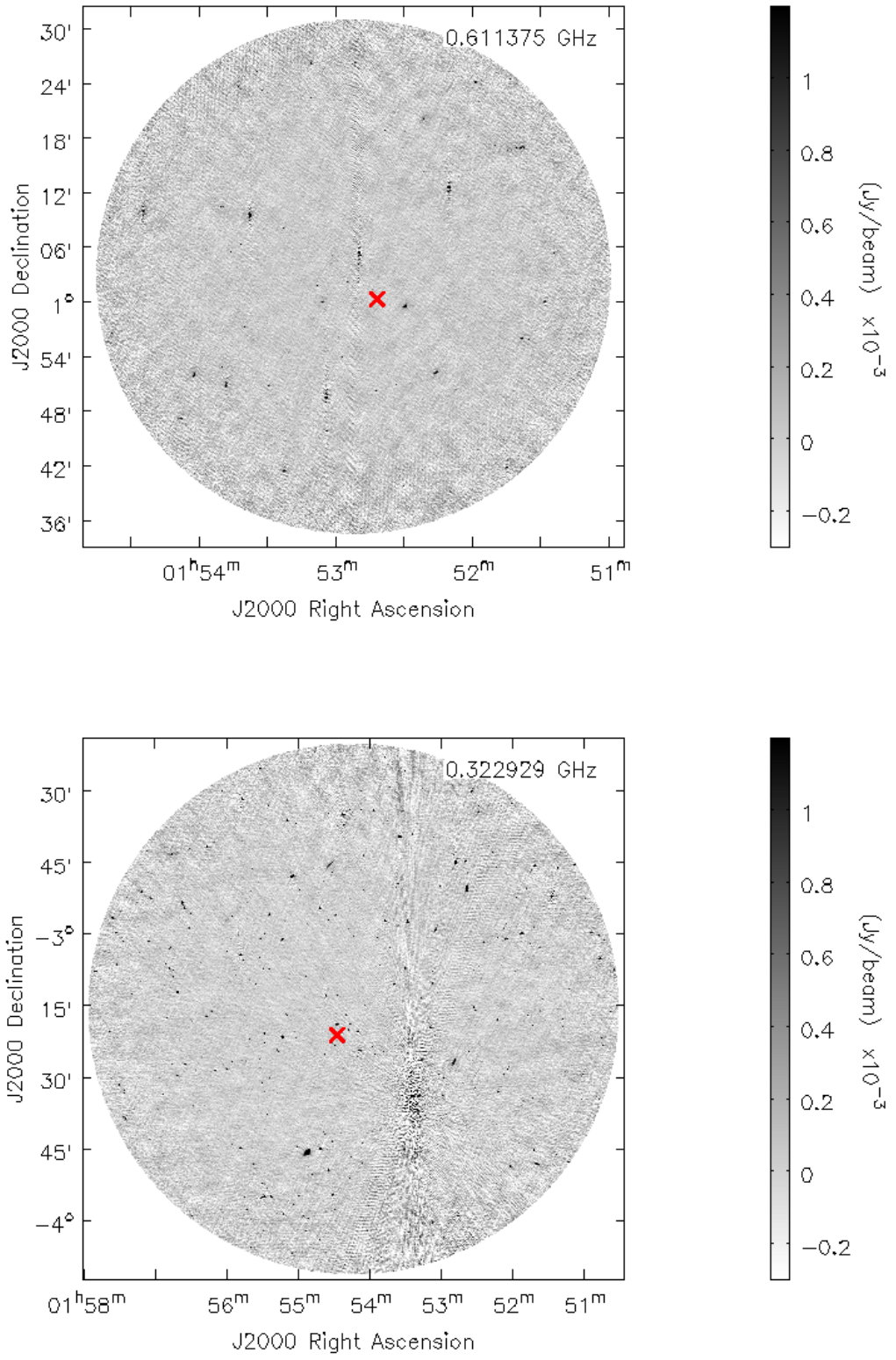

Figure A.8: full field of view GSB primary beam corrected images. The red crosses indicates the ACT SZ peak. *Top:* ACT-CL J0152.6+0100 is at redshift $z = 0.229$. The rms noise of the image is 89.9 μJy/beam. *Bottom:* ACT-CL J0154.4−0321 is at redshift $z = 0.444$. The rms noise of the image is 84.6 μJy/beam.

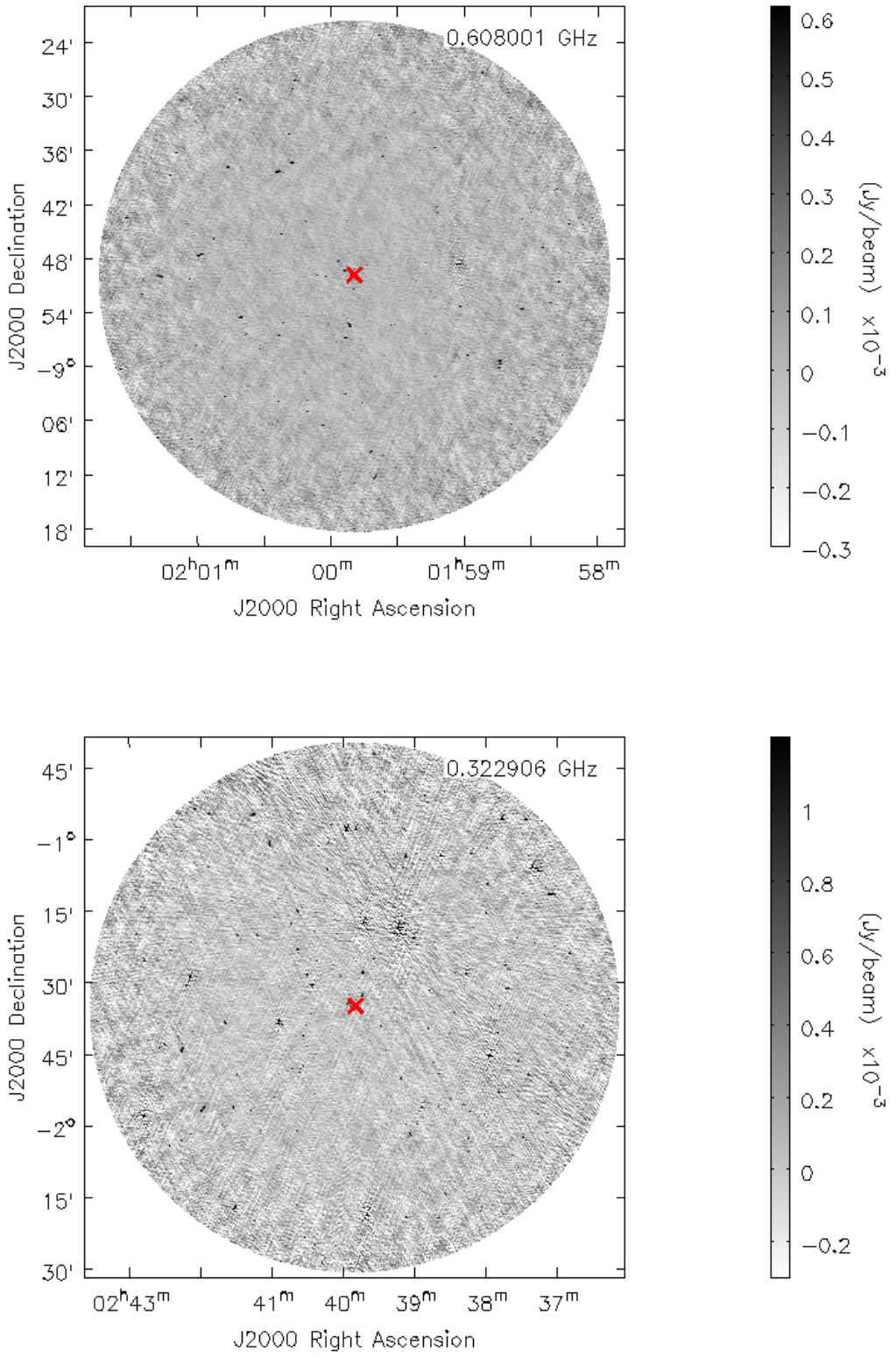

Figure A.9: full field of view GSB primary beam corrected images. The red crosses indicates the ACT SZ peak. *Top:* ACT-CL J0159.8−0849 is at redshift $z = 0.408$. The rms noise of the image is 48.7 μJy/beam. *Bottom:* ACT-CL J0239.8−0134 is at redshift $z = 0.375$. The rms noise of the image is 123.2 μJy/beam.

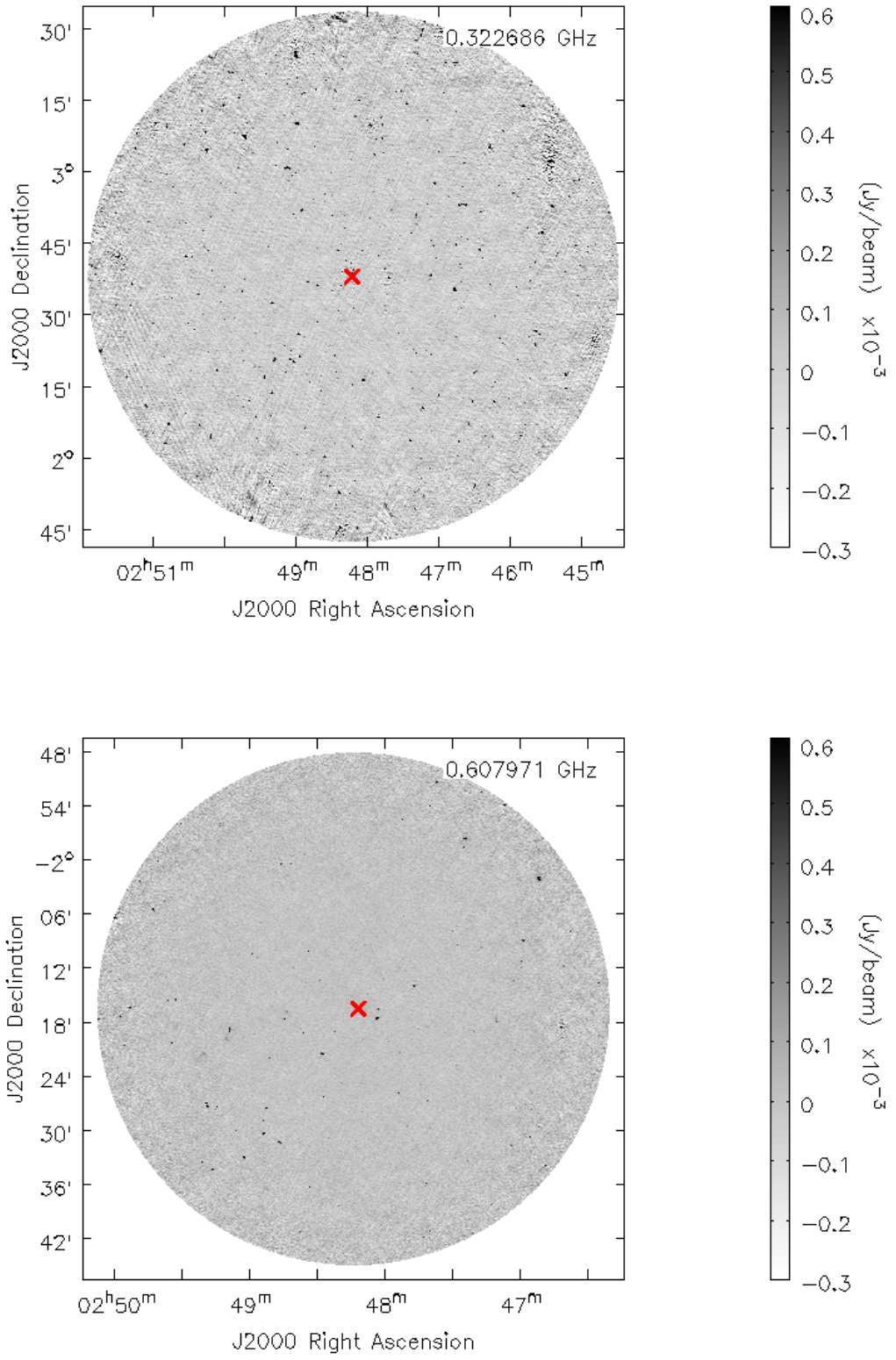

Figure A.10: full field of view GSB primary beam corrected images. The red crosses indicates the ACT SZ peak. *Top:* ACT-CL J0248.1+0238 is at redshift $z = 0.556$. The rms noise of the image is 57.1 μJy/beam. *Bottom:* ACT-CL J0248.1−0216 is at redshift $z = 0.238$. The rms noise of the image is 32.4 μJy/beam.

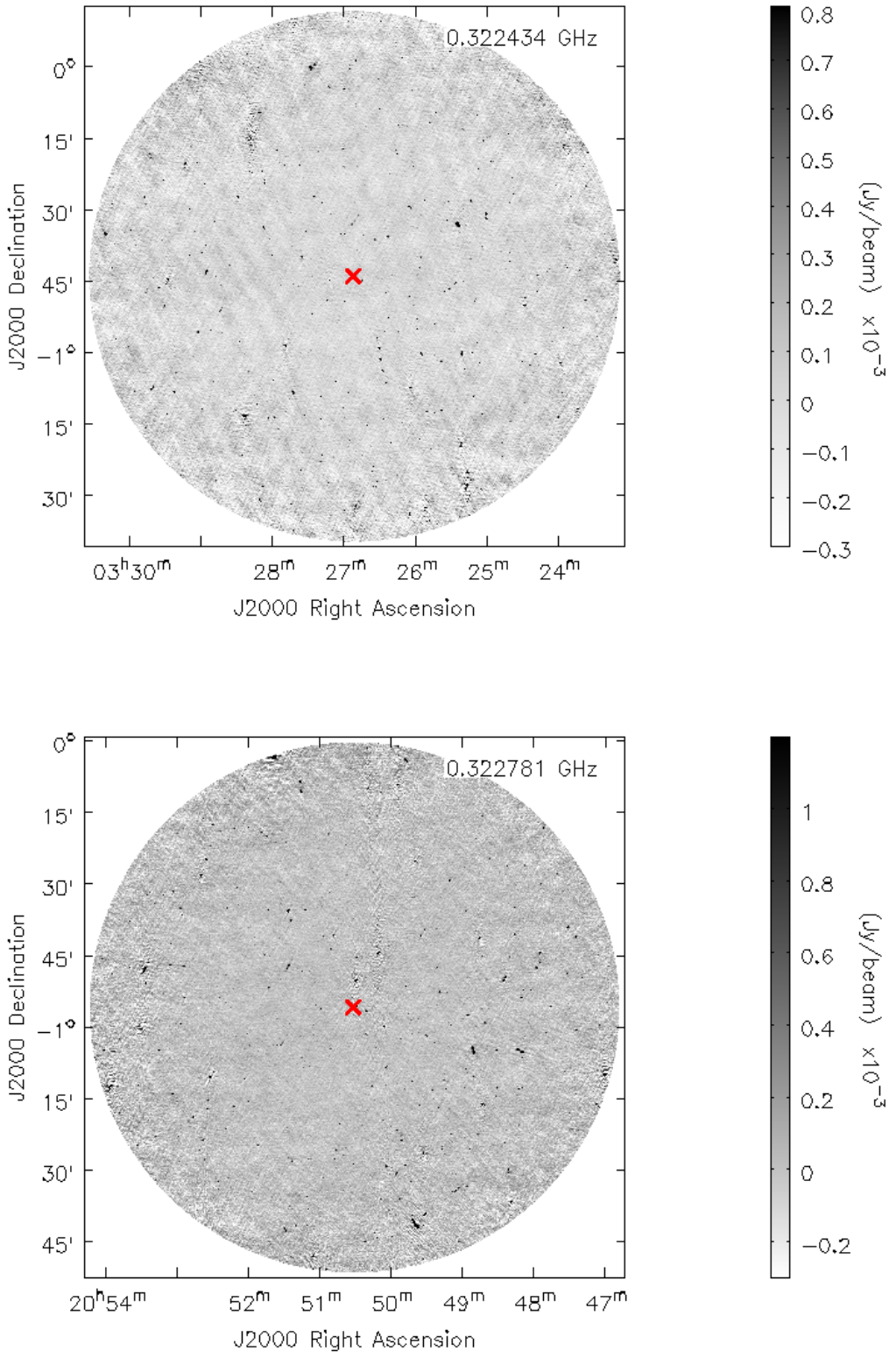

Figure A.11: full field of view GSB primary beam corrected images. The red crosses indicates the ACT SZ peak. *Top:* ACT-CL J0326.8−0043 is at redshift $z = 0.447$. The rms noise of the image is 69.6 μJy/beam. *Bottom:* ACT-CL J2050.5−0055 is at redshift $z = 0.623$. The rms noise of the image is 64.6 μJy/beam.

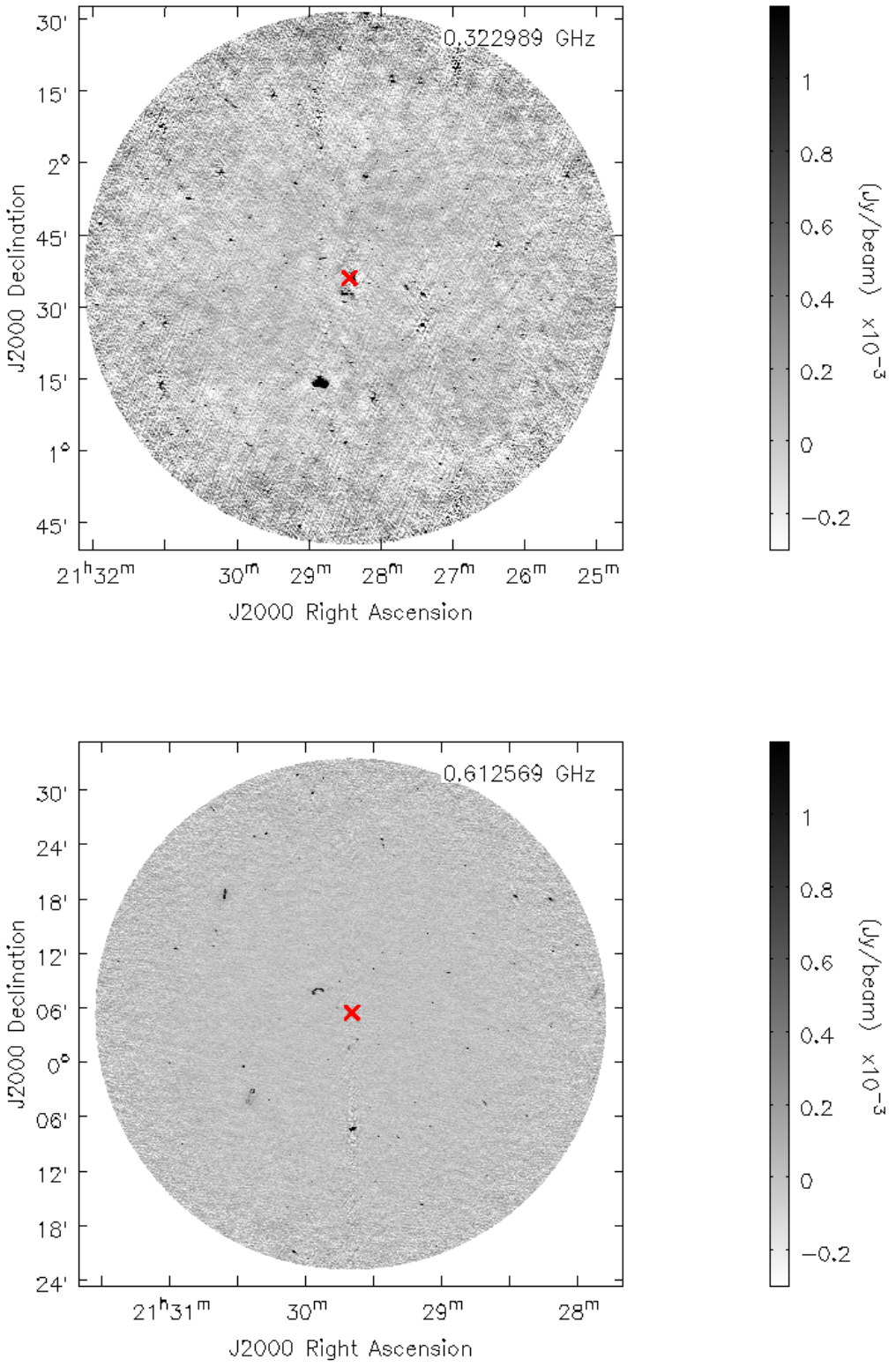

Figure A.12: full field of view GSB primary beam corrected images. The red crosses indicates the ACT SZ peak. *Top:* ACT-CL J2128.4+0135 is at redshift z = 0.386. The rms noise of the image is 134.0 μJy/beam. The higher noise level might be due to the sparse uv coverage which lead to poor image synthesis. *Bottom:* ACT-CL J2129.6+0005 is at redshift z = 0.234. The rms noise of the image is 51.3 μJy/beam.

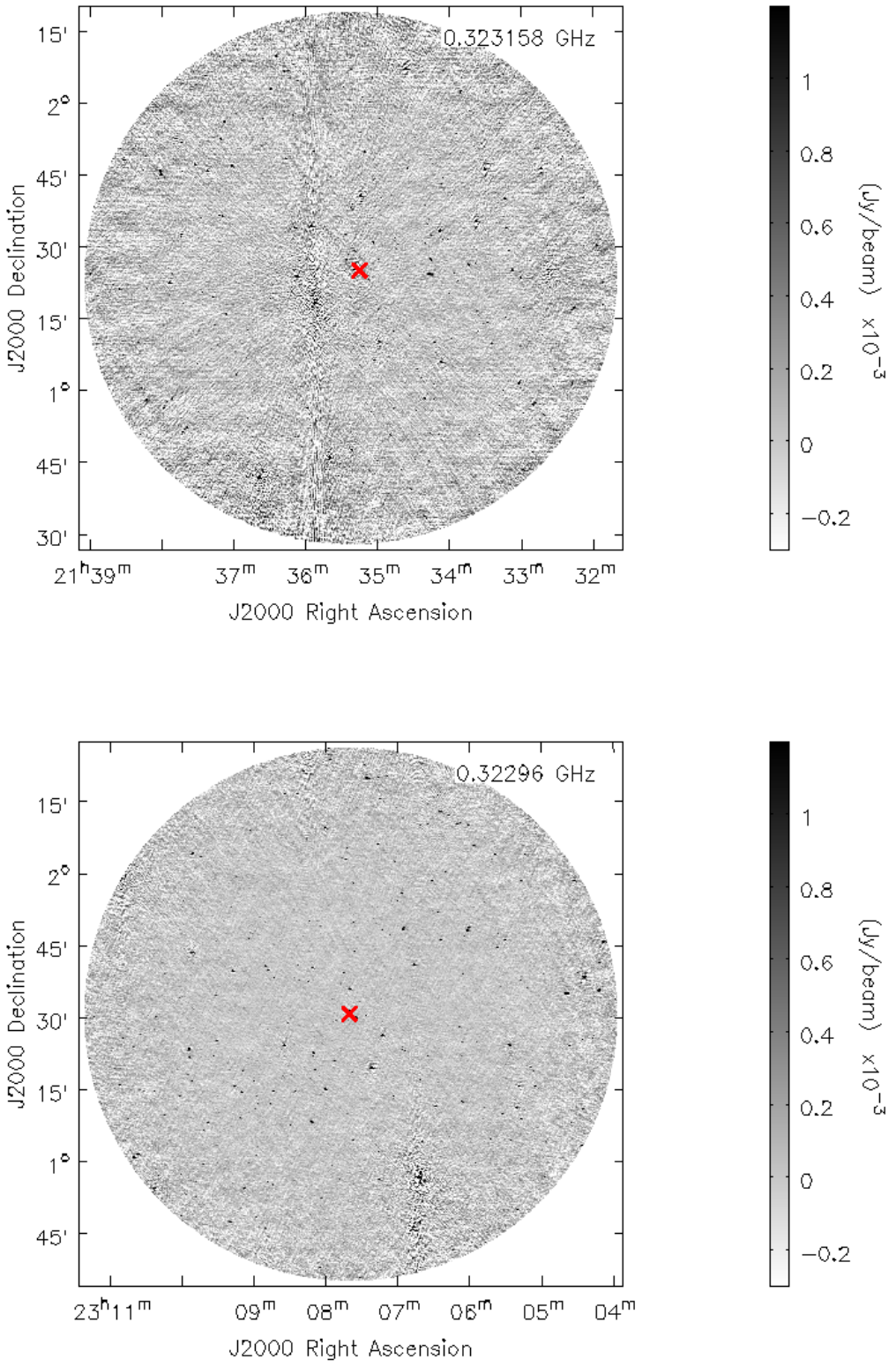

Figure A.13: full field of view GSB primary beam corrected images. The red crosses indicates the ACT SZ peak. *Top:* ACT-CL J2135.2+0125 is at redshift $z = 0.23$. The rms noise of the image is 190.3 μJy/beam. The north-south striping caused by a bright source in the field reduces the image quality and results in high noise levels. *Bottom:* ACT-CL J2307.6+0130 is at redshift $z = 0.389$. The rms noise of the image is 78.7 μJy/beam.

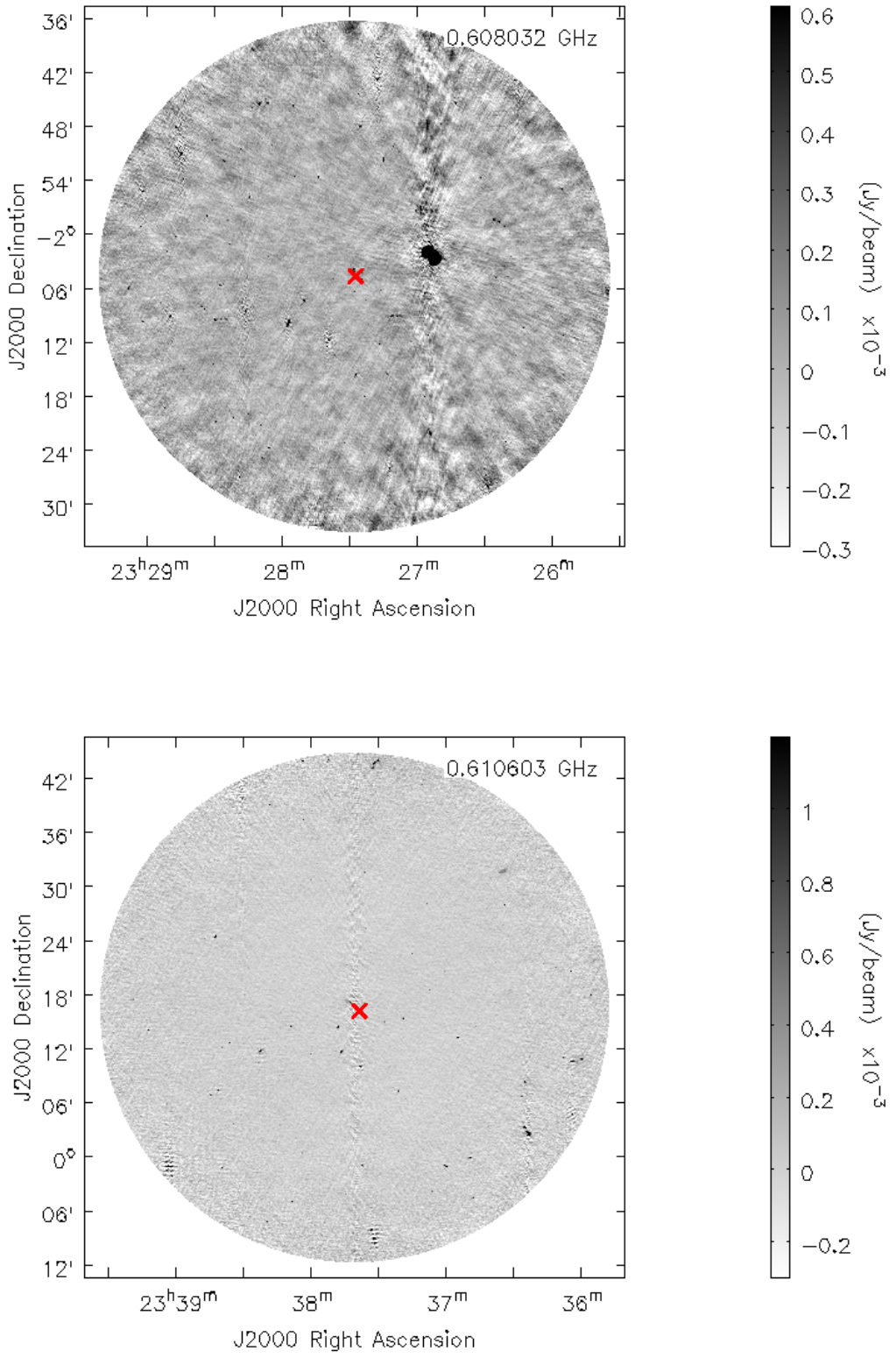

Figure A.14: full field of view GSB primary beam corrected images. The red crosses indicates the ACT SZ peak. *Top:* ACT-CL J2327.4−0204 is at redshift $z = 0.699$. The rms noise of the image is 64.6 μJy/beam. *Bottom:* ACT-CL J2337.6+0016 is at redshift $z = 0.277$. The rms noise of the image is 45.8 μJy/beam.

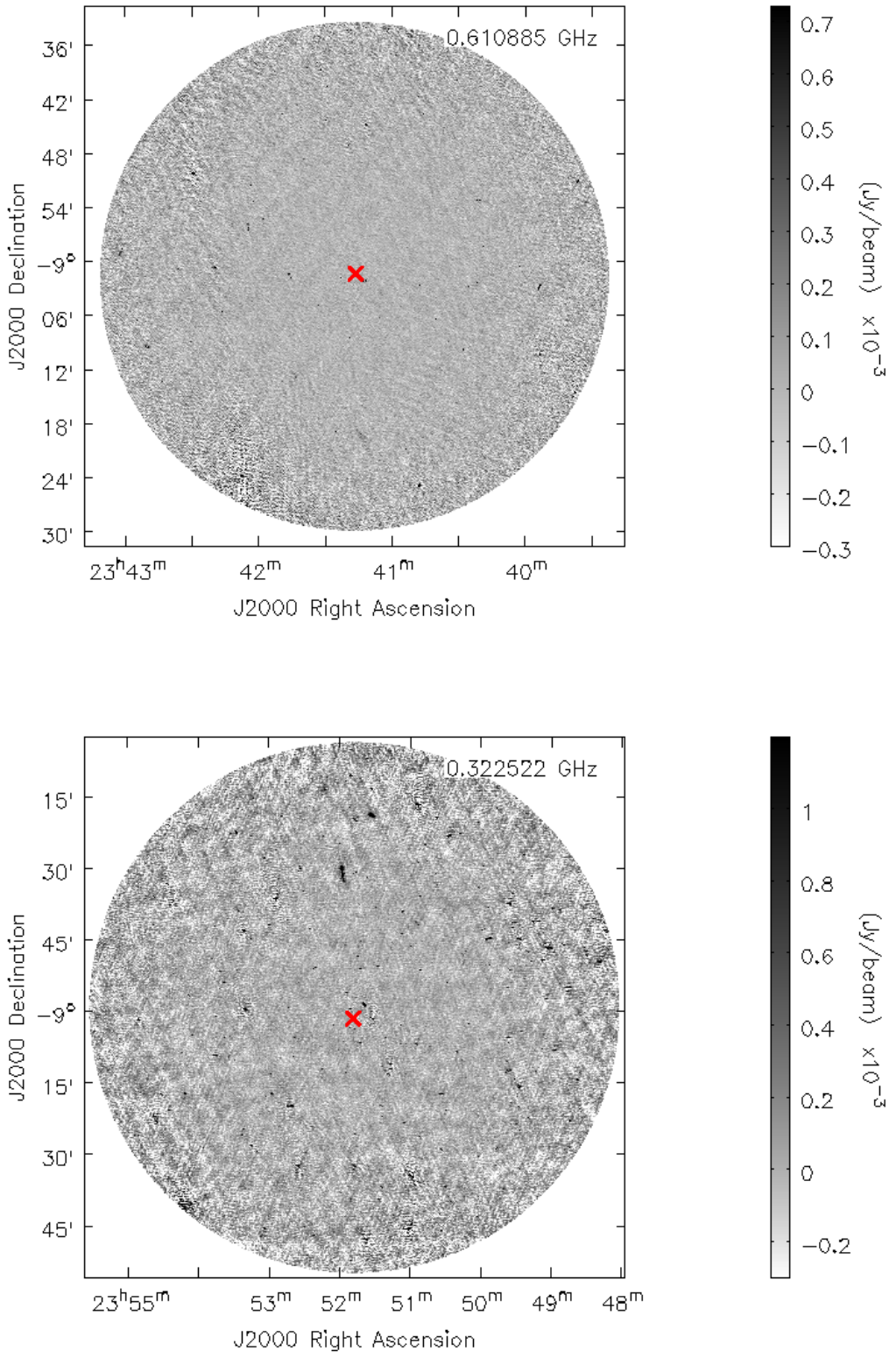

Figure A.15: full field of view GSB primary beam corrected images. The red crosses indicates the ACT SZ peak. *Top:* ACT-CL J2341.2−0901 is at redshift $z = 0.251$. The rms noise of the image is 27.2 μJy/beam. *Bottom:* ACT-CL J2351.7−0859 is at redshift $z = 0.392$. The rms noise of the image is 19.3 μJy/beam.

A.2 GWB full resolution radio images

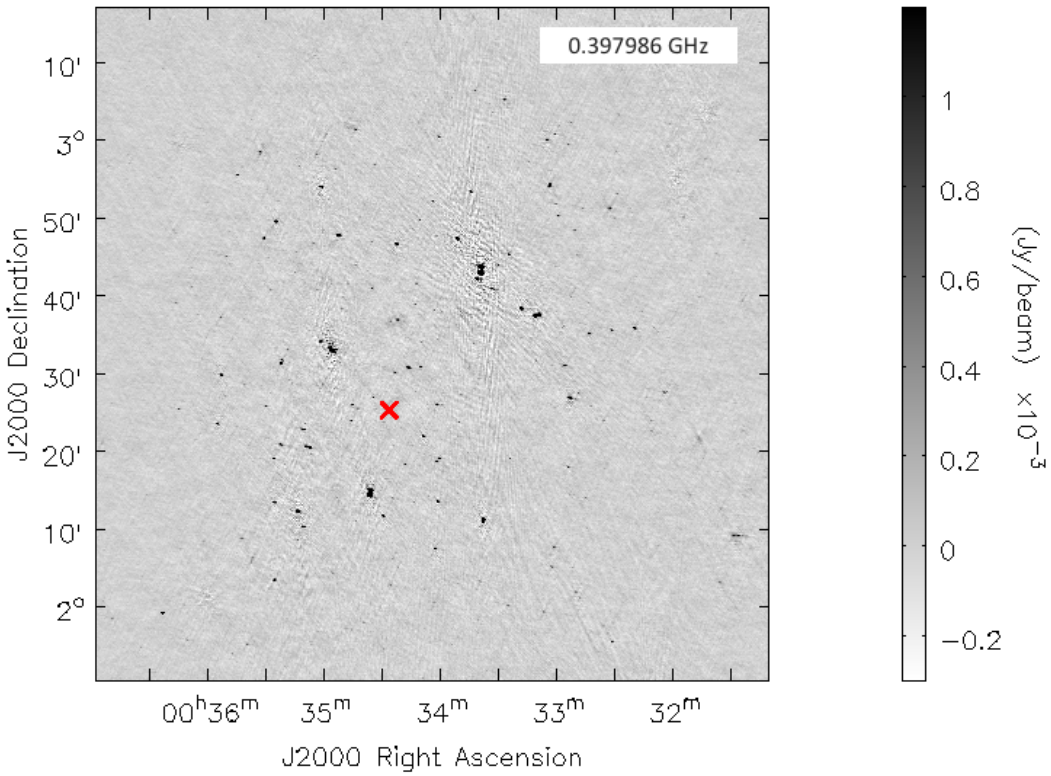

Figure A.16: SPAM-reduced GWB full field of view image of ACT-CL J0034.4+0225 which is at redshift $z = 0.382$. The rms noise of the image is 75.8 μJy/beam. The red crosses indicates the ACT SZ peak.

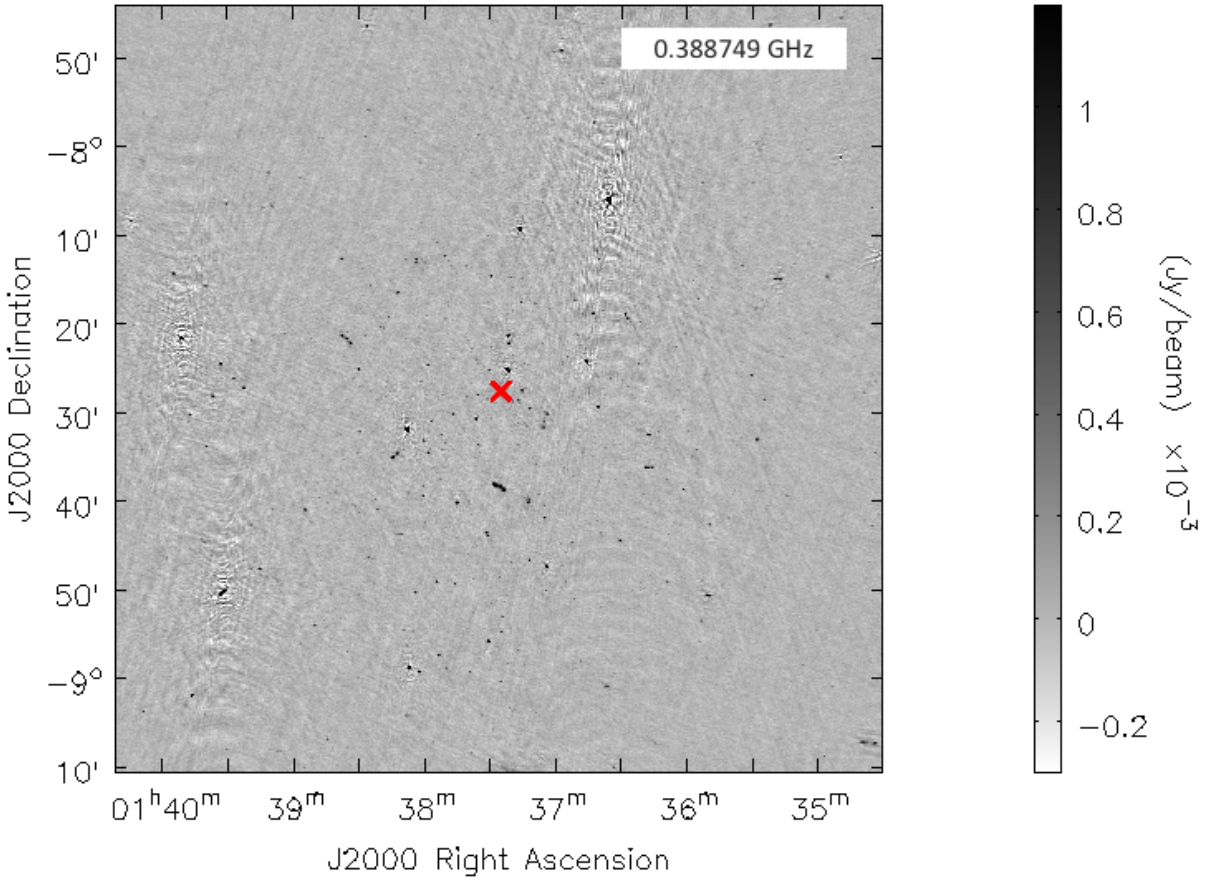

Figure A.17: SPAM-reduced GWB full field of view image of ACT-CL J0137.4−0127 which is at redshift $z = 0.568$. The rms noise of the image is 74.5 μJy/beam. The red crosses indicates the ACT SZ peak.

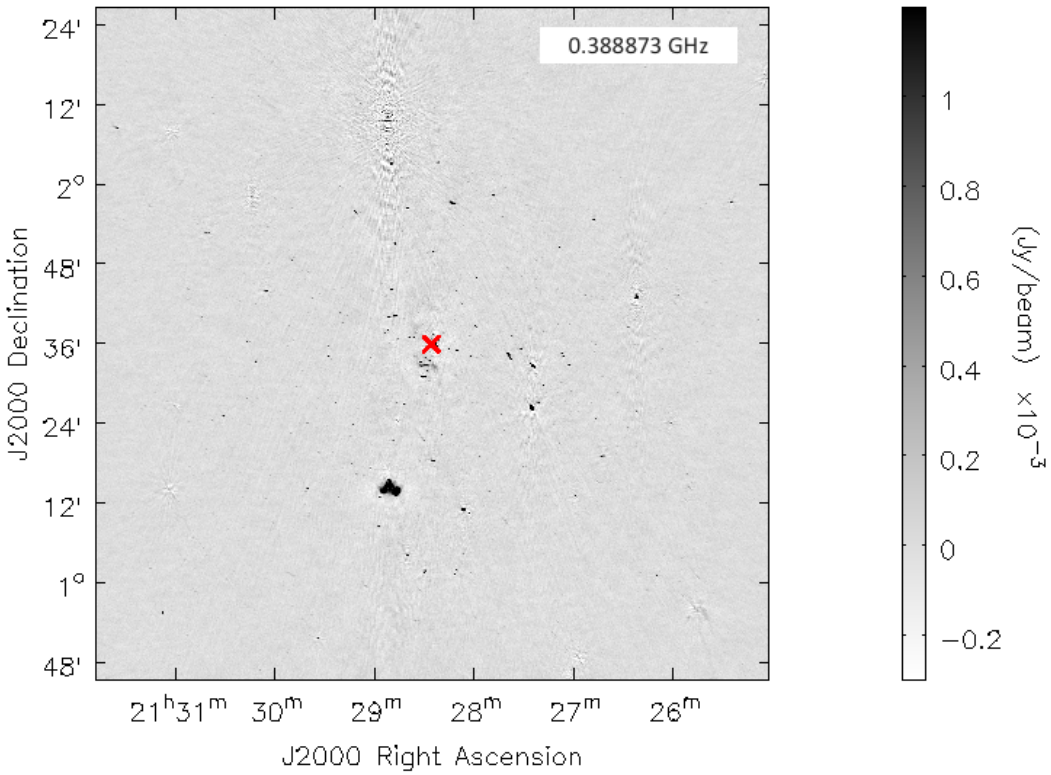

Figure A.18: SPAM-reduced GWB full field of view image of ACT-CL J2128.4+0135 which is at redshift z = 0.386. The rms noise of the image is 134.0 μJy/beam. The red crosses indicates the ACT SZ peak.

APPENDIX B

MEERKAT IMAGES

We present the full resolution images of the clusters that were observed using MeeKAT. The resulting images were reduced using OXKAT

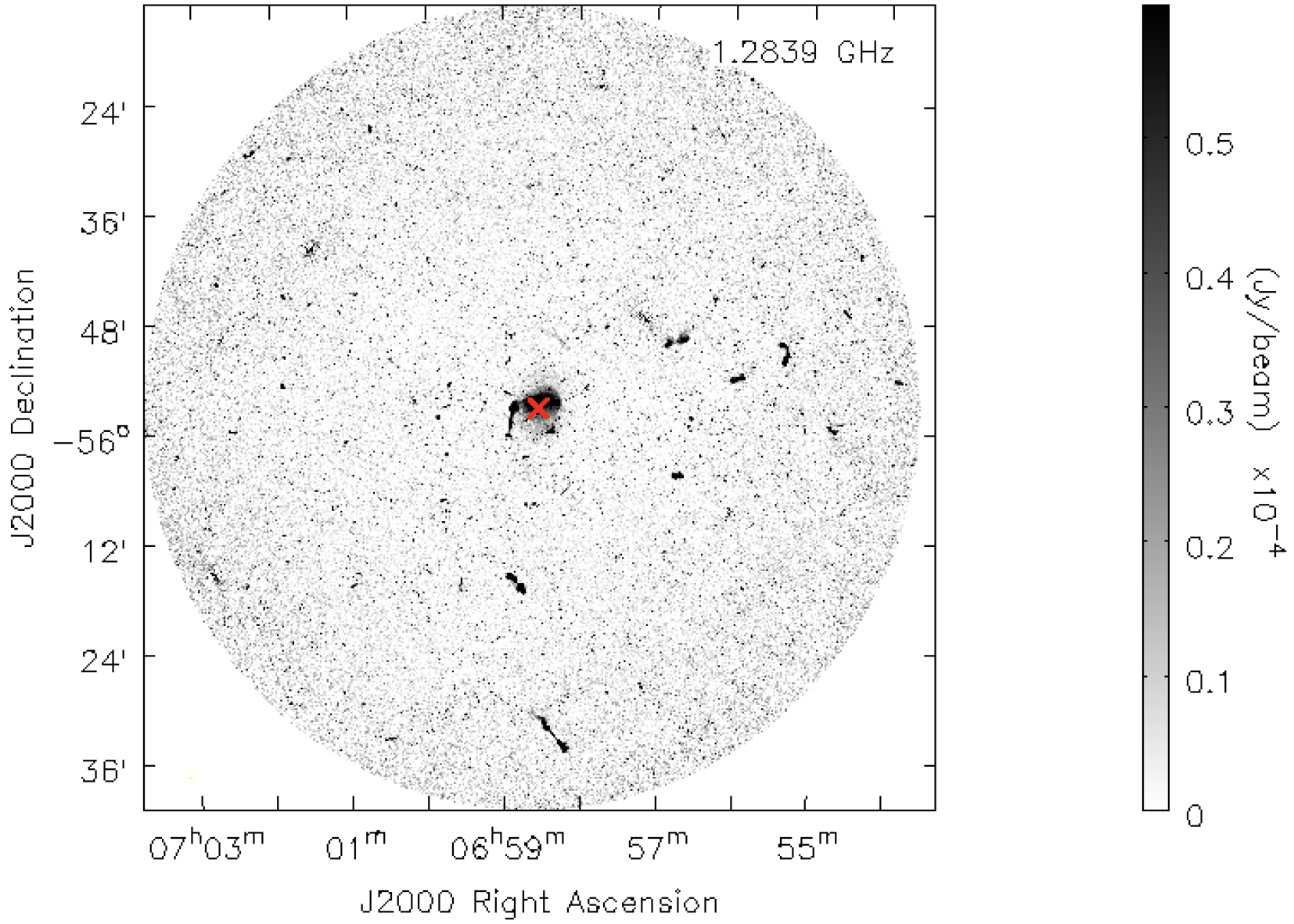

Figure B.1: Primary beam corrected, full field of view image of the Bullet cluster. The rms noise of the image is 8.5 μJy/beam and the cluster centre is indicated by the red cross.

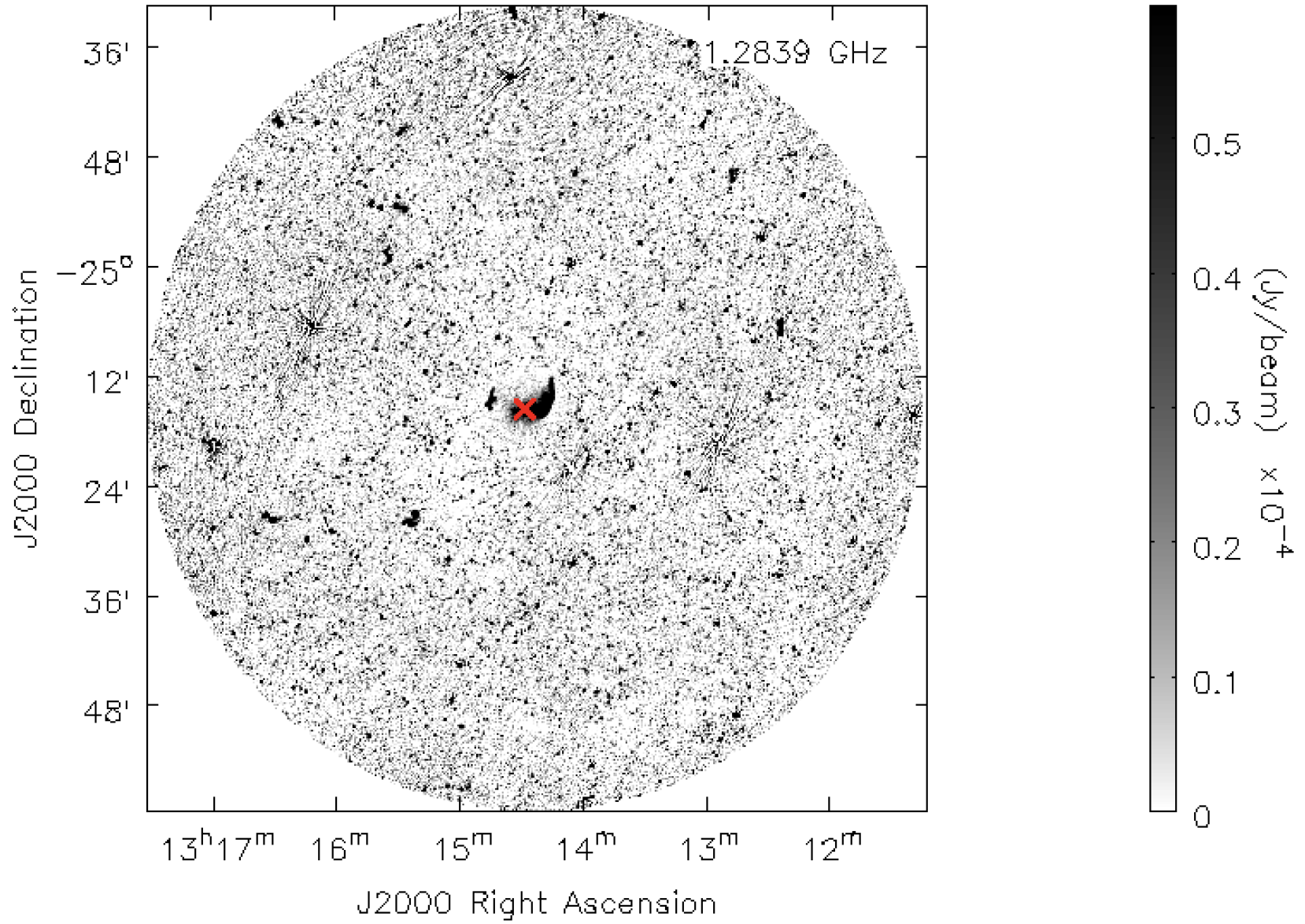

Figure B.2: Primary beam corrected, full field of view image of RXC J1314.4−2515. The rms noise of the image is 9.3 μJy/beam and the cluster centre is indicated by the red cross.

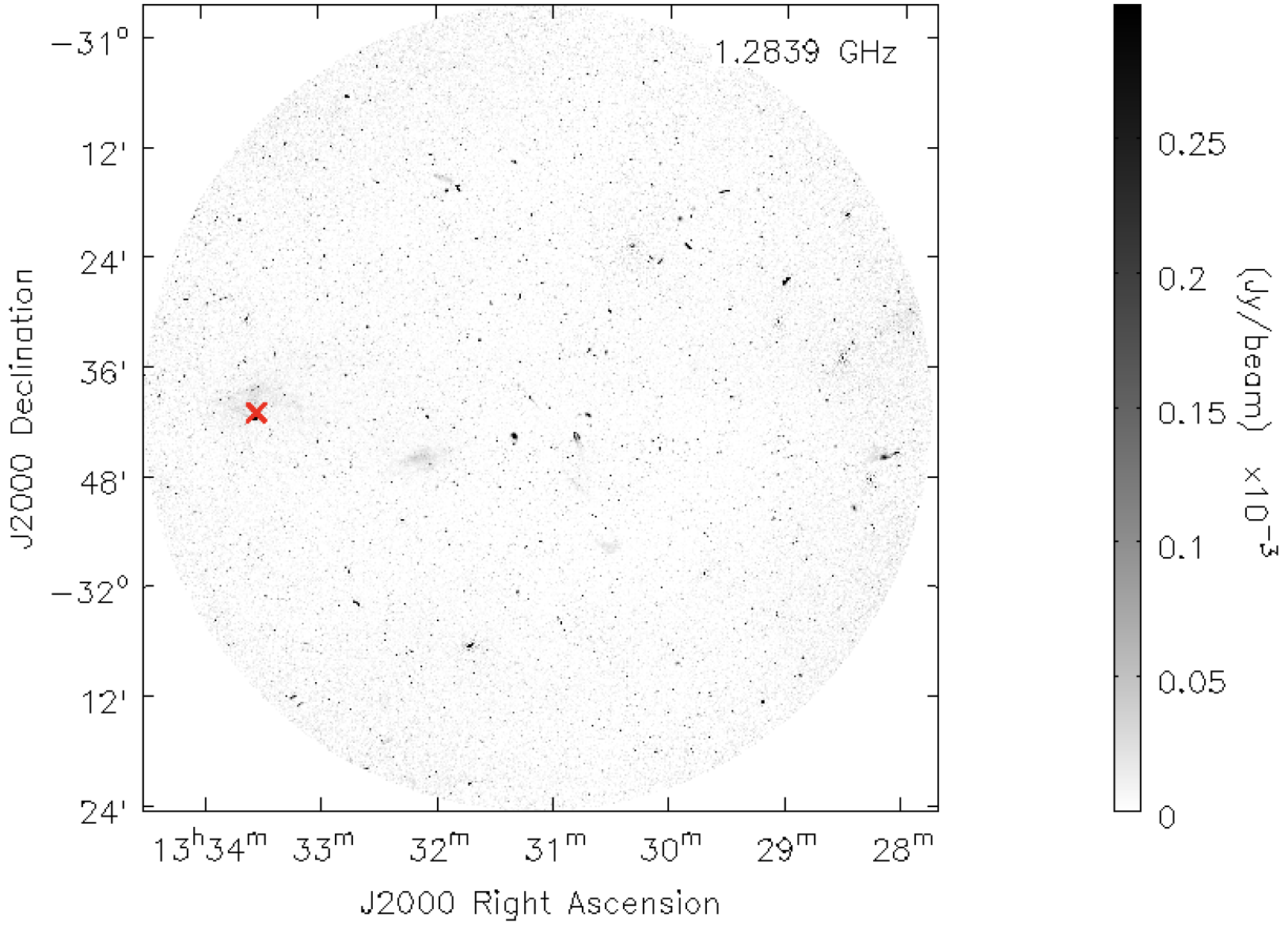

Figure B.3: Primary beam corrected, full field of view image of Abell 3562. The rms noise of the image is 12.8 μJy/beam and the cluster centre is indicated by the red cross.

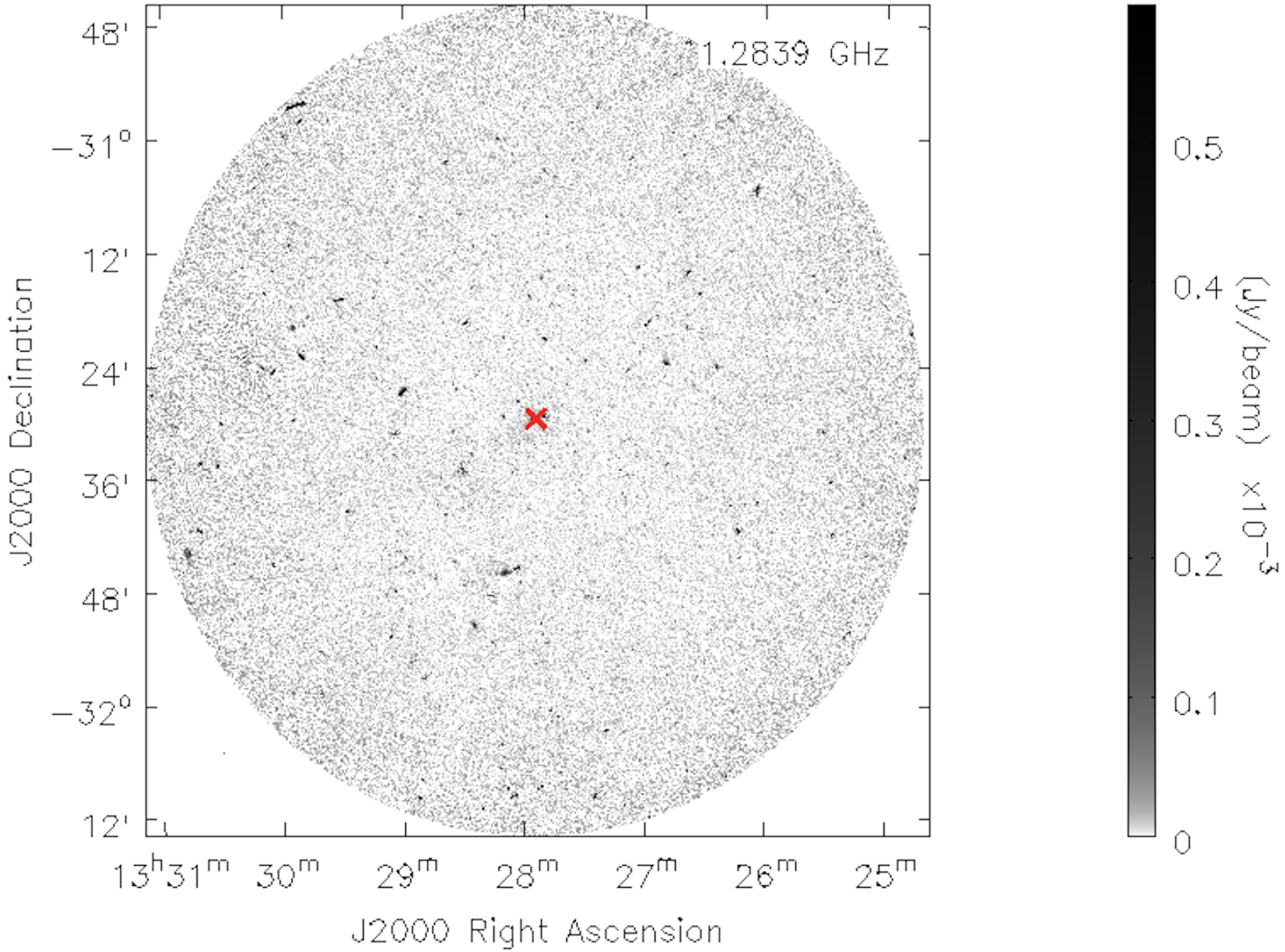

Figure B.4: Primary beam corrected, full field of view image of Abell 3558. The rms noise of the image is 8.2 μJy/beam and the cluster centre is indicated by the red cross.

BIBLIOGRAPHY

Abbott, T. M. C., Abdalla, F. B., Allam, S., Amara, A., Annis, J., Asorey, J., Avila, S., Ballester, O., Banerji, M., Barkhouse, W., Baruah, L., Baumer, M., Bechtol, K., Becker, M. R., Benoit-Lévy, A., Bernstein, G. M., Bertin, E., Blazek, J., Bocquet, S., Brooks, D., Brout, D., Buckley-Geer, E., Burke, D. L., Busti, V., Campisano, R., Cardiel-Sas, L., Carnero Rosell, A., Carrasco Kind, M., Carretero, J., Castander, F. J., Cawthon, R., Chang, C., Chen, X., Conselice, C., Costa, G., Crocce, M., Cunha, C. E., D'Andrea, C. B., da Costa, L. N., Das, R., Daues, G., Davis, T. M., Davis, C., De Vicente, J., DePoy, D. L., DeRose, J., Desai, S., Diehl, H. T., Dietrich, J. P., Dodelson, S., Doel, P., Drlica-Wagner, A., Eifler, T. F., Elliott, A. E., Evrard, A. E., Farahi, A., Fausti Neto, A., Fernandez, E., Finley, D. A., Flaugher, B., Foley, R. J., Fosalba, P., Friedel, D. N., Frieman, J., García-Bellido, J., Gaztanaga, E., Gerdes, D. W., Giannantonio, T., Gill, M. S. S., Glazebrook, K., Goldstein, D. A., Gower, M., Gruen, D., Gruendl, R. A., Gschwend, J., Gupta, R. R., Gutierrez, G., Hamilton, S., Hartley, W. G., Hinton, S. R., Hislop, J. M., Hollowood, D., Honscheid, K., Hoyle, B., Huterer, D., Jain, B., James, D. J., Jeltema, T., Johnson, M. W. G., Johnson, M. D., Kacprzak, T., Kent, S., Khullar, G., Klein, M., Kovacs, A., Koziol, A. M. G., Krause, E., Kremin, A., Kron, R., Kuehn, K., Kuhlmann, S., Kuropatkin, N., Lahav, O., Lasker, J., Li, T. S., Li, R. T., Liddle, A. R., Lima, M., Lin, H., López-Reyes, P., MacCrann, N., Maia, M. A. G., Maloney, J. D., Manera, M., March, M., Marriner, J., Marshall, J. L., Martini, P., McClintock, T., McKay, T., McMahon,

R. G., Melchior, P., Menanteau, F., Miller, C. J., Miquel, R., Mohr, J. J., Morganson, E., Mould, J., Neilsen, E., Nichol, R. C., Nogueira, F., Nord, B., Nugent, P., Nunes, L., Ogando, R. L. C., Old, L., Pace, A. B., Palmese, A., Paz-Chinchón, F., Peiris, H. V., Percival, W. J., Petravick, D., Plazas, A. A., Poh, J., Pond, C., Porredon, A., Pujol, A., Refregier, A., Reil, K., Ricker, P. M., Rollins, R. P., Romer, A. K., Roodman, A., Rooney, P., Ross, A. J., Rykoff, E. S., Sako, M., Sanchez, M. L., Sanchez, E., Santiago, B., Saro, A., Scarpine, V., Scolnic, D., Serrano, S., Sevilla-Noarbe, I., Sheldon, E., Shipp, N., Silveira, M. L., Smith, M., Smith, R. C., Smith, J. A., Soares-Santos, M., Sobreira, F., Song, J., Stebbins, A., Suchyta, E., Sullivan, M., Swanson, M. E. C., Tarle, G., Thaler, J., Thomas, D., Thomas, R. C., Troxel, M. A., Tucker, D. L., Vikram, V., Vivas, A. K., Walker, A. R., Wechsler, R. H., Weller, J., Wester, W., Wolf, R. C., Wu, H., Yanny, B., Zenteno, A., Zhang, Y., Zuntz, J., DES Collaboration, Juneau, S., Fitzpatrick, M., Nikutta, R., Nidever, D., Olsen, K., Scott, A., and NOAO Data Lab (2018). The Dark Energy Survey: Data Release 1. *Astrophys. J. Supp.*, 239(2):18.

Abell, G. O. (1958). The Distribution of Rich Clusters of Galaxies. *Astrophys. J. Supp.*, 3:211.

Ackermann, M., Ajello, M., Allafort, A., Baldini, L., Ballet, J., Barbiellini, G., Bastieri, D., Bechtol, K., Bellazzini, R., Blandford, R. D., Blasi, P., Bloom, E. D., Bonamente, E., Borgland, A. W., Bouvier, A., Brandt, T. J., Bregeon, J., Brigida, M., Bruel, P., Buehler, R., Buson, S., Caliandro, G. A., Cameron, R. A., Caraveo, P. A., Carrigan, S., Casandjian, J. M., Cavazzuti, E., Cecchi, C., Çelik, Ö., Charles, E., Chekhtman, A., Cheung, C. C., Chiang, J., Ciprini, S., Claus, R., Cohen-Tanugi, J., Colafrancesco, S., Cominsky, L. R., Conrad, J., Dermer, C. D., de Palma, F., Silva, E. d. C. e., Drell, P. S., Dubois, R., Dumora, D., Edmonds, Y., Farnier, C., Favuzzi, C., Frailis, M., Fukazawa, Y., Funk, S., Fusco, P., Gargano, F., Gasparrini, D., Gehrels, N., Germani, S., Giglietto, N., Giordano, F., Giroletti, M., Glanzman, T., Godfrey, G., Grenier, I. A., Grondin, M. H., Guiriec, S., Hadasch, D., Harding, A. K., Hayashida, M., Hays, E., Horan, D., Hughes, R. E., Jeltema, T. E., Jóhannesson, G., Johnson, A. S., Johnson, T. J., Johnson, W. N., Kamae, T., Katagiri, H., Kataoka, J., Kerr, M., Knödlseder, J., Kuss, M., Lande, J., Latronico, L., Lee, S. H., Lemoine-Goumard, M., Longo, F., Loparco, F., Lott, B., Lovellette, M. N., Lubrano, P., Madejski, G. M., Makeev, A., Mazziotta, M. N., Michel-

son, P. F., Mitthumsiri, W., Mizuno, T., Moiseev, A. A., Monte, C., Monzani, M. E., Morselli, A., Moskalenko, I. V., Murgia, S., Naumann-Godo, M., Nolan, P. L., Norris, J. P., Nuss, E., Ohsugi, T., Omodei, N., Orlando, E., Ormes, J. F., Ozaki, M., Paneque, D., Panetta, J. H., Pepe, M., Pesce-Rollins, M., Petrosian, V., Pfrommer, C., Piron, F., Porter, T. A., Profumo, S., Rainò, S., Rando, R., Razzano, M., Reimer, A., Reimer, O., Reposeur, T., Ripken, J., Ritz, S., Rodriguez, A. Y., Romani, R. W., Roth, M., Sadrozinski, H. F. W., Sander, A., Saz Parkinson, P. M., Scargle, J. D., Sgrò, C., Siskind, E. J., Smith, P. D., Spandre, G., Spinelli, P., Starck, J. L., Stawarz, Ł., Strickman, M. S., Strong, A. W., Suson, D. J., Tajima, H., Takahashi, H., Takahashi, T., Tanaka, T., Thayer, J. B., Thayer, J. G., Tibaldo, L., Tibolla, O., Torres, D. F., Tosti, G., Tramacere, A., Uchiyama, Y., Usher, T. L., Vandenbroucke, J., Vasileiou, V., Vilchez, N., Vitale, V., Waite, A. P., Wang, P., Winer, B. L., Wood, K. S., Yang, Z., Ylinen, T., and Ziegler, M. (2010). GeV Gamma-ray Flux Upper Limits from Clusters of Galaxies. *Astrophys. J. Lett.*, 717(1):L71–L78.

Aguerri, J. A. L. and Sánchez-Janssen, R. (2010). A study of catalogued nearby galaxy clusters in the SDSS-DR4. II. Cluster substructure. *Astron. Astrophys.*, 521:A28.

Akimoto, F., Kondou, K., Furuzawa, A., Tawara, Y., and Yamashita, K. (2003). Spatial Distributions of A3558 in the Core Region of the Shapley Supercluster. *Astrophys. J.*, 596(1):170–180.

Akritas, M. G. and Bershady, M. A. (1996). Linear Regression for Astronomical Data with Measurement Errors and Intrinsic Scatter. *Astrophys. J.*, 470:706.

Allen, S. W., Evrard, A. E., and Mantz, A. B. (2011). Cosmological Parameters from Observations of Galaxy Clusters. *Annu. Rev. Astron. Astrophys.*, 49(1):409–470.

Andersson, K., Benson, B. A., Ade, P. A. R., Aird, K. A., Armstrong, B., Bautz, M., Bleem, L. E., Staniszewski, Z., Stark, A. A., Stubbs, C. W., Vand erlinde, K., Vieira, J. D., Vikhlinin, A., Williamson, R., Yang, Y., Zahn, O., and Zenteno, A. (2011). X-Ray Properties of the First Sunyaev-Zel'dovich Effect Selected Galaxy Cluster Sample from the South Pole Telescope. *Astrophys. J.*, 738(1):48.

Andrade-Santos, F., Jones, C., Forman, W. R., Lovisari, L., Vikhlinin, A., van Weeren, R. J., Murray, S. S., Arnaud, M., Pratt, G. W., Démoclès, J., Kraft, R., Mazzotta, P., Böhringer, H., Chon, G., Giacintucci, S., Clarke, T. E., Borgani, S., David, L., Douspis, M., Pointecouteau, E., Dahle, H., Brown, S., Aghanim, N., and Rasia, E. (2017). The Fraction of Cool-core Clusters in X-Ray versus SZ Samples Using Chandra Observations. *Astrophys. J.*, 843(1):76.

Appenzeller, I., Fricke, K., Fürtig, W., Gässler, W., Häfner, R., Harke, R., Hess, H. J., Hummel, W., Jürgens, P., Kudritzki, R. P., Mantel, K. H., Meisl, W., Muschielok, B., Nicklas, H., Rupprecht, G., Seifert, W., Stahl, O., Szeifert, T., and Tarantik, K. (1998). Successful commissioning of FORS1 - the first optical instrument on the VLT. *The Messenger*, 94:1–6.

Arnaud, M., Pratt, G. W., Piffaretti, R., Böhringer, H., Croston, J. H., and Pointecouteau, E. (2010). The universal galaxy cluster pressure profile from a representative sample of nearby systems (REXCESS) and the Y_{SZ} - M_{500} relation. *Astron. Astrophys.*, 517:A92.

Atwood, W. B., Abdo, A. A., Ackermann, M., Althouse, W., Anderson, B., Axelsson, M., Baldini, L., Ballet, J., Band, D. L., Barbiellini, G., Bartelt, J., Bastieri, D., Baughman, B. M., Bechtol, K., Bédérède, D., Bellardi, F., Bellazzini, R., Berenji, B., Bignami, G. F., Bisello, D., Bissaldi, E., Blandford, R. D., Bloom, E. D., Bogart, J. R., Bonamente, E., Bonnell, J., Borgland, A. W., Bouvier, A., Bregeon, J., Brez, A., Brigida, M., Bruel, P., Burnett, T. H., Busetto, G., Caliandro, G. A., Cameron, R. A., Caraveo, P. A., Carius, S., Carlson, P., Casandjian, J. M., Cavazzuti, E., Ceccanti, M., Cecchi, C., Charles, E., Chekhtman, A., Cheung, C. C., Chiang, J., Chipaux, R., Cillis, A. N., Ciprini, S., Claus, R., Cohen-Tanugi, J., Condamoor, S., Conrad, J., Corbet, R., Corucci, L., Costamante, L., Cutini, S., Davis, D. S., Decotigny, D., DeKlotz, M., Dermer, C. D., de Angelis, A., Digel, S. W., do Couto e Silva, E., Drell, P. S., Dubois, R., Dumora, D., Edmonds, Y., Fabiani, D., Farnier, C., Favuzzi, C., Flath, D. L., Fleury, P., Focke, W. B., Funk, S., Fusco, P., Gargano, F., Gasparrini, D., Gehrels, N., Gentit, F. X., Germani, S., Giebels, B., Giglietto, N., Giommi, P., Giordano, F., Glanzman, T., Godfrey, G., Grenier, I. A., Grondin, M. H., Grove, J. E., Guillemot, L., Guiriec, S., Haller, G., Harding, A. K., Hart, P. A., Hays, E., Healey, S. E., Hirayama, M., Hjalmarsdotter, L., Horn, R., Hughes,

R. E., Jóhannesson, G., Johansson, G., Johnson, A. S., Johnson, R. P., Johnson, T. J., Johnson, W. N., Kamae, T., Katagiri, H., Kataoka, J., Kavelaars, A., Kawai, N., Kelly, H., Kerr, M., Klamra, W., Knödlseder, J., Kocian, M. L., Komin, N., Kuehn, F., Kuss, M., Landriu, D., Latronico, L., Lee, B., Lee, S. H., Lemoine-Goumard, M., Lionetto, A. M., Longo, F., Loparco, F., Lott, B., Lovellette, M. N., Lubrano, P., Madejski, G. M., Makeev, A., Marangelli, B., Massai, M. M., Mazziotta, M. N., McEnery, J. E., Menon, N., Meurer, C., Michelson, P. F., Minuti, M., Mirizzi, N., Mitthumsiri, W., Mizuno, T., Moiseev, A. A., Monte, C., Monzani, M. E., Moretti, E., Morselli, A., Moskalenko, I. V., Murgia, S., Nakamori, T., Nishino, S., Nolan, P. L., Norris, J. P., Nuss, E., Ohno, M., Ohsugi, T., Omodei, N., Orlando, E., Ormes, J. F., Paccagnella, A., Paneque, D., Panetta, J. H., Parent, D., Pearce, M., Pepe, M., Perazzo, A., Pesce-Rollins, M., Picozza, P., Pieri, L., Pinchera, M., Piron, F., Porter, T. A., Poupard, L., Rainò, S., Rando, R., Rapposelli, E., Razzano, M., Reimer, A., Reimer, O., Reposeur, T., Reyes, L. C., Ritz, S., Rochester, L. S., Rodriguez, A. Y., Romani, R. W., Roth, M., Russell, J. J., Ryde, F., Sabatini, S., Sadrozinski, H. F. W., Sanchez, D., Sander, A., Sapozhnikov, L., Parkinson, P. M. S., Scargle, J. D., Schalk, T. L., Scolieri, G., Sgrò, C., Share, G. H., Shaw, M., Shimokawabe, T., Shrader, C., Sierpowska-Bartosik, A., Siskind, E. J., Smith, D. A., Smith, P. D., Spandre, G., Spinelli, P., Starck, J. L., Stephens, T. E., Strickman, M. S., Strong, A. W., Suson, D. J., Tajima, H., Takahashi, H., Takahashi, T., Tanaka, T., Tenze, A., Tether, S., Thayer, J. B., Thayer, J. G., Thompson, D. J., Tibaldo, L., Tibolla, O., Torres, D. F., Tosti, G., Tramacere, A., Turri, M., Usher, T. L., Vilchez, N., Vitale, V., Wang, P., Watters, K., Winer, B. L., Wood, K. S., Ylinen, T., and Ziegler, M. (2009). The Large Area Telescope on the Fermi Gamma-Ray Space Telescope Mission. *Astrophys. J.*, 697(2):1071–1102.

Aubourg, É., Bailey, S., Bautista, J. E., Beutler, F., Bhardwaj, V., Bizyaev, D., Blanton, M., Blomqvist, M., Bolton, A. S., Bovy, J., Brewington, H., Brinkmann, J., Brownstein, J. R., Burden, A., Busca, N. G., Carithers, W., Chuang, C.-H., Comparat, J., Croft, R. A. C., Cuesta, A. J., Dawson, K. S., Delubac, T., Eisenstein, D. J., Font-Ribera, A., Ge, J., Le Goff, J. M., Gontcho, S. G. A., Gott, J. R., Gunn, J. E., Guo, H., Guy, J., Hamilton, J.-C., Ho, S., Honscheid, K., Howlett, C., Kirkby, D., Kitaura, F. S., Kneib, J.-P., Lee, K.-G., Long, D., Lupton,

R. H., Magaña, M. V., Malanushenko, V., Malanushenko, E., Manera, M., Maraston, C., Margala, D., McBride, C. K., Miralda-Escudé, J., Myers, A. D., Nichol, R. C., Noterdaeme, P., Nuza, S. E., Olmstead, M. D., Oravetz, D., Pâris, I., Padmanabhan, N., Palanque-Delabrouille, N., Pan, K., Pellejero-Ibanez, M., Percival, W. J., Petitjean, P., Pieri, M. M., Prada, F., Reid, B., Rich, J., Roe, N. A., Ross, A. J., Ross, N. P., Rossi, G., Rubiño-Martín, J. A., Sánchez, A. G., Samushia, L., Génova-Santos, R. T., Scóccola, C. G., Schlegel, D. J., Schneider, D. P., Seo, H.-J., Sheldon, E., Simmons, A., Skibba, R. A., Slosar, A., Strauss, M. A., Thomas, D., Tinker, J. L., Tojeiro, R., Vazquez, J. A., Viel, M., Wake, D. A., Weaver, B. A., Weinberg, D. H., Wood-Vasey, W. M., Yèche, C., Zehavi, I., Zhao, G.-B., and BOSS Collaboration (2015). Cosmological implications of baryon acoustic oscillation measurements. *Physical Review D.*, 92(12):123516.

Bardelli, S., Pisani, A., Ramella, M., Zucca, E., and Zamorani, G. (1998). A substructure analysis of the A3558 cluster complex. *Mon. Not. R. Astron. Soc.*, 300(2):589–598.

Bardelli, S., Zucca, E., Malizia, A., Zamorani, G., Scaramella, R., and Vettolani, G. (1996). A study of the core of the Shapley concentration. II. ROSAT observation of A 3558. *Astron. Astrophys.*, 305:435.

Barrena, R., Biviano, A., Ramella, M., Falco, E. E., and Seitz, S. (2002). The dynamical status of the cluster of galaxies 1E0657-56. *Astron. Astrophys.*, 386:816–828.

Bartalucci, I., Arnaud, M., Pratt, G. W., Démoclès, J., and Lovisari, L. (2019). The Most Massive galaxy Clusters (M2C) across cosmic time: link between radial total mass distribution and dynamical state. *Astron. Astrophys.*, 628:A86.

Bassett, B. and Hlozek, R. (2010). *Baryon acoustic oscillations*, page 246.

Basu, K. (2012). A Sunyaev-Zel'dovich take on cluster radio haloes - I. Global scaling and bi-modality using Planck data. *Mon. Not. R. Astron. Soc.*, 421(1):L112–L116.

Bernardi, G., Venturi, T., Cassano, R., Dallacasa, D., Brunetti, G., Cuciti, V., Johnston-Hollitt, M., Oozeer, N., and Smirnov, O. M. (2016). A KAT-7 view of a low-mass sample of galaxy clusters. *arXiv e-prints*, page arXiv:1603.07595.

Birkinshaw, M. (1999). The Sunyaev-Zel'dovich effect. *Phys. Rep.*, 310(2-3):97–195.

Bîrzan, L., Rafferty, D. A., Brüggen, M., Botteon, A., Brunetti, G., Cuciti, V., Edge, A. C., Morganti, R., Röttgering, H. J. A., and Shimwell, T. W. (2020). LOFAR observations of X-ray cavity systems. *Mon. Not. R. Astron. Soc.*, 496(3):2613–2635.

Bîrzan, L., Rafferty, D. A., Cassano, R., Brunetti, G., van Weeren, R. J., Brüggen, M., Intema, H. T., de Gasperin, F., Andrade-Santos, F., Botteon, A., Röttgering, H. J. A., and Shimwell, T. W. (2019). A massive cluster at z = 0.288 caught in the process of formation: The case of Abell 959. *Mon. Not. R. Astron. Soc.*, 487(4):4775–4789.

Blandford, R. and Eichler, D. (1987). Particle acceleration at astrophysical shocks: A theory of cosmic ray origin. *Phys. Rep.*, 154(1):1–75.

Blasi, P. (2001). The non-thermal radiation-cluster merger connection. *Astroparticle Physics*, 15(2):223–240.

Blasi, P. and Colafrancesco, S. (1999). Cosmic rays, radio halos and nonthermal X-ray emission in clusters of galaxies. *Astroparticle Physics*, 12(3):169–183.

Bleem, L. E., Bocquet, S., Stalder, B., Gladders, M. D., Ade, P. A. R., Allen, S. W., Anderson, A. J., Annis, J., Ashby, M. L. N., Austermann, J. E., Avila, S., Avva, J. S., Bayliss, M., Beall, J. A., Bechtol, K., Bender, A. N., Benson, B. A., Bertin, E., Bianchini, F., Blake, C., Brodwin, M., Brooks, D., Wang, G., Weller, J., Whitehorn, N., Wu, W. L. K., Yefremenko, V., and Zhang, Y. (2020). The SPTpol Extended Cluster Survey. *Astrophys. J. Supp.*, 247(1):25.

Bleem, L. E., Stalder, B., de Haan, T., Aird, K. A., Allen, S. W., Applegate, D. E., Ashby, M. L. N., Bautz, M., Bayliss, M., Benson, B. A., Bocquet, S., Brodwin, M., Carlstrom, J. E., Chang, C. L., Chiu, I., Cho, H. M., Clocchiatti, A., Crawford, T. M., Crites, A. T., Desai, S.,

Dietrich, J. P., Dobbs, M. A., Foley, R. J., Forman, W. R., George, E. M., Gladders, M. D., Gonzalez, A. H., Halverson, N. W., Hennig, C., Hoekstra, H., Holder, G. P., Holzapfel, W. L., Hrubes, J. D., Jones, C., Keisler, R., Knox, L., Lee, A. T., Leitch, E. M., Liu, J., Lueker, M., Luong-Van, D., Mantz, A., Marrone, D. P., McDonald, M., McMahon, J. J., Meyer, S. S., Mocanu, L., Mohr, J. J., Murray, S. S., Padin, S., Pryke, C., Reichardt, C. L., Rest, A., Ruel, J., Ruhl, J. E., Saliwanchik, B. R., Saro, A., Sayre, J. T., Schaffer, K. K., Schrabback, T., Shirokoff, E., Song, J., Spieler, H. G., Stanford, S. A., Staniszewski, Z., Stark, A. A., Story, K. T., Stubbs, C. W., Vanderlinde, K., Vieira, J. D., Vikhlinin, A., Williamson, R., Zahn, O., and Zenteno, A. (2015). Galaxy Clusters Discovered via the Sunyaev-Zel'dovich Effect in the 2500-Square-Degree SPT-SZ Survey. *Astrophys. J. Supp.*, 216(2):27.

Bocquet, S., Dietrich, J. P., Schrabback, T., Bleem, L. E., Klein, M., Allen, S. W., Applegate, D. E., Ashby, M. L. N., Bautz, M., Bayliss, M., Benson, B. A., Brodwin, M., Bulbul, E., Canning, R. E. A., Capasso, R., Carlstrom, J. E., Chang, C. L., Chiu, I., Cho, H. M., Clocchiatti, A., Crawford, T. M., Crites, A. T., de Haan, T., Desai, S., Dobbs, M. A., Foley, R. J., Forman, W. R., Garmire, G. P., George, E. M., Gladders, M. D., Gonzalez, A. H., Grandis, S., Gupta, N., Halverson, N. W., Hlavacek-Larrondo, J., Hoekstra, H., Holder, G. P., Holzapfel, W. L., Hou, Z., Hrubes, J. D., Huang, N., Jones, C., Khullar, G., Knox, L., Kraft, R., Lee, A. T., von der Linden, A., Luong-Van, D., Mantz, A., Marrone, D. P., McDonald, M., McMahon, J. J., Meyer, S. S., Mocanu, L. M., Mohr, J. J., Morris, R. G., Padin, S., Patil, S., Pryke, C., Rapetti, D., Reichardt, C. L., Rest, A., Ruhl, J. E., Saliwanchik, B. R., Saro, A., Sayre, J. T., Schaffer, K. K., Shirokoff, E., Stalder, B., Stanford, S. A., Staniszewski, Z., Stark, A. A., Story, K. T., Strazzullo, V., Stubbs, C. W., Vanderlinde, K., Vieira, J. D., Vikhlinin, A., Williamson, R., and Zenteno, A. (2019). Cluster Cosmology Constraints from the 2500 deg^2 SPT-SZ Survey: Inclusion of Weak Gravitational Lensing Data from Magellan and the Hubble Space Telescope. *Astrophys. J.*, 878(1):55.

Böhringer, H. (2008). Statistical properties of galaxy clusters. *Astronomische Nachrichten*, 329(2):135.

Bonafede, A., Brüggen, M., Rafferty, D., Zhuravleva, I., Riseley, C. J., van Weeren, R. J., Farnes, J. S., Vazza, F., Savini, F., Wilber, A., Botteon, A., Brunetti, G., Cassano, R., Ferrari, C., de Gasperin, F., Orrú, E., Pizzo, R. F., Röttgering, H. J. A., and Shimwell, T. W. (2018). LOFAR discoveryof radio emission in MACS J0717.5+3745. *Mon. Not. R. Astron. Soc.*, 478(3):2927–2938.

Bonafede, A., Brunetti, G., Vazza, F., Simionescu, A., Giovannini, G., Bonnassieux, E., Shimwell, T. W., Brüggen, M., van Weeren, R. J., Botteon, A., Brienza, M., Cassano, R., Drabent, A., Feretti, L., de Gasperin, F., Gastaldello, F., di Gennaro, G., Rossetti, M., Rottgering, H. J. A., Stuardi, C., and Venturi, T. (2020). The Coma cluster at LOFAR frequencies I: insights into particle acceleration mechanisms in the radio bridge. *arXiv e-prints*, page arXiv:2011.08856.

Bonafede, A., Feretti, L., Giovannini, G., Govoni, F., Murgia, M., Taylor, G. B., Ebeling, H., Allen, S., Gentile, G., and Pihlström, Y. (2009). Revealing the magnetic field in a distant galaxy cluster: discovery of the complex radio emission from MACS J0717.5 +3745. *Astron. Astrophys.*, 503(3):707–720.

Bonafede, A., Feretti, L., Murgia, M., Govoni, F., Giovannini, G., and Vacca, V. (2010). Galaxy cluster magnetic fields from radio polarized emission. *arXiv e-prints*, page arXiv:1009.1233.

Bonafede, A., Intema, H. T., Brüggen, M., Girardi, M., Nonino, M., Kantharia, N., van Weeren, R. J., and Röttgering, H. J. A. (2014). Evidence for Particle Re-acceleration in the Radio Relic in the Galaxy Cluster PLCKG287.0+32.9. *Astrophys. J.*, 785(1):1.

Booth, R. S., de Blok, W. J. G., Jonas, J. L., and Fanaroff, B. (2009). MeerKAT Key Project Science, Specifications, and Proposals. *arXiv e-prints*, page arXiv:0910.2935.

Boschin, W. (2002). A deep cluster survey in Chandra archival data. First results. *Astron. Astrophys.*, 396:397–409.

Boschin, W., Girardi, M., and Gastaldello, F. (2020). A spectroscopic survey of Abell 1703: is it a rare relaxed cluster hosting a radio halo or a usual merging system? *Mon. Not. R. Astron. Soc.*, 492(2):2405–2417.

Botteon, A., Brunetti, G., Ryu, D., and Roh, S. (2020). Shock acceleration efficiency in radio relics. *Astron. Astrophys.*, 634:A64.

Botteon, A., Gastaldello, F., Brunetti, G., and Kale, R. (2016). A M $\gtrsim$ 3 shock in 'El Gordo' cluster and the origin of the radio relic. *Mon. Not. R. Astron. Soc.*, 463(2):1534–1542.

Bradač, M., Clowe, D., Gonzalez, A. H., Marshall, P., Forman, W., Jones, C., Markevitch, M., Randall, S., Schrabback, T., and Zaritsky, D. (2006). Strong and Weak Lensing United. III. Measuring the Mass Distribution of the Merging Galaxy Cluster 1ES 0657-558. *Astrophys. J.*, 652(2):937–947.

Brentjens, M. A. (2008). Deep Westerbork observations of Abell 2256 at 350 MHz. *Astron. Astrophys.*, 489(1):69–83.

Briggs, D. (1995). *High Fidelity Deconvolution of Moderately Resolved Sources*. D. Briggs.

Brown, S. and Rudnick, L. (2011). Diffuse radio emission in/around the Coma cluster: beyond simple accretion. *Mon. Not. R. Astron. Soc.*, 412(1):2–12.

Brüggen, M., Bykov, A., Ryu, D., and Röttgering, H. (2012). Magnetic Fields, Relativistic Particles, and Shock Waves in Cluster Outskirts. *Space Sci. Rev.*, 166(1-4):187–213.

Brüggen, M. and Vazza, F. (2020). Analytical model for cluster radio relics. *Mon. Not. R. Astron. Soc.*, 493(2):2306–2317.

Brunetti, G. and Blasi, P. (2005). Alfvénic reacceleration of relativistic particles in galaxy clusters in the presence of secondary electrons and positrons. *Mon. Not. R. Astron. Soc.*, 363(4):1173–1187.

Brunetti, G. and Jones, T. W. (2014). Cosmic Rays in Galaxy Clusters and Their Nonthermal Emission. *International Journal of Modern Physics D*, 23(4):1430007–98.

Brunetti, G. and Lazarian, A. (2016). Stochastic reacceleration of relativistic electrons by turbulent reconnection: a mechanism for cluster-scale radio emission? *Mon. Not. R. Astron. Soc.*, 458(3):2584–2595.

Brunetti, G., Rudnick, L., Cassano, R., Mazzotta, P., Donnert, J., and Dolag, K. (2013). Is the Sunyaev-Zeldovich effect responsible for the observed steepening in the spectrum of the Coma radio halo? *Astron. Astrophys.*, 558:A52.

Brunetti, G., Setti, G., Feretti, L., and Giovannini, G. (2001). Particle injection and reacceleration in clusters of galaxies and the EUV excess: the case of Coma. *New Astron.*, 6(1):1–15.

Brunetti, G., Venturi, T., Dallacasa, D., Cassano, R., Dolag, K., Giacintucci, S., and Setti, G. (2007). Cosmic Rays and Radio Halos in Galaxy Clusters: New Constraints from Radio Observations. *Astrophys. J. Lett.*, 670(1):L5–L8.

Brunetti, G., Zimmer, S., and Zandanel, F. (2017). Relativistic protons in the Coma galaxy cluster: first gamma-ray constraints ever on turbulent reacceleration. *Mon. Not. R. Astron. Soc.*, 472(2):1506–1525.

Buddendiek, A., Schrabback, T., Greer, C. H., Hoekstra, H., Sommer, M., Eifler, T., Erben, T., Erler, J., Hicks, A. K., High, F. W., Hildebrandt, H., Marrone, D. P., Morris, R. G., Muzzin, A., Reiprich, T. H., Schirmer, M., Schneider, P., and von der Linden, A. (2015). Optical and Sunyaev-Zel'dovich observations of a new sample of distant rich galaxy clusters in the ROSAT All Sky. *Mon. Not. R. Astron. Soc.*, 450(4):4248–4276.

Buote, D. A. and Tsai, J. C. (1995). Quantifying the Morphologies and Dynamical Evolution of Galaxy Clusters. I. The Method. *Astrophys. J.*, 452:522.

Calvi, V., Stiavelli, M., Bradley, L., Pizzella, A., and Kim, S. (2014). The Effect of Surface Brightness Dimming in the Selection of High-z Galaxies. *Astrophys. J.*, 796(2):102.

Caprioli, D. and Spitkovsky, A. (2014). Simulations of Ion Acceleration at Non-relativistic Shocks. II. Magnetic Field Amplification. *Astrophys. J.*, 794(1):46.

Carilli, C. L. and Taylor, G. B. (2002). Cluster Magnetic Fields. *Annu. Rev. Astron. Astrophys.*, 40:319–348.

Carlstrom, J. E., Ade, P. A. R., Aird, K. A., Benson, B. A., Bleem, L. E., Busetti, S., Chang, C. L., Chauvin, E., Cho, H. M., Crawford, T. M., Crites, A. T., Dobbs, M. A., Halverson, N. W., Heimsath, S., Holzapfel, W. L., Hrubes, J. D., Joy, M., Keisler, R., Lanting, T. M., Lee, A. T., Leitch, E. M., Leong, J., Lu, W., Lueker, M., Luong-Van, D., McMahon, J. J., Mehl, J., Meyer, S. S., Mohr, J. J., Montroy, T. E., Padin, S., Plagge, T., Pryke, C., Ruhl, J. E., Schaffer, K. K., Schwan, D., Shirokoff, E., Spieler, H. G., Staniszewski, Z., Stark, A. A., Tucker, C., Vanderlinde, K., Vieira, J. D., and Williamson, R. (2011). The 10 Meter South Pole Telescope. *Pub. Astron. Soc. Pacific*, 123(903):568.

Carlstrom, J. E., Holder, G. P., and Reese, E. D. (2002). Cosmology with the Sunyaev-Zel'dovich Effect. *Annu. Rev. Astron. Astrophys.*, 40:643–680.

Carrasco, M., Barrientos, L. F., Anguita, T., García-Vergara, C., Bayliss, M., Gladders, M., Gilbank, D., Yee, H. K. C., and West, M. (2017). VLT/Magellan Spectroscopy of 29 Strong Lensing Selected Galaxy Clusters. *Astrophys. J.*, 834(2):210.

Cassano, R., Botteon, A., Di Gennaro, G., Brunetti, G., Sereno, M., Shimwell, T. W., van Weeren, R. J., Brüggen, M., Gastaldello, F., Izzo, L., Bîrzan, L., Bonafede, A., Cuciti, V., de Gasperin, F., Röttgering, H. J. A., Hardcastle, M., Mechev, A. P., and Tasse, C. (2019). LOFAR Discovery of a Radio Halo in the High-redshift Galaxy Cluster PSZ2 G099.86+58.45. *Astrophys. J. Lett.*, 881(1):L18.

Cassano, R., Brunetti, G., and Setti, G. (2006). Statistics of giant radio haloes from electron reacceleration models. *Mon. Not. R. Astron. Soc.*, 369(4):1577–1595.

Cassano, R., Brunetti, G., Setti, G., Govoni, F., and Dolag, K. (2007). New scaling relations in cluster radio haloes and the re-acceleration model. *Mon. Not. R. Astron. Soc.*, 378(4):1565–1574.

Cassano, R., Brunetti, G., and Venturi, T. (2011). The Connection between Radio Halos and Cluster Mergers and the Statistical Properties of the Radio Halo Population. *Journal of Astrophysics and Astronomy*, 32:519–527.

Cassano, R., Ettori, S., Brunetti, G., Giacintucci, S., Pratt, G. W., Venturi, T., Kale, R., Dolag, K., and Markevitch, M. (2013). Revisiting Scaling Relations for Giant Radio Halos in Galaxy Clusters. *Astrophys. J.*, 777(2):141.

Cavagnolo, K. W. (2008). *Investigating feedback and relaxation in clusters of galaxies with the Chandra X-ray Observatory*. PhD thesis, Michigan State University.

Cavagnolo, K. W., Donahue, M., Voit, G. M., and Sun, M. (2009). Intracluster Medium Entropy Profiles for a Chandra Archival Sample of Galaxy Clusters. *Astrophys. J. Supp.*, 182(1):12–32.

Chandra, P., Ray, A., and Bhatnagar, S. (2004). The Late-Time Radio Emission from SN 1993J at Meter Wavelengths. *Astrophys. J.*, 612(2):974–987.

Clarke, T. E. and Ensslin, T. (2006a). Mergers, relics and magnetic fields: The complex case of A2256. *Astronomische Nachrichten*, 327:553.

Clarke, T. E. and Ensslin, T. A. (2006b). Deep 1.4 GHz Very Large Array Observations of the Radio Halo and Relic in Abell 2256. *Astron. J.*, 131(6):2900–2912.

Clarke, T. E., Kronberg, P. P., and Böhringer, H. (2001). A New Radio-X-Ray Probe of Galaxy Cluster Magnetic Fields. *Astrophys. J. Lett.*, 547(2):L111–L114.

Clowe, D., Bradač, M., Gonzalez, A. H., Markevitch, M., Randall, S. W., Jones, C., and Zaritsky, D. (2006). A Direct Empirical Proof of the Existence of Dark Matter. *Astrophys. J. Lett.*, 648(2):L109–L113.

Clowe, D., Gonzalez, A., and Markevitch, M. (2004). Weak-Lensing Mass Reconstruction of the Interacting Cluster 1E 0657-558: Direct Evidence for the Existence of Dark Matter. *Astrophys. J.*, 604(2):596–603.

Cohen, A. S., Lane, W. M., Cotton, W. D., Kassim, N. E., Lazio, T. J. W., Perley, R. A., Condon, J. J., and Erickson, W. C. (2007). The VLA Low-Frequency Sky Survey. *Astron. J.*, 134(3):1245–1262.

Colavincenzo, M., Tan, X., Ammazzalorso, S., Camera, S., Regis, M., Xia, J.-Q., and Fornengo, N. (2020). Searching for gamma-ray emission from galaxy clusters at low redshift. *Mon. Not. R. Astron. Soc.*, 491(3):3225–3244.

Condon, J. J., Cotton, W. D., Greisen, E. W., Yin, Q. F., Perley, R. A., Taylor, G. B., and Broderick, J. J. (1998). The NRAO VLA Sky Survey. *Astron. J.*, 115(5):1693–1716.

Cornwell, T. J. and Perley, R. A. (1992). Radio-interferometric imaging of very large fields. The problem of non-coplanar arrays. *Astron. Astrophys.*, 261:353–364.

Cotton, W. D., Condon, J. J., Perley, R. A., Kassim, N., Lazio, J., Cohen, A., Lane, W., and Erickson, W. C. (2004). Beyond the isoplanatic patch in the VLA Low-frequency Sky Survey. In Oschmann, Jacobus M., J., editor, *Ground-based Telescopes*, volume 5489 of *Society of Photo-Optical Instrumentation Engineers (SPIE) Conference Series*, pages 180–189.

Cuciti, V., Cassano, R., Brunetti, G., Dallacasa, D., de Gasperin, F., Ettori, S., Giacintucci, S., Kale, R., Pratt, G. W., van Weeren, R. J., and Venturi, T. (2021a). Radio halos in a mass-selected sample of 75 galaxy clusters. II. Statistical analysis. *arXiv e-prints*, page arXiv:2101.01641.

Cuciti, V., Cassano, R., Brunetti, G., Dallacasa, D., Kale, R., Ettori, S., and Venturi, T. (2015). Occurrence of radio halos in galaxy clusters. Insight from a mass-selected sample. *Astron. Astrophys.*, 580:A97.

Cuciti, V., Cassano, R., Brunetti, G., Dallacasa, D., van Weeren, R. J., Giacintucci, S., Bonafede, A., de Gasperin, F., Ettori, S., Kale, R., Pratt, G. W., and Venturi, T. (2021b). Radio halos in a mass-selected sample of 75 galaxy clusters. I. Sample selection and data analysis. *arXiv e-prints*, page arXiv:2101.01640.

de Gasperin, F., Intema, H. T., Ridl, J., Salvato, M., van Weeren, R., Bonafede, A., Greiner, J., Cassano, R., and Brüggen, M. (2017a). Tracing low-mass galaxy clusters using radio relics: the discovery of Abell 3527-bis. *Astron. Astrophys.*, 597:A15.

de Gasperin, F., Intema, H. T., Shimwell, T. W., Brunetti, G., Brüggen, M., Enßlin, T. A., van Weeren, R. J., Bonafede, A., and Röttgering, H. J. A. (2017b). Gentle reenergization of electrons in merging galaxy clusters. *Science Advances*, 3(10):e1701634.

de Gasperin, F., Intema, H. T., van Weeren, R. J., Dawson, W. A., Golovich, N., Wittman, D., Bonafede, A., and Brüggen, M. (2015). A powerful double radio relic system discovered in PSZ1 G108.18-11.53: evidence for a shock with non-uniform Mach number? *Mon. Not. R. Astron. Soc.*, 453(4):3483–3498.

de Gasperin, F., van Weeren, R. J., Brüggen, M., Vazza, F., Bonafede, A., and Intema, H. T. (2014). A new double radio relic in PSZ1 G096.89+24.17 and a radio relic mass-luminosity relation. *Mon. Not. R. Astron. Soc.*, 444(4):3130–3138.

Dehghan, S., Johnston-Hollitt, M., Franzen, T. M. O., Norris, R. P., and Miller, N. A. (2014). Bent-tailed Radio Sources in the Australia Telescope Large Area Survey of the Chandra Deep Field South. *Astron. J.*, 148(5):75.

Dennison, B. (1980). Formation of radio halos in clusters of galaxies from cosmic-ray protons. *Astrophys. J. Lett.*, 239:L93–L96.

Di Gennaro, G., van Weeren, R. J., Brunetti, G., Cassano, R., Brüggen, M., Hoeft, M., Shimwell, T. W., Röttgering, H. J. A., Bonafede, A., Botteon, A., Cuciti, V., Dallacasa, D., de Gasperin, F., Domínguez-Fernández, P., Enßlin, T. A., Gastaldello, F., Mandal, S., Rossetti, M., and Simionescu, A. (2020). Fast magnetic field amplification in distant galaxy clusters. *Nature Astronomy*.

Di Gennaro, G., Venturi, T., Dallacasa, D., Giacintucci, S., Merluzzi, P., Busarello, G., Mercurio, A., Bardelli, S., Gastaldello, F., Grado, A., Haines, C. P., Limatola, L., and Rossetti, M. (2018).

Cosmic dance in the Shapley Concentration Core. I. A study of the radio emission of the BCGs and tailed radio galaxies. *Astron. Astrophys.*, 620:A25.

Di Mascolo, L., Churazov, E., and Mroczkowski, T. (2019a). A joint ALMA-Bolocam-Planck SZ study of the pressure distribution in RX J1347.5-1145. *Mon. Not. R. Astron. Soc.*, 487(3):4037–4056.

Di Mascolo, L., Mroczkowski, T., Churazov, E., Markevitch, M., Basu, K., Clarke, T. E., Devlin, M., Mason, B. S., Randall, S. W., Reese, E. D., Sunyaev, R., and Wik, D. R. (2019b). An ALMA+ACA measurement of the shock in the Bullet Cluster. *Astron. Astrophys.*, 628:A100.

Dietrich, J. P., Bocquet, S., Schrabback, T., Applegate, D., Hoekstra, H., Grandis, S., Mohr, J. J., Allen, S. W., Bayliss, M. B., Benson, B. A., Bleem, L. E., Brodwin, M., Bulbul, E., Capasso, R., Chiu, I., Crawford, T. M., Gonzalez, A. H., de Haan, T., Klein, M., von der Linden, A., Mantz, A. B., Marrone, D. P., McDonald, M., Raghunathan, S., Rapetti, D., Reichardt, C. L., Saro, A., Stalder, B., Stark, A., Stern, C., and Stubbs, C. (2019). Sunyaev-Zel'dovich effect and X-ray scaling relations from weak lensing mass calibration of 32 South Pole Telescope selected galaxy clusters. *Mon. Not. R. Astron. Soc.*, 483(3):2871–2906.

Domínguez-Fernández, P., Brüggen, M., Vazza, F., Banda-Barragán, W. E., Rajpurohit, K., Mignone, A., Mukherjee, D., and Vaidya, B. (2020). Morphology of radio relics I: What causes the substructure of synchrotron emission? *Mon. Not. R. Astron. Soc.*.

Donnert, J. and Brunetti, G. (2014). An efficient Fokker-Planck solver and its application to stochastic particle acceleration in galaxy clusters. *Mon. Not. R. Astron. Soc.*, 443(4):3564–3577.

Donnert, J., Dolag, K., Brunetti, G., Cassano, R., and Bonafede, A. (2010). Radio haloes from simulations and hadronic models - I. The Coma cluster. *Mon. Not. R. Astron. Soc.*, 401(1):47–54.

Donnert, J., Vazza, F., Brüggen, M., and ZuHone, J. (2018). Magnetic Field Amplification in Galaxy Clusters and Its Simulation. *Space Sci. Rev.*, 214(8):122.

Dorman, L. (2019). Cosmic ray origin: Why cosmic ray (Astroparticle) phenomenon is universal in the Universe? What is the main driver of cosmic ray particle generation? *Advances in Space Research*, 64(12):2418–2425.

Drury, L. O. (1983). REVIEW ARTICLE: An introduction to the theory of diffusive shock acceleration of energetic particles in tenuous plasmas. *Reports on Progress in Physics*, 46(8):973–1027.

Duchesne, S. W., Johnston-Hollitt, M., Bartalucci, I., Hodgson, T., and Pratt, G. W. (2020). SPT-CL J2032-5627: a new Southern double relic cluster observed with ASKAP. *arXiv e-prints*, page arXiv:2008.00660.

Duchesne, S. W., Johnston-Hollitt, M., Offringa, A. R., Pratt, G. W., Zheng, Q., and Dehghan, S. (2017). Diffuse galaxy cluster emission at 168 MHz within the Murchison Widefield Array Epoch of Reionization 0-hour field. *arXiv e-prints*, page arXiv:1707.03517.

Ebrahimpour, L., Viana, P. T. P., Manolopoulou, M., Vergara-Cervantes, C., Romer, A. K., Bhargava, S., Giles, P., Bermeo-Hernandez, A., Collins, C. A., Hilton, M., Hoyle, B., Liddle, A. R., Mann, R. G., Mayers, J. A., Miller, C. J., Nichol, R. C., Rooney, P. J., Sahlén, M., and Stott, J. P. (2018). The XMM Cluster Survey: joint modelling of the $L_{\rm X} - T$ scaling relation for clusters and groups of galaxies. *arXiv e-prints*, page arXiv:1805.03465.

Eckert, D., Jauzac, M., Vazza, F., Owers, M. S., Kneib, J. P., Tchernin, C., Intema, H., and Knowles, K. (2016). A shock front at the radio relic of Abell 2744. *Mon. Not. R. Astron. Soc.*, 461(2):1302–1307.

Eckert, D., Molendi, S., and Paltani, S. (2011). The cool-core bias in X-ray galaxy cluster samples. I. Method and application to HIFLUGCS. *Astron. Astrophys.*, 526:A79.

Ehlert, K., Weinberger, R., Pfrommer, C., and Springel, V. (2020). Connecting turbulent velocities and magnetic fields in galaxy cluster simulations with active galactic nuclei jets. *arXiv e-prints*, page arXiv:2011.13964.

Eisenstein, D. and White, M. (2004). Theoretical uncertainty in baryon oscillations. *Physical Review D.*, 70(10):103523.

Enard, D. (1991). The European Southern Observatory Very Large Telescope. *Journal of Optics*, 22(2):33–50.

Enßlin, T., Pfrommer, C., Miniati, F., and Subramanian, K. (2011). Cosmic ray transport in galaxy clusters: implications for radio halos, gamma-ray signatures, and cool core heating. *Astron. Astrophys.*, 527:A99.

Enßlin, T. A. and Gopal-Krishna (2001a). Are cluster radio relics revived fossil radio cocoons? In Laing, R. A. and Blundell, K. M., editors, *Particles and Fields in Radio Galaxies Conference*, volume 250 of *Astronomical Society of the Pacific Conference Series*, page 454.

Enßlin, T. A. and Gopal-Krishna (2001b). Reviving fossil radio plasma in clusters of galaxies by adiabatic compression in environmental shock waves. *Astron. Astrophys.*, 366:26–34.

Ettori, S., Bardelli, S., De Grandi, S., Molendi, S., Zamorani, G., and Zucca, E. (2000). BeppoSAX-ROSAT PSPC observations of the Shapley supercluster: A3562. *Mon. Not. R. Astron. Soc.*, 318(1):239–249.

Fanaroff, B. L. and Riley, J. M. (1974). The morphology of extragalactic radio sources of high and low luminosity. *Mon. Not. R. Astron. Soc.*, 167:31P–36P.

Feretti, L., Brunetti, G., Giovannini, G., Kassim, N., Orrú, E., and Setti, G. (2004a). Properties and Spectral Behaviour of Cluster Radio Halos. *Journal of Korean Astronomical Society*, 37(5):315–322.

Feretti, L., Giovannini, G., Govoni, F., and Murgia, M. (2012). Clusters of galaxies: observational properties of the diffuse radio emission. *Astron. Astrophys. Rev.*, 20:54.

Feretti, L., Orrù, E., Brunetti, G., Giovannini, G., Kassim, N., and Setti, G. (2004b). Spectral index maps of the radio halos in Abell 665 and Abell 2163. *Astron. Astrophys.*, 423:111–119.

Feretti, L., Schuecker, P., Böhringer, H., Govoni, F., and Giovannini, G. (2005). Diffuse radio emission in a REFLEX cluster. *Astron. Astrophys.*, 444(1):157–164.

Fermi, E. (1949). On the Origin of the Cosmic Radiation. *Physical Review*, 75(8):1169–1174.

Ferrari, C., Govoni, F., Schindler, S., Bykov, A. M., and Rephaeli, Y. (2008). Observations of Extended Radio Emission in Clusters. *Space Sci. Rev.*, 134(1-4):93–118.

Finoguenov, A., Henriksen, M. J., Briel, U. G., de Plaa, J., and Kaastra, J. S. (2004). XMM-Newton Study of A3562 and Its Immediate Shapley Environs. *Astrophys. J.*, 611(2):811–820.

Fujita, Y., Kohri, K., Yamazaki, R., and Kino, M. (2007). Nonthermal Emission Associated with Strong AGN Outbursts at the Centers of Galaxy Clusters. *Astrophys. J. Lett.*, 663(2):L61–L64.

Gaensler, B. M., Beck, R., and Feretti, L. (2004). The origin and evolution of cosmic magnetism. *New Astron. Rev.*, 48(11-12):1003–1012.

Gao, J., Zou, H., Zhou, X., and Kong, X. (2020). A Catalog of Galaxy Clusters Identified from SCUSS, SDSS, and UNWISE. *Pub. Astron. Soc. Pacific*, 132(1008):024101.

Gaspari, M., Brighenti, F., and Ruszkowski, M. (2013). Solving the cooling flow problem through mechanical AGN feedback. *Astronomische Nachrichten*, 334(4-5):394.

Ge, C., Sun, M., Liu, R.-Y., Rudnick, L., Sarazin, C., Forman, W., Jones, C., Chen, H., Liu, W., Yagi, M., Boselli, A., Fossati, M., and Gavazzi, G. (2019). A merger shock in Abell 1367. *Mon. Not. R. Astron. Soc.*, 486(1):L36–L40.

Gendron-Marsolais, M., Hlavacek-Larrondo, J., van Weeren, R. J., Rudnick, L., Clarke, T. E., Sebastian, B., Mroczkowski, T., Fabian, A. C., Blundell, K. M., Sheldahl, E., Nyland, K., Sanders, J. S., Peters, W. M., and Intema, H. T. (2020). High-resolution VLA low radio frequency observations of the Perseus cluster: radio lobes, mini-halo, and bent-jet radio galaxies. *Mon. Not. R. Astron. Soc.*, 499(4):5791–5805.

George, L. T., Dwarakanath, K. S., Johnston-Hollitt, M., Intema, H. T., Hurley-Walker, N., Bell, M. E., Callingham, J. R., For, B.-Q., Gaensler, B., Hancock, P. J., Hindson, L., Kapińska, A. D., Lenc, E., McKinley, B., Morgan, J., Offringa, A., Procopio, P., Staveley-Smith, L., Wayth, R. B., Wu, C., and Zheng, Q. (2017). A study of halo and relic radio emission in merging clusters using the Murchison Widefield Array. *Mon. Not. R. Astron. Soc.*, 467(1):936–949.

Ghizzardi, S., Rossetti, M., and Molendi, S. (2010). Cold fronts in galaxy clusters. *Astron. Astrophys.*, 516:A32.

Giacconi, R., Branduardi, G., Briel, U., Epstein, A., Fabricant, D., Feigelson, E., Forman, W., Gorenstein, P., Grindlay, J., Gursky, H., Harnden, F. R., Henry, J. P., Jones, C., Kellogg, E., Koch, D., Murray, S., Schreier, E., Seward, F., Tananbaum, H., Topka, K., Van Speybroeck, L., Holt, S. S., Becker, R. H., Boldt, E. A., Serlemitsos, P. J., Clark, G., Canizares, C., Markert, T., Novick, R., Helfand, D., and Long, K. (1979). The Einstein (HEAO 2) X-ray Observatory. *Astrophys. J.*, 230:540–550.

Giacconi, R., Murray, S., Gursky, H., Kellogg, E., Schreier, E., and Tananbaum, H. (1972). The Uhuru catalog of X-ray sources. *Astrophys. J.*, 178:281–308.

Giacintucci, S., Markevitch, M., Brunetti, G., ZuHone, J. A., Venturi, T., Mazzotta, P., and Bourdin, H. (2014a). Mapping the Particle Acceleration in the Cool Core of the Galaxy Cluster RX J1720.1+2638. *Astrophys. J.*, 795(1):73.

Giacintucci, S., Markevitch, M., Cassano, R., Venturi, T., Clarke, T. E., and Brunetti, G. (2017). Occurrence of Radio Minihalos in a Mass-limited Sample of Galaxy Clusters. *Astrophys. J.*, 841(2):71.

Giacintucci, S., Markevitch, M., Cassano, R., Venturi, T., Clarke, T. E., Kale, R., and Cuciti, V. (2019). Expanding the Sample of Radio Minihalos in Galaxy Clusters. *Astrophys. J.*, 880(2):70.

Giacintucci, S., Markevitch, M., Johnston-Hollitt, M., Wik, D. R., Wang, Q. H. S., and Clarke, T. E. (2020). Discovery of a Giant Radio Fossil in the Ophiuchus Galaxy Cluster. *Astrophys. J.*, 891(1):1.

Giacintucci, S., Markevitch, M., Venturi, T., Clarke, T. E., Cassano, R., and Mazzotta, P. (2014b). New Detections of Radio Minihalos in Cool Cores of Galaxy Clusters. *Astrophys. J.*, 781(1):9.

Giacintucci, S., Venturi, T., Bardelli, S., Dallacasa, D., and Zucca, E. (2004). AGN and starburst radio activity in the A3558 cluster complex. *Astron. Astrophys.*, 419:71–87.

Giacintucci, S., Venturi, T., Brunetti, G., Bardelli, S., Dallacasa, D., Ettori, S., Finoguenov, A., Rao, A. P., and Zucca, E. (2005). Spectral properties and origin of the radio halo in A3562. *Astron. Astrophys.*, 440(3):867–879.

Giovannini, G., Bonafede, A., Feretti, L., Govoni, F., Murgia, M., Ferrari, F., and Monti, G. (2009). Radio halos in nearby (z ¡ 0.4) clusters of galaxies. *Astron. Astrophys.*, 507(3):1257–1270.

Giovannini, G., Cau, M., Bonafede, A., Ebeling, H., Feretti, L., Girardi, M., Gitti, M., Govoni, F., Ignesti, A., Murgia, M., Taylor, G. B., and Vacca, V. (2020). Diffuse radio sources in a statistically complete sample of high-redshift galaxy clusters. *Astron. Astrophys.*, 640:A108.

Giovannini, G., Feretti, L., Venturi, T., Kim, K. T., and Kronberg, P. P. (1993). The Halo Radio Source Coma C and the Origin of Halo Sources. *Astrophys. J.*, 406:399.

Gitti, M., Brunetti, G., and Setti, G. (2002). Modeling the interaction between ICM and relativistic plasma in cooling flows: The case of the Perseus cluster. *Astron. Astrophys.*, 386:456–463.

Gitti, M., Tozzi, P., Brunetti, G., Cassano, R., Dallacasa, D., Edge, A., Ettori, S., Feretti, L., Ferrari, C., Giacintucci, S., Giovannini, G., Hogan, M., and Venturi, T. (2015). The SKA view of cool-core clusters: evolution of radio mini-halos and AGN feedback. In *Advancing Astrophysics with the Square Kilometre Array (AASKA14)*, page 76.

Golovich, N., Dawson, W. A., Wittman, D. M., Jee, M. J., Benson, B., Lemaux, B., van Weeren, R. J., Andrade-Santos, F., Sobral, D., de Gasperin, F., Bruggen, M., Bradac, M., Finner, K., and Peter, A. (2017). Merging Cluster Collaboration: Optical and Spectroscopic Survey of a Radio-Selected Sample of Twenty Nine Merging Galaxy Clusters. *arXiv e-prints*, page arXiv:1711.01347.

Golovich, N., Dawson, W. A., Wittman, D. M., van Weeren, R. J., Andrade-Santos, F., Jee, M. J., Benson, B., de Gasperin, F., Venturi, T., Bonafede, A., Sobral, D., Ogrean, G. A., Lemaux, B. C., Bradač, M., Brüggen, M., and Peter, A. (2019). Merging Cluster Collaboration: A Panchromatic Atlas of Radio Relic Mergers. *Astrophys. J.*, 882(1):69.

Govoni, F., Feretti, L., Giovannini, G., Böhringer, H., Reiprich, T. H., and Murgia, M. (2001). Radio and X-ray diffuse emission in six clusters of galaxies. *Astron. Astrophys.*, 376:803–819.

Govoni, F., Murgia, M., Feretti, L., Giovannini, G., Dallacasa, D., and Taylor, G. B. (2005). A2255: The first detection of filamentary polarized emission in a radio halo. *Astron. Astrophys.*, 430:L5–L8.

Guo, X., Sironi, L., and Narayan, R. (2014). Non-thermal Electron Acceleration in Low Mach Number Collisionless Shocks. II. Firehose-mediated Fermi Acceleration and its Dependence on Pre-shock Conditions. *Astrophys. J.*, 797(1):47.

Gupta, Y., Ajithkumar, B., Kale, H. S., Nayak, S., Sabhapathy, S., Sureshkumar, S., Swami, R. V., Chengalur, J. N., Ghosh, S. K., Ishwara-Chandra, C. H., Joshi, B. C., Kanekar, N., Lal, D. V., and Roy, S. (2017). The upgraded GMRT: opening new windows on the radio Universe. *Current Science*, 113(4):707–714.

Guth, A. H. (1981). Inflationary universe: A possible solution to the horizon and flatness problems. *Physical Review D.*, 23(2):347–356.

Hamaker, J. P., Bregman, J. D., and Sault, R. J. (1996). Understanding radio polarimetry. I. Mathematical foundations. *Astron. Astrophys. Supp.*, 117:137–147.

Hanisch, R. J. (1982). Common properties of clusters of galaxies containing radio halos and implications for models of radio halo formation. *Astron. Astrophys.*, 116(1):137–146.

Harwood, J. J., Hardcastle, M. J., and Croston, J. H. (2015). Spectral ageing in the lobes of cluster-centre FR II radio galaxies. *Mon. Not. R. Astron. Soc.*, 454(4):3403–3422.

Harwood, J. J., Hardcastle, M. J., Croston, J. H., and Goodger, J. L. (2013). Spectral ageing in the lobes of FR-II radio galaxies: new methods of analysis for broad-band radio data. *Mon. Not. R. Astron. Soc.*, 435(4):3353–3375.

Hasselfield, M., Moodley, K., Bond, J. R., Das, S., Devlin, M. J., Dunkley, J., Dünner, R., Fowler, J. W., Gallardo, P., Gralla, M. B., Hajian, A., Halpern, M., Hincks, A. D., Marriage, T. A., Marsden, D., Niemack, M. D., Nolta, M. R., Page, L. A., Partridge, B., Schmitt, B. L., Sehgal, N., Sievers, J., Staggs, S. T., Swetz, D. S., Switzer, E. R., and Wollack, E. J. (2013). The Atacama Cosmology Telescope: Beam Measurements and the Microwave Brightness Temperatures of Uranus and Saturn. *Astrophys. J. Supp.*, 209(1):17.

Henriksen, M. J. and Mushotzky, R. F. (1986). The X-Ray Spectrum of the Coma Cluster of Galaxies. *Astrophys. J.*, 302:287.

Heywood, I. (2020). oxkat: Semi-automated imaging of MeerKAT observations.

Higuchi, Y., Okabe, N., Merluzzi, P., Haines, C. P., Busarello, G., Grado, A., and Mercurio, A. (2020). Shapley supercluster survey: mapping the dark matter distribution. *Mon. Not. R. Astron. Soc.*, 497(1):52–66.

Hilton, M., Hasselfield, M., Sifón, C., Battaglia, N., Aiola, S., Bharadwaj, V., Bond, J. R., Choi, S. K., Crichton, D., Datta, R., Devlin, M. J., Dunkley, J., Dünner, R., Gallardo, P. A., Gralla, M., Hincks, A. D., Ho, S.-P. P., Hubmayr, J., Huffenberger, K. M., Hughes, J. P., Koopman, B. J., Kosowsky, A., Louis, T., Madhavacheril, M. S., Marriage, T. A., Maurin, L., McMahon, J., Miyatake, H., Moodley, K., Næss, S., Nati, F., Newburgh, L., Niemack, M. D., Oguri, M., Page, L. A., Partridge, B., Schmitt, B. L., Sievers, J., Spergel, D. N., Staggs, S. T., Trac, H., van Engelen, A., Vavagiakis, E. M., and Wollack, E. J. (2018). The Atacama Cosmology

Telescope: The Two-season ACTPol Sunyaev-Zel'dovich Effect Selected Cluster Catalog. *Astrophys. J. Supp.*, 235(1):20.

Hilton, M., Sifón, C., Naess, S., Madhavacheril, M., Oguri, M., Rozo, E., Rykoff, E., Abbott, T. M. C., Adhikari, S., Aguena, M., Aiola, S., Allam, S., Amodeo, S., Amon, A., Annis, J., Ansarinejad, B., Aros-Bunster, C., Austermann, J. E., Avila, S., Bacon, D., Battaglia, N., Beall, J. A., Becker, D. T., Bernstein, G. M., Bertin, E., Bhandarkar, T., Bhargava, S., Bond, J. R., Brooks, D., Burke, D. L., Calabrese, E., Carretero, J., Choi, S. K., Choi, A., Conselice, C., da Costa, L. N., Costanzi, M., Crichton, D., Crowley, K. T., Dünner, R., Denison, E. V., Devlin, M. J., Dicker, S. R., Diehl, H. T., Dietrich, J. P., Doel, P., Duff, S. M., Duivenvoorden, A. J., Dunkley, J., Everett, S., Ferraro, S., Ferrero, I., Ferté, A., Flaugher, B., Frieman, J., Gallardo, P. A., García-Bellido, J., Gaztanaga, E., Gerdes, D. W., Giles, P., Golec, J. E., Gralla, M. B., Grandis, S., Gruen, D., Gruendl, R. A., Gschwend, J., Gutierrez, G., Han, D., Hartley, W. G., Hasselfield, M., Hill, J. C., Hilton, G. C., Hincks, A. D., Hinton, S. R., Ho, S.-P. P., Honscheid, K., Hoyle, B., Hubmayr, J., Huffenberger, K. M., Hughes, J. P., Jaelani, A. T., Jain, B., James, D. J., Jeltema, T., Kent, S., Carrasco Kind, M., Knowles, K., Koopman, B. J., Kuehn, K., Lahav, O., Lima, M., Lin, Y.-T., Lokken, M., Loubser, S. I., MacCrann, N., Maia, M. A. G., Marriage, T. A., Martin, J., McMahon, J., Melchior, P., Menanteau, F., Miquel, R., Miyatake, H., Moodley, K., Morgan, R., Mroczkowski, T., Nati, F., Newburgh, L. B., Niemack, M. D., Nishizawa, A. J., Ogando, R. L. C., Orlowski-Scherer, J., Page, L. A., Palmese, A., Partridge, B., Paz-Chinchón, F., Phakathi, P., Plazas, A. A., Robertson, N. C., Romer, A. K., Carnero Rosell, A., Salatino, M., Sanchez, E., Schaan, E., Schillaci, A., Sehgal, N., Serrano, S., Shin, T., Simon, S. M., Smith, M., Soares-Santos, M., Spergel, D. N., Staggs, S. T., Storer, E. R., Suchyta, E., Swanson, M. E. C., Tarle, G., Thomas, D., To, C., Trac, H., Ullom, J. N., Vale, L. R., Van Lanen, J., Vavagiakis, E. M., De Vicente, J., Wilkinson, R. D., Wollack, E. J., Xu, Z., and Zhang, Y. (2020). The Atacama Cosmology Telescope: A Catalog of ¿ 4000 Sunyaev-Zel'dovich Galaxy Clusters. *arXiv e-prints*, page arXiv:2009.11043.

Hitomi Collaboration, Aharonian, F., Akamatsu, H., Akimoto, F., Allen, S. W., Anabuki, N., Angelini, L., Arnaud, K., Audard, M., Awaki, H., Axelsson, M., Bamba, A., Bautz, M., Bland-

ford, R., Brenneman, L., Brown, G. V., Bulbul, E., Cackett, E., Chernyakova, M., Chiao, M., Coppi, P., Costantini, E., de Plaa, J., den Herder, J.-W., Done, C., Dotani, T., Ebisawa, K., Eckart, M., Enoto, T., Ezoe, Y., Fabian, A. C., Ferrigno, C., Foster, A., Fujimoto, R., Fukazawa, Y., Furuzawa, A., Galeazzi, M., Gallo, L., Gandhi, P., Giustini, M., Goldwurm, A., Gu, L., Guainazzi, M., Haba, Y., Hagino, K., Hamaguchi, K., Harrus, I., Hatsukade, I., Hayashi, K., Hayashi, T., Hayashida, K., Hiraga, J., Hornschemeier, A., Hoshino, A., Hughes, J., Iizuka, R., Inoue, H., Inoue, Y., Ishibashi, K., Ishida, M., Ishikawa, K., Ishisaki, Y., Itoh, M., Iyomoto, N., Kaastra, J., Kallman, T., Kamae, T., Kara, E., Kataoka, J., Katsuda, S., Katsuta, J., Kawaharada, M., Kawai, N., Kelley, R., Khangulyan, D., Kilbourne, C., King, A., Kitaguchi, T., Kitamoto, S., Kitayama, T., Kohmura, T., Kokubun, M., Koyama, S., Koyama, K., Kretschmar, P., Krimm, H., Kubota, A., Kunieda, H., Laurent, P., Lebrun, F., Lee, S.-H., Leutenegger, M., Limousin, O., Loewenstein, M., Long, K. S., Lumb, D., Madejski, G., Maeda, Y., Maier, D., Makishima, K., Markevitch, M., Matsumoto, H., Matsushita, K., McCammon, D., McNamara, B., Mehdipour, M., Miller, E., Miller, J., Mineshige, S., Mitsuda, K., Mitsuishi, I., Miyazawa, T., Mizuno, T., Mori, H., Mori, K., Moseley, H., Mukai, K., Murakami, H., Murakami, T., Mushotzky, R., Nagino, R., Nakagawa, T., Nakajima, H., Nakamori, T., Nakano, T., Nakashima, S., Nakazawa, K., Nobukawa, M., Noda, H., Nomachi, M., O'Dell, S., Odaka, H., Ohashi, T., Ohno, M., Okajima, T., Ota, N., Ozaki, M., Paerels, F., Paltani, S., Parmar, A., Petre, R., Pinto, C., Pohl, M., Porter, F. S., Pottschmidt, K., Ramsey, B., Reynolds, C., Russell, H., Safi-Harb, S., Saito, S., Sakai, K., Sameshima, H., Sato, G., Sato, K., Sato, R., Sawada, M., Schartel, N., Serlemitsos, P., Seta, H., Shidatsu, M., Simionescu, A., Smith, R., Soong, Y., Stawarz, L., Sugawara, Y., Sugita, S., Szymkowiak, A., Tajima, H., Takahashi, H., Takahashi, T., Takeda, S., Takei, Y., Tamagawa, T., Tamura, K., Tamura, T., Tanaka, T., Tanaka, Y., Tanaka, Y., Tashiro, M., Tawara, Y., Terada, Y., Terashima, Y., Tombesi, F., Tomida, H., Tsuboi, Y., Tsujimoto, M., Tsunemi, H., Tsuru, T., Uchida, H., Uchiyama, H., Uchiyama, Y., Ueda, S., Ueda, Y., Ueno, S., Uno, S., Urry, M., Ursino, E., de Vries, C., Watanabe, S., Werner, N., Wik, D., Wilkins, D., Williams, B., Yamada, S., Yamaguchi, H., Yamaoka, K., Yamasaki, N. Y., Yamauchi, M., Yamauchi, S., Yaqoob, T., Yatsu, Y., Yonetoku, D., Yoshida, A., Yuasa, T., Zhuravleva, I., and Zoghbi, A. (2016). The quiescent

intracluster medium in the core of the Perseus cluster. *Nature.*, 535(7610):117–121.

Högbom, J. A. (1974). Aperture Synthesis with a Non-Regular Distribution of Interferometer Baselines. *Astron. Astrophys. Supp.*, 15:417.

Hu, Y., Lazarian, A., Li, Y., Zhuravleva, I., and Gendron-Marsolais, M.-L. (2020). Probing Magnetic Field Morphology in Galaxy Clusters with the Gradient Technique. *Astrophys. J.*, 901(2):162.

HyeongHan, K., Jee, M. J., Rudnick, L., Parkinson, D., Finner, K., Yoon, M., Lee, W., Brunetti, G., Brüggen, M., Collier, J. D., Hopkins, A. M., Michałowski, M. J., Norris, R. P., and Riseley, C. (2020). Discovery of a Radio Relic in the Massive Merging Cluster SPT-CL J2023-5535 from the ASKAP-EMU Pilot Survey. *Astrophys. J.*, 900(2):127.

Ignesti, A., Brunetti, G., Gitti, M., and Giacintucci, S. (2020). Radio and X-ray connection in radio mini-halos: Implications for hadronic models. *Astron. Astrophys.*, 640:A37.

Intema, H. T. (2014). SPAM: A data reduction recipe for high-resolution,low-frequency radio-interferometric observations. In *Astronomical Society of India Conference Series*, volume 13 of *Astronomical Society of India Conference Series*, page 469.

Intema, H. T., Jagannathan, P., Mooley, K. P., and Frail, D. A. (2017). The GMRT 150 MHz all-sky radio survey. First alternative data release TGSS ADR1. *Astron. Astrophys.*, 598:A78.

Jaffe, W. J. (1977). Origin and transport of electrons in the halo radio source in the Coma cluster. *Astrophys. J.*, 212:1–7.

Jaffe, W. J., Perola, G. C., and Valentijn, E. A. (1976). A Westerbork survey of rich clusters of galaxies. III. Observations of the Coma cluster at 610 MHz. *Astron. Astrophys.*, 49:179–192.

Jansky, K. G. (1933). Radio Waves from Outside the Solar System. *Nature.*, 132(3323):66.

Jimenez-Gallardo, A., Massaro, F., Prieto, M. A., Missaglia, V., Stuardi, C., Paggi, A., Ricci, F., Kraft, R. P., Liuzzo, E., Tremblay, G. R., Baum, S. A., O'Dea, C. P., Wilkes, B. J.,

Kuraszkiewicz, J., Forman, W. R., and Harris, D. E. (2020). Completing the 3CR Chandra Snapshot Survey: Extragalactic Radio Sources at High Redshift. *Astrophys. J. Supp.*, 250(1):7.

Johnson, A. R., Rudnick, L., Jones, T. W., Mendygral, P. J., and Dolag, K. (2020). Characterizing the Uncertainty in Cluster Magnetic Fields Derived from Rotation Measures. *Astrophys. J.*, 888(2):101.

Jonas, J. and MeerKAT Team (2016). The MeerKAT Radio Telescope. In *MeerKAT Science: On the Pathway to the SKA*, page 1.

Joye, W. A. and Mandel, E. (2003). New Features of SAOImage DS9. In Payne, H. E., Jedrzejewski, R. I., and Hook, R. N., editors, *Astronomical Data Analysis Software and Systems XII*, volume 295 of *Astronomical Society of the Pacific Conference Series*, page 489.

Käfer, F., Finoguenov, A., Eckert, D., Clerc, N., Ramos-Ceja, M. E., Sanders, J. S., and Ghirardini, V. (2020). Toward the low-scatter selection of X-ray clusters. Galaxy cluster detection with eROSITA through cluster outskirts. *Astron. Astrophys.*, 634:A8.

Kale, R. and Dwarakanath, K. S. (2010). Spectral Index Studies of the Diffuse Radio Emission in Abell 2256: Implications for Merger Activity. *Astrophys. J.*, 718(2):939–946.

Kale, R. and Ishwara-Chandra, C. H. (2020). CAPTURE: Interferometric pipeline for image creation from GMRT data.

Kale, R., Shende, K. M., and Parekh, V. (2019). A radio halo surrounding the Brightest Cluster Galaxy in RXCJ0232.2-4420: a mini-halo in transition? *Mon. Not. R. Astron. Soc.*, 486(1):L80–L84.

Kale, R., Venturi, T., Giacintucci, S., Dallacasa, D., Cassano, R., Brunetti, G., Cuciti, V., Macario, G., and Athreya, R. (2015). The Extended GMRT Radio Halo Survey. II. Further results and analysis of the full sample. *Astron. Astrophys.*, 579:A92.

Kale, R., Venturi, T., Giacintucci, S., Dallacasa, D., Cassano, R., Brunetti, G., Macario, G., and Athreya, R. (2013). The Extended GMRT Radio Halo Survey. I. New upper limits on radio halos and mini-halos. *Astron. Astrophys.*, 557:A99.

Kale, R., Wik, D. R., Giacintucci, S., Venturi, T., Brunetti, G., Cassano, R., Dallacasa, D., and de Gasperin, F. (2017). Discovery of a radio relic in the low mass, merging galaxy cluster PLCK G200.9-28.2. *Mon. Not. R. Astron. Soc.*, 472(1):940–948.

Kang, H. and Ryu, D. (2015). Curved Radio Spectra of Weak Cluster Shocks. *Astrophys. J.*, 809(2):186.

Kempner, J. C. and Sarazin, C. L. (2001). Radio Halo and Relic Candidates from the Westerbork Northern Sky Survey. *Astrophys. J.*, 548(2):639–651.

Kenyon, J. S., Smirnov, O. M., Grobler, T. L., and Perkins, S. J. (2018). CUBICAL - fast radio interferometric calibration suite exploiting complex optimization. *Mon. Not. R. Astron. Soc.*, 478(2):2399–2415.

Keshet, U. (2010). Common origin for radio relics and halos: galaxy cluster-wide, homogeneous cosmic-ray distribution, and evolving magnetic fields. *arXiv e-prints*, page arXiv:1011.0729.

Kettenis, M., van Langevelde, H. J., Reynolds, C., and Cotton, B. (2006). ParselTongue: AIPS Talking Python. In Gabriel, C., Arviset, C., Ponz, D., and Enrique, S., editors, *Astronomical Data Analysis Software and Systems XV*, volume 351 of *Astronomical Society of the Pacific Conference Series*, page 497.

Knowles, K., Baker, A. J., Basu, K., Bharadwaj, V., de Gasperin, F., Deane, R., Devlin, M., Dicker, S., Ferrari, C., Hilton, M., Hughes, J. P., Intema, H., Makhathini, S., Moodley, K., Oozeer, N., Pfrommer, C., Sievers, J., Sikhosana, S. P., Smirnov, O., Sommer, M. W., Stanchfield, S., van der Heyden, K., and Zwart, J. (2016a). MERGHERS: An SZ-selected cluster survey with MeerKAT. In *MeerKAT Science: On the Pathway to the SKA*, page 30.

Knowles, K., Baker, A. J., Bond, J. R., Gallardo, P. A., Gupta, N., Hilton, M., Hughes, J. P., Intema, H., López-Caraballo, C. H., Moodley, K., Schmitt, B. L., Sievers, J., Sifón, C., and

Wollack, E. (2019). GMRT 610 MHz observations of galaxy clusters in the ACT equatorial sample. *Mon. Not. R. Astron. Soc.*, 486(1):1332–1349.

Knowles, K., Intema, H. T., Baker, A. J., Bharadwaj, V., Bond, J. R., Cress, C., Gupta, N., Hajian, A., Hilton, M., Hincks, A. D., Hlozek, R., Hughes, J. P., Lindner, R. R., Marriage, T. A., Menanteau, F., Moodley, K., Niemack, M. D., Reese, E. D., Sievers, J., Sifón, C., Srianand, R., and Wollack, E. J. (2016b). A giant radio halo in a low-mass SZ-selected galaxy cluster: ACT-CL J0256.5+0006. *Mon. Not. R. Astron. Soc.*, 459(4):4240–4258.

Knowles, K., Pillay, D. S., Amodeo, S., Baker, A. J., Basu, K., Crichton, D., de Gasperin, F., Devlin, M., Ferrari, C., Hilton, M., Huffenberger, K. M., Hughes, J. P., Koopman, B. J., Moodley, K., Mroczkowski, T., Naess, S., Nati, F., Newburgh, L. B., Oozeer, N., Page, L., Partridge, B., Pfrommer, C., Salatino, M., Schillaci, A., Sifón, C., Smirnov, O., Sikhosana, S. P., Wollack, E. J., and Xu, Z. (2020). MERGHERS Pilot: MeerKAT discovery of diffuse emission in nine massive Sunyaev-Zel'dovich-selected galaxy clusters from ACT. *arXiv e-prints*, page arXiv:2012.15088.

Kravtsov, A. V. and Borgani, S. (2012). Formation of Galaxy Clusters. *Annu. Rev. Astron. Astrophys.*, 50:353–409.

Kronberg, P. P. (1994). Extragalactic magnetic fields. *Reports on Progress in Physics*, 57(4):325–382.

Krymskii, G. F. (1977). A regular mechanism for the acceleration of charged particles on the front of a shock wave. *Soviet Physics Doklady*, 22:327.

Kull, A. and Böhringer, H. (1999). Detection of filamentary X-ray structure in the core of the Shapley supercluster. *Astron. Astrophys.*, 341:23–28.

Landry, D., Bonamente, M., Giles, P., Maughan, B., Joy, M., and Murray, S. (2013). Chandra measurements of a complete sample of X-ray luminous galaxy clusters: the gas mass fraction. *Mon. Not. R. Astron. Soc.*, 433(4):2790–2811.

Large, M. I., Mathewson, D. S., and Haslam, C. G. T. (1959). A High-resolution Survey of the Andromeda Nebula at 408 Mc./S. *Nature.*, 183(4670):1250–1251.

Liang, H. (2000). Diffuse Cluster-wide Radio Halos. *arXiv e-prints*, pages astro–ph/0012166.

Liang, H., Hunstead, R. W., Birkinshaw, M., and Andreani, P. (2000). A Powerful Radio Halo in the Hottest Known Cluster of Galaxies 1E 0657-56. *Astrophys. J.*, 544(2):686–701.

Lindner, R. R., Baker, A. J., Hughes, J. P., Battaglia, N., Gupta, N., Knowles, K., Marriage, T. A., Menanteau, F., Moodley, K., Reese, E. D., and Srianand, R. (2014). The Radio Relics and Halo of El Gordo, a Massive z = 0.870 Cluster Merger. *Astrophys. J.*, 786(1):49.

Locatelli, N. T., Rajpurohit, K., Vazza, F., Gastaldello, F., Dallacasa, D., Bonafede, A., Rossetti, M., Stuardi, C., Bonassieux, E., Brunetti, G., Brüggen, M., and Shimwell, T. (2020). Discovering the most elusive radio relic in the sky: diffuse shock acceleration caught in the act? *Mon. Not. R. Astron. Soc.*, 496(1):L48–L53.

Lonsdale, C. J. (2005). Configuration Considerations for Low Frequency Arrays. In Kassim, N., Perez, M., Junor, W., and Henning, P., editors, *From Clark Lake to the Long Wavelength Array: Bill Erickson's Radio Science*, volume 345 of *Astronomical Society of the Pacific Conference Series*, page 399.

Louis, T., Grace, E., Hasselfield, M., Lungu, M., Maurin, L., Addison, G. E., Ade, P. A. R., Aiola, S., Allison, R., Amiri, M., Angile, E., Battaglia, N., Beall, J. A., de Bernardis, F., Bond, J. R., Britton, J., Calabrese, E., Cho, H.-m., Choi, S. K., Coughlin, K., Crichton, D., Crowley, K., Datta, R., Devlin, M. J., Dicker, S. R., Dunkley, J., Dünner, R., Ferraro, S., Fox, A. E., Gallardo, P., Gralla, M., Halpern, M., Henderson, S., Hill, J. C., Hilton, G. C., Hilton, M., Hincks, A. D., Hlozek, R., Ho, S. P. P., Huang, Z., Hubmayr, J., Huffenberger, K. M., Hughes, J. P., Infante, L., Irwin, K., Muya Kasanda, S., Klein, J., Koopman, B., Kosowsky, A., Li, D., Madhavacheril, M., Marriage, T. A., McMahon, J., Menanteau, F., Moodley, K., Munson, C., Naess, S., Nati, F., Newburgh, L., Nibarger, J., Niemack, M. D., Nolta, M. R., Nuñez, C., Page, L. A., Pappas, C., Partridge, B., Rojas, F., Schaan, E., Schmitt, B. L., Sehgal, N.,

Sherwin, B. D., Sievers, J., Simon, S., Spergel, D. N., Staggs, S. T., Switzer, E. R., Thornton, R., Trac, H., Treu, J., Tucker, C., Van Engelen, A., Ward, J. T., and Wollack, E. J. (2017). The Atacama Cosmology Telescope: two-season ACTPol spectra and parameters. *Journal of Cosmology and Astroparticle Physics.*, 2017(6):031.

Malu, S., Datta, A., and Sandhu, P. (2016). First detection at 5.5 and 9 GHz of the radio relics in bullet cluster with ATCA. *Astrophys. Space Sci.*, 361(8):255.

Mandal, S., Intema, H. T., van Weeren, R. J., Shimwell, T. W., Botteon, A., Brunetti, G., de Gasperin, F., Brüggen, M., Di Gennaro, G., Kraft, R., Röttgering, H. J. A., Hardcastle, M., and Tasse, C. (2020). Revived fossil plasma sources in galaxy clusters. *Astron. Astrophys.*, 634:A4.

Markevitch, M. (2006). Chandra Observation of the Most Interesting Cluster in the Universe. In Wilson, A., editor, *The X-ray Universe 2005*, volume 604 of *ESA Special Publication*, page 723.

Markevitch, M. (2010). Intergalactic shock fronts. *arXiv e-prints*, page arXiv:1010.3660.

Markevitch, M., Gonzalez, A. H., David, L., Vikhlinin, A., Murray, S., Forman, W., Jones, C., and Tucker, W. (2002). A Textbook Example of a Bow Shock in the Merging Galaxy Cluster 1E 0657-56. *Astrophys. J. Lett.*, 567(1):L27–L31.

Markevitch, M., Govoni, F., Brunetti, G., and Jerius, D. (2005). Bow Shock and Radio Halo in the Merging Cluster A520. *Astrophys. J.*, 627(2):733–738.

Markevitch, M. and Vikhlinin, A. (1997). Comparison of ASCA and ROSAT Cluster Temperatures: A2256, A3558, and AWM 7. *Astrophys. J.*, 474(1):84–90.

Markevitch, M. and Vikhlinin, A. (2007). Shocks and cold fronts in galaxy clusters. *Phys. Rep.*, 443(1):1–53.

Markevitch, M., Vikhlinin, A., Mazzotta, P., and VanSpeybroeck, L. (2000). Temperature Structure of Four Merging Clusters Obtained with Chandra. *arXiv e-prints*, pages astro–ph/0012215.

Mauduit, J. C. and Mamon, G. A. (2007). Suppressed radio emission in supercluster galaxies: enhanced ram pressure in merging clusters? *Astron. Astrophys.*, 475(1):169–185.

Maughan, B. J., Jones, C., Forman, W., and Van Speybroeck, L. (2008). Images, Structural Properties, and Metal Abundances of Galaxy Clusters Observed with Chandra ACIS-I at 0.1 ¡ z ¡ 1.3. *Astrophys. J. Supp.*, 174(1):117–135.

Mazzotta, P., Bourdin, H., Giacintucci, S., Markevitch, M., and Venturi, T. (2011). Study of the M shock wave propagation in RXJ1314.4-2515. *Mem. Societa Astronomica Italiana*, 82:495.

McDonald, M., McNamara, B. R., Voit, G. M., Bayliss, M., Benson, B. A., Brodwin, M., Canning, R. E. A., Florian, M. K., Garmire, G. P., Gaspari, M., Gladders, M. D., Hlavacek-Larrondo, J., Kara, E., Reichardt, C. L., Russell, H. R., Saro, A., Sharon, K., Somboonpanyakul, T., Tremblay, G. R., and van Weeren, R. J. (2019). Anatomy of a Cooling Flow: The Feedback Response to Pure Cooling in the Core of the Phoenix Cluster. *Astrophys. J.*, 885(1):63.

McMullin, J. P., Waters, B., Schiebel, D., Young, W., and Golap, K. (2007). CASA Architecture and Applications. In Shaw, R. A., Hill, F., and Bell, D. J., editors, *Astronomical Data Analysis Software and Systems XVI*, volume 376 of *Astronomical Society of the Pacific Conference Series*, page 127.

Menanteau, F., González, J., Juin, J.-B., Marriage, T. A., Reese, E. D., Acquaviva, V., Aguirre, P., Appel, J. W., Baker, A. J., Barrientos, L. F., Battistelli, E. S., Bond, J. R., Das, S., Deshpande, A. J., Devlin, M. J., Dicker, S., Dunkley, J., Dünner, R., Essinger-Hileman, T., Fowler, J. W., Hajian, A., Halpern, M., Hasselfield, M., Hernández-Monteagudo, C., Hilton, M., Hincks, A. D., Hlozek, R., Huffenberger, K. M., Hughes, J. P., Infante, L., Irwin, K. D., Klein, J., Kosowsky, A., Lin, Y.-T., Marsden, D., Moodley, K., Niemack, M. D., Nolta, M. R., Page,

L. A., Parker, L., Partridge, B., Sehgal, N., Sievers, J., Spergel, D. N., Staggs, S. T., Swetz, D., Switzer, E., Thornton, R., Trac, H., Warne, R., and Wollack, E. (2010). The Atacama Cosmology Telescope: Physical Properties and Purity of a Galaxy Cluster Sample Selected via the Sunyaev-Zel'dovich Effect. *Astrophys. J.*, 723(2):1523–1541.

Menanteau, F., Sifón, C., Barrientos, L. F., Battaglia, N., Bond, J. R., Crichton, D., Das, S., Devlin, M. J., Dicker, S., Dünner, R., Gralla, M., Hajian, A., Hasselfield, M., Hilton, M., Hincks, A. D., Hughes, J. P., Infante, L., Kosowsky, A., Marriage, T. A., Marsden, D., Moodley, K., Niemack, M. D., Nolta, M. R., Page, L. A., Partridge, B., Reese, E. D., Schmitt, B. L., Sievers, J., Spergel, D. N., Staggs, S. T., Switzer, E., and Wollack, E. J. (2013). The Atacama Cosmology Telescope: Physical Properties of Sunyaev-Zel'dovich Effect Clusters on the Celestial Equator. *Astrophys. J.*, 765(1):67.

Merluzzi, P., Busarello, G., Haines, C. P., Mercurio, A., Okabe, N., Pimbblet, K. J., Dopita, M. A., Grado, A., Limatola, L., Bourdin, H., Mazzotta, P., Capaccioli, M., Napolitano, N. R., and Schipani, P. (2015). Shapley Supercluster Survey: Galaxy evolution from filaments to cluster cores. *Mon. Not. R. Astron. Soc.*, 446(1):803–822.

Miley, G. K. and Perola, G. C. (1975). The Large Scale Radio Structure of NGC 1275. *Astron. Astrophys.*, 45:223.

Miniati, F., Jones, T. W., Kang, H., and Ryu, D. (2001). Cosmic-Ray Electrons in Groups and Clusters of Galaxies: Primary and Secondary Populations from a Numerical Cosmological Simulation. *Astrophys. J.*, 562(1):233–253.

Molnar, S. (2015). Cluster Physics with Merging Galaxy Clusters. *Frontiers in Astronomy and Space Sciences*, 2:7.

Monteiro-Oliveira, R., Cypriano, E. S., Vitorelli, A. Z., Ribeiro, A. L. B., Sodré, L., Dupke, R., and Mendes de Oliveira, C. (2018). New insights on the dissociative merging galaxy cluster Abell 2034. *Mon. Not. R. Astron. Soc.*, 481(1):1097–1114.

Mroczkowski, T., Nagai, D., Basu, K., Chluba, J., Sayers, J., Adam, R., Churazov, E., Crites, A., Di Mascolo, L., Eckert, D., Macias-Perez, J., Mayet, F., Perotto, L., Pointecouteau, E., Romero, C., Ruppin, F., Scannapieco, E., and ZuHone, J. (2019). Astrophysics with the Spatially and Spectrally Resolved Sunyaev-Zeldovich Effects. A Millimetre/Submillimetre Probe of the Warm and Hot Universe. *Space Sci. Rev.*, 215(1):17.

Murgia, M., Govoni, F., Markevitch, M., Feretti, L., Giovannini, G., Taylor, G. B., and Carretti, E. (2009). Comparative analysis of the diffuse radio emission in the galaxy clusters A1835, A2029, and Ophiuchus. *Astron. Astrophys.*, 499(3):679–695.

Noordam, J. E. (2004). LOFAR calibration challenges. In Oschmann, Jacobus M., J., editor, *Ground-based Telescopes*, volume 5489 of *Society of Photo-Optical Instrumentation Engineers (SPIE) Conference Series*, pages 817–825.

Noordam, J. E. and Smirnov, O. M. (2010). The MeqTrees software system and its use for third-generation calibration of radio interferometers. *Astron. Astrophys.*, 524:A61.

Nurgaliev, D., McDonald, M., Benson, B. A., Bleem, L., Bocquet, S., Forman, W. R., Garmire, G. P., Gupta, N., Hlavacek-Larrondo, J., Mohr, J. J., Nagai, D., Rapetti, D., Stark, A. A., Stubbs, C. W., and Vikhlinin, A. (2017). Testing for X-Ray-SZ Differences and Redshift Evolution in the X-Ray Morphology of Galaxy Clusters. *Astrophys. J.*, 841(1):5.

Offringa, A. R., McKinley, B., Hurley-Walker, N., Briggs, F. H., Wayth, R. B., Kaplan, D. L., Bell, M. E., Feng, L., Neben, A. R., Hughes, J. D., Rhee, J., Murphy, T., Bhat, N. D. R., Bernardi, G., Bowman, J. D., Cappallo, R. J., Corey, B. E., Deshpande, A. A., Emrich, D., Ewall-Wice, A., Gaensler, B. M., Goeke, R., Greenhill, L. J., Hazelton, B. J., Hindson, L., Johnston-Hollitt, M., Jacobs, D. C., Kasper, J. C., Kratzenberg, E., Lenc, E., Lonsdale, C. J., Lynch, M. J., McWhirter, S. R., Mitchell, D. A., Morales, M. F., Morgan, E., Kudryavtseva, N., Oberoi, D., Ord, S. M., Pindor, B., Procopio, P., Prabu, T., Riding, J., Roshi, D. A., Shankar, N. U., Srivani, K. S., Subrahmanyan, R., Tingay, S. J., Waterson, M., Webster, R. L., Whitney, A. R., Williams, A., and Williams, C. L. (2014). WSCLEAN: an implementation of a fast, generic wide-field imager for radio astronomy. *Mon. Not. R. Astron. Soc.*, 444(1):606–619.

Offringa, A. R. and Smirnov, O. (2017). An optimized algorithm for multiscale wideband deconvolution of radio astronomical images. *Mon. Not. R. Astron. Soc.*, 471(1):301–316.

Offringa, A. R., van de Gronde, J. J., and Roerdink, J. B. T. M. (2012). A morphological algorithm for improving radio-frequency interference detection. *Astron. Astrophys.*, 539:A95.

Omar, A. (2019). Role of intracluster supernovae in radio mini-haloes in galaxy clusters. *Mon. Not. R. Astron. Soc.*, 484(1):L141–L146.

Orrú, E., Murgia, M., Feretti, L., Govoni, F., Brunetti, G., Giovannini, G., Girardi, M., and Setti, G. (2007). Low-frequency study of two clusters of galaxies: A2744 and A2219. *Astron. Astrophys.*, 467(3):943–954.

Paraficz, D., Kneib, J. P., Richard, J., Morandi, A., Limousin, M., Jullo, E., and Martinez, J. (2016). The Bullet cluster at its best: weighing stars, gas, and dark matter. *Astron. Astrophys.*, 594:A121.

Parekh, V., van der Heyden, K., Ferrari, C., Angus, G., and Holwerda, B. (2015). Morphology parameters: substructure identification in X-ray galaxy clusters. *Astron. Astrophys.*, 575:A127.

Patra, N. N., Kanekar, N., Chengalur, J. N., Sharma, R., de Villiers, M., Ajit Kumar, B., Bhattacharyya, B., Bhalerao, V., Bombale, R., Buch, K. D., Dixit, B., Ghalame, A., Gupta, Y., Hande, P., Hande, S., Hariharan, K., Kale, R., Lokhande, S., Phakatkar, S., Prajapati, A., Rai, S. K., Raybole, P., Roy, J., Shaikh, A. K., and Sureshkumar, S. (2019). The expanded Giant Metrewave Radio Telescope. *Mon. Not. R. Astron. Soc.*, 483(3):3007–3021.

Peebles, P. J. E. (1980). *The large-scale structure of the universe*.

Peebles, P. J. E. and Yu, J. T. (1970). Primeval Adiabatic Perturbation in an Expanding Universe. *Astrophys. J.*, 162:815.

Penzias, A. A. and Wilson, R. W. (1965). A Measurement of Excess Antenna Temperature at 4080 Mc/s. *Astrophys. J.*, 142:419–421.

Perley, R. A. and Butler, B. J. (2013). An Accurate Flux Density Scale from 1 to 50 GHz. *Astrophys. J. Supp.*, 204(2):19.

Petrosian, V. and Bykov, A. M. (2008). Particle Acceleration Mechanisms. *Space Sci. Rev.*, 134(1-4):207–227.

Pfrommer, C. and Enßlin, T. A. (2004). Constraining the population of cosmic ray protons in cooling flow clusters with γ-ray and radio observations: Are radio mini-halos of hadronic origin? *Astron. Astrophys.*, 413:17–36.

Piffaretti, R., Arnaud, M., Pratt, G. W., Pointecouteau, E., and Melin, J. B. (2011). The MCXC: a meta-catalogue of x-ray detected clusters of galaxies. *Astron. Astrophys.*, 534:A109.

Pinzke, A., Oh, S. P., and Pfrommer, C. (2017). Turbulence and particle acceleration in giant radio haloes: the origin of seed electrons. *Mon. Not. R. Astron. Soc.*, 465(4):4800–4816.

Planck Collaboration, Ade, P. A. R., Aghanim, N., Argüeso, F., Armitage-Caplan, C., Arnaud, M., Ashdown, M., Atrio-Barandela, F., Aumont, J., Baccigalupi, C., Banday, A. J., Barreiro, R. B., Bartlett, J. G., Battaner, E., Beelen, A., Benabed, K., Benoît, A., Benoit-Lévy, A., Bernard, J. P., Bersanelli, M., Bielewicz, P., Bobin, J., Bock, J. J., Bonaldi, A., Bonavera, L., Bond, J. R., Borrill, J., Bouchet, F. R., Bridges, M., Bucher, M., Burigana, C., Butler, R. C., Cardoso, J. F., Carvalho, P., Catalano, A., Challinor, A., Chamballu, A., Chen, X., Chiang, H. C., Chiang, L. Y., Christensen, P. R., Church, S., Clemens, M., Clements, D. L., Colombi, S., Colombo, L. P. L., Couchot, F., Coulais, A., Crill, B. P., Curto, A., Cuttaia, F., Danese, L., Davies, R. D., Davis, R. J., de Bernardis, P., de Rosa, A., de Zotti, G., Delabrouille, J., Delouis, J. M., Désert, F. X., Dickinson, C., Diego, J. M., Dole, H., Donzelli, S., Doré, O., Douspis, M., Dupac, X., Efstathiou, G., Enßlin, T. A., Eriksen, H. K., Finelli, F., Forni, O., Frailis, M., Franceschi, E., Galeotta, S., Ganga, K., Giard, M., Giardino, G., Giraud-Héraud, Y., González-Nuevo, J., Górski, K. M., Gratton, S., Gregorio, A., Gruppuso, A., Hansen, F. K., Hanson, D., Harrison, D. L., Henrot-Versillé, S., Hernández-Monteagudo, C., Herranz, D., Hildebrandt, S. R., Hivon, E., Hobson, M., Holmes, W. A., Hornstrup, A., Hovest, W., Huffenberger, K. M.,

Jaffe, A. H., Jaffe, T. R., Jones, W. C., Juvela, M., Keihänen, E., Keskitalo, R., Kisner, T. S., Kneissl, R., Knoche, J., Knox, L., Kunz, M., Kurki-Suonio, H., Lagache, G., Lähteenmäki, A., Lamarre, J. M., Lasenby, A., Laureijs, R. J., Lawrence, C. R., Leahy, J. P., Leonardi, R., León-Tavares, J., Leroy, C., Lesgourgues, J., Liguori, M., Lilje, P. B., Linden-Vørnle, M., López-Caniego, M., Lubin, P. M., Macías-Pérez, J. F., Maffei, B., Maino, D., Mandolesi, N., Maris, M., Marshall, D. J., Martin, P. G., Martínez-González, E., Masi, S., Massardi, M., Matarrese, S., Matthai, F., Mazzotta, P., McGehee, P., Meinhold, P. R., Melchiorri, A., Mendes, L., Mennella, A., Migliaccio, M., Mitra, S., Miville-Deschênes, M. A., Moneti, A., Montier, L., Morgante, G., Mortlock, D., Munshi, D., Murphy, J. A., Naselsky, P., Nati, F., Natoli, P., Negrello, M., Netterfield, C. B., Nørgaard-Nielsen, H. U., Noviello, F., Novikov, D., Novikov, I., O'Dwyer, I. J., Osborne, S., Oxborrow, C. A., Paci, F., Pagano, L., Pajot, F., Paladini, R., Paoletti, D., Partridge, B., Pasian, F., Patanchon, G., Pearson, T. J., Perdereau, O., Perotto, L., Perrotta, F., Piacentini, F., Piat, M., Pierpaoli, E., Pietrobon, D., Plaszczynski, S., Pointecouteau, E., Polenta, G., Ponthieu, N., Popa, L., Poutanen, T., Pratt, G. W., Prézeau, G., Prunet, S., Puget, J. L., Rachen, J. P., Reach, W. T., Rebolo, R., Reinecke, M., Remazeilles, M., Renault, C., Ricciardi, S., Riller, T., Ristorcelli, I., Rocha, G., Rosset, C., Roudier, G., Rowan-Robinson, M., Rubiño-Martín, J. A., Rusholme, B., Sandri, M., Santos, D., Savini, G., Scott, D., Seiffert, M. D., Shellard, E. P. S., Spencer, L. D., Starck, J. L., Stolyarov, V., Stompor, R., Sudiwala, R., Sunyaev, R., Sureau, F., Sutton, D., Suur-Uski, A. S., Sygnet, J. F., Tauber, J. A., Tavagnacco, D., Terenzi, L., Toffolatti, L., Tomasi, M., Tristram, M., Tucci, M., Tuovinen, J., Türler, M., Umana, G., Valenziano, L., Valiviita, J., Van Tent, B., Varis, J., Vielva, P., Villa, F., Vittorio, N., Wade, L. A., Walter, B., Wandelt, B. D., Yvon, D., Zacchei, A., and Zonca, A. (2014). Planck 2013 results. XXVIII. The Planck Catalogue of Compact Sources. *Astron. Astrophys.*, 571:A28.

Planck Collaboration, Ade, P. A. R., Aghanim, N., Arnaud, M., Ashdown, M., Aumont, J., Baccigalupi, C., Baker, M., Balbi, A., Banday, A. J., Barreiro, R. B., Bartlett, J. G., Battaner, E., Benabed, K., Bennett, K., Benoît, A., Bernard, J. P., Bersanelli, M., Bhatia, R., Bock, J. J., Bonaldi, A., Bond, J. R., Borrill, J., Bouchet, F. R., Bradshaw, T., Bremer, M., Bucher,

M., Burigana, C., Butler, R. C., Cabella, P., Cantalupo, C. M., Cappellini, B., Cardoso, J. F., Carr, R., Casale, M., Catalano, A., Cayón, L., Challinor, A., Chamballu, A., Charra, J., Chary, R. R., Chiang, L. Y., Chiang, C., Christensen, P. R., Clements, D. L., Colombi, S., Couchot, F., Coulais, A., Crill, B. P., Crone, G., Crook, M., Cuttaia, F., Danese, L., D'Arcangelo, O., Davies, R. D., Davis, R. J., de Bernardis, P., de Bruin, J., de Gasperis, G., de Rosa, A., de Zotti, G., Delabrouille, J., Delouis, J. M., Désert, F. X., Dick, J., Dickinson, C., Dolag, K., Dole, H., Donzelli, S., Doré, O., Dörl, U., Douspis, M., Dupac, X., Efstathiou, G., Enßlin, T. A., Eriksen, H. K., Finelli, F., Foley, S., Forni, O., Fosalba, P., Frailis, M., Franceschi, E., Freschi, M., Gaier, T. C., Galeotta, S., Gallegos, J., Gandolfo, B., Ganga, K., Giard, M., Giardino, G., Gienger, G., Giraud-Héraud, Y., González, J., González-Nuevo, J., Górski, K. M., Gratton, S., Gregorio, A., Gruppuso, A., Guyot, G., Haissinski, J., Hansen, F. K., Harrison, D., Helou, G., Henrot-Versillé, S., Hernández-Monteagudo, C., Herranz, D., Hildebrandt, S. R., Hivon, E., Hobson, M., Holmes, W. A., Hornstrup, A., Hovest, W., Hoyland, R. J., Huffenberger, K. M., Jaffe, A. H., Jagemann, T., Jones, W. C., Juillet, J. J., Juvela, M., Kangaslahti, P., Keihänen, E., Keskitalo, R., Kisner, T. S., Kneissl, R., Knox, L., Krassenburg, M., Kurki-Suonio, H., Lagache, G., Lähteenmäki, A., Lamarre, J. M., Lange, A. E., Lasenby, A., Laureijs, R. J., Lawrence, C. R., Leach, S., Leahy, J. P., Leonardi, R., Leroy, C., Lilje, P. B., Linden-Vørnle, M., López-Caniego, M., Lowe, S., Lubin, P. M., Macías-Pérez, J. F., Maciaszek, T., MacTavish, C. J., Maffei, B., Maino, D., Mandolesi, N., Mann, R., Maris, M., Martínez-González, E., Masi, S., Massardi, M., Matarrese, S., Matthai, F., Mazzotta, P., McDonald, A., McGehee, P., Meinhold, P. R., Melchiorri, A., Melin, J. B., Mendes, L., Mennella, A., Mevi, C., Miniscalco, R., Mitra, S., Miville-Deschênes, M. A., Moneti, A., Montier, L., Morgante, G., Morisset, N., Mortlock, D., Munshi, D., Murphy, A., Naselsky, P., Natoli, P., Netterfield, C. B., Nørgaard-Nielsen, H. U., Noviello, F., Novikov, D., Novikov, I., O'Dwyer, I. J., Ortiz, I., Osborne, S., Osuna, P., Oxborrow, C. A., Pajot, F., Paladini, R., Partridge, B., Pasian, F., Passvogel, T., Patanchon, G., Pearson, D., Pearson, T. J., Perdereau, O., Perotto, L., Perrotta, F., Piacentini, F., Piat, M., Pierpaoli, E., Plaszczynski, S., Platania, P., Pointecouteau, E., Polenta, G., Ponthieu, N., Popa, L., Poutanen, T., Prézeau, G., Prunet, S., Puget, J. L., Rachen, J. P., Reach, W. T., Rebolo, R., Reinecke, M., Reix, J. M., Renault, C., Ricciardi, S., Riller, T.,

Ristorcelli, I., Rocha, G., Rosset, C., Rowan-Robinson, M., Rubiño-Martín, J. A., Rusholme, B., Salerno, E., Sandri, M., Santos, D., Savini, G., Schaefer, B. M., Scott, D., Seiffert, M. D., Shellard, P., Simonetto, A., Smoot, G. F., Sozzi, C., Starck, J. L., Sternberg, J., Stivoli, F., Stolyarov, V., Stompor, R., Stringhetti, L., Sudiwala, R., Sunyaev, R., Sygnet, J. F., Tapiador, D., Tauber, J. A., Tavagnacco, D., Taylor, D., Terenzi, L., Texier, D., Toffolatti, L., Tomasi, M., Torre, J. P., Tristram, M., Tuovinen, J., Türler, M., Tuttlebee, M., Umana, G., Valenziano, L., Valiviita, J., Varis, J., Vibert, L., Vielva, P., Villa, F., Vittorio, N., Wade, L. A., Wandelt, B. D., Watson, C., White, S. D. M., White, M., Wilkinson, A., Yvon, D., Zacchei, A., and Zonca, A. (2011). Planck early results. I. The Planck mission. *Astron. Astrophys.*, 536:A1.

Planck Collaboration, Ade, P. A. R., Aghanim, N., Arnaud, M., Ashdown, M., Aumont, J., Baccigalupi, C., Banday, A. J., Barreiro, R. B., Barrena, R., Bartlett, J. G., Bartolo, N., Battaner, E., Battye, R., Benabed, K., Benoît, A., Benoit-Lévy, A., Bernard, J. P., Bersanelli, M., Bielewicz, P., Bikmaev, I., Böhringer, H., Bonaldi, A., Bonavera, L., Bond, J. R., Borrill, J., Bouchet, F. R., Bucher, M., Burenin, R., Burigana, C., Butler, R. C., Calabrese, E., Cardoso, J. F., Carvalho, P., Catalano, A., Challinor, A., Chamballu, A., Chary, R. R., Chiang, H. C., Chon, G., Christensen, P. R., Clements, D. L., Colombi, S., Colombo, L. P. L., Combet, C., Comis, B., Couchot, F., Coulais, A., Crill, B. P., Curto, A., Cuttaia, F., Dahle, H., Danese, L., Davies, R. D., Davis, R. J., de Bernardis, P., de Rosa, A., de Zotti, G., Delabrouille, J., Désert, F. X., Dickinson, C., Diego, J. M., Dolag, K., Dole, H., Donzelli, S., Doré, O., Douspis, M., Ducout, A., Dupac, X., Efstathiou, G., Eisenhardt, P. R. M., Elsner, F., Enßlin, T. A., Eriksen, H. K., Falgarone, E., Fergusson, J., Feroz, F., Ferragamo, A., Finelli, F., Forni, O., Frailis, M., Fraisse, A. A., Franceschi, E., Frejsel, A., Galeotta, S., Galli, S., Ganga, K., Génova-Santos, R. T., Giard, M., Giraud-Héraud, Y., Gjerløw, E., González-Nuevo, J., Górski, K. M., Grainge, K. J. B., Gratton, S., Gregorio, A., Gruppuso, A., Gudmundsson, J. E., Hansen, F. K., Hanson, D., Harrison, D. L., Hempel, A., Henrot-Versillé, S., Hernández-Monteagudo, C., Herranz, D., Hildebrandt, S. R., Hivon, E., Hobson, M., Holmes, W. A., Hornstrup, A., Hovest, W., Huffenberger, K. M., Hurier, G., Jaffe, A. H., Jaffe, T. R., Jin, T., Jones, W. C., Juvela, M., Keihänen, E., Keskitalo, R., Khamitov, I., Kisner, T. S., Kneissl, R., Knoche, J., Kunz, M., Kurki-Suonio,

H., Lagache, G., Lamarre, J. M., Lasenby, A., Lattanzi, M., Lawrence, C. R., Leonardi, R., Lesgourgues, J., Levrier, F., Liguori, M., Lilje, P. B., Linden-Vørnle, M., López-Caniego, M., Lubin, P. M., Macías-Pérez, J. F., Maggio, G., Maino, D., Mak, D. S. Y., Mandolesi, N., Mangilli, A., Martin, P. G., Martínez-González, E., Masi, S., Matarrese, S., Mazzotta, P., McGehee, P., Mei, S., Melchiorri, A., Melin, J. B., Mendes, L., Mennella, A., Migliaccio, M., Mitra, S., Miville-Deschênes, M. A., Moneti, A., Montier, L., Morgante, G., Mortlock, D., Moss, A., Munshi, D., Murphy, J. A., Naselsky, P., Nastasi, A., Nati, F., Natoli, P., Netterfield, C. B., Nørgaard-Nielsen, H. U., Noviello, F., Novikov, D., Novikov, I., Olamaie, M., Oxborrow, C. A., Paci, F., Pagano, L., Pajot, F., Paoletti, D., Pasian, F., Patanchon, G., Pearson, T. J., Perdereau, O., Perotto, L., Perrott, Y. C., Perrotta, F., Pettorino, V., Piacentini, F., Piat, M., Pierpaoli, E., Pietrobon, D., Plaszczynski, S., Pointecouteau, E., Polenta, G., Pratt, G. W., Prézeau, G., Prunet, S., Puget, J. L., Rachen, J. P., Reach, W. T., Rebolo, R., Reinecke, M., Remazeilles, M., Renault, C., Renzi, A., Ristorcelli, I., Rocha, G., Rosset, C., Rossetti, M., Roudier, G., Rozo, E., Rubiño-Martín, J. A., Rumsey, C., Rusholme, B., Rykoff, E. S., Sandri, M., Santos, D., Saunders, R. D. E., Savelainen, M., Savini, G., Schammel, M. P., Scott, D., Seiffert, M. D., Shellard, E. P. S., Shimwell, T. W., Spencer, L. D., Stanford, S. A., Stern, D., Stolyarov, V., Stompor, R., Streblyanska, A., Sudiwala, R., Sunyaev, R., Sutton, D., Suur-Uski, A. S., Sygnet, J. F., Tauber, J. A., Terenzi, L., Toffolatti, L., Tomasi, M., Tramonte, D., Tristram, M., Tucci, M., Tuovinen, J., Umana, G., Valenziano, L., Valiviita, J., Van Tent, B., Vielva, P., Villa, F., Wade, L. A., Wandelt, B. D., Wehus, I. K., White, S. D. M., Wright, E. L., Yvon, D., Zacchei, A., and Zonca, A. (2016). Planck 2015 results. XXVII. The second Planck catalogue of Sunyaev-Zeldovich sources. *Astron. Astrophys.*, 594:A27.

Planck Collaboration, Aghanim, N., Akrami, Y., Ashdown, M., Aumont, J., Baccigalupi, C., Ballardini, M., Banday, A. J., Barreiro, R. B., Bartolo, N., Basak, S., Battye, R., Benabed, K., Bernard, J. P., Bersanelli, M., Bielewicz, P., Bock, J. J., Bond, J. R., Borrill, J., Bouchet, F. R., Boulanger, F., Bucher, M., Burigana, C., Butler, R. C., Calabrese, E., Cardoso, J. F., Carron, J., Challinor, A., Chiang, H. C., Chluba, J., Colombo, L. P. L., Combet, C., Contreras, D., Crill, B. P., Cuttaia, F., de Bernardis, P., de Zotti, G., Delabrouille, J., Delouis, J. M., Di

Valentino, E., Diego, J. M., Doré, O., Douspis, M., Ducout, A., Dupac, X., Dusini, S., Efstathiou, G., Elsner, F., Enßlin, T. A., Eriksen, H. K., Fantaye, Y., Farhang, M., Fergusson, J., Fernandez-Cobos, R., Finelli, F., Forastieri, F., Frailis, M., Fraisse, A. A., Franceschi, E., Frolov, A., Galeotta, S., Galli, S., Ganga, K., Génova-Santos, R. T., Gerbino, M., Ghosh, T., González-Nuevo, J., Górski, K. M., Gratton, S., Gruppuso, A., Gudmundsson, J. E., Hamann, J., Handley, W., Hansen, F. K., Herranz, D., Hildebrandt, S. R., Hivon, E., Huang, Z., Jaffe, A. H., Jones, W. C., Karakci, A., Keihänen, E., Keskitalo, R., Kiiveri, K., Kim, J., Kisner, T. S., Knox, L., Krachmalnicoff, N., Kunz, M., Kurki-Suonio, H., Lagache, G., Lamarre, J. M., Lasenby, A., Lattanzi, M., Lawrence, C. R., Le Jeune, M., Lemos, P., Lesgourgues, J., Levrier, F., Lewis, A., Liguori, M., Lilje, P. B., Lilley, M., Lindholm, V., López-Caniego, M., Lubin, P. M., Ma, Y. Z., Macías-Pérez, J. F., Maggio, G., Maino, D., Mandolesi, N., Mangilli, A., Marcos-Caballero, A., Maris, M., Martin, P. G., Martinelli, M., Martínez-González, E., Matarrese, S., Mauri, N., McEwen, J. D., Meinhold, P. R., Melchiorri, A., Mennella, A., Migliaccio, M., Millea, M., Mitra, S., Miville-Deschênes, M. A., Molinari, D., Montier, L., Morgante, G., Moss, A., Natoli, P., Nørgaard-Nielsen, H. U., Pagano, L., Paoletti, D., Partridge, B., Patanchon, G., Peiris, H. V., Perrotta, F., Pettorino, V., Piacentini, F., Polastri, L., Polenta, G., Puget, J. L., Rachen, J. P., Reinecke, M., Remazeilles, M., Renzi, A., Rocha, G., Rosset, C., Roudier, G., Rubiño-Martín, J. A., Ruiz-Granados, B., Salvati, L., Sandri, M., Savelainen, M., Scott, D., Shellard, E. P. S., Sirignano, C., Sirri, G., Spencer, L. D., Sunyaev, R., Suur-Uski, A. S., Tauber, J. A., Tavagnacco, D., Tenti, M., Toffolatti, L., Tomasi, M., Trombetti, T., Valenziano, L., Valiviita, J., Van Tent, B., Vibert, L., Vielva, P., Villa, F., Vittorio, N., Wandelt, B. D., Wehus, I. K., White, M., White, S. D. M., Zacchei, A., and Zonca, A. (2020). Planck 2018 results. VI. Cosmological parameters. *Astron. Astrophys.*, 641:A6.

Quintana, H., Proust, D., Dünner, R., Carrasco, E. R., and Reisenegger, A. (2020). A redshift database towards the Shapley supercluster region. *Astron. Astrophys.*, 638:A27.

Quintana, H., Ramirez, A., Melnick, J., Raychaudhury, S., and Slezak, E. (1995). The Shapley Supercluster. I. Spectroscopic Observations in the Central Region. *Astron. J.*, 110:463.

Radovich, M., Puddu, E., Bellagamba, F., Roncarelli, M., Moscardini, L., Bardelli, S., Grado, A., Getman, F., Maturi, M., Huang, Z., Napolitano, N., McFarland, J., Valentijn, E., and Bilicki, M. (2017). Searching for galaxy clusters in the Kilo-Degree Survey. *Astron. Astrophys.*, 598:A107.

Raja, R., Rahaman, M., Datta, A., van Weeren, R. J., Intema, H. T., and Paul, S. (2021). A low-frequency radio halo survey of the South Pole Telescope SZ-selected clusters with the GMRT. *Mon. Not. R. Astron. Soc.*, 500(2):2236–2249.

Rajpurohit, K., Brunetti, G., Bonafede, A., van Weeren, R. J., Botteon, A., Vazza, F., Hoeft, M., Riseley, C. J., Bonnassieux, E., Brienza, M., Forman, W. R., Röttgering, H. J. A., Rajpurohit, A. S., Locatelli, N., Shimwell, T. W., Cassano, R., Di Gennaro, G., Brüggen, M., Wittor, D., Drabent, A., and Ignesti, A. (2020a). Physical insights from the spectrum of the radio halo in MACS J0717.5+3745. *arXiv e-prints*, page arXiv:2012.14373.

Rajpurohit, K., Hoeft, M., Vazza, F., Rudnick, L., van Weeren, R. J., Wittor, D., Drabent, A., Brienza, M., Bonnassieux, E., Locatelli, N., Kale, R., and Dumba, C. (2020b). New mysteries and challenges from the Toothbrush relic: wideband observations from 550 MHz to 8 GHz. *Astron. Astrophys.*, 636:A30.

Rajpurohit, K., Vazza, F., Hoeft, M., Loi, F., Beck, R., Vacca, V., Kierdorf, M., van Weeren, R. J., Wittor, D., Govoni, F., Murgia, M., Riseley, C. J., Locatelli, N., Drabent, A., and Bonnassieux, E. (2020d). A perfect power-law spectrum even at highest frequencies: The Toothbrush relic. *arXiv e-prints*, page arXiv:2008.02694.

Rajpurohit, K., Vazza, F., Hoeft, M., Loi, F., Beck, R., Vacca, V., Kierdorf, M., van Weeren, R. J., Wittor, D., Govoni, F., Murgia, M., Riseley, C. J., Locatelli, N., Drabent, A., and Bonnassieux, E. (2020c). A perfect power-law spectrum even at the highest frequencies: The Toothbrush relic. *Astron. Astrophys.*, 642:L13.

Ramos-Ceja, M. E., Pacaud, F., Reiprich, T. H., Migkas, K., Lovisari, L., and Schellenberger, G.

(2019). Projection effects in galaxy cluster samples: insights from X-ray redshifts. *Astron. Astrophys.*, 626:A48.

Reimer, O., Pohl, M., Sreekumar, P., and Mattox, J. R. (2003). EGRET Upper Limits on the High-Energy Gamma-Ray Emission of Galaxy Clusters. *Astrophys. J.*, 588(1):155–164.

Rephaeli, Y. and Gruber, D. (2003). RXTE Observations of A2256. *arXiv e-prints*, pages astro–ph/0305354.

Richard-Laferrière, A., Hlavacek-Larrondo, J., Nemmen, R. S., Rhea, C. L., Taylor, G. B., Prasow-Émond, M., Gendron-Marsolais, M., Latulippe, M., Edge, A. C., Fabian, A. C., Sanders, J. S., Hogan, M. T., and Demontigny, G. (2020). On the relation between mini-halos and AGN feedback in clusters of galaxies. *Mon. Not. R. Astron. Soc.*, 499(2):2934–2958.

Riess, A. G., Filippenko, A. V., Challis, P., Clocchiatti, A., Diercks, A., Garnavich, P. M., Gilliland, R. L., Hogan, C. J., Jha, S., Kirshner, R. P., Leibundgut, B., Phillips, M. M., Reiss, D., Schmidt, B. P., Schommer, R. A., Smith, R. C., Spyromilio, J., Stubbs, C., Suntzeff, N. B., and Tonry, J. (1998). Observational Evidence from Supernovae for an Accelerating Universe and a Cosmological Constant. *Astron. J.*, 116(3):1009–1038.

Rossetti, M., Ghizzardi, S., Molendi, S., and Finoguenov, A. (2007). A cluster in a crowded environment: XMM-Newton and Chandra observations of A3558. *Astron. Astrophys.*, 463(3):839–851.

Rykoff, E. S., Rozo, E., Hollowood, D., Bermeo-Hernandez, A., Jeltema, T., Mayers, J., Romer, A. K., Rooney, P., Saro, A., Vergara Cervantes, C., Wechsler, R. H., Wilcox, H., Abbott, T. M. C., Abdalla, F. B., Allam, S., Annis, J., Benoit-Lévy, A., Bernstein, G. M., Bertin, E., Brooks, D., Burke, D. L., Capozzi, D., Carnero Rosell, A., Carrasco Kind, M., Castander, F. J., Childress, M., Collins, C. A., Cunha, C. E., D'Andrea, C. B., da Costa, L. N., Davis, T. M., Desai, S., Diehl, H. T., Dietrich, J. P., Doel, P., Evrard, A. E., Finley, D. A., Flaugher, B., Fosalba, P., Frieman, J., Glazebrook, K., Goldstein, D. A., Gruen, D., Gruendl, R. A., Gutierrez, G., Hilton, M., Honscheid, K., Hoyle, B., James, D. J., Kay, S. T., Kuehn, K.,

Kuropatkin, N., Lahav, O., Lewis, G. F., Lidman, C., Lima, M., Maia, M. A. G., Mann, R. G., Marshall, J. L., Martini, P., Melchior, P., Miller, C. J., Miquel, R., Mohr, J. J., Nichol, R. C., Nord, B., Ogando, R., Plazas, A. A., Reil, K., Sahlén, M., Sanchez, E., Santiago, B., Scarpine, V., Schubnell, M., Sevilla-Noarbe, I., Smith, R. C., Soares-Santos, M., Sobreira, F., Stott, J. P., Suchyta, E., Swanson, M. E. C., Tarle, G., Thomas, D., Tucker, D., Uddin, S., Viana, P. T. P., Vikram, V., Walker, A. R., Zhang, Y., and DES Collaboration (2016). The RedMaPPer Galaxy Cluster Catalog From DES Science Verification Data. *Astrophys. J. Supp.*, 224(1):1.

Ryle, M. and Vonberg, D. D. (1946). Solar Radiation on 175 Mc./s. *Nature.*, 158(4010):339–340.

Ryu, D., Kang, H., Hallman, E., and Jones, T. W. (2003). Cosmological Shock Waves and Their Role in the Large-Scale Structure of the Universe. *Astrophys. J.*, 593(2):599–610.

Sahlén, M., Viana, P. T. P., Liddle, A. R., Romer, A. K., Davidson, M., Hosmer, M., Lloyd-Davies, E., Sabirli, K., Collins, C. A., Freeman, P. E., Hilton, M., Hoyle, B., Kay, S. T., Mann, R. G., Mehrtens, N., Miller, C. J., Nichol, R. C., Stanford, S. A., and West, M. J. (2009). The XMM Cluster Survey: forecasting cosmological and cluster scaling-relation parameter constraints. *Mon. Not. R. Astron. Soc.*, 397(2):577–607.

Sarazin, C. L. (1988). *X-ray emission from clusters of galaxies*.

Sarazin, C. L. (2002). *The Physics of Cluster Mergers*, volume 272, pages 1–38.

Savini, F., Bonafede, A., Brüggen, M., van Weeren, R., Brunetti, G., Intema, H., Botteon, A., Shimwell, T., Wilber, A., Rafferty, D., Giacintucci, S., Cassano, R., Cuciti, V., de Gasperin, F., Röttgering, H., Hoeft, M., and White, G. (2018). First evidence of diffuse ultra-steep-spectrum radio emission surrounding the cool core of a cluster. *Mon. Not. R. Astron. Soc.*, 478(2):2234–2242.

Schlickeiser, R., Sievers, A., and Thiemann, H. (1987). The diffuse radio emission from the Coma cluster. *Astron. Astrophys.*, 182:21–35.

Sekhar, S. and Athreya, R. (2018). Two Procedures to Flag Radio Frequency Interference in the UV Plane. *Astron. J.*, 156(1):9.

Shalchi, A. (2020). Perpendicular Transport of Energetic Particles in Magnetic Turbulence. *Space Sci. Rev.*, 216(2):23.

Shapley, H. (1930). Note on a Remote Cloud of Galaxies in Centaurus. *Harvard College Observatory Bulletin*, 874:9–12.

Shimwell, T. W., Brown, S., Feain, I. J., Feretti, L., Gaensler, B. M., and Lage, C. (2014). Deep radio observations of the radio halo of the bullet cluster 1E 0657-55.8. *Mon. Not. R. Astron. Soc.*, 440(4):2901–2915.

Shimwell, T. W., Luckin, J., Brüggen, M., Brunetti, G., Intema, H. T., Owers, M. S., Röttgering, H. J. A., Stroe, A., van Weeren, R. J., Williams, W. L., Cassano, R., de Gasperin, F., Heald, G. H., Hoang, D. N., Hardcastle, M. J., Sridhar, S. S., Sabater, J., Best, P. N., Bonafede, A., Chyży, K. T., Enßlin, T. A., Ferrari, C., Haverkorn, M., Hoeft, M., Horellou, C., McKean, J. P., Morabito, L. K., Orrù, E., Pizzo, R., Retana-Montenegro, E., and White, G. J. (2016). A plethora of diffuse steep spectrum radio sources in Abell 2034 revealed by LOFAR. *Mon. Not. R. Astron. Soc.*, 459(1):277–290.

Shimwell, T. W., Markevitch, M., Brown, S., Feretti, L., Gaensler, B. M., Johnston-Hollitt, M., Lage, C., and Srinivasan, R. (2015). Another shock for the Bullet cluster, and the source of seed electrons for radio relics. *Mon. Not. R. Astron. Soc.*, 449(2):1486–1494.

Shitanishi, J. A., Pierpaoli, E., Sayers, J., Golwala, S. R., Ameglio, S., Mantz, A. B., Mroczkowski, T. K., Rasia, E., and Siegel, S. (2018). Thermodynamic profiles of galaxy clusters from a joint X-ray/SZ analysis. *Mon. Not. R. Astron. Soc.*, 481(1):749–792.

Shweta, A., Athreya, R., and Sekhar, S. (2020). Reenergization of Radio Halo Electrons in the Merging Galaxy Cluster A2163. *Astrophys. J.*, 897(2):115.

Sifón, C., Battaglia, N., Hasselfield, M., Menanteau, F., Barrientos, L. F., Bond, J. R., Crichton, D., Devlin, M. J., Dünner, R., Hilton, M., Hincks, A. D., Hlozek, R., Huffenberger, K. M., Hughes, J. P., Infante, L., Kosowsky, A., Marsden, D., Marriage, T. A., Moodley, K., Niemack, M. D., Page, L. A., Spergel, D. N., Staggs, S. T., Trac, H., and Wollack, E. J. (2016). The

Atacama Cosmology Telescope: dynamical masses for 44 SZ-selected galaxy clusters over 755 square degrees. *Mon. Not. R. Astron. Soc.*, 461(1):248–270.

Sifón, C., Menanteau, F., Hasselfield, M., Marriage, T. A., Hughes, J. P., Barrientos, L. F., González, J., Infante, L., Addison, G. E., Baker, A. J., Battaglia, N., Bond, J. R., Crichton, D., Das, S., Devlin, M. J., Dunkley, J., Dünner, R., Gralla, M. B., Hajian, A., Hilton, M., Hincks, A. D., Kosowsky, A. B., Marsden, D., Moodley, K., Niemack, M. D., Nolta, M. R., Page, L. A., Partridge, B., Reese, E. D., Sehgal, N., Sievers, J., Spergel, D. N., Staggs, S. T., Thornton, R. J., Trac, H., and Wollack, E. J. (2013). The Atacama Cosmology Telescope: Dynamical Masses and Scaling Relations for a Sample of Massive Sunyaev-Zel'dovich Effect Selected Galaxy Clusters. *Astrophys. J.*, 772(1):25.

Slee, O. B. and Reynolds, J. E. (1984). Steep-spectrum radio sources in clusters of galaxies - the southern sample. *Proceedings of the Astronomical Society of Australia*, 5:516–528.

Smirnov, O. M. (2011). Revisiting the radio interferometer measurement equation. I. A full-sky Jones formalism. *Astron. Astrophys.*, 527:A106.

Smirnov, O. M. and Tasse, C. (2015). Radio interferometric gain calibration as a complex optimization problem. *Mon. Not. R. Astron. Soc.*, 449(3):2668–2684.

Sommer, M. W. and Basu, K. (2014). A comparative study of radio halo occurrence in SZ and X-ray selected galaxy cluster samples. *Mon. Not. R. Astron. Soc.*, 437(3):2163–2179.

Springel, V., Pakmor, R., Pillepich, A., Weinberger, R., Nelson, D., Hernquist, L., Vogelsberger, M., Genel, S., Torrey, P., Marinacci, F., and Naiman, J. (2018). First results from the IllustrisTNG simulations: matter and galaxy clustering. *Mon. Not. R. Astron. Soc.*, 475(1):676–698.

Strüder, L., Briel, U., Dennerl, K., Hartmann, R., Kendziorra, E., Meidinger, N., Pfeffermann, E., Reppin, C., Aschenbach, B., Bornemann, W., Bräuninger, H., Burkert, W., Elender, M., Freyberg, M., Haberl, F., Hartner, G., Heuschmann, F., Hippmann, H., Kastelic, E., Kemmer,

S., Kettenring, G., Kink, W., Krause, N., Müller, S., Oppitz, A., Pietsch, W., Popp, M., Predehl, P., Read, A., Stephan, K. H., Stötter, D., Trümper, J., Holl, P., Kemmer, J., Soltau, H., Stötter, R., Weber, U., Weichert, U., von Zanthier, C., Carathanassis, D., Lutz, G., Richter, R. H., Solc, P., Böttcher, H., Kuster, M., Staubert, R., Abbey, A., Holland, A., Turner, M., Balasini, M., Bignami, G. F., La Palombara, N., Villa, G., Buttler, W., Gianini, F., Lainé, R., Lumb, D., and Dhez, P. (2001). The European Photon Imaging Camera on XMM-Newton: The pn-CCD camera. *Astron. Astrophys.*, 365:L18–L26.

Stuardi, C., Bonafede, A., Wittor, D., Vazza, F., Botteon, A., Locatelli, N., Dallacasa, D., Golovich, N., Hoeft, M., van Weeren, R. J., Brüggen, M., and de Gasperin, F. (2019). Particle re-acceleration and Faraday-complex structures in the RXC J1314.4-2515 galaxy cluster. *Mon. Not. R. Astron. Soc.*, 489(3):3905–3926.

Sunyaev, R. A. and Zeldovich, Y. B. (1970). The Spectrum of Primordial Radiation, its Distortions and their Significance. *Comments on Astrophysics and Space Physics*, 2:66.

Sunyaev, R. A. and Zeldovich, Y. B. (1972). The Observations of Relic Radiation as a Test of the Nature of X-Ray Radiation from the Clusters of Galaxies. *Comments on Astrophysics and Space Physics*, 4:173.

Swarup, G., Ananthakrishnan, S., Kapahi, V. K., Rao, A. P., Subrahmanya, C. R., and Kulkarni, V. K. (1991). The Giant Metre-Wave Radio Telescope. *Current Science*, 60:95.

Swetz, D. S., Ade, P. A. R., Amiri, M., Appel, J. W., Battistelli, E. S., Burger, B., Chervenak, J., Devlin, M. J., Dicker, S. R., Doriese, W. B., Dünner, R., Essinger-Hileman, T., Fisher, R. P., Fowler, J. W., Halpern, M., Hasselfield, M., Hilton, G. C., Hincks, A. D., Irwin, K. D., Jarosik, N., Kaul, M., Klein, J., Lau, J. M., Limon, M., Marriage, T. A., Marsden, D., Martocci, K., Mauskopf, P., Moseley, H., Netterfield, C. B., Niemack, M. D., Nolta, M. R., Page, L. A., Parker, L., Staggs, S. T., Stryzak, O., Switzer, E. R., Thornton, R., Tucker, C., Wollack, E., and Zhao, Y. (2011). Overview of the Atacama Cosmology Telescope: Receiver, Instrumentation, and Telescope Systems. *Astrophys. J. Supp.*, 194(2):41.

Takey, A., Durret, F., Márquez, I., Ellien, A., Molham, M., and Plat, A. (2019). The 3XMM/SDSS Stripe 82 Galaxy Cluster Survey - II. X-ray and optical properties of the cluster sample. *Mon. Not. R. Astron. Soc.*, 486(4):4863–4879.

Tanaka, Y., Inoue, H., and Holt, S. S. (1994). The X-Ray Astronomy Satellite ASCA. *Pub. Astron. Soc. Japan*, 46:L37–L41.

Tarenghi, M. and Wilson, R. N. (1989). The ESO NTT (New Technology Telescope): The first active optics telescope. In Roddier, F. J., editor, *Active telescope systems*, volume 1114 of *Society of Photo-Optical Instrumentation Engineers (SPIE) Conference Series*, pages 302–313.

Tasse, C. (2014). Nonlinear Kalman filters for calibration in radio interferometry. *Astron. Astrophys.*, 566:A127.

Tasse, C., Hugo, B., Mirmont, M., Smirnov, O., Atemkeng, M., Bester, L., Hardcastle, M. J., Lakhoo, R., Perkins, S., and Shimwell, T. (2018). Faceting for direction-dependent spectral deconvolution. *Astron. Astrophys.*, 611:A87.

Thierbach, M., Klein, U., and Wielebinski, R. (2003). The diffuse radio emission from the Coma cluster at 2.675 GHz and 4.85 GHz. *Astron. Astrophys.*, 397:53–61.

Thompson, A. R. (1999). Fundamentals of Radio Interferometry. In Taylor, G. B., Carilli, C. L., and Perley, R. A., editors, *Synthesis Imaging in Radio Astronomy II*, volume 180 of *Astronomical Society of the Pacific Conference Series*, page 11.

Thompson, A. R., Moran, J. M., and Swenson, George W., J. (2017). *Interferometry and Synthesis in Radio Astronomy, 3rd Edition*.

Timmerman, R., van Weeren, R. J., McDonald, M., Ignesti, A., McNamara, B. R., Hlavacek-Larrondo, J., and Röttgering, H. J. A. (2020). Very Large Array observations of the mini-halo and AGN feedback in the Phoenix cluster. *arXiv e-prints*, page arXiv:2009.13238.

Tucker, W., Blanco, P., Rappoport, S., David, L., Fabricant, D., Falco, E. E., Forman, W., Dressler, A., and Ramella, M. (1998). 1E 0657-56: A Contender for the Hottest Known Cluster of Galaxies. *Astrophys. J. Lett.*, 496(1):L5–L8.

Tucker, W. H., Tananbaum, H., and Remillard, R. A. (1995). A Search for "Failed Clusters" of Galaxies. *Astrophys. J.*, 444:532.

Urdampilleta, I., Akamatsu, H., Mernier, F., Kaastra, J. S., de Plaa, J., Ohashi, T., Ishisaki, Y., and Kawahara, H. (2018). X-ray study of the double radio relic Abell 3376 with Suzaku. *Astron. Astrophys.*, 618:A74.

Vacca, V., Feretti, L., Giovannini, G., Govoni, F., Murgia, M., Perley, R. A., and Clarke, T. E. (2014). Spectral index image of the radio halo in the cluster Abell 520, which hosts the famous bow shock. *Astron. Astrophys.*, 561:A52.

Valtchanov, I., Murphy, T., Pierre, M., Hunstead, R., and Lémonon, L. (2002). Abell 1451 and 1RXS J131423.6-251521: A multi-wavelength study of two dynamically perturbed clusters of galaxies. *Astron. Astrophys.*, 392:795–805.

van Haarlem, M. P., Wise, M. W., Gunst, A. W., Heald, G., McKean, J. P., Hessels, J. W. T., de Bruyn, A. G., Nijboer, R., Swinbank, J., Fallows, R., Brentjens, M., Nelles, A., Beck, R., Falcke, H., Fender, R., Hörandel, J., Koopmans, L. V. E., Mann, G., Miley, G., Röttgering, H., Stappers, B. W., Wijers, R. A. M. J., Zaroubi, S., van den Akker, M., Alexov, A., Anderson, J., Anderson, K., van Ardenne, A., Arts, M., Asgekar, A., Avruch, I. M., Batejat, F., Bähren, L., Bell, M. E., Bell, M. R., van Bemmel, I., Bennema, P., Bentum, M. J., Bernardi, G., Best, P., Bîrzan, L., Bonafede, A., Boonstra, A. J., Braun, R., Bregman, J., Breitling, F., van de Brink, R. H., Broderick, J., Broekema, P. C., Brouw, W. N., Brüggen, M., Butcher, H. R., van Cappellen, W., Ciardi, B., Coenen, T., Conway, J., Coolen, A., Corstanje, A., Damstra, S., Davies, O., Deller, A. T., Dettmar, R. J., van Diepen, G., Dijkstra, K., Donker, P., Doorduin, A., Dromer, J., Drost, M., van Duin, A., Eislöffel, J., van Enst, J., Ferrari, C., Frieswijk, W., Gankema, H., Garrett, M. A., de Gasperin, F., Gerbers, M., de Geus, E., Grießmeier, J. M.,

Grit, T., Gruppen, P., Hamaker, J. P., Hassall, T., Hoeft, M., Holties, H. A., Horneffer, A., van der Horst, A., van Houwelingen, A., Huijgen, A., Iacobelli, M., Intema, H., Jackson, N., Jelic, V., de Jong, A., Juette, E., Kant, D., Karastergiou, A., Koers, A., Kollen, H., Kondratiev, V. I., Kooistra, E., Koopman, Y., Koster, A., Kuniyoshi, M., Kramer, M., Kuper, G., Lambropoulos, P., Law, C., van Leeuwen, J., Lemaitre, J., Loose, M., Maat, P., Macario, G., Markoff, S., Masters, J., McFadden, R. A., McKay-Bukowski, D., Meijering, H., Meulman, H., Mevius, M., Middelberg, E., Millenaar, R., Miller-Jones, J. C. A., Mohan, R. N., Mol, J. D., Morawietz, J., Morganti, R., Mulcahy, D. D., Mulder, E., Munk, H., Nieuwenhuis, L., van Nieuwpoort, R., Noordam, J. E., Norden, M., Noutsos, A., Offringa, A. R., Olofsson, H., Omar, A., Orrú, E., Overeem, R., Paas, H., Pandey-Pommier, M., Pandey, V. N., Pizzo, R., Polatidis, A., Rafferty, D., Rawlings, S., Reich, W., de Reijer, J. P., Reitsma, J., Renting, G. A., Riemers, P., Rol, E., Romein, J. W., Roosjen, J., Ruiter, M., Scaife, A., van der Schaaf, K., Scheers, B., Schellart, P., Schoenmakers, A., Schoonderbeek, G., Serylak, M., Shulevski, A., Sluman, J., Smirnov, O., Sobey, C., Spreeuw, H., Steinmetz, M., Sterks, C. G. M., Stiepel, H. J., Stuurwold, K., Tagger, M., Tang, Y., Tasse, C., Thomas, I., Thoudam, S., Toribio, M. C., van der Tol, B., Usov, O., van Veelen, M., van der Veen, A. J., ter Veen, S., Verbiest, J. P. W., Vermeulen, R., Vermaas, N., Vocks, C., Vogt, C., de Vos, M., van der Wal, E., van Weeren, R., Weggemans, H., Weltevrede, P., White, S., Wijnholds, S. J., Wilhelmsson, T., Wucknitz, O., Yatawatta, S., Zarka, P., Zensus, A., and van Zwieten, J. (2013). LOFAR: The LOw-Frequency ARray. *Astron. Astrophys.*, 556:A2.

van Moorsel, G., Kemball, A., and Greisen, E. (1996). AIPS Developments in the Nineties. In Jacoby, G. H. and Barnes, J., editors, *Astronomical Data Analysis Software and Systems V*, volume 101 of *Astronomical Society of the Pacific Conference Series*, page 37.

van Weeren, R. J., Andrade-Santos, F., Dawson, W. A., Golovich, N., Lal, D. V., Kang, H., Ryu, D., Brìggen, M., Ogrean, G. A., Forman, W. R., Jones, C., Placco, V. M., Santucci, R. M., Wittman, D., Jee, M. J., Kraft, R. P., Sobral, D., Stroe, A., and Fogarty, K. (2017). The case for electron re-acceleration at galaxy cluster shocks. *Nature Astronomy*, 1:0005.

van Weeren, R. J., Brüggen, M., Röttgering, H. J. A., and Hoeft, M. (2011). Relics as Probes of Galaxy Cluster Mergers. *Journal of Astrophysics and Astronomy*, 32:505–508.

van Weeren, R. J., Brunetti, G., Brüggen, M., Andrade-Santos, F., Ogrean, G. A., Williams, W. L., Röttgering, H. J. A., Dawson, W. A., Forman, W. R., de Gasperin, F., Hardcastle, M. J., Jones, C., Miley, G. K., Rafferty, D. A., Rudnick, L., Sabater, J., Sarazin, C. L., Shimwell, T. W., Bonafede, A., Best, P. N., Bîrzan, L., Cassano, R., Chyży, K. T., Croston, J. H., Dijkema, T. J., Enßlin, T., Ferrari, C., Heald, G., Hoeft, M., Horellou, C., Jarvis, M. J., Kraft, R. P., Mevius, M., Intema, H. T., Murray, S. S., Orrú, E., Pizzo, R., Sridhar, S. S., Simionescu, A., Stroe, A., van der Tol, S., and White, G. J. (2016). LOFAR, VLA, and Chandra Observations of the Toothbrush Galaxy Cluster. *Astrophys. J.*, 818(2):204.

van Weeren, R. J., de Gasperin, F., Akamatsu, H., Brüggen, M., Feretti, L., Kang, H., Stroe, A., and Zandanel, F. (2019). Diffuse Radio Emission from Galaxy Clusters. *Space Sci. Rev.*, 215(1):16.

van Weeren, R. J., Röttgering, H. J. A., Rafferty, D. A., Pizzo, R., Bonafede, A., Brüggen, M., Brunetti, G., Ferrari, C., Orrù, E., Heald, G., McKean, J. P., Tasse, C., de Gasperin, F., Bîrzan, L., van Zwieten, J. E., van der Tol, S., Shulevski, A., Jackson, N., Offringa, A. R., Conway, J., Intema, H. T., Clarke, T. E., van Bemmel, I., Miley, G. K., White, G. J., Hoeft, M., Cassano, R., Macario, G., Morganti, R., Wise, M. W., Horellou, C., Valentijn, E. A., Wucknitz, O., Kuijken, K., Enßlin, T. A., Anderson, J., Asgekar, A., Avruch, I. M., Beck, R., Bell, M. E., Bell, M. R., Bentum, M. J., Bernardi, G., Best, P., Boonstra, A. J., Brentjens, M., van de Brink, R. H., Broderick, J., Brouw, W. N., Butcher, H. R., van Cappellen, W., Ciardi, B., Eislöffel, J., Falcke, H., Fender, R., Garrett, M. A., Gerbers, M., Gunst, A., van Haarlem, M. P., Hamaker, J. P., Hassall, T., Hessels, J. W. T., Koopmans, L. V. E., Kuper, G., van Leeuwen, J., Maat, P., Millenaar, R., Munk, H., Nijboer, R., Noordam, J. E., Pandey, V. N., Pandey-Pommier, M., Polatidis, A., Reich, W., Scaife, A. M. M., Schoenmakers, A., Sluman, J., Stappers, B. W., Steinmetz, M., Swinbank, J., Tagger, M., Tang, Y., Vermeulen, R., de Vos,

M., and van Haarlem, M. P. (2012). First LOFAR observations at very low frequencies of cluster-scale non-thermal emission: the case of Abell 2256. *Astron. Astrophys.*, 543:A43.

van Weeren, R. J., Shimwell, T. W., Botteon, A., Brunetti, G., Brüggen, M., Boxelaar, J. M., Cassano, R., Di Gennaro, G., Andrade-Santos, F., Bonnassieux, E., Bonafede, A., Cuciti, V., Dallacasa, D., de Gasperin, F., Gastaldello, F., Hardcastle, M. J., Hoeft, M., Kraft, R. . P., Mandal, S., Rossetti, M., Röttgering, H. J. A., Tasse, C., and Wilber, A. G. (2020). LOFAR observations of galaxy clusters in HETDEX. *arXiv e-prints*, page arXiv:2011.02387.

Vavilova, I., Elyiv, A., Dobrycheva, D., and Melnyk, O. (2020). The Voronoi tessellation method in astronomy. *arXiv e-prints*, page arXiv:2012.08965.

Vazza, F. and Brüggen, M. (2014). Do radio relics challenge diffusive shock acceleration? *Mon. Not. R. Astron. Soc.*, 437(3):2291–2296.

Venturi, T., Bardelli, S., Dallacasa, D., Brunetti, G., Giacintucci, S., Hunstead, R. W., and Morganti, R. (2003). The radio halo in the merging cluster A3562. *Astron. Astrophys.*, 402:913–920.

Venturi, T., Bardelli, S., Dallacasa, D., Di Gennaro, G., Gastaldello, F., Giacintucci, S., and Rossetti, M. (2017a). Extended Radio Emission in the Perhipheral Regions of the Shapley Concentration Core. *Galaxies*, 5(1):16.

Venturi, T., Bardelli, S., Morganti, R., and Hunstead, R. W. (2000). Radio properties of the Shapley Concentration - III. Merging clusters in the A3558 complex. *Mon. Not. R. Astron. Soc.*, 314(3):594–610.

Venturi, T., Giacintucci, S., Brunetti, G., Cassano, R., Bardelli, S., Dallacasa, D., and Setti, G. (2007). GMRT radio halo survey in galaxy clusters at z = 0.2-0.4. I. The REFLEX sub-sample. *Astron. Astrophys.*, 463(3):937–947.

Venturi, T., Giacintucci, S., Dallacasa, D., Cassano, R., Brunetti, G., Bardelli, S., and Setti, G. (2008). GMRT radio halo survey in galaxy clusters at z = 0.2-0.4. II. The eBCS clusters and analysis of the complete sample. *Astron. Astrophys.*, 484(2):327–340.

Venturi, T., Giacintucci, S., Dallacasa, D., Cassano, R., Brunetti, G., Macario, G., and Athreya, R. (2013). Low frequency follow up of radio haloes and relics in the GMRT Radio Halo Cluster Survey. *Astron. Astrophys.*, 551:A24.

Venturi, T., Giovannini, G., and Feretti, L. (1990). High-Sensitivity Radio Observations of the Coma Cluster of Galaxies. *Astron. J.*, 99:1381.

Venturi, T., Rossetti, M., Brunetti, G., Farnsworth, D., Gastaldello, F., Giacintucci, S., Lal, D. V., Rudnick, L., Shimwell, T. W., Eckert, D., Molendi, S., and Owers, M. (2017b). The two-component giant radio halo in the galaxy cluster Abell 2142. *Astron. Astrophys.*, 603:A125.

Vikhlinin, A., McNamara, B. R., Forman, W., Jones, C., Quintana, H., and Hornstrup, A. (1998). A Catalog of 200 Galaxy Clusters Serendipitously Detected in the ROSAT PSPC Pointed Observations. *Astrophys. J.*, 502(2):558–581.

Voges, W. (1992). The ROSAT All-Sky X-ray survey. Environment Observation and Climate Modelling Through International Space Projects.

Voges, W., Aschenbach, B., Boller, T., Bräuninger, H., Briel, U., Burkert, W., Dennerl, K., Englhauser, J., Gruber, R., Haberl, F., Hartner, G., Hasinger, G., Kürster, M., Pfeffermann, E., Pietsch, W., Predehl, P., Rosso, C., Schmitt, J. H. M. M., Trümper, J., and Zimmermann, H. U. (1999). The ROSAT all-sky survey bright source catalogue. *Astron. Astrophys.*, 349:389–405.

Vogt, C., Dolag, K., and Enßlin, T. A. (2005). PACERMAN- II. Application and statistical characterization of improved RM maps. *Mon. Not. R. Astron. Soc.*, 358(3):732–741.

Weinberg, D. H., Mortonson, M. J., Eisenstein, D. J., Hirata, C., Riess, A. G., and Rozo, E. (2013). Observational probes of cosmic acceleration. *Phys. Rep.*, 530(2):87–255.

Wen, Z. L. and Han, J. L. (2013). Substructure and dynamical state of 2092 rich clusters of galaxies derived from photometric data. *Mon. Not. R. Astron. Soc.*, 436(1):275–293.

Wilber, A., Brüggen, M., Bonafede, A., Savini, F., Shimwell, T., van Weeren, R. J., Rafferty, D., Mechev, A. P., Intema, H., Andrade-Santos, F., Clarke, A. O., Mahony, E. K., Morganti, R.,

Prandoni, I., Brunetti, G., Röttgering, H., Mandal, S., de Gasperin, F., and Hoeft, M. (2018). LOFAR discovery of an ultra-steep radio halo and giant head-tail radio galaxy in Abell 1132. *Mon. Not. R. Astron. Soc.*, 473(3):3536–3546.

Willson, M. A. G. (1970). Radio observations of the cluster of galaxies in Coma Berenices - the 5C4 survey. *Mon. Not. R. Astron. Soc.*, 151:1.

Xie, C., van Weeren, R. J., Lovisari, L., Andrade-Santos, F., Botteon, A., Brüggen, M., Bulbul, E., Churazov, E., Clarke, T. E., Forman, W. R., Intema, H. T., Jones, C., Kraft, R. P., Lal, D. V., Mroczkowski, T., and Zitrin, A. (2020). The discovery of radio halos in the frontier fields clusters Abell S1063 and Abell 370. *Astron. Astrophys.*, 636:A3.

Yee, H. K. C. and Gladders, M. D. (2002). Optical Surveys for Galaxy Clusters. In Chen, L.-W., Ma, C.-P., Ng, K.-W., and Pen, U.-L., editors, *AMiBA 2001: High-Z Clusters, Missing Baryons, and CMB Polarization*, volume 257 of *Astronomical Society of the Pacific Conference Series*, page 109.

Yokoyama, S. L. and Ohira, Y. (2020). Particle Acceleration in a Shock Wave Propagating to an Inhomogeneous Medium. *Astrophys. J.*, 897(1):50.

Yuan, Z. S. and Han, J. L. (2020). Dynamical state for 964 galaxy clusters from Chandra X-ray images. *Mon. Not. R. Astron. Soc.*, 497(4):5485–5497.

Yuan, Z. S., Han, J. L., and Wen, Z. L. (2015). The Scaling Relations and the Fundamental Plane for Radio Halos and Relics of Galaxy Clusters. *Astrophys. J.*, 813(1):77.

Zandanel, F., Pfrommer, C., and Prada, F. (2014). On the physics of radio haloes in galaxy clusters: scaling relations and luminosity functions. *Mon. Not. R. Astron. Soc.*, 438(1):124–144.

Zenteno, A., Hernández-Lang, D., Klein, M., Vergara Cervantes, C., Hollowood, D. L., Bhargava, S., Palmese, A., Strazzullo, V., Romer, A. K., Mohr, J. J., Jeltema, T., Saro, A., Lidman, C., Gruen, D., Ojeda, V., Katzenberger, A., Aguena, M., Allam, S., Avila, S., Bayliss, M.,

Bertin, E., Brooks, D., Buckley-Geer, E., Burke, D. L., Capasso, R., Carnero Rosell, A., Carrasco Kind, M., Carretero, J., Castander, F. J., Costanzi, M., da Costa, L. N., De Vicente, J., Desai, S., Diehl, H. T., Doel, P., Eifler, T. F., Evrard, A. E., Flaugher, B., Floyd, B., Fosalba, P., Frieman, J., García-Bellido, J., Gerdes, D. W., Gonzalez, J. R., Gruendl, R. A., Gschwend, J., Gutierrez, G., Hartley, W. G., Hinton, S. R., Honscheid, K., James, D. J., Kuehn, K., Lahav, O., Lima, M., McDonald, M., Maia, M. A. G., March, M., Melchior, P., Menanteau, F., Miquel, R., Ogando, R. L. C., Paz-Chinchón, F., Plazas, A. A., Roodman, A., Rykoff, E. S., Sanchez, E., Scarpine, V., Schubnell, M., Serrano, S., Sevilla-Noarbe, I., Smith, M., Soares-Santos, M., Suchyta, E., Swanson, M. E. C., Tarle, G., Thomas, D., Varga, T. N., Walker, A. R., Wilkinson, R. D., and DES Collaboration (2020). A joint SZ-X-ray-optical analysis of the dynamical state of 288 massive galaxy clusters. *Mon. Not. R. Astron. Soc.*, 495(1):705–725.

Zhu, Y., Wang, Y.-H., Zhao, H.-H., Jia, S.-M., Li, C.-K., and Chen, Y. (2019). The Y $_{SZ,Planck}$ - Y $_{SZ,XMM}$ scaling relation and its difference between cool-core and non-cool-core clusters. *Research in Astronomy and Astrophysics*, 19(7):104.

Zimbardo, G. and Perri, S. (2017). Superdiffusive shock acceleration at galaxy cluster shocks. *Nature Astronomy*, 1:0163.

Zimbardo, G. and Perri, S. (2018). Understanding the radio spectral indices of galaxy cluster relics by superdiffusive shock acceleration. *Mon. Not. R. Astron. Soc.*, 478(4):4922–4930.

ZuHone, J. A., Brunetti, G., Giacintucci, S., and Markevitch, M. (2015). Testing Secondary Models for the Origin of Radio Mini-Halos in Galaxy Clusters. *Astrophys. J.*, 801(2):146.

Zwicky, F. (1933). Die Rotverschiebung von extragalaktischen Nebeln. *Helvetica Physica Acta*, 6:110–127.

Zwicky, F. (1938). On the Clustering of Nebulae. *Pub. Astron. Soc. Pacific*, 50(296):218–220.

Zwicky, F. and Kowal, C. T. (1968). *"Catalogue of Galaxies and of Clusters of Galaxies", Volume VI*.